Production and Properties of Two Dimensional Borocarbonitrides Using Chemical Vapor Deposition Growth

A thesis submitted for the degree of

Doctor of Philosophy in Materials



Eoin O'Sullivan

Oriel College, University of Oxford

Trinity 2023

Declaration

I confirm that the work presented in this thesis is my own work. No part of this thesis has been accepted or is currently being submitted for any degree, diploma, certificate or other qualification in this University or elsewhere. This thesis is my own work, except where indicated.

Abstract

Graphene and hexagonal boron nitride (hBN) are two of the most widely studied two-dimensional (2D) nanomaterials and their development is considered mature in the field. Although they possess a similar structure, their opto-electronic properties vary significantly – graphene is a zero-bandgap material while hBN has a wide band gap. Recently, synthesis of hybrid structures of these materials, comprised of boron, carbon and nitrogen, has piqued interest due to the tuneability of the opto-electronic and chemical properties of the system by its atomic composition and their arrangement within the network. Formally known as borocarbonitrides (BCN), synthesis of these structures is a promising field of research due to potential applications in catalysis, energy storage, and opto-electronics. However, cost-effective, scalable methods to produce high quality BCN materials are required for adoption. This thesis aims to address this research gap by establishing a low-cost synthesis protocol for 2D BCN structures, using safe-to-handle precursors, methane and ammonia borane, and facile synthesis apparatus, atmospheric pressure chemical vapor deposition (APCVD).

Pristine metal substrates of Cu and Fe are investigated and reviewed for the APCVD growth of 2D BCN. It is found that for *surface-mediated* growth of carbon doped hBN (hBN-C) on Cu, different growth mechanisms are present at various partial pressures of methane, affecting the material's morphology and opto-electronic properties in differing ways. For modulation of the bandgap of hBN, C doping is restricted to low partial pressures of CH_4 only. At higher partial pressures, C segregation and graphene formation occurs, which restores the bandgap of hBN, something which has not been reported in the literature. Performing complementary Density Functional Theory (DFT) calculations, the first comparative study on the atomic processes of B, C and N on Cu reveals insights into the behaviour of the precursors on the substrate, and sheds light on the different growth mechanisms observed at the various methane partial pressures employed during our hBN-C CVD study on Cu.

Mechanical robustness of films is a consideration for certain applications and so multi-layer growth of hBN-C films is investigated for the first time via a *segregation-mediated* growth mechanism on Fe substrates. Even at significantly higher partial pressures of methane, no sign of C and BN segregation is observed, while a tuneable optical bandgap from 5.92 eV to 5.31 eV is found, suggesting the segregation growth mechanism on Fe is more accommodating when synthesising carbon doped hBN than surface-mediated growth on Cu.

In parallel to CVD investigations, DFT methods are employed to study the opto-electronic properties of hBCN materials. Due to the propensity for graphene and hBN to segregate, graphene-hBN lateral heterostructures are chosen as the system for study, assessing their viability as photo-catalysts in the water-splitting reaction. Seven systems are investigated, starting from pure hBN and increasing the C content of the carbon domain at the centre until a pure graphene domain is obtained. Three systems are found to have suitable opto-electronic properties of band-gap and band-edge potentials for the hydrogen evolution reaction (HER) and oxygen evolution reaction (OER), with two of these showing photo-activity in the solar spectrum, and are proposed as potential photo-catalysts for further future investigations.

Over the course of this study, challenges were identified in using aged or low-purity ammonia-borane for hBN growth. Experiments using commercially available, low-purity precursor were compared with results from syntheses using high purity ammonia-borane, which has not been carried out in the literature previously. The low purity AB precursor resulted in ubiquitous growth of silica nanoplatelets on the Cu surface, interfering with hBN deposition. The origin of these structures is investigated, highlighting the importance of appropriate precursor and CVD apparatus selection in hBN synthesis. A growth mechanism for the structures is presented based on the diffusion limited aggregation model of growth, which occurs as a result of SiO_2 contamination via the quartz CVD reactor and B_xO_y activation by the low-purity precursor. Improved CVD protocols are outlined to avoid their formation in future studies.

Finally, a simple, cost-effective and up-scalable method to produce high-quality porous BCN-metal composites is developed based on prior BCN growth studies on Cu pristine metal foils. Using Cu metal powders, porous metal scaffolds were realised via thermal annealing, which can offer a significant cost reduction compared to commercially available alternatives. 3D BCN@Cu foam composites were realised via *simultaneous* and *sequential* deposition techniques, providing BCN materials with different morphologies and level of B,N doping which can add functionality to the Cu foam for many future far-reaching applications.

Preface

Conference Posters and Presentations

May 2022	***Comparing Carbon Doping in MOVPE and APCVD hBN films***
	Poster presentation
	MRS Spring Meeting, Honolulu, Hawaii (virtual)
March 2021	***Investigating Carbon Doping in Hexagonal Boron Nitride***
	Poster presentation
	NT21, Rice University, Texas (virtual)
February 2019	***BCN Nanomaterial Growth and Electronics***
	Research presentation
	Department of Materials, University of Oxford

Publications

1. **"Density Functional Theory Investigation of 2D Phase Separated Graphene/Hexagonal Boron Nitride Monolayers; Band Gap, Band Edge Positions, and Photo Activity"**, E O'Sullivan, N Grobert, M Swart. (*in submission)*

2. **"Mechanisms of h-BCN APCVD Growth on Copper: DFT Insights and Experimental Observations"**, E O'Sullivan, D McGurty, J Ballentine, M Swart, N Grobert. (*written up*)

3. **"Purity Matters: Inhibited hBN Deposition and Borosilicate Formation from Low-Grade Ammonia Borane on Copper"**, E O'Sullivan, J Ballentine, D McGurty, N Grobert. (*written up)*

4. **"Electrophoretic Deposition of Reduced Carbon Nanotube Solutions as a Route to the Production of Pure Buckyfilms with Retention of Starting Material Nanostructure"**, J Ballentine, D McGurty, E O'Sullivan, A Wang, B Bauer, B Maciejewska and N Grobert. (*written up)*

5. **"Two-Step Aerosol Assisted Synthesis of Structurally Uniform $B_xC_yN_z$ Nanotubes: Tuning Properties via Co-Doping"**, D McGurty, E O'Sullivan, J Ballentine, K L Ng, P Holdway, B Maciejewska and N Grobert. (*written up*)

Acknowledgements

This work would not have been possible without the many people who supported me throughout this rather protracted process of completing a DPhil.

In the NbD research group, I formed friendships which will far outlast our time spent toiling away in the lab. To Pierre Romain, the big mountain man, your infectious giddiness made even the glummest of days in Begbroke that bit brighter, thank you. To the chefs Dr. Pablo Velasco and Dr Albert Xiao, BBQ food will never taste the same after attending your fantastic all-day cook outs. The days we spent at Ashton's Eyot are some of my fondest memories.

Many thanks to Dr. Colin Johnston, Dr. Philip Holdway, Nicola Flannigan, and Chris Salter of the OMCS team at Begbroke. Their training and data acquisition on the various characterisation equipment made my work infinitely smoother. Similarly, I would like to acknowledge Greg Cook, Dr. Neil Young, Dr. Ian Griffiths and Jennifer Holter for their help with operating the various electron microscopes in the DCCEM.

Despite the many attempts by COVID to thwart international travel and research, I was fortunate enough to work and collaborate with the Institut de Quimica Computacional I Catàlisi at the University of Girona. I would like to express my sincere gratitude to Professor Marcel Swart for his guidance on the computational work in this thesis, as well as his patience for my many questions along the way. My trip to Girona was one of the highlights of my PhD, thank you for making this possible. Furthermore, thanks to the HPC-Europa3 programme and the Barcelona Supercomputing Centre for facilitating these collaborative connections.

To my Oriel crew, thank you for the fantastic memories forged during my time at Oxford. I would like to thank Lukas Boehnert for allowing me to play Art Garfunkel to his Paul Simon over the years of playing music together. Jack Mazzotti, I still laugh thinking about the number of ticks you encountered in Loch Lomond. I am truly lucky to have met you both on my first day at Oriel (LEJends). I also wish to thank Mike Selby, Philip Gavin, Chase Harrison, Josh Hyde, Tanmayee Deshprabhu, Luke Young, Dr. Jessica Rushton and Dr. Angelica de Vido for making our Middle Common Room at Oriel a community.

I would like to thank my teammates and friends in OURFC (sorry, but there are too many to name). You made my last year in Oxford a special one for so many reasons.

For my brothers; Dr. John Ballentine and Dillon McGurty. We have been on this journey together from Day 1, experiencing each other's highs and lows, terrific milestones, and tough losses. Enduring this odyssey would not have been possible without you both, so thank you. Charles Darwin once wrote, "a man's friendships are a measure of his worth" and with you both, I feel all the richer.

For my siblings; Ross, Sive and Cian. Thanks for ensuring I never had 'serious notions' from being at Oxford. Hopefully, Nana will still give me the student treatment even after I finish this PhD.

For my parents; John and Áine. Thank you for your constant love and support. Your attitudes towards life have given me perspective when I needed it most. Thank you for making me the man I am today. I hope that I have and will continue to make you proud.

Finally, for Dr. Lauren Cullen, the Bonnie to my Clyde. Thank you for being the Superwoman that you are. You have provided me with endless kindness, support, and patience throughout this journey. I can't wait to see where life takes us next.

Contents

Declaration i
Abstract ii
Preface iv
Acknowledgements v
List of symbols and abbreviations 6
Chapter 1 - Introduction 1
1.1. Motivation, prospective applications, and challenges 2
1.2. Thesis structure 3
1.3. Literature Review 5
1.3.1. 2D nanomaterials; the Flatlands 5
1.3.2. sp^2 hybridised systems – atomic and electronic structure 5
1.3.3. Hexagonal boron nitride; structure, properties, and potential applications 8
1.3.4. Hexagonal borocarbonitride; structure, properties, and potential applications 17
1.3.5. 2D Material Synthesis Overview 29
Chapter 2 – Characterisation Methods 42
2.1. Scanning Electron Microscope 43
2.2. Energy dispersive x-ray spectroscopy 46
2.3. Transmission electron microscopy 47
2.4. Optical Microscopy 48
2.5. Optical Profilometry 49
2.6. X-ray Photoelectron Spectroscopy 51
2.7. Raman Spectroscopy 54
2.8. UV-vis Spectroscopy 57
2.9. Materials Modelling 59
2.9.1. Ab-initio theory 60
2.9.2. Born-Oppenheimer Approximation 61
2.9.3. Hartree-Fock theory 61
2.9.4. Electron Correlation 62
2.9.5. Density Functional Theory (DFT) 63
Chapter 3 – Synthesis of Borocarbonitride Materials on Pristine Metal Foils 67
3.1 Introduction 68
3.2. Materials and Methods 69
3.3. Results & Discussion 76
3.3.1. Theoretical Insights into the Atomic Processes of B, C and N on Cu(111) 76
3.3.2. hBN Synthesis on Pristine Copper 84

3.3.3. Carbon doped hBN grown on Cu metal foils 95
3.3.4. Multilayered hBN Synthesis on Pristine Iron 120
3.3.5. Carbon doping of hBN films grown on Fe 127
3.4. Conclusion, summary and outlook; 134
Chapter 4 - 2D Phase Separated Graphene/hBN toward catalysis: a DFT Study 136
4.1. Introduction 137
4.2. Materials and Methods 139
4.3. Results and Discussion 140
4.4. Conclusion, summary and outlook; 157
Chapter 5 – Growth of B, N doped silica nanoplatelets on copper through low-purity ammonia borane activation 159
5.1. Introduction 160
5.2. Materials and Methods 162
5.3. Results and Discussion 163
5.3.1. APCVD growth of hBN on copper using aged ammonia borane 163
5.3.2. Formation of silicate particles on copper using low-purity ammonia borane 166
5.3.3. Washing and recrystallization of AB precursor 175
5.3.4. Ball milling of ammonia borane with hBN powder for enhanced borazine selectivity 177
5.3.5. Proposed mechanism for B,N doped silica growth 182
5.4. Conclusion 186
Chapter 6 - Porous Nanomaterial 3D Foam Composites 189
6.1. Introduction 190
6.2. Materials and Methods 195
6.3. Results & Discussion 197
6.3.1. Synthesis of Porous 3D metal foam from Cu powder 197
6.3.2. Graphene on copper foam 198
6.3.3. hBN on copper foam 202
6.3.4. Graphene-hBN on copper foam 205
6.3.5. hBCN on copper foam 209
6.4. Conclusion 213
Chapter 7 - Conclusions & Future work 216
7.1. Summary of findings 217
7.2. Future Research Directions 221
8. Appendices 226
8.1. Appendix I: Cost analysis of Cu@BCN vs Pt-coated electrode 226
8.2. Appendix II: Synthesis of 2D BCN Materials on Pristine Metal Foils 240
8.3. Appendix III: 2D lateral Graphene/hBN heterostructures toward catalysis - a DFT Study .. 242
8.4. Appendix IV: Step-wise CVD growth of Gr-hBN heterostructures on Cu metal foils……..247

8.4. Appendix V: B, N doped silica nanoplatelets on copper through low-purity ammonia borane activation……..250

9. Bibliography 250

List of figures

Figure 1; BCN reports and citations. 2
Figure 2; Structure of layered materials hexagonal boron nitride (hBN) and graphite..... 5
Figure 3; Superposition of 2 honeycomb lattices, A and B. 6
Figure 4; band structures of (a) graphene and (b) hBN sp^2 lattices using the tight binding approach... 7
Figure 5; Various crystallographic structures of BN..... 8
Figure 6; Electronic applications of hBN 9
Figure 7; hBN as electrode materials..... 10
Figure 8; Optical properties of bulk hBN 11
Figure 9; DUV emission and detection with hBN 13
Figure 10; Catalytic synergy in hBN catalytic supports. 15
Figure 11; Metal supported hBN as electrocatalysts..... 16
Figure 12; Ternary phase diagram, showing the different phases in the B-C-N system. 17
Figure 13; Structure of hBCN systems; (i) segregated hBN/Gr (ii) homogenous BCN 19
Figure 14; Vertically stacked hBCN materials..... 20
Figure 15; Band gap reduction with C point defects in hBN..... 21
Figure 16; C doped hBN as active materials in electronic devices..... 22
Figure 17; Opto-electronic properties of C doped hBN 24
Figure 18; Catalytic efficiency enhancement in BCN materials..... 25
Figure 19; HER/OER activity of hBCN materials..... 27
Figure 20; BCN as sensing materials..... 28
Figure 21; Pyrolysis for 2D BCN material production 31
Figure 22; Molecular Beam Epitaxy for 2D BCN material production.. 32
Figure 23; Simplified CVD set up for 2D materials 33
Figure 24: Influence of catalytic substrate on hBN CVD growth..... 34
Figure 25; Alloyed metal substrates for 2D hBCN growth 36
Figure 26; LMCats for CVD growth of 2D hBCN 37
Figure 27; Substrate engineering for large single crystal growth 38
Figure 28: Common precursors used for hBCN growth via CVD..... 40
Figure 29, Scanning electron microscopy (SEM) working principles 43
Figure 30; SEM contrast between 2DM and underlying substrate and imaging features..... 45
Figure 31; Energy Dispersive X-ray Spectroscopy (EDX) working principles..... 46
Figure 32; Transmission Electron Microscope - apparatus and experimental details..... 48
Figure 33; Optical Microscope working principle and experimental details 49
Figure 34; Optical profilometry working principle and examples of data analysis 50
Figure 35; XPS working principle and examples of data analysis..... 52
Figure 36; XPS energy values from literature on BCN materials..... 53
Figure 37; Raman spectroscopy of graphene materials 55
Figure 38; Raman spectrum of hBN 56
Figure 39; Raman characteristics of 2D BCN 57
Figure 40; UV-vis characterisation of BCN using Tauc and Urbach plots. 59
Figure 41; Jacob's ladder; choosing the appropriate correlation function in DFT 65
Figure 42; Schematic of the APCVD set up used in this thesis 72
Figure 43; 2D material film transfer using PMMA support layer 74

Figure 44; Adsorption sites on Cu(111).....77
Figure 45; Sublayer site of B in Cu(111).....78
Figure 46; Equilibrium shapes of hBN on Cu; triangular domains 79
Figure 47; Energies of diffusion and penetration of B, C and N atoms on the Cu(111) surface. 80
Figure 48; Potential energy surfaces of B, C and N along diffusion paths on the surface and into the sublayer of Cu.....82
Figure 49; SEM image of hBCN grown on Cu with overlaid atomic structure visual 83
Figure 50; Growth parameters for APCVD hBN synthesis studies on Cu 86
Figure 51; hBN film quality using different loading mass of AB.....87
Figure 52; Effect of heating temperature of AB 88
Figure 53; Optimised growth of hBN. 90
Figure 54; TEM analysis of optimised hBN film 92
Figure 55; Opto-electronic characterisation of optimised hBN film.....94
Figure 56; SEM of $hBNC_1$ growth at (a) t = 60 mins and (b) t =120 mins.....98
Figure 57; SEM and Raman Characterisation of $hBNC_2$ growth. 99
Figure 58; TEM images of $hBNC_2$ sample with amorphous regions observed. 100
Figure 59; Raman characterisation of samples synthesised under low p.p methane. 101
Figure 60; SEM and Raman characterisation of $hBNC_3$ sample 103
Figure 61; TEM analysis of $hBNC_3$ showing additional regions of rotated adlayer growth 105
Figure 62; Characterisation of $hBNC_4$ sample.....109
Figure 63; TEM analysis of $hBNC_4$ sample.....111
Figure 64; XPS characterisation of hBN and $hBNC_x$ samples 113
Figure 65; Calculated formation energies of doped graphene structures.....115
Figure 66; UV-vis spectroscopic characterisation of hBN and hBNC samples.....116
Figure 67; Structural properties of iron allotropes.....121
Figure 68; Schematic of the CVD process for segregated growth.....123
Figure 69; Influence of cooling rate on hBN film coverage 124
Figure 70; Influence of holding temperature on film thickness.....125
Figure 71, Characterisation of BNNTs formed on Fe foil. 126
Figure 72; XPS analysis of hBN and hBN-C grown on Fe 129
Figure 73; EDX analysis of (a) hBN and (b) $hBNC_6$ on Fe.....130
Figure 74; TEM analysis of hBN and $hBNC_6$ samples.....131
Figure 75; Opto-electronic characterisation of hBN-C samples synthesised on Fe foils.....132
Figure 76; Atomic structures of calculated monolayer BN-C islands in Chapter 4.....141
Figure 77; Formation energies per C atom vs. carbon concentration of the structure. 142
Figure 78; Electronic band gap vs α for various hBCN structures. 143
Figure 79; Partial density of states (PDOS) for the structures calculated.....145
Figure 80; Visualisation of HOMO and LUMO orbitals for the various systems 146
Figure 81; Band edges of the BNCx structures in comparison to optimal band edge positions for HER/OER and CO2RR.....148
Figure 82; HOMO and LUMO levels of the three optimal BN-C structures modified at pH = 7 and T = 298 K. 151
Figure 83; Oscillator strength with respect to excitation energy for the various BN-C stru.....152
Figure 84, Characterisation of Gr-hBN lateral heterostructures grown on Cu.....154
Figure 85, Comparison of Gr-hBN full-film heterostructures resulting from SMCat and LMCat growth on Cu.....157
Figure 86; Particulate impurities observed in hBN CVD growth studies.....161
Figure 87; hBN synthesis carried out using aged ammonia borane precursor (Sigma Aldrich – 97% purity) after 6 months.....164
Figure 88; FTIR of ammonia borane precursor at various ages.....165
Figure 89; SEM of hBN growth using lower purity AB, (TCL - 85% purity).....167

Figure 90; EDX of growth structures resulting on Cu foil after growth with low-purity AB..... 168
Figure 91; Interpretation of the growth structures as determined via XPS..... 169
Figure 92; XPS analysis of silicon content in Cu foil pre-synthesis, post synthesis and in the control experiment..... 171
Figure 93; XPS analysis of Cu foil and of ultra-pure Cu foil..... 173
Figure 94; SEM analysis of hBN synthesis carried out on KOH + acetic acid cleaned 99.8% purity Cu foil and ultra-high purity Cu foil..... 174
Figure 95; FTIR analysis of as received (black) and washed (blue) TCI AB precursor..... 176
Figure 96; SEM of hBN growth using washed and recrystallised AB precursor..... 177
Figure 97; SEM analysis of hBN synthesis using AB precursor ball milled with hBN powder..... 179
Figure 98; OP measurements of B,N doped SiOx structures transferred onto Si/SiO2 substrate..... 180
Figure 99; TEM analysis of growth structures seen in Figure 96..... 181
Figure 100; Growth mechanism for B,N doped silica layers on copper..... 184
Figure 101; Viscosity of various silica based materials across a temperature scale..... 185
Figure 102; Schematic for the CVD formation of 2DM-metal foam composites and 2DM foams... 191
Figure 103; Applications of 2D graphene - 3D metal foam composites..... 193
Figure 104; Applications of BCN freestanding foams..... 195
Figure 105; Synthesis of bare Cu foam template..... 198
Figure 106; SEM analysis of graphene deposition on Cu foam..... 199
Figure 107; Etching and washing of Cu foam..... 200
Figure 108; Characterisation of Graphene foam..... 201
Figure 109; SEM analysis of hBN deposition on Cu foam..... 203
Figure 110;Characterisation of hBN foam..... 205
Figure 111; Sequential graphene-hBN deposition on Cu foam..... 206
Figure 112; XPS of Gr-BN deposition on Cu foam..... 207
Figure 113; Raman analysis of the Gr-hBN foam..... 208
Figure 114; hBCN 'one-pot' synthesis on Cu foam template..... 209
Figure 115; XPS analysis of hBCN-Cu foams..... 211
Figure 116; SEM of hBCN foam after removal of Cu template..... 212
Figure 118; Raman analysis of the hBCN foam..... 213

List of tables

Table 1; Relative energies of the B and N atoms at various adsorption sites on the Cu(111) surface, exhibiting the relative stabilities of the precursor atoms at each site. All energies here are in eV and are referenced to the fcc site adsorption energy. The absolute energies are in brackets..... 77
Table 2; Reported domain sizes of CVD hBN on Cu (* denotes LPCVD)..... 91
Table 3; Gas flow composition for growth of $hBNC_x$ samples..... 97
Table 4; Gas flow composition for C doped hBN samples synthesised on Fe foil..... 127
Table 5; % C composition, domain size ratio parameter (α), formation energy per C atom and band gap values for the BN-C structures analysed in this study..... 141
Table 6; HOMO, LUMO levels for the various hBCN systems investigated, their chemical potential vs. NHE as well as voltage offset from their respective oxidation and reduction potentials..... 149

List of symbols and abbreviations

2D	two-dimensional
AB	ammonia-borane
AP	atmospheric pressure
BCN	borocarbonitride
BZ	Brillouin zone
CA	catalyst-assisted
CBM	conduction band minimum
CO2RR	carbon dioxide reduction reaction
Cu	copper
CVD	chemical vapor deposition
DFT	density functional theory
D-Gr	defective graphene
DUV	deep ultra-violet
E_b	binding energy
EDX	energy-dispersive x-ray spectroscopy
EELS	electron energy-loss spectroscopy
E_f	Fermi energy
E_g	bandgap
E_k	kinetic energy
EP	electropolish
fcc	face centred cubic
Fe	Iron
FET	field effect transistor
FFT	fast fourier transform
FTIR	fourier transform infrared spectroscopy
FWHM	full width at half maximum
GGA	generalised gradient approximation
GO	graphene oxide

Gr	graphene
hBN	hexagonal boron nitride
hcp	hexagonal close packed
HER	hydrogen evolution reaction
HF	Hartree-Fock
HK	Hohenberg-Kohn
HOMO	highest occupied molecular orbital
HSE06	Heyd, Scuzeria, and Ernzerhof hybrid functional
HTHP	high temperature high pressure
IBSD	ion beam sputtered deposition
IR	infrared
KMC	kinetic Monte-Carlo
LDA	local density approximation
LMB	lithium metal battery
LMCat	liquid metal catalyst
LPCVD	low pressure CVD
LPE	liquid phase exfoliation
LUMO	lowest unoccupied molecular orbital
MBE	molecular beam epitaxy
MD	molecular dynamics
MOVPE	metal-organo vapor phase epitaxy
NHE	normal hydrogen electrode
NIST	National Institute of Standards and Technology
NP	nanoparticle
OER	oxygen evolution reaction
OM	optical microscopy
OP	optical profilometry
ORR	oxygen reduction reaction
PBE	Perdew–Burke-Ernzerhof exchange functional
PLD	pulsed laser deposition

PMMA	poly(methyl methacrylate)
p.p.	partial pressure
RF	radio frequency
SAC	single atom catalyst
SCF	self-consistent field
SCM	Software for Chemistry and Materials
SEM	scanning electron microscopy
SMSI	strong metal-substrate interaction
SPE	single photon emitter
STM	scanning tunnelling microscope
TD-DFT	time dependent density functional theory
TEM	transmission electron microscope
TGA	thermo-gravimetric analysis
TISE	time independent Schrodinger equation
VBM	valance band maximum
XPS	x-ray photoelectron spectroscopy
XRD	x-ray diffraction
ε	dielectric constant
κ	thermal conductivity
μ_x	chemical potential of species ‘x’

Chapter 1

Introduction

1.1. Motivation, prospective applications, and challenges

2D borocarbonitride (BCN) is a ternary class of material with varied structure and properties depending on its composition. The material has attracted attention due to the tuneability of electrical, optical, and chemical properties with only slight variation in the composition and arrangement of boron, carbon and nitrogen atoms in the network. The numerous possible stoichiometries and spatial distributions of B, C and N within the network provides a wide range of permutations of BCN materials, and with that a wide range of material properties that can be exploited. In the past decade, the number of BCN related publications has almost tripled (Figure 1). As this burgeoning field develops, BCN materials are finding applications in several technologically relevant areas; in energy research on supercapacitors [1-4] and lithium-ion batteries [5, 6], in both photo- and electro-catalysis [7-18], in sensing [19-21], and in opto-electronics as single photon emitter materials [22, 23] and materials for DUV emission/detection [24, 25].

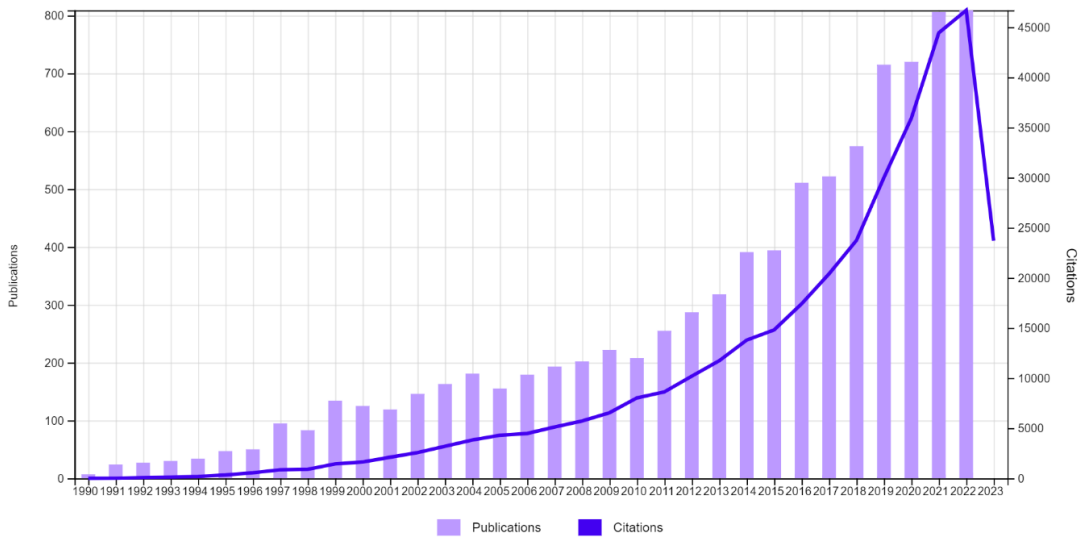


Figure 1; Number of citations (line) and publications (bar) for reports involving the term 'boron carbon nitride' or 'borocarbonitride' for the range 1990 – 2022.

One major challenge surrounding 2D hBCN research is in developing a scalable production method that allows for precise defect tailoring of high quality 2D sheets whilst also being cost-effective. Techniques such as pyrolysis, ball milling and liquid phase exfoliation allow for large-scale production, yet drawbacks exist with low crystal quality, crystallite size and poor defect control. Bottom-up approaches, such as molecular beam epitaxy (MBE) and metal-organo vapor phase epitaxy (MOVPE) allow for high-quality, wafer scale growth, but require expensive equipment and complicated processing techniques. The chemical vapor deposition method is an effective solution to these problems, having already been proven to synthesise high quality 2D graphene and hBN at scale, and at a fraction of the cost of high-end techniques like MBE. The main challenge of this synthesis technique is the optimisation of growth parameters to achieve crystalline growth. This thesis considers these obstacles, using low-cost and non-toxic precursors, ammonia borane and methane, and a simple synthesis protocol, atmospheric CVD, to produce hBCN materials with tuneable properties in a facile and cost-effective manner.

1.2. Thesis structure

In this chapter (**Chapter 1**), the significance of 2D materials and the place of hBN and hBCN materials in this context is explained. The major growth processes for 2D hBN and hBCN are introduced alongside the challenges faced by each synthesis method.

In **Chapter 2**, relevant information regarding the characterisation techniques used in this thesis and how they pertain to the materials under study is discussed. The underlying theory behind the computational techniques employed (density functional theory, DFT) are also explained.

In **Chapter 3**, CVD growth of "C doped" hBN using ammonia-borane and methane is investigated on pristine metal substrates, Cu and Fe. The atomic processes of precursors of B, C and N are determined on the (111) facet of Cu through DFT calculations to shed light on the

early conditions of growth. The influence of methane partial pressure on hBN doping and the resulting structures is investigated on Cu, through a surface mediated growth mechanism. To synthesise multi-layered films, precipitation mediated growth of C doped hBN on Fe substrates is investigated, in order to produce thicker films with tuneable opto-electronic properties.

In **Chapter 4**, DFT calculations are employed to determine the optoelectronic properties of phase-separated graphene/hBN monolayers and assess their suitability as photocatalysts in water splitting and CO_2 reduction. Step-wise synthesis of lateral graphene-hBN heterostructures is trialled on the Cu substrate using synthesis protocols derived in Chapter 3.

Chapter 5 is an investigation into the effect of impurities in ammonia borane (AB) on hBN synthesis, whereby a low-purity AB is trialled for hBN growth. The low-purity AB precursor resulted in ubiquitous growth of silica nanoplatelets on the Cu surface, interfering with hBN deposition. Similar structures have been sparsely reported in hBN synthesis studies, without any detailed explanation for their occurrence. This chapter explains the origin of such structures and proposes a growth mechanism for their formation. Based on this, improved CVD protocols are outlined to avoid their formation in future studies.

In **Chapter 6,** growth of 2D layers of graphene, hBN and hBCN on 3D porous Cu foams is reported. An cost-effective method of forming porous metal templates from metal powders is employed to synthesise metal foam-2D material composites. Non-toxic precursors and simple processing techniques are used, similar to those employed in Chapter 3, to produce 3D structures possessing a much larger functional surface area.

A final summary of this thesis and potential future work directions are presented in **Chapter 7.**

1.3. Literature Review

1.3.1. 2D nanomaterials; the Flatlands

The "flatlands" refers to materials that are 2D locally but exist in a quasi-3D configuration with ripples in the sheet. The first-identified of these, graphene, was successfully isolated from a single sheet of graphite in 2004 [26]. Since then, the last decade and a half has seen an exponential increase in research output towards isolation and application of novel 2D materials. In particular, special interest has been shown in hexagonal layered materials with strong in-plane, sp^2 hybridised bonds and weak inter-layer van der Waals forces. Figure 2 shows the structure of two of these layered materials, hBN and graphite. This thesis is mainly concerned with such layered materials, composed of boron, carbon and nitrogen, forming graphene, hexagonal boron nitride and hexagonal borocarbonitride.

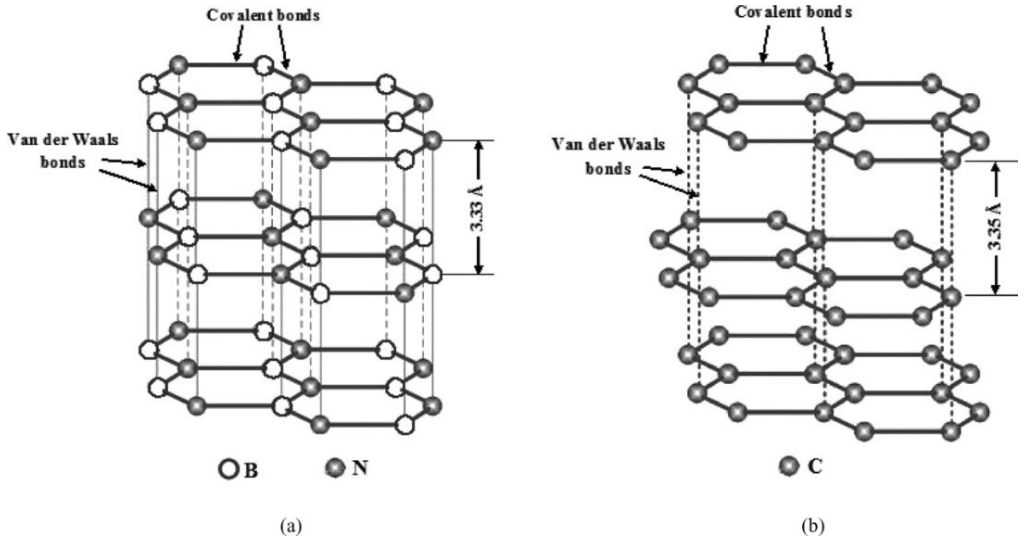


Figure 2; Structure of the layered materials (a) hexagonal boron nitride (hBN) and (b) graphite. Reproduced from *[27]*.

1.3.2. sp^2 hybridised systems – atomic and electronic structure

To convey the tuneable nature of hBCN, we look at the physics of the sp^2 system, focusing on its extreme counterparts, graphene and hBN. In graphene, comprised solely of carbon, there exists delocalisation across extremely long distances as electron density is shared across the

covalent π-bonding network. As such, graphene is highly conductive, and in its band structure we observe a Dirac point [28]. In hBN, made up of boron and nitrogen, electrons are highly localised due to atomic differences in electronegativity and polarity of the B-N π-bonds. This results in hBN being an insulator, where the π valence band is mainly comprised of contributions by the nitrogen sublattice, and the conduction band by the boron sublattice [29].

A simple exercise which effectively shows this band gap re-ordering can be carried out through calculation of the dispersion relation for sp^2 bonded materials using the Tight Binding Approximation [30, 31]. The hexagonal lattice can be described as a superposition of two coupled sublattices A and B, as shown in Figure 3 below;

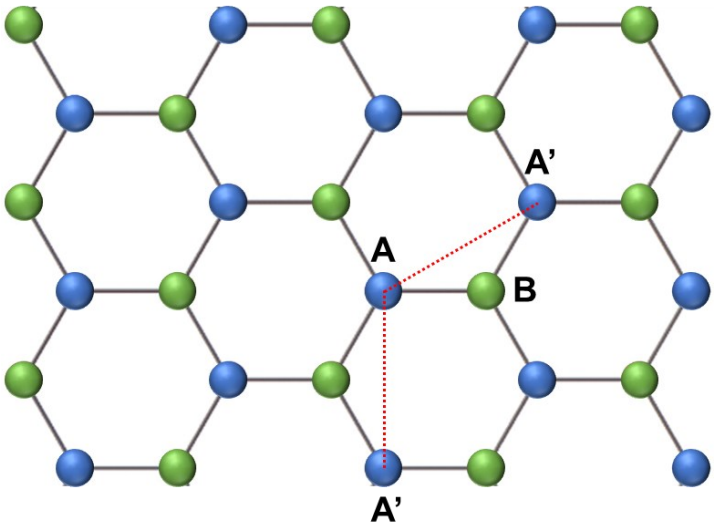


Figure 3; Superposition of 2 honeycomb lattices, A and B.

Therefore, with a two-atom basis, we can solve the Hamiltonian;

$$\begin{vmatrix} H_{AA} - E & H_{AB} \\ H_{BA} & H_{BB} - E \end{vmatrix} = 0 \qquad (1)$$

where H_{AA} and H_{BB} describe the energy on the sublattices A and B, and H_{AB} the hybridization energy due to hopping between the sublattices.

Solving this determinant for E;

$$E_{\pm} = \frac{1}{2}\left(H_{AA} + H_{BB} \pm \sqrt{(H_{AA} - H_{BB})^2 + 4|H_{AB}|^2}\right) \qquad (2)$$

If the two sublattices are indistinguishable (i.e. in graphene, $H_{AA} = H_{BB}$), then the bonding π and antibonding π^* bands have a point of degeneracy at the Dirac point (where $H_{AB} = 0$). If the sublattices are distinct, then $H_{AA} \neq H_{BB}$ and there will exist a band gap between the E_+ and E_- values. Figure 4 shows the band structure for graphene and hBN, derived via the tight binding approximation of a honeycomb lattice.

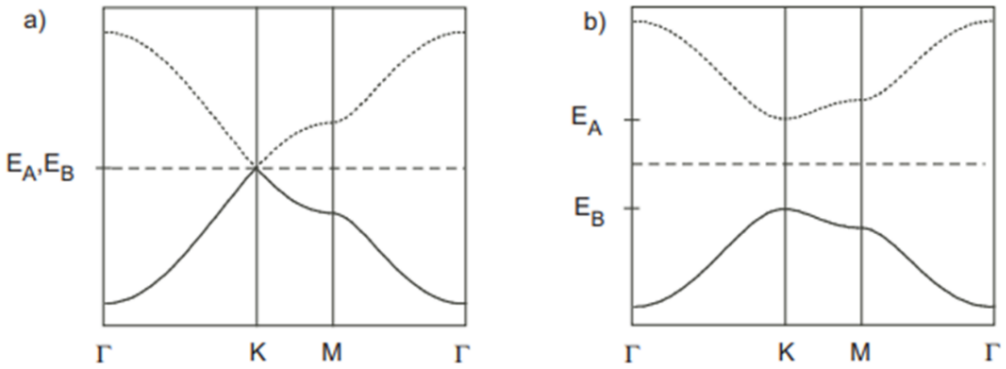


Figure 4; band structures of (a) graphene and (b) hBN sp^2 lattices using the tight binding approach. (a) uses two indistinguishable sublattices such that $E_A = E_B$ resulting in a Dirac point at K (b) uses two distinguishable sublattices such that a gap opens up (band gap), where $E_g = E_A - E_B$ at point K. Reproduced from [31].

This conveys the essential physics of the honeycomb system and the tunability of its electronic structure, simply by altering the atomic constituents. While graphene has received much of the attention in the development of 2D hexagonal materials, hBN has followed closely behind. Most recently, interest has been shown in tailoring the physiochemical properties of hBN via introduction with carbon to the network (and *vice versa*), forming structural allotropes of the material hBCN with properties between that of intrinsic hBN and graphene. In the next sections, I discuss in detail the literature surrounding the hexagonal materials presented in this thesis, namely boron nitride and boron carbon nitride before then reviewing the foremost synthesis methods for these materials.

1.3.3. Hexagonal boron nitride; structure, properties, and potential applications

Boron Nitride (BN) is a chemically inert compound comprised of alternating boron and nitrogen atoms in its crystal lattice. BN exhibits many stable polymorphs, both amorphous and crystalline which include; hexagonal BN (hBN), cubic BN (cBN), wurtzite BN (wBN), rhombohedral BN (rBN), shown in Figure 5, below.

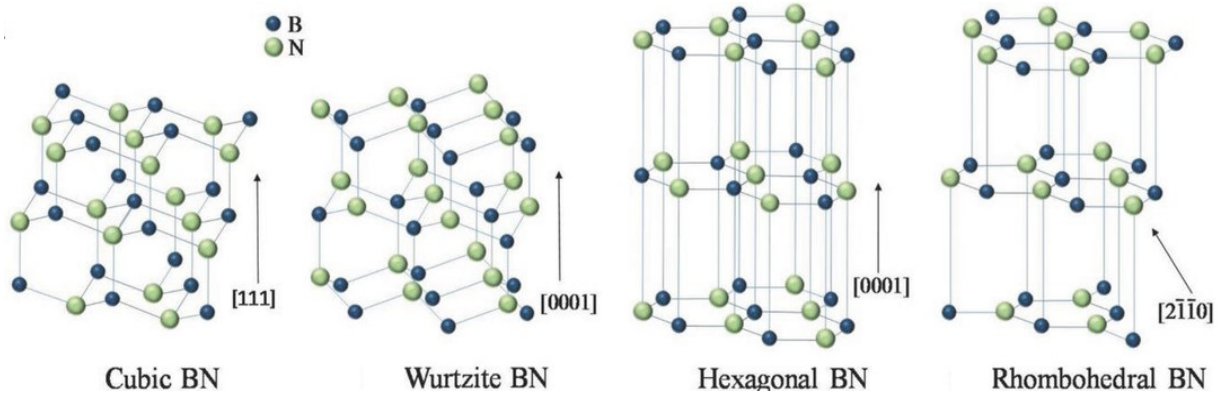


Figure 5; Various crystallographic structures of BN. Adapted from [32].

hBN is a layered, inorganic, hexagonal crystal with a structure analogous to graphite and similar lattice constants (a_{hBN} = 2.50 Å and c_{hBN} = 6.65 Å, a_{Gr} = 2.46 Å and c_{Gr} = 6.708 Å [33]). However, where graphite prefers AB stacking of its layers, hBN favours eclipsed AA' stacking; BN planes stacked commensurately with empty π-orbitals of boron atoms lying below filled π-orbitals of the nitrogen atoms. Weak out-of-plane forces from van der Waals interactions between layers, result in an interlayer distance of 0.333 nm, similar to that of graphene.

Electrical Properties; Substrates play a critical role in device performance in 2D materials. Scattering from impurities and surface defects can significantly affect the working device. 2D hBN is interesting in this regard; it has minimal lattice mismatch with hexagonal materials like graphene (~1.7%), an atomically flat surface, and is free of dangling bonds or trap impurities. As an insulating, dielectric material (ε = 3 - 4), with strong dielectric breakdown strength, hBN is used as a dielectric substrate in 2D material devices improving charge carrier mobility in

electronic devices, often besting the standard SiO_2/Si substrate [34, 35]. hBN is also used as an active component in electronic devices, for example, as a tunnelling barrier in FET devices (Figure 6, a-c) [36-38].

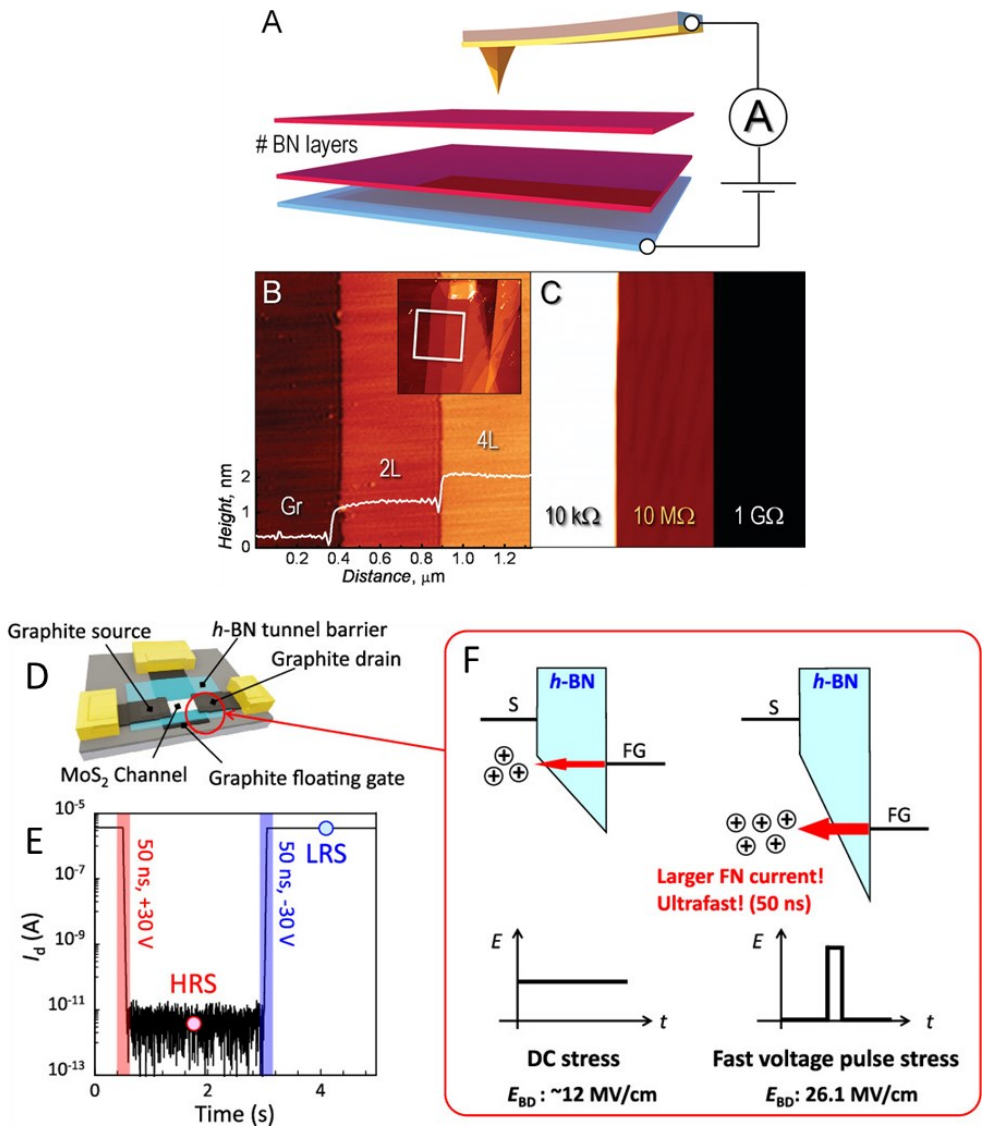


Figure 6; The insulating nature of hBN makes it useful as a tunnelling barrier in FET devices. (a) shows the schematic of the C-AFM measurements used to deduce the tunnelling current through hBN layers (b) Topography measurements which correspond to the leakage current measurements in (c). There is little variation in leakage current across each step height. The tunnelling resistance increases by a factor of three with each bilayer added. Reproduced from [36]. (d) Schematic of the ultrafast non-volatile memory device constructed using a hBN tunnelling barrier in [39] (e) 50 ns response time to switch from high resistive state (HRS) to low resistive state (LRS). (f) Schematic showing band structure response to DC and short voltage pulses with hBN as tunnelling barrier. The dielectric breakdown strength of hBN under short pulses is found to be 26.1 MV/cm. Reproduced from [39]

Sasaki *et al.* report a high breakdown strength of hBN (26.1 MV cm^{-1} in pulse form) as being responsible for the large, localised tunnelling currents observed in their non-volatile memory

device, and allowing for ultra-fast switching operations (Figure 6, d-f) [39]. These reports attribute the robust performance of their devices to the defect-free nature of the hBN tunnelling barrier layer, typically generated from mechanical exfoliation, making industrial scaling of these devices a challenge until scalable growth methods such as CVD methods mature.

In energy storage applications, the inherent chemical stability of hBN has proved useful as capping layers for battery electrodes, improving the lifetime and efficiency of operation. Copper electrodes coated with hBN (via CVD) for lithium metal batteries (LMBs) show increased stability for Li plating/stripping, with lower overpotentials and higher coulombic efficiencies over long cycles, enhancing longevity [40]. Figure 7 shows how this increase in longevity occurs; depositing a hBN film as a capping layer on a lithium target can significantly reduce dendrite formation upon cycling and enhance the long term stability of the LMB [41].

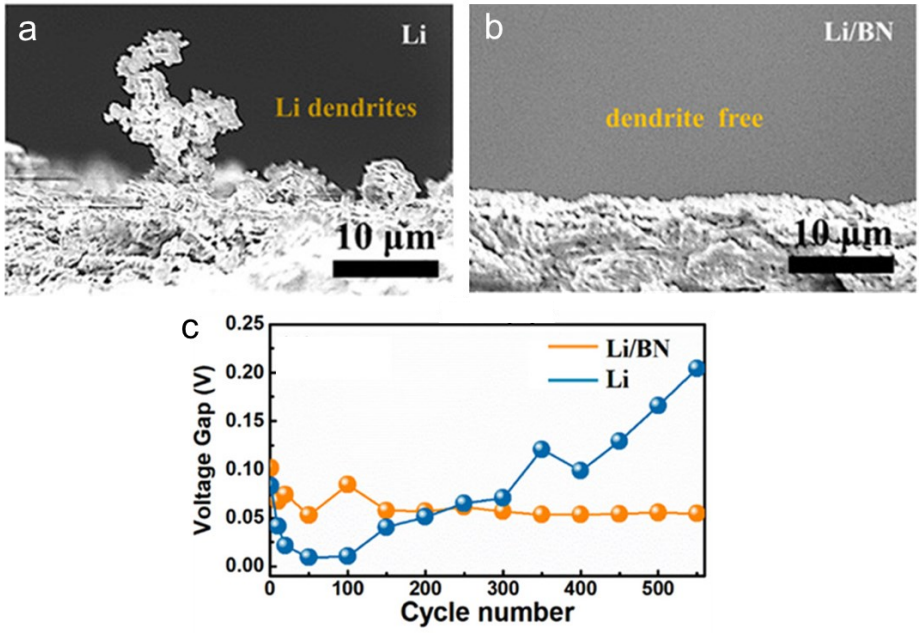


Figure 7; hBN layers on the surface of electrodes can enhance cyclability and performance. Lithium dendrites form upon cycling in the bare Li anode, while on the hBN/Li anode, uniform Li plating occurs. (a,b) SEM images showing the surface of the Li anode after cycling on the (a) bare Li electrode and (b) Li/BN electrode. (c) Voltage hysteresis of hBN plated Li anodes and bare Li anodes, with hBN coated anodes exhibiting enhanced long-term stability in comparison to the bare Li anode. Reproduced from *[41]*

Optical properties; Recently, hBN was determined to have an *indirect* bandgap of 5.95 eV, unusually wide for an indirect band gap material (E_{Si} = 1.12 eV, E_{Ge} = 0.8 eV) [42]. At

monolayer thickness, hBN is reported has a direct gap [43], yet in bulk form, this has been shown to be an indirect gap [42], requiring the emission of a phonon to fulfil momentum conservation in the carrier excitation/emission process. Unusually, this occurs with such efficiency in hBN due to the location of the conduction band minimum (CBM) and valence band maximum (VBM); the CBM sits at the M-point of the Brillouin zone (BZ), whereas the VBM is located close to the K point (shown in Figure 8). This is different from many other indirect semiconductors (Si, Ge, etc.), where their VBM are located at the BZ centre (Γ).

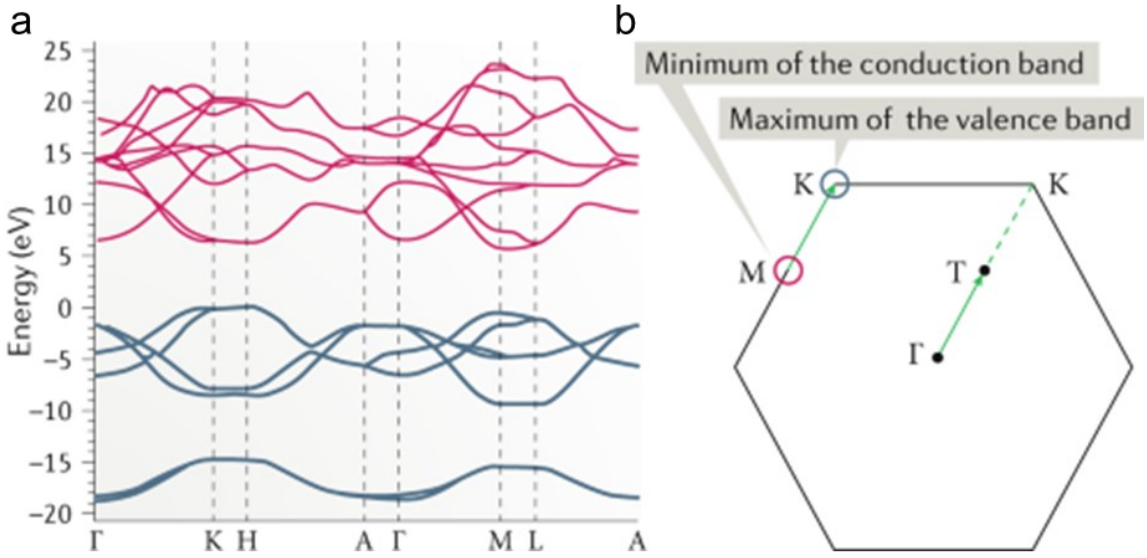


Figure 8; Optical properties of bulk hBN. (a) Electronic band structure of hBN shows an indirect band gap with the CBM located at the M symmetry point and the VBM located at the K symmetry point. (b) First Brillouin Zone (BZ) of hBN showing the high symmetry points M, K and Γ. As both CBM and VBM reside on the edge of the BZ, a phonon Γ->T is needed for recombination. Reproduced from [44]

In hBN, phonon-assisted recombination occurs with phonons Γ–>T as seen in Figure 8, and not to the BZ edge, as occurs in other indirect semiconductors. As such, in hBN, intense deep ultra-violet (DUV) emission is possible, with an internal quantum efficiency of ~40%, close to that of direct bandgap semiconductors [45]. This efficiency of DUV emission in hBN makes it an exciting material for DUV optoelectronics where UV lasing at 215-230 nm can be achieved (Figure 9, a) [46-48]. As such, hBN could be an energy efficient alternative to energy intensive halogen lamps in the DUV region. Similarly, hBN can been used for DUV

photodetection, showing fast response and decay under DUV illumination (Figure 9, d-e). Furthermore, responsivity of devices is localised in the DUV region (Figure 9, f) [49-52].

In hBN, many of the emissions that occur below its intrinsic band gap are a result of defects in the lattice. Such defects are known to reduce the lifetime of phonons in the material and, as such, are detrimental for its use in applications such as IR photonics. However, they are central to hBN's promise as a material for single photon emission (SPE). SPE materials possess high quantum efficiency, brightness, and are preferably optically stable. Research into SPEs in hBN is a relatively new field, first reported in 2016 by Tran *et al.* [53]. 2D hBN has shown visible SPE at room temperatures [53] and is the only material that can produce SPEs in the DUV range (> 4 eV) [54], making hBN an exciting platform for integration into next generation photonic circuits. Figure 9 (b, c) show the UV emission spectrum and map for a hBN flake. So far there is no consensus on the origin of the many SPEs in hBN, that is, which defects are responsible for which emissions. However, the scientific community is working hard to elucidate their relationships [22, 54-60]. Currently, quantum technologies, such as quantum computing, quantum communication and quantum sensing, are in their infancy. To achieve their potential, a new range of quantum components like SPEs found in hBN need to be developed and fully understood.

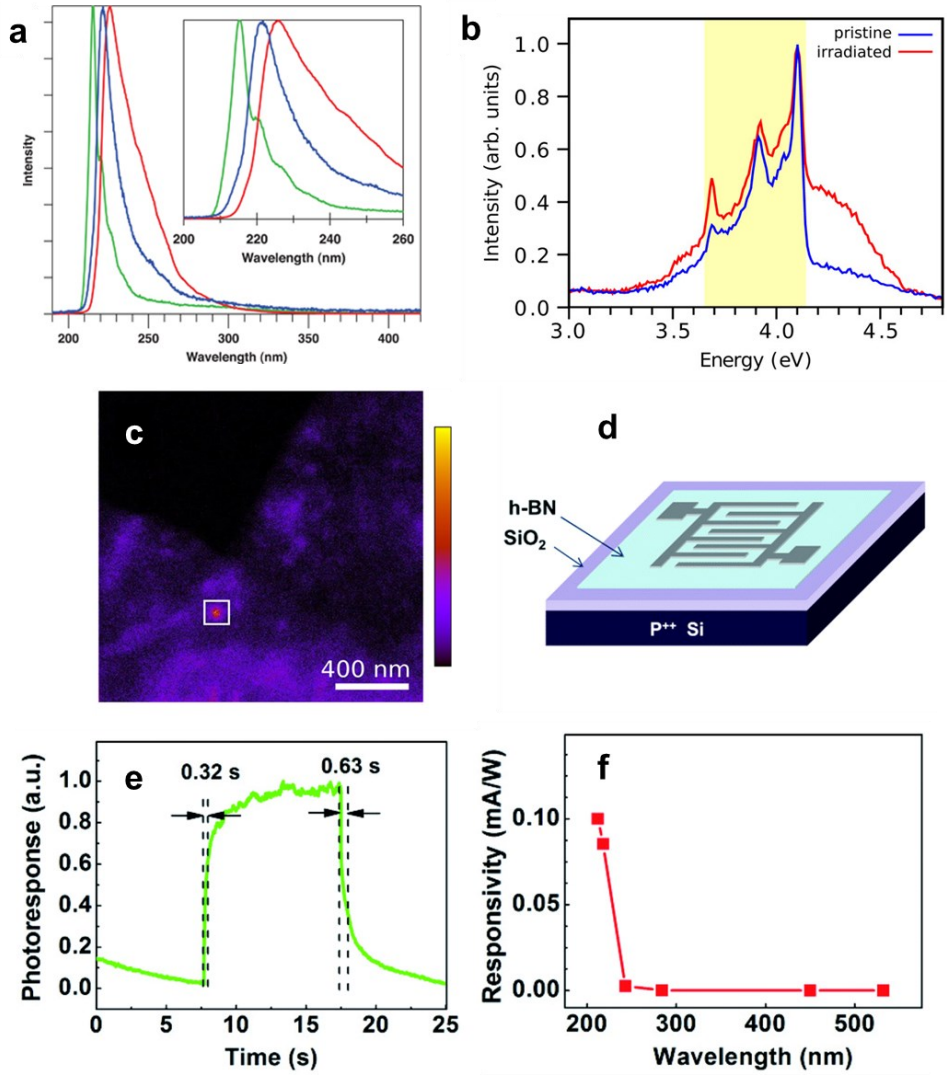


Figure 9; DUV emission and absorption is exhibited from hBN crystals cathodoluminescence (CL) and photodetection studies. (a) Spectral variations are observed from different morphologies of hBN (single crystal and deformed crystals), shown in green, blue and red. Reproduced from [46]. DUV SPE emission is also observed in hBN. (b) shows the CL spectrum for the spot on the hBN flake shown in (c). (c) is a spatial CL map for the energy window 3.7 – 4.1 eV. Reproduced from [54].(d) schematic of a metal-semiconductor-metal photodetector formed using hBN epilayers. (e) Fast photo-response for the rise and decay of the device illuminated under 212 nm laser. (f) DUV response of hBN photodetector in the 200 nm region. (d-f) are reproduced from [50].

Thermal properties; As a monolayer, hBN has exceptionally high thermal conductivity (κ) of 751 W m^{-1} K^{-1} at room temperature (second largest value for κ per g among all semiconductors and insulators) [61]. Still, it is far lower than that of graphene (κ = 5,000 W m^{-1} K^{-1} [62]). hBN possesses a high thermal oxidation resistance, withstanding temperatures of up to 1000 ˚C in air [63]. Single layer hBN is more reactive due to its low dimensionality and confinement effects and begins to oxidise around 700 ˚C in air and can sustain oxidation up to 850 ˚C [64]

(higher than that of graphene which begins oxidising in air at 400 ˚C [65]) . hBN's exceptional thermal transport properties in combination with its enhanced thermal oxidation resistance in comparison to graphene, make it an appealing candidate in applications in thermal management where it is used in composites with enhanced thermal resistance and heat transport [66, 67].

Catalytic properties; hBN has not been a thoroughly researched material in catalysis due to reports of it being highly insulating and inert. However, paradoxically, although highly inert, it has its own catalytic activity. For example, hBN sheets and BN nanotubes (BNNTs) have both exhibited great selectivity in the conversion of C_3H_8 to C_3H_6 [68]. hBN has also been used as a support material for more catalytically active species. In this aspect, hBN is an attractive material for this due to its high thermal stability and chemical corrosion resistance. Several studies on hBN based composites have shown enhanced activity in comparison to the intrinsic active material. Core-shell Co@hBN nanoparticles (NPs), used for the hydrogenation of nitroarenes, combined the activity of Co with the stability of hBN, resulting in a reduction in agglomeration of Co NPs and an increase in the active surface of the media [69].

In metal NP supported composites, there often exists a strong metal support interaction (SMSI) which can have positive or negative effect on the overall catalyst performance. With hBN, SMSI is rarely reported, likely due to the inertness of the material. However, boron-oxygen bonds present as defects in the hBN lattice have been reported to act as localised SMSI sites. Sheng *et al.* were able to tune the selectivity of products in the dehydrogenation of ethylbenzene to styrene using a FeO_x/hBN catalyst via tuning of the BO_x species present in the hBN support [70]. An almost identical design strategy was employed by Wang *et al*. in the dehydrogenation of propane towards propylene by Pt/hBN, where the SMSI interaction and selectivity of the Pt catalyst with hBN was tuned via BO_x formation. In doing so, they were able to achieve selectivity of 99% towards propylene (Figure 10).

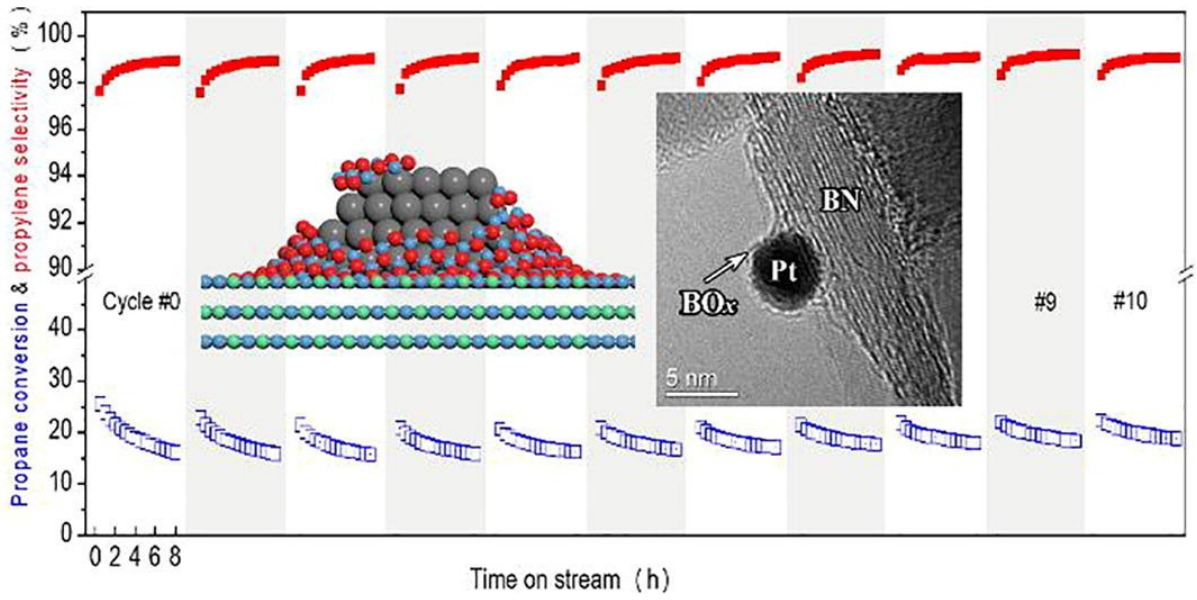


Figure 10; Catalytic synergy in hBN catalytic supports. Pt NPs anchored on hBN show enhanced selectivity and stability towards propane dehydration to propylene. TEM image inset shows the BO_x capping layer, formed through oxidation of hBN, from the activity of the Pt NP can be tuned *[71]*

Computational studies of the HER/OER activity of hBN on metal supports have been carried out by Perilli *et al.* via DFT. Here, the free energy of adsorbed atomic hydrogen, ΔG_H^*, was calculated for pristine, defective (B, N and B+N vacancies) and metal doped (Cu, Ni, Co, Fe) structures of hBN on the (111) Cu surface [72]. An ideal HER electrocatalyst should possess a near neutral free energy of adsorbed atomic hydrogen ($\Delta G_H^* = 0$). By tuning the defects of the hBN layer, the hBN/M interaction be tuned such that H^* adsorbs-desorbs freely, greatly facilitating the HER process. Their results found that h-BN/Cu(111) layers with mono or di-vacancies were found to have ΔG_H^* close to 0 eV as well as metal doped structures, suggesting modification via defects of the hBN ad-layer on Cu is a route to optimising the systems HER performance (Figure 11 a). A similar study on pristine, defective and Cu-doped hBN on Cu(111) substrates found that trapped Cu clusters at hBN defects performed as excellent electrocatalysts in the oxygen evolution reaction (OER), the compliment to HER as the other partial reaction taking place during the water splitting process, with low theoretical overpotentials and free energy cost of O_2 release (Figure 11 b) [73].

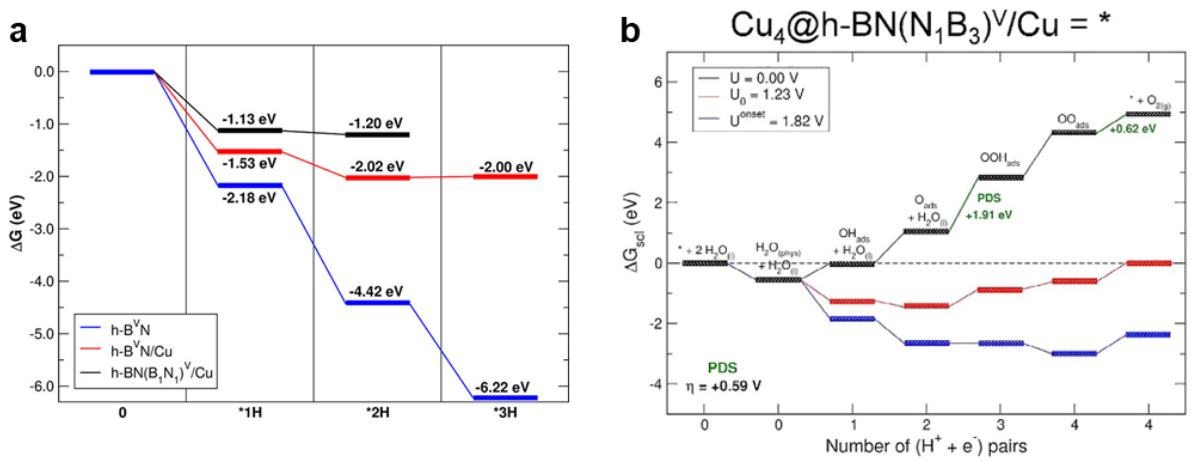


Figure 11; Metal supported hBN as electrocatalysts. (a) DFT analysis of ΔG of H^* adsorption onto defective hBN for the HER; hB^vN (boron vacancy) is blue and shows strong interaction and free energy of the system decreases with each successive H^* adsorbed, hB^vN/Cu shows a weaker interaction due to the Cu substrate and only a slight decrease in free energy with successive adsorptions. $hBN(BN)^v/Cu$ shows the smallest free energy suggesting that this configuration is optimal for HER. Reproduced from *[72]*. (b) DFT analysis of ΔG for various reaction steps of the OER process. A defective hBN sheet, doped with a Cu_4 cluster exhibits low overpotential (η = +0.59 V), low free-energy cost of O_2 desorption (0.62 eV), making it an interesting system for electrocatalytic OER. Black lines correspond to an electrode potential of U=0 V, red lines correspond to the equilibrium potential U_0, and blue lines correspond to the onset potential U^{onset}. Reproduced from *[73]*.

Copper coated with hBN or defective hBN (such as BCN) could potentially offer an interesting alternative to traditional electrocatalysts, especially considering its lower cost compared to non-noble metal catalysts. While copper alone lags behind the activity levels of advanced traditional catalysts like Pt for HER and Ir for OER, further improvements in catalytic performance through novel functionalisation methods of the Cu surface could make it a strong competitor in the market for electrocatalysts used in water splitting and other energy conversion applications. A rudimentary analysis of the material costs for a 5 x 5 cm^2 active material electrode of Cu functionalised with BCN via CVD vs a Pt-coated electrode reveals the potential economic feasibility of this system with costs of precursors being almost half that of Pt electrodes (see Appendix I for calculation).

In conclusion, hBN is being re-examined as an inert material in the catalytic sense. Many of the applications of hBN in catalysis have resulted from the ability to tune properties such as the selectivity, stability, and catalytic activity of the overall material, through controlling the type and concentration of defects in the hBN lattice and interaction with other active materials.

As such, efforts should be made to expand the catalogue in synthesising new forms of defective hBN. This thesis attempts to do just this, looking at C defects introduced during CVD growth of hBN, as well as the formation of graphene-hBN phase separated structures which also may be used to tune the catalytic properties.

1.3.4. Hexagonal borocarbonitride; structure, properties, and potential applications

BCN materials are a ternary compound composed of boron, carbon and nitrogen. Different compositions of B:C:N may exhibit different polymorphs, each with distinct properties (Figure 12). B-C-N systems commonly exhibit one of three bonding structures; (1) cubic or diamond phases with sp^3 tetrahedral hybridisation, (2) hexagonal crystals (like graphene or hBN) with sp^2 hybridisation and (3) rhombohedral crystals such as B_4C. Each of these structures has its own unique material properties, and these can be tailored, relatively, based on the atomic composition of B, C and N in the structure. In this thesis, as a 1:1 stochiometric precursor is used for B and N, such that our synthesis will likely result in structures along the line from C to BN, as seen along the dotted blue line in Figure 12.

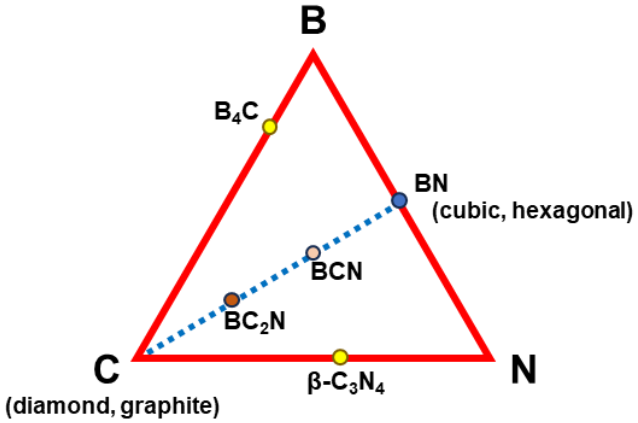


Figure 12; Ternary phase diagram, showing the different phases in the B-C-N system.

hBN and graphene domain segregation is often observed in 2D hexagonal BCN materials (Figure 13, a). This is largely due to the propensity of B to form strong polar bonds with N and C to form covalent arrangements with itself. Observing the bond energies (a key factor in stability) the trend is as follows; B-N - 4.00 eV > C-C - 3.71 eV > N-C - 2.83 eV > B-C - 2.59 eV [74]. Thus, by maximising the number of B-N and C-C bonds, the overall structure is increasingly more stable [75]. While many theoretical studies have focused on exotic arrangements of B-C-N and their interesting properties (similar to those in Figure 13, c), no truly homogenous BCN material has been reported experimentally.

In segregated BCN structures, the shape of these immiscible domains with respect to one another is determined by the interfacial energy between the two phases, and the chemical potential of the system. Liu *et al.* studied, computationally, the interface energies between armchair and zigzag edges of hBN with graphene patches embedded and showed how equilibrium shapes of C can be tuned via the chemical potential of B and N in the system, shown in Figure 13, b [76]. At high boron or nitrogen chemical potential, triangular domains of C were favoured, however at medium potentials, hexagonal depositions were energetically preferred. Typically, CVD processes, such as those used in this thesis, are concerned with kinetics rather than thermodynamics of the system, however, knowledge of the equilibrium shapes is often useful.

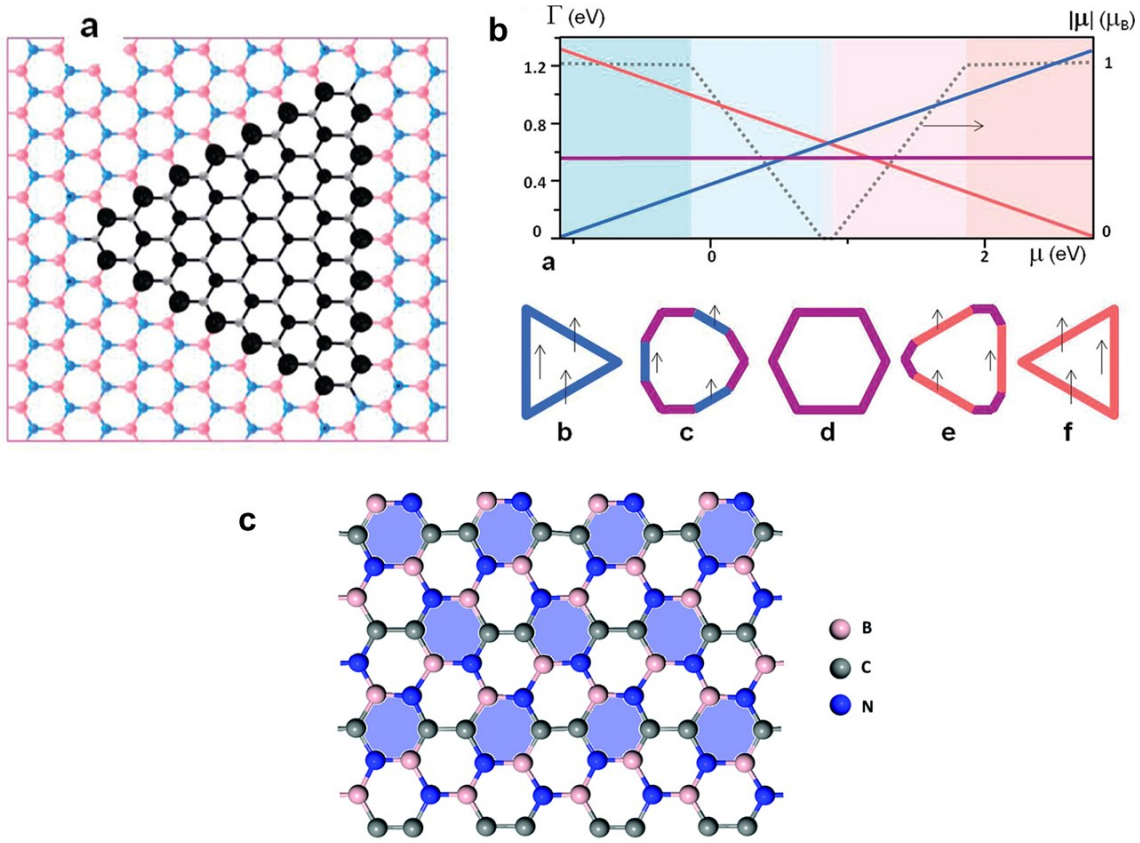


Figure 13; (a) B-C-N systems tend to segregate into hBN (pink and red atoms) and graphene regions (black atoms). (b) The shape of the embedded graphene domain can be tuned via the chemical potential of the system. Energies for the boron-rich zigzag (pink), armchair (purple) and nitrogen-rich zigzag (blue) interfaces, as a function of chemical potential of B. (c) Homogenous BCN systems are often studied theoretically but are yet to be realised experimentally due to their energetically unfavourable bonding arrangements. The blue and white hexagonal colourings are used to guide the reader between various $B_2C_2N_2$ bonding environments. (a,b) reproduced from *[76]* with (c) reproduced from *[77]*.

As well in-plane hBCN materials, vertically stacked out-of-plane hBCN materials can also exist, shown in Figure 14. Such layered hBCN is expected to have similar lattice constants to that of hBN and graphene but will differ slightly depending on the composition of the material in question [78]. This value may differ from one configuration to another depending on factors such as types of stacking, structural defects, and bonding distortions.

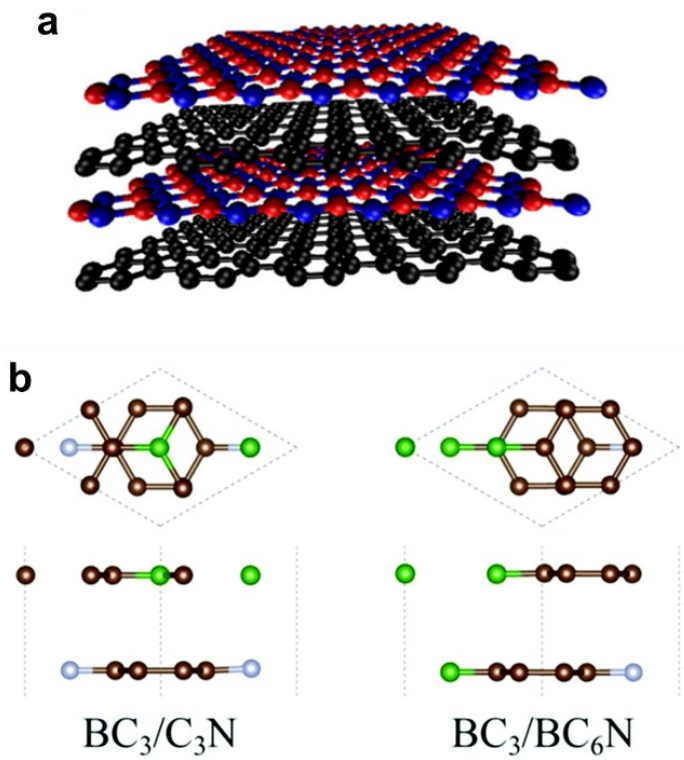


Figure 14; Vertically stacked hBCN materials typically comprise of stacked hBN and graphene sheets, as shown in (a). (b) More exotic stacked BCN systems have also been investigated theoretically. (a) is reproduced from *[79]*. (b) is reproduced from *[78]*.

Electrical properties; hBCN has electrical properties between that of hBN and graphene. Due to the numerous arrangements of hBN and graphene nanodomains in the B-C-N system, as well as their distribution, the compositionally dependent electronic band structure is complex and typically requires computational modelling techniques such as *ab initio* density functional theory (DFT) to elucidate [58, 80-85]. Ren *et al*. used periodic DFT calculations to determine the electronic properties of BCN alloys where small clusters of C atoms ($n \leq 6$) embedded in a hBN network [85]. Their study found that even numbered C motifs were the most stable in the hBN network and at just 14 at. % carbon, the band gap, E_g, could be reduced to 65% that of intrinsic hBN (calculated at 4.7 eV to 3 eV) highlighting the tuneability of the BCN system (Figure 15). Similar work is carried out in this thesis, where the band gap structures, and band edge potentials of phase separated graphene-hBN monolayers are investigated (Chapter 3, Section 3.3.6).

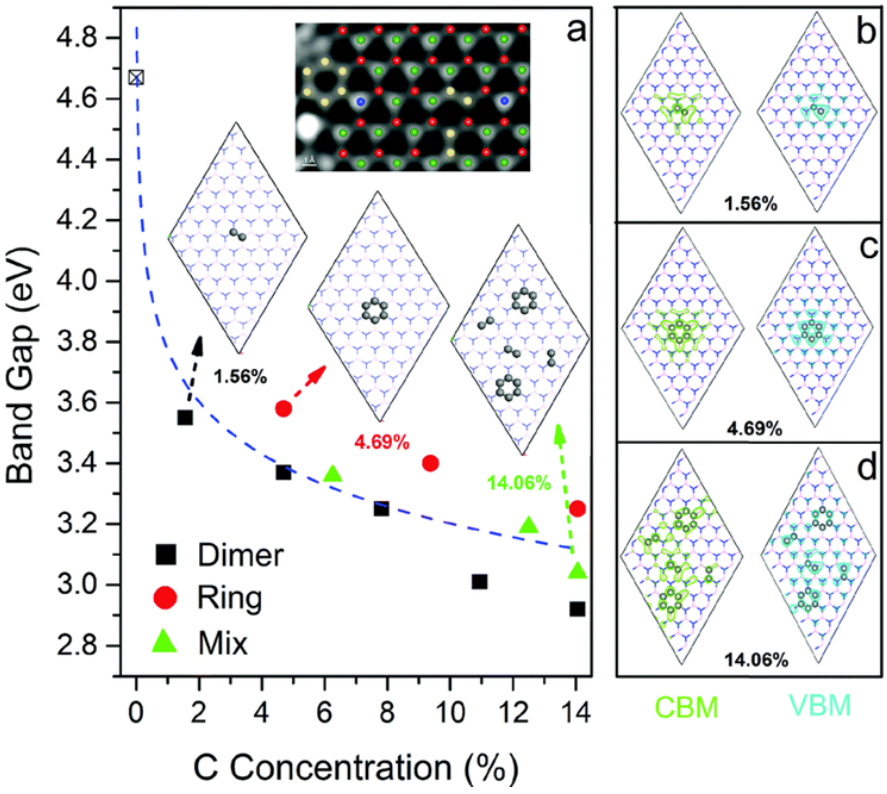


Figure 15; DFT study of C point defects in hBN. (a) shows a plot of band gap vs. carbon concentration in the modelled hBN sheet for dimer, ring and mixed type defects. (b-d) Electron distribution of CBM and VBM states in real space for hBN models with (b) 1.56%, (c) 4.69%, and (d) 14.06% C showing localisation of CBM and VBM states around the C atoms. Reproduced from *[85]*

Recently, highly crystalline C doped hBN was realised via high temperature, high pressure (HTHP) methods and exhibited significantly enhanced current injection in devices [86]. In the device, electrical current is observed at ~ 0.01 V nm^{-1}, much smaller than the electric field breakdown of hBN at ~0.31 V nm^{-1} (Figure 16 e). Similarly, high quality bulk crystals of C doped hBN are used in 2D memristor devices, where defects introduced via C doping form a conductive filament in the device, allowing it to switch between high and low resistive states (Figure 16 a) [87]. The BCN material here was synthesised via precipitation from a molten Ni-Cr flux at 1600°C and, as such, scalability is an issue. Researchers in this study called for CVD methods to meet that of HTHP methods, such that wafer scale C doped hBN films with controlled defect density can be realised for building large-scale C-hBN memristor arrays. This thesis aims to address part of this research gap by investigating C doping of hBN via CVD.

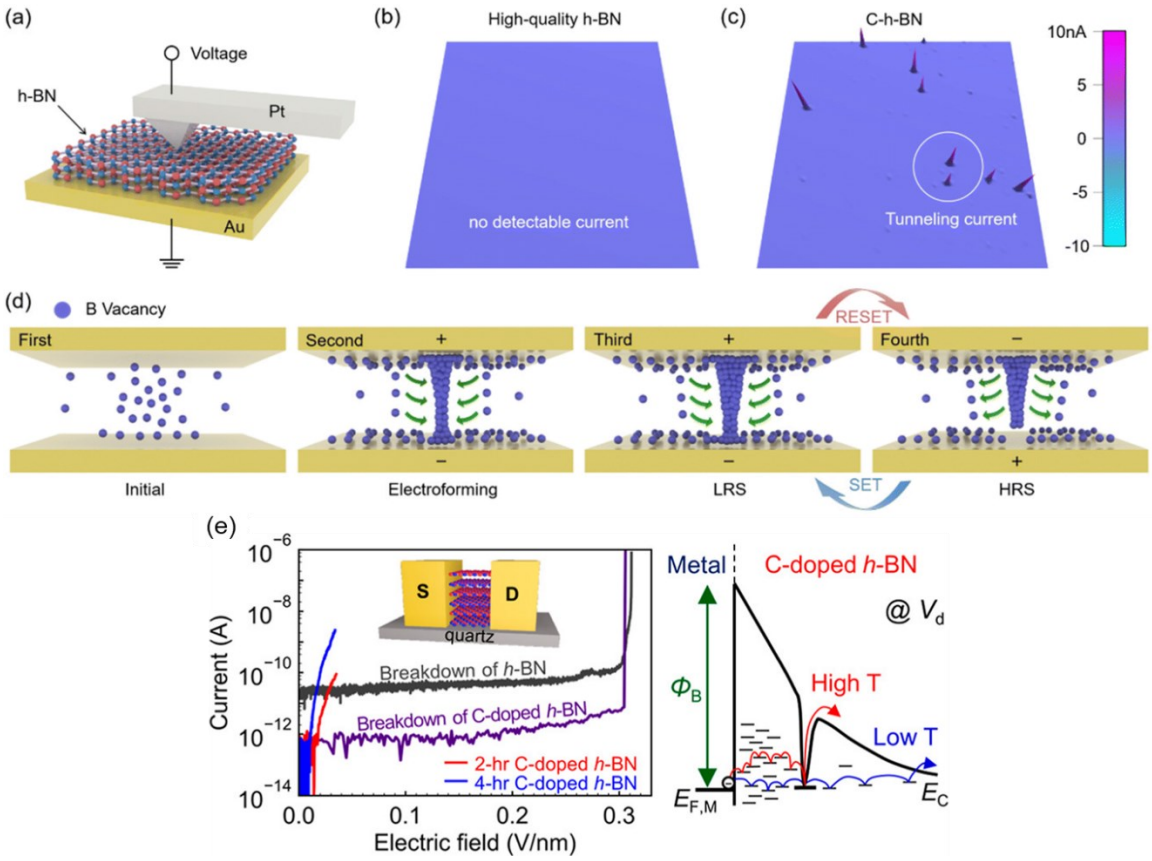


Figure 16; C doped hBN as active materials in electronic devices. (a) Schematic of the C doped hBN memristor device and C-AFM set-up (b,c) C-AFM scan of (b) intrinsic hBN and (c) C doped hBN. The C hBN layer shows regions of high current flow, where electrons can tunnel through the film. (d) Schematic of the resistive switching process; boron vacancies result from the C doping of hBN. Under an applied voltage, vacancies migrate towards the top electrode, until fully connected to the bottom electrode, forming a conductive filament (CF) and low resistive state (LRS). Under switching in polarity, reverse migration of boron vacancies rupture from the CF forming a high resistive state (HRS). Reproduced from *[87]*. (e) Enhanced current injection into C doped hBN. Difference in injected current observed in 2 hours (blue) and 4 hours (red) carbon doped hBN and the current detected in the transverse dielectric breakdown of undoped hBN (black) and 4 h carbon doped hBN (purple). Schematic of device is inset. RHS depicts current injection into the device via defect hopping from C defects much smaller in magnitude than the Schottky barrier height at the metal/*h*-BN interface. Reproduced from *[86]*.

BCN materials have also found application in electrochemical supercapacitors, where the introduction of BN in graphene-based structures (C > BN) has improved the capacitive behaviour of the material [2, 3]. In lithium-ion batteries, hBCN anodes show excellent specific capacity in comparison to the graphite electrode (652 $mAhg^{-1}$ at 100 mAg^{-1} for hBCN sample versus 372 $mAhg^{-1}$ for graphite) [6] and hold the current record for maximum voltage range in lithium-ion capacitors at 4.8V [1].

Optical properties; BCN materials have a tuneable optical bandgap typically below that of hBN (E_g = 6 eV), determined by the chemical composition and bonding in the material.

Experimentally, macroscopic optical characterisation can be carried out through UV-vis spectroscopic data and Tauc plot extrapolation. However, macroscopic BCN materials are typically an assembly of various BCN bonding arrangements, rather than a repeating crystalline material. It can be difficult to distinguish the origin of contributions towards the absorption and optical bandgap of the material, and as such, *ab initio* methods are often used [80, 88-91].

In quantum applications, SPEs can be introduced into hBN via C-based defects. TD-DFT calculations have been used to study C-dopant related SPEs in hBN, identifying the carbon ring (6C) defect in hBN as being responsible for the experimentally observed 4.1 eV DUV emission signal [60] as well as several C-related arrangements in the range 0.7 – 6.1 eV [58]. Mendelson *et al.* used experimental (MBE/MOVPE) and computational techniques to show that certain carbon impurities in hBN layers were the source of single photon emission in the visible spectral range [22]. Similarly, recent experimental work on C doped hBN via CVD showed how the density of SPEs could be enhanced with the introduction of methane during hBN synthesis [23]. In DUV applications, Carbon doped hBN has also shown improved efficacy in DUV photodetectors in comparison with intrinsic hBN. Wang *et al.* utilised C doping via IBSD to improve hBN's performance in DUV photodetectors (Figure 17 g-h)[25].

As a functional material C doped hBN is relatively new to opto-electronics with new applications and functionalities being uncovered regularly. As such, attention should be given to the exploration of the synthesis of new hBCN materials and their properties.

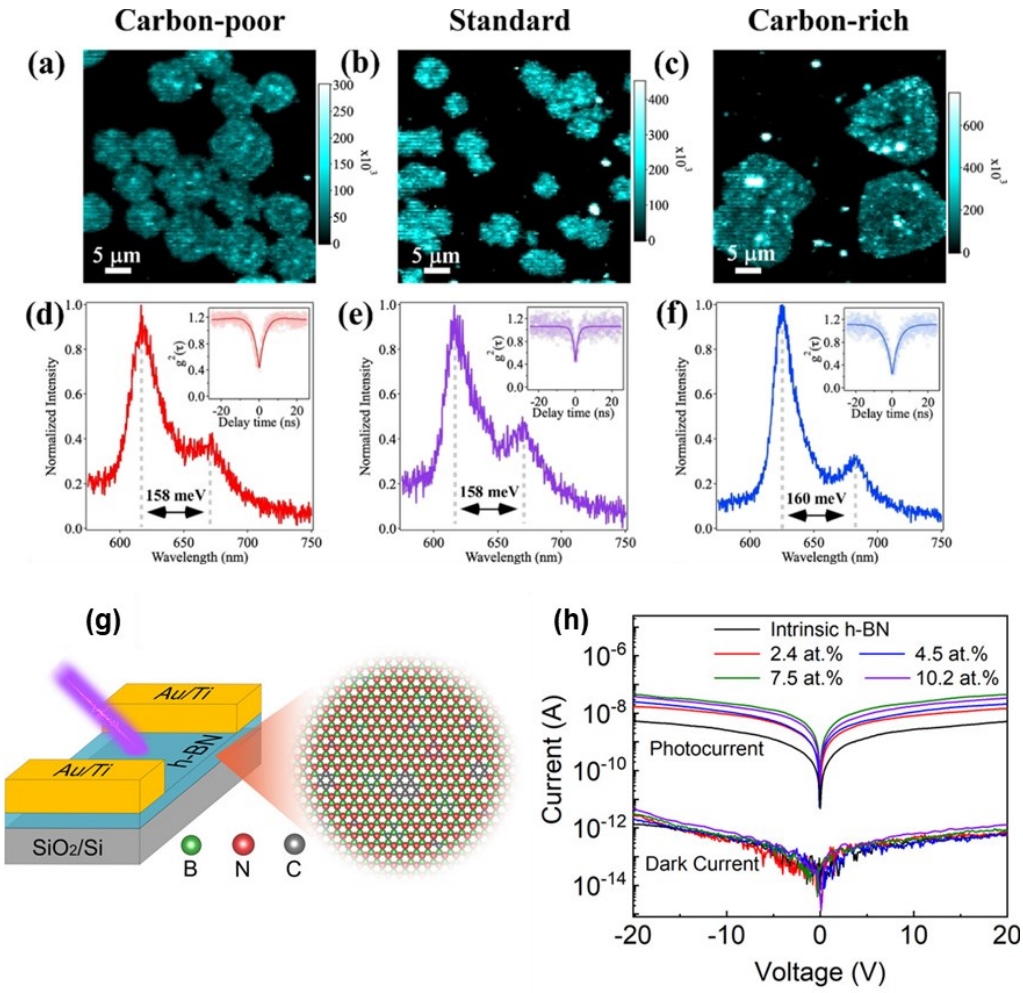


Figure 17; SPEs in hBN layers grown via APCVD show enhanced density of emitters in C doped samples; (a-c) Spatial intensity maps of emission in the 600 – 700 nm range. (d-f) Intensity vs wavelength spectra for maps (a-c). Reproduced from [23]. (j) DUV photodetector constructed from C doped hBN (h) Optical performance of the device visualised in (g). The photocurrent generated by the C doped hBN is almost a factor of 10 larger than intrinsic hBN. Atomic % are referring to carbon. Reproduced from [25].

Thermal properties; hBCN has been shown, both experimentally and theoretically, to possess a much lower thermal conductivity than intrinsic hBN or graphene [92, 93]. Attri *et al.* observed that few layer BCN synthesised via pyrolysis had a low thermal conductivity of 0.58 – 1.86 W m^{-1} K^{-1} at 300K, depending on composition, which they attribute to significant phonon scattering effects in the material due to loss of crystallinity [93]. Oxidation resistance is less studied in hBCN than in hBN, however it is expected to fall below that of hBN (T_{ox} = 1000 ˚C in air). Carbon introduced to the hBN lattice results in the introduction of point defects,

disordered nanodomains and grain boundaries, disturbing the crystallinity of the material, thus lowering its oxidative resistance.

Catalytic properties; For hBN, vacancy-type defects or boron-oxide defects were seen to improve catalytic processes and it is thought that incorporation of carbon atoms into hBN can have a similar enhancing effect. Band gap engineering through carbon doping can make it possible to control the chemical activity of hBN through modulation of the electron density close to the Fermi level. Figure 18 (a) exhibits this, where computationally calculated band structures of C based point-defect structures in hBN are shown [94].

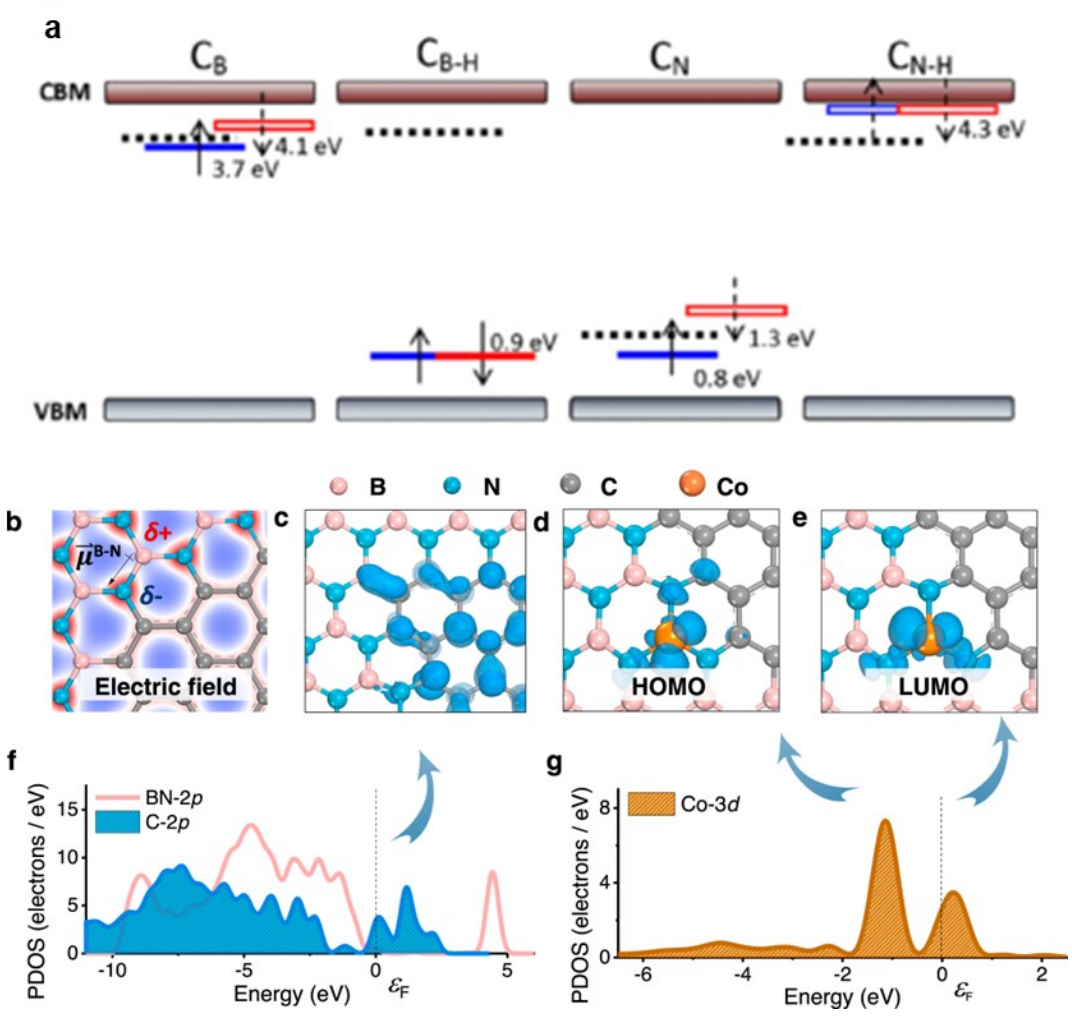


Figure 18; (a) Band structure of hBN with C point defects showing how the Fermi level changes with doping. *[94]* BCN as a catalyst support. (b) visualisation of the electric dipole of the B-N bond at the edge of BN/Gr. (c) Orbital density of C atoms in the BCN network (d) HOMO and (e) LUMO visualisation of Co adsorbed on BCN (f) band structure of hBN and C regions in the BCN network superimposed. The 2p orbitals of C lie at the Fermi level. (g) band structure of Co adsorbed on the BCN sheet where the HOMO lies at the Fermi energy *[95]*.

Similar to hBN, BCN has been employed as a catalyst support for Co single atom catalysts (SACs) in the sustainable conversion of organic chlorides [95]. Here, the BCN support outperformed graphene and N-doped graphene supports. Computational studies (Figure 18, b-g) showed that, due to the polarity of the B-N bond, Co was able to readily adsorb on the positively charged B atom. Furthermore, the HOMO of the C network in the BCN motif and the HOMO of the Mo SAC supported on BCN are both found near the Fermi level, which is beneficial for electron donation in the network.

In the case of fuel cells and water splitting devices, BCN materials have been investigated as replacement materials for the costly, and resource-scarce catalytic standard, Pt. Tabassum *et al.* were able to tune the activity of BCN composites via their atomic composition, forming an efficient hydrogen evolution reaction (HER) electrocatalyst with an onset potential of -56 mV and an overpotential of 70 mV (vs. RHE) (sample number (6) in Figure 19, a) comparable to that of Pt/C (sample number (7) in Figure 19, a) [15]. Analysis of the Tafel slopes of the same samples (Figure 19, b) showed a higher value of 100 mV dec^{-1} for the optimised BCN sample compared to that of Pt/C (34 mV dec^{-1}), meaning a higher overpotential required for higher current, presumably due to the band gap in the BCN structure.

Arévalo *et al.* reported enhanced electrocatalytic activity for CVD BCN films grown on titanium for the OER, the compliment reaction to HER, in alkaline solutions (Figure 19, c-d) [18]. Here, the BCN film acted as a transparent conductive electrode for the photogenerated charge carriers generated close to the TiO_x surface (Figure 19 c). As shown in Figure 21, d, the response from bare TiO_x is negligible even at high voltages. TiO_x-BCN showed a significant increase in current which was improved upon even further in the TiC-BCN sample (170-fold increase), exhibiting how addition of BCN to a metallic surface can tune and enhance its activity.

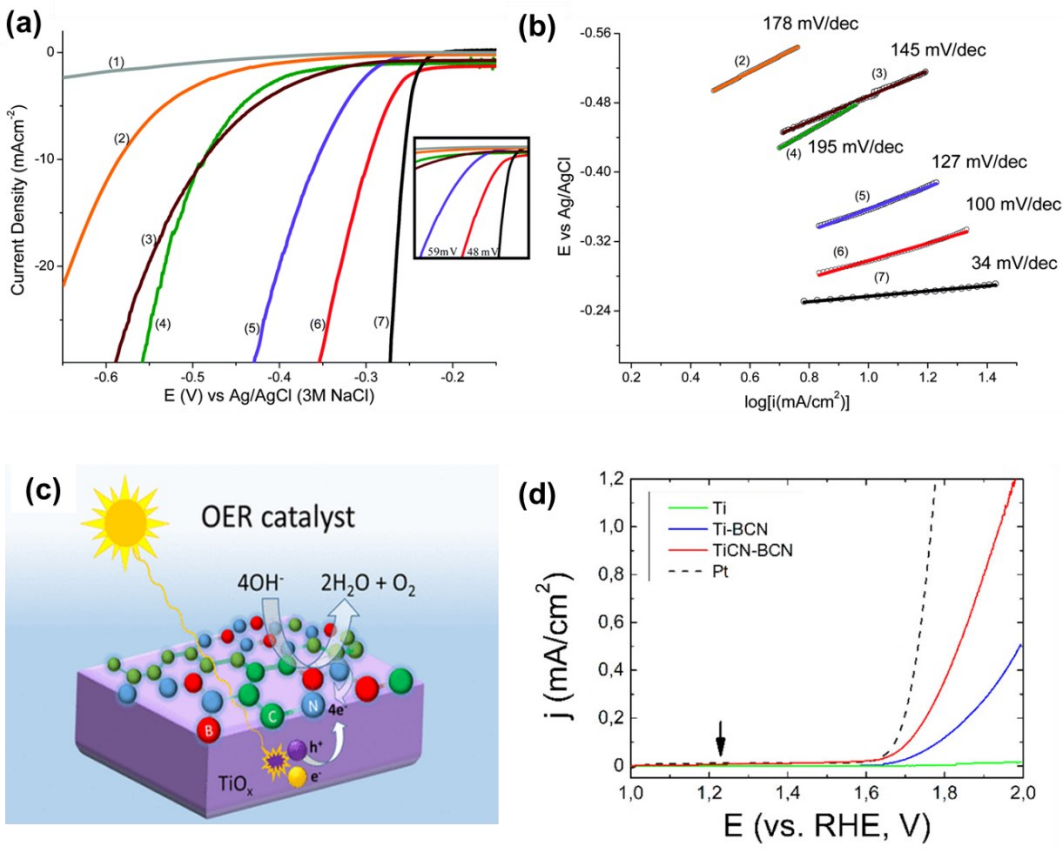


Figure 19; HER activity of BCN nanosheets with varying atomic ratios of B-C-N. (7) is the standard Pt/C electrode and (6) – (1) are BCN samples decreasing in C content, with (1) being the lowest. (b) Associated Tafel slopes [15] (c) Schematic of CVD grown BCN film on Ti for OER (d) Catalytic activity of Ti is enhanced significantly by the presence of the BCN film and even more so in the TiC-BCN sample [18].

It should also be noted that many theoretical investigations have modelled the properties of exotic BCN arrangements, with many of them suggesting efficient catalysis for water splitting, ORR and CO_2 reduction [82, 83, 89, 96]. However, as mentioned, truly homogenous hBCN materials are thermodynamically less stable, and thus difficult to realise experimentally. In this thesis, I instead investigate, theoretically, phase separated structures of hBCN and their material properties towards the water splitting and carbon dioxide reduction reactions (CO_2RR).

In conclusion, hBCN materials have shown promise as both catalytic supports and active materials in a wide variety of applications, where they exhibit increased functionality compared to the intrinsic substrate/active material as well as counterparts of graphene and hBN. Introduction of C to the hBN network introduces mid-gap states in hBN, enhancing the

conductivity as well as tuning the reactivity of the material. In graphene, BN co-doping is shown to introduce new bonding functionalities and improve catalytic efficiency in composites, where polar BN bonds introduced to the network bind with active species such as SACs. As such, they are a promising material platform for sustainable energy storage and conversion.

Sensing; hBCN materials can offer improvements in selectivity and detection limits in sensing devices through tuning of the electrochemical interaction of dopant sites of the respective hBN or graphene network with the analyte. In the case of highly carbonaceous BCN, BN doping opens up the band gap of the graphene sheet, allowing for improved sensing capabilities sensor selectivity [21].

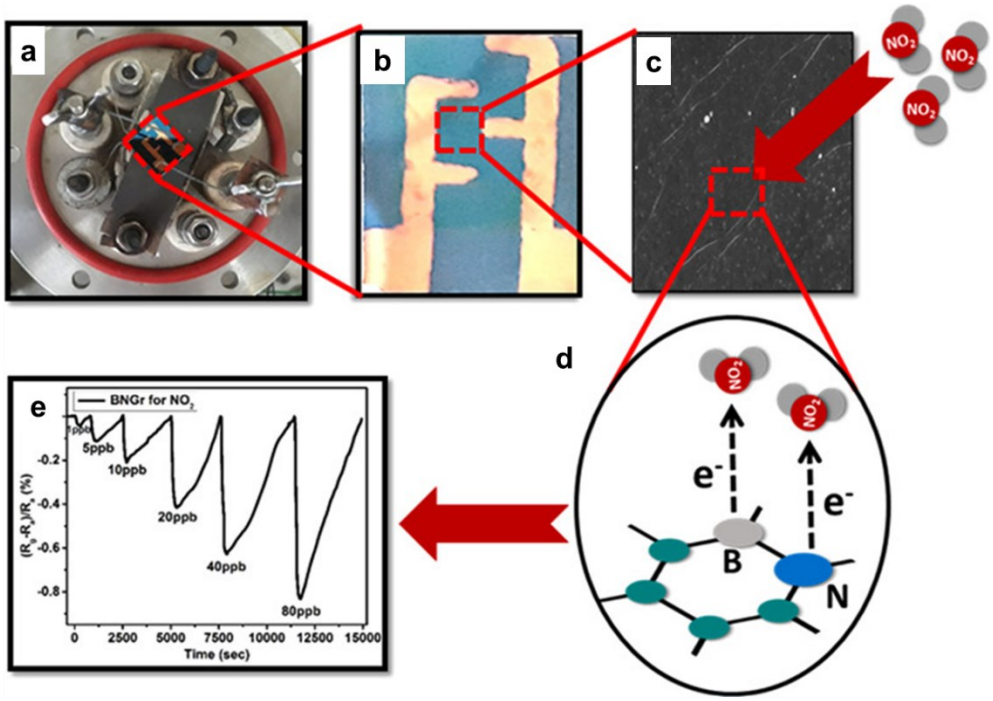


Figure 20; NO_2 sensor fabricated using BN co-doped graphene (BN-Gr) (a) Testing set-up of BN-Gr device) (b) optical image of the active material and deposited electrodes (c) SEM image of BN-Gr sheet (d) Schematic of the BN orbital interaction with the NO_2 gas molecules (e) Response of the NO_2 sensing device at different ppb of NO_2. Detection limit is 1 ppb. Reproduced from [19]

Srivastava *et al.* designed an NO_2 gas sensor from CVD grown BN-doped graphene (BN-Gr), exhibiting ultrasensitive detection of NO_2 molecules (1 ppb) at room temperature [19]. They employ DFT calculations to study the interaction between NO_2 and the BN doped graphene

sheet. The intrinsic Gr sheet showed little interaction with the NO_2 molecule due to no charge difference between the two. However, a greater charge density is present between the adsorbed NO_2 molecule and the BN-Gr nanosheet, improving their interaction/charge transfer and thus detectability.

1.3.5. 2D Material Synthesis Overview

The following section details synthesis methods to produce 2D graphene, hBN and hBCN layers. The main approaches to their synthesis fall under the headings of "top-down" and "bottom-up" methods. Top-down routes start with the bulk crystal and through various processing steps, results in 2D nanolayers of the bulk crystal. Certain top-down approaches, such as mechanical exfoliation (scotch tape method), have been very useful in creating high quality devices for the fundamental study of 2D materials, however the processing times are slow. Other industrial-scalable top-down methods, like chemical exfoliation, liquid-phase exfoliation or ball-milling, offer a high-output rate, however, issues with defect control, homogeneity and yield/efficiency still need to be addressed. Bottom-up approaches refer to techniques in which 2D layers are synthesised from the atomic or molecular building blocks of the growth material. These techniques typically offer enhanced control over the growth and quality of the 2D material in comparison to top-down methods, at the expense of being more costly and often requiring more sophisticated synthesis machinery. Methods which fall into the bottom-up category include pulsed laser deposition (PLD), Ion Beam Sputtered Deposition (IBSD), molecular beam epitaxy (MBE), pyrolysis, and chemical vapor deposition (CVD). In hBCN synthesis, the most prevalent synthesis methods are pyrolysis, which produces highly variable, defective structures, Molecular Beam Epitaxy (MBE), which offers high precision control in 2D deposition, and CVD methods, which lie somewhere in between the two. These

synthesis methods are given a brief overview in the following section as they relate to hBCN synthesis and their final applications.

1.3.5.1. Pyrolysis

Pyrolysis involves the thermal decomposition and conversion of a material at elevated temperatures, in an inert or reactive atmosphere for several hours. 2D nanosheets of graphene [97], BN [98, 99] and BCN [2, 9, 10, 14, 17, 100-102] have been synthesised via high-temperature pyrolysis of compounds containing their constituent elements. This technique benefits from being low-cost and able to produce large quantities of material. However, it typically produces highly defective 2D layers with poor control over their concentration and defect type [99]. In many reports, B and N precursors, boric acid and urea, respectively, are reacted with a carbon source such as graphene oxide [9, 102], PEG polymer (shown in Figure 21) [10], activated charcoal [100], glucose [14] at high temperatures to produce a BCN material. In certain applications where plentiful defects can be useful, such as in catalysis, these defective materials often show enhanced catalytic activity in comparison to their hBN or graphene analogues [9, 14].

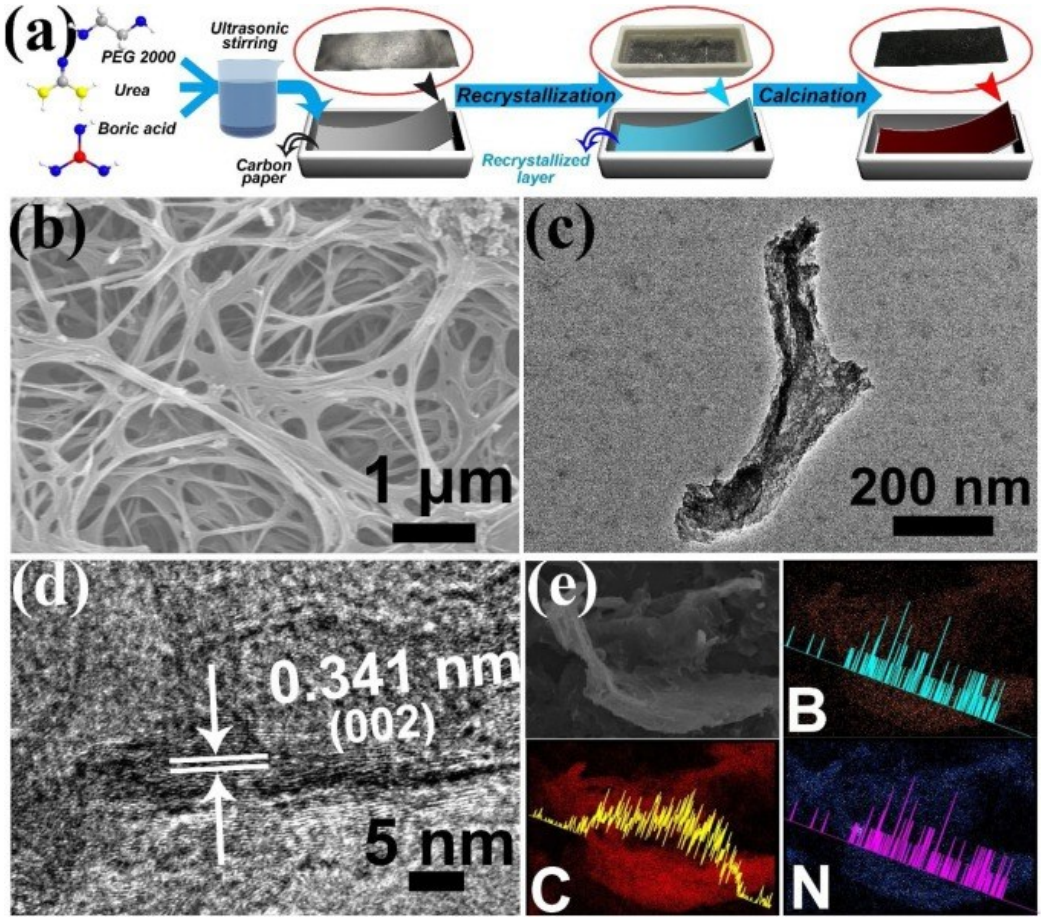


Figure 21; Formation of BCN nanofibers via pyrolysis (a) Schematic of the synthesis process (b) SEM image of the BCN nanofibers (c)nanostructure of the BCN material showing c-spacing of 0.341 nm (e) Elemental mapping of BCN via EDX showing a line profile of the intensity of B, C and N in the sample. [10]

1.3.5.2. Molecular Beam Epitaxy

Molecular beam epitaxy (MBE) is a layer-by-layer deposition technique that employs a high level of molecular control, typically requiring ultra-high vacuum conditions. As a result, 2D crystals synthesised are of high quality. A typical MBE set-up consists of Knudsen effusion cells (K-cells), located at the bottom of the ultra-high vacuum chamber, below the growth substrate (schematic shown in Figure 22). Each K-cell contains ultra-high purity element in solid form (e.g. 99.999% purity B) and elements such as N can also be introduced in ultra-pure gaseous form.

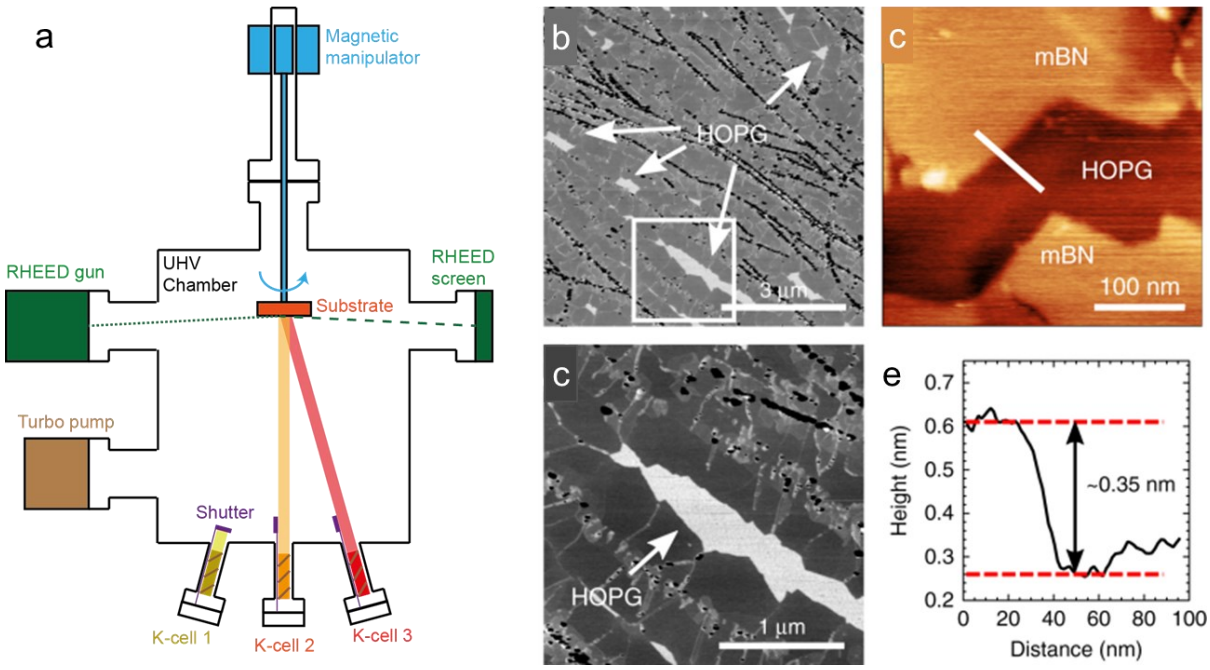


Figure 22; (a) Schematic of MBE set up. (b-e) hBN deposited on highly ordered pyrolytic graphite (HOPG) via MBE. Reproduced from *[103]*. (b) SEM image of hBN grown on HOPG. Exposed HOPG is highlighted by the white arrows. White box is the area shown in the close-up SEM image (c). (d) AFM scan of hBN edge on HOPG with the line profile shown in (e). A step height of 0.35 nm is observed, showing monolayer growth on HOPG. Adapted from [43].

To initiate growth, the K-cells are heated until the elements in each cell reach a sublimation point. Then, the shutter of the required cell is opened, and elemental vapor diffuses though the chamber towards the substrate where it gets deposited. In the case of hBN, where an N source is required, nitrogen plasma is used to create a reactive N source. This method has been used to grow high quality graphene, hBN[43, 48, 104], C doped hBN[22] as well as stacked graphene/hBN vdW structures. Extremely accurate control over the growth can be achieved, making MBE useful in applications where high-quality layers and excellent control over layer numbers (Figure 22, b-e) and defects is necessary. C doped hBN synthesised via MBE has been shown to produce quantum emitters in the visible spectral range opening up applications for the material in quantum optics [22]. The main drawback of this technique is the cost of production. Due to the requirements of ultra-high vacuum, high temperatures (1800 °C +) and atom-layer deposition control, production costs with this technique are high and deposition times are long to ensure high quality growth.

1.3.5.3. Chemical Vapor Deposition

Chemical Vapor Deposition (CVD) is the synthesis technique employed in this thesis. The process involves introducing precursors in the vapor phase into a high temperature reaction chamber. In the gas phase, precursors decompose under thermal treatment and deposit on the growth substrate forming a solid phase material. A rudimentary set up of a CVD reactor is shown in Figure 23. Gas lines, controlled via mass flow controllers, carry precursors in the vapor phase into the CVD reactor where they react and condense on the growth substrate.

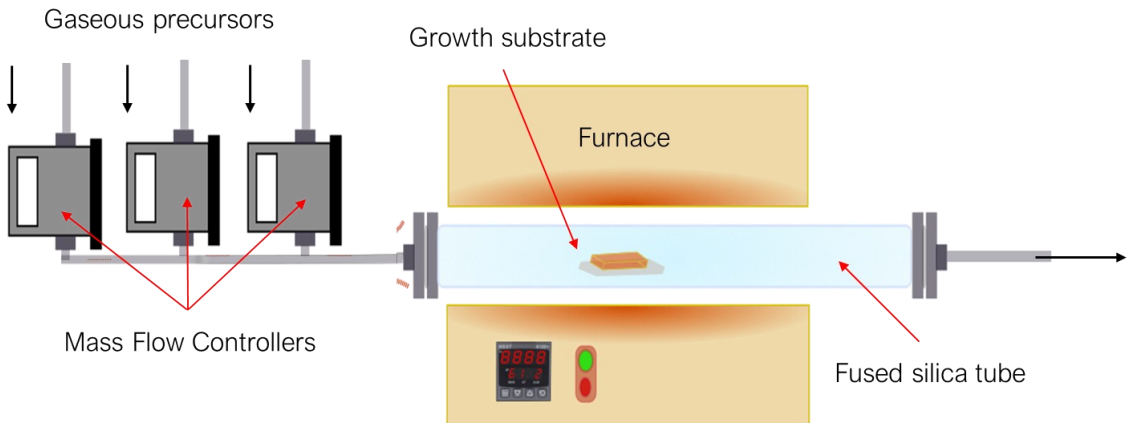


Figure 23; Simplified CVD set up for 2D materials. Gas lines carry precursors in the vapor phase into the reactor where they react and condense on the growth substrate.

Various modifications can be carried out to improve the CVD process, such as plasma enhanced CVD, where precursors are 'activated' via formation of a plasma, which can allow for growth of graphene or hBN at lower temperatures. Low pressure CVD (LPCVD) is also popular, which allows for enhanced monolayer growth as the reaction moves from mass transport limited to surface reaction limited at lower pressures but increases the complexity of the CVD process [105]. Enhanced evaporation of the catalyst, as well as increased etching of domains are problems often observed in LPCVD growth studies [106]. Cold-wall CVD is another technique whereby only the substrate or holder is heated via resistive heating or radio frequency (RF) induction[107, 108]. Such a technique reduces the impact of gas phase side-reactions which

can degrade the synthesis as well as allowing for rapid sample heating and cooling for quicker synthesis times.

Growth Substrates for CVD of hBCN

For CVD deposition, particularly 2D materials, the substrate plays a significant role in the qualities of the resultant film. In the case of 2D hBN and graphene, simple deposition onto dielectric substrates such as silicon or sapphire typically results in turbostratic and defective growth due to the high temperatures required for crystallisation [109]. However, using a catalytic growth substrate, the crystallinity of the 2D layers is enhanced and large single crystal domains can be synthesised (Figure 24, a) [110].

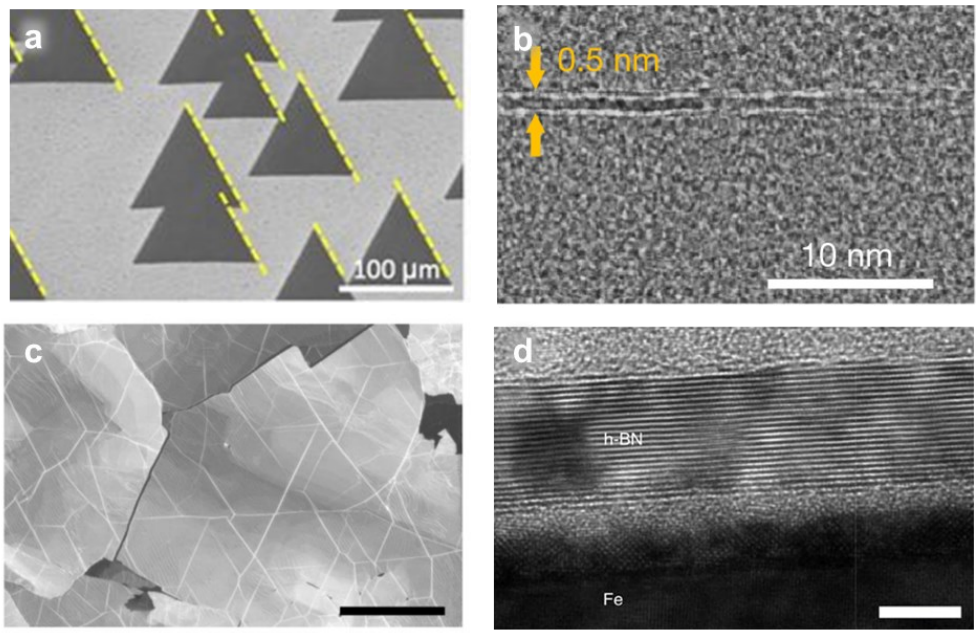


Figure 24:Influence of catalytic substrate on hBN growth. (a) Well ordered crystalline domains can be grown via *surface mediated* growth on the Cu surface, as seen in the SEM image. Dashed yellow lines show the high degree of alignment on Cu [111] (b) Due to the nature of the substrate, growth is limited to mono- to few-layered growth. TEM image shows a cross-section of hBN film grown on Cu, transferred onto SiO_2 [112] (c) Due to the higher solubility of precursors, growth on Fe can produce multilayered film growth. SEM image shows a thick hBN film grown on the Fe substrate. Grain boundaries between thick crystal domains can be clearly identified. Scale bar is 20 µm. (d) Multi-layered nature of hBN grown on Fe shown via cross sectional TEM. Scale bar is 20 nm. (c,d) are adapted from [113]

The choice of this catalytic substrate is significant due to the resultant effects on the final film. On Cu, mono to few-layered films of hBN or graphene often result due to the low solubility of

the precursors in the substrate, and films are grown via a surface mediated growth mechanism (Figure 24, b). On Fe, the solubility of precursors in the metal substrate is higher, and this can be exploited to grow thicker films via bulk segregation (Figure 24, c-d). By controlling the cooling rate of a C/BN saturated substrate, it is possible to control the phase segregation from the substrate, and by controlling the holding temperature, control the relative solubility of the material, resulting in a tunability of the films thickness [113, 114]. While hBN and graphene growth have been widely reported on Cu and Fe growth substrates, hBCN films have only seldom been studied on Cu foils, with no reports yet having looked at Fe as a growth substrate for hBCN.

Alloying substrates is another form of controlling the CVD growth process. By alloying different metals together to form a substrate, catalytic activity as well as substrate solubility can be beneficially modified to improve the uniformity and quality of the 2D film. In hBCN growth studies, Lu *et al.* reported that by alloying Cu with Ni, the quality of the graphene regions in a graphene/h-BN in-plane heterostructure were significantly improved, as determined from Raman analysis (Figure 25, a-c) [115]. They ascribe this enhanced film quality to the increased capacity for dissolving carbon into the Cu-Ni substrate. On Cu, typically only surface diffusion occurs, and the growth resulting was diffusion limited. With both surface diffusion and bulk segregation mechanisms present in the Cu-Ni substrate, C atoms reach the growth front of graphene domains at a faster rate and allow for high-quality, attachment-limited growth. Further studies on hBCN CVD growth on Cu-Ni by Lu *et al.* observed that graphene adlayers often tend to nucleate below the in-plane heterostructure [116]. Graphene adlayers were found to preferentially nucleate along the hBN-Gr heteroboundaries and extend underneath the structure, with the hBN edges acting as energy-favorable sites for adlayer formation (Figure 25, d-i). Interestingly, high quality monolayer growth was observed below the hBN domain (red arrow in SEM image (h) and similar coloured Raman spectrum in (i)),

while few-layered graphene was observed at the external edges (blue arrows in (h) and spectrum in (i)).

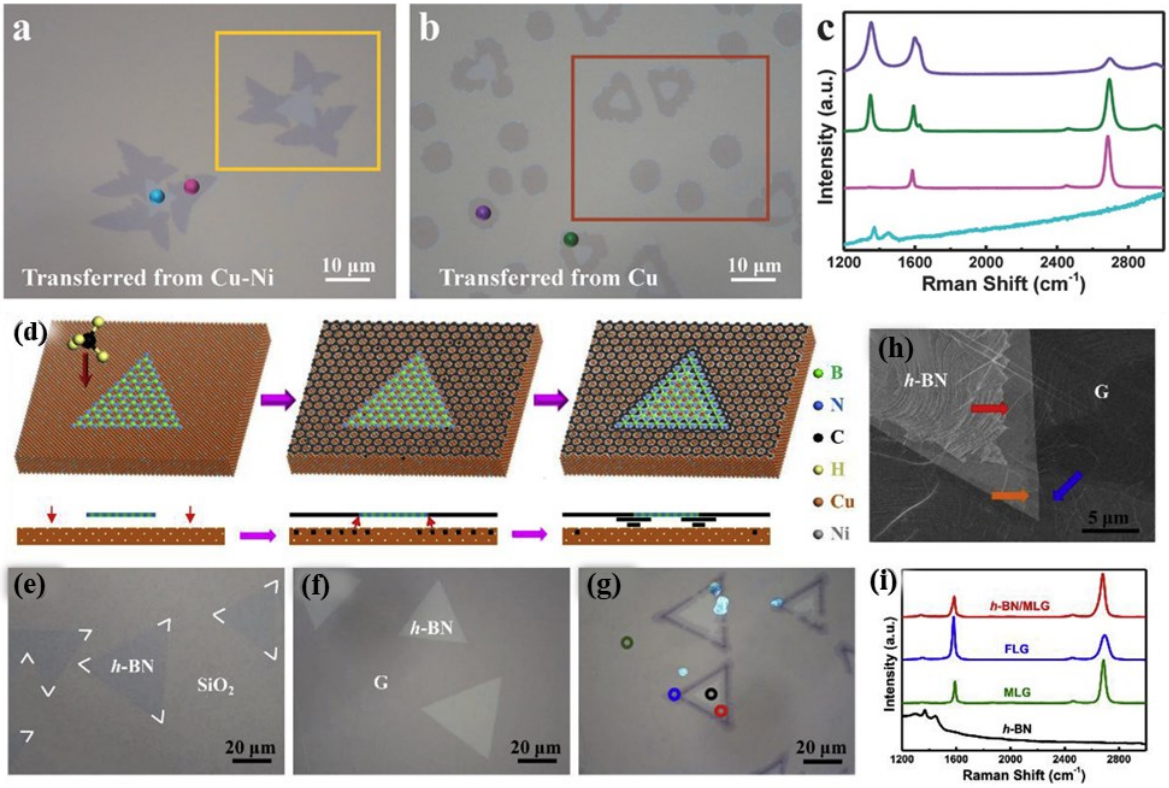


Figure 25; Graphene/h-BN heterostructures grown on alloyed substrates; Cu-Ni. (a,b) Optical images of the graphene/h-BN heterostructures grown on (a) Cu–Ni and (b) Cu. (c) Raman spectra taken from the marked areas with corresponding color dots in (a) and (b). (d) schematic of how graphene precipitates during hBCN growth on Cu-Ni substrates.The hBN edges act as nucleation sites for graphene phase segregation from the substrate. (e-g) OM images of Cu-Ni grown (e) hBN (f) hBN/Gr in-plane heterostructure (g) and hBN/Gr stacked heterostructure on Si/SiO_2 substrates. (h) SEM image of a hBN/Gr stacked heterostructure. The red, blue and orange arrows point out the areas of hBN / mono-layer graphene (hBN/MLG), few-layer graphene (FLG), and hBN/few-layer graphene (hBN/FLG), respectively. (f) Raman spectra taken from the marked circles in (g) with corresponding colours. Images (a-c) are reproduced from [115] and (d-i) from [116].

Recent work in CVD of 2D hBCN materials has looked at novel form of CVD growth using liquid metal catalyst substrates, referred to as LMCats. Lee *et al.* reported self-collimated growth of centimetre sized single crystals of hBN using a liquid-metal catalyst (LMCat) gold substrate [117]. In the absence of crystalline faceted structure on the surface of the metal, circular hBN domains grew on the molten Au surface, rotating to form a self-aligned single crystal (Figure 26, a-b). On Cu, LMCat synthesis has shown promise in synthesising highly aligned and homogeneous graphene domains for future graphene-hBN based heterostructures.

Nucleated graphene domains move freely and rotate during growth, without substrate induced strain, and highly ordered structures can be realised (Figure 26, c-f) [118]. By then introducing a B/N precursor, a highly ordered graphene-hBN continuous array can be synthesised [119, 120]. In particular, M. Li *et al.* demonstrated precise control over the domain sizes of hBN:C and their density in forming super-ordered arrays of hBN/Graphene using this technique (Figure 26, g-h)[119].

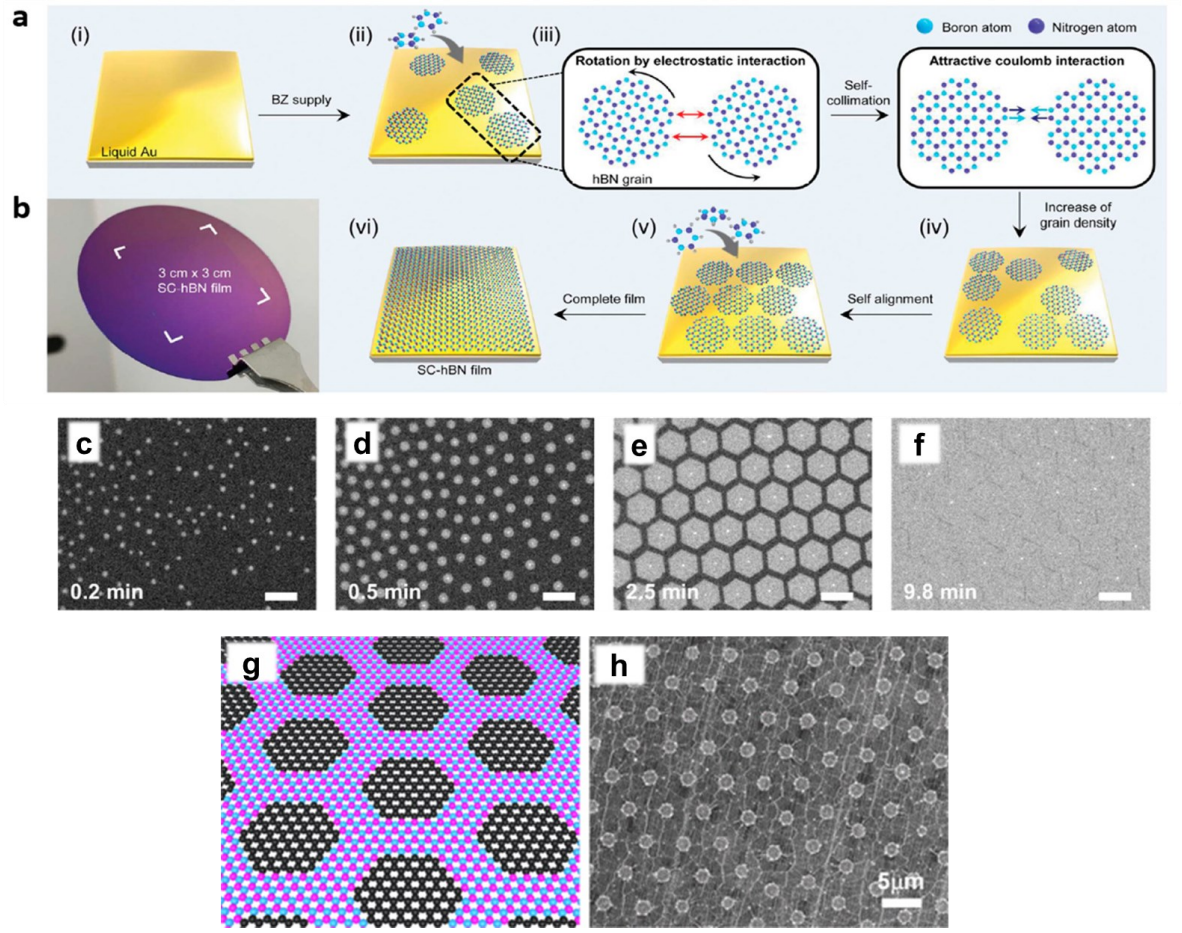


Figure 26; LMCats for CVD growth of 2D hBCN. (a) growth of single crystal hBN via liquid metal catalyst (Au). Domains of hBN rotate from electrostatic interactions and self—align on the molten surface of Au to form a centimetre scale single crystal. (b) Wafer showing a 3 x 3cm^2 single crystal hBN film grown from Au and transferred onto Si/SiO_2. (c-f) SEM images of graphene nucleation and growth on molten Cu after (c) 0.2 min (d) 0.5min (e) 2.5 min and full film convergence at (f) 9.8 min. Highly ordered graphene domains are realised before full film convergence. By introducing hBN precursors prior to this, hBCN heterostructures can be realised. (g) shows an illustration of this arrangement, and (h) a wide view SEM of the CVD grown heterostructure. (a,b) reproduced from [117], (c-f) from [118], (g,h) from [119]

In a similar vein, controlling the CVD growth process can be achieved by precisely tuning the facet of the substrate, i.e. single crystal 2D material growth on a single crystal metal catalyst

substrate. It has been known for some time that the orientation of the facet of the metal has a significant effect on the resultant film in terms of domain shapes, sizes and thickness [32, 121]. Single crystal substrates have typically been expensive to produce as their preparation is time consuming and needs to be carefully controlled. However, recent advances in metallurgy have made it increasingly feasible to produce large scale, high-index, single crystal metal foils through seeded, single crystal growth [111]. With this, CVD techniques have been able to achieve growth of centimetre-size single crystals of graphene [122] and hBN [117, 123-125] on metal supports. Still, research is needed to decode the appropriate facets and step edges for optimum single crystal growth. In a report from Wang *et al.,* DFT studies found that BN adsorption on the <211> edge of the Cu (110) facet was the most stable bonding site (Figure 27, a-b), which resulted in growth of unidirectionally aligned domains of hBN, forming a single 100 cm^2 crystal on a Cu(110) substrate with <211> edges [123] (Figure 27, c-d). A similar 'lattice edge' technique is used for the unidirectional growth of large-area, single crystal graphene (Figure 27, e), [111].

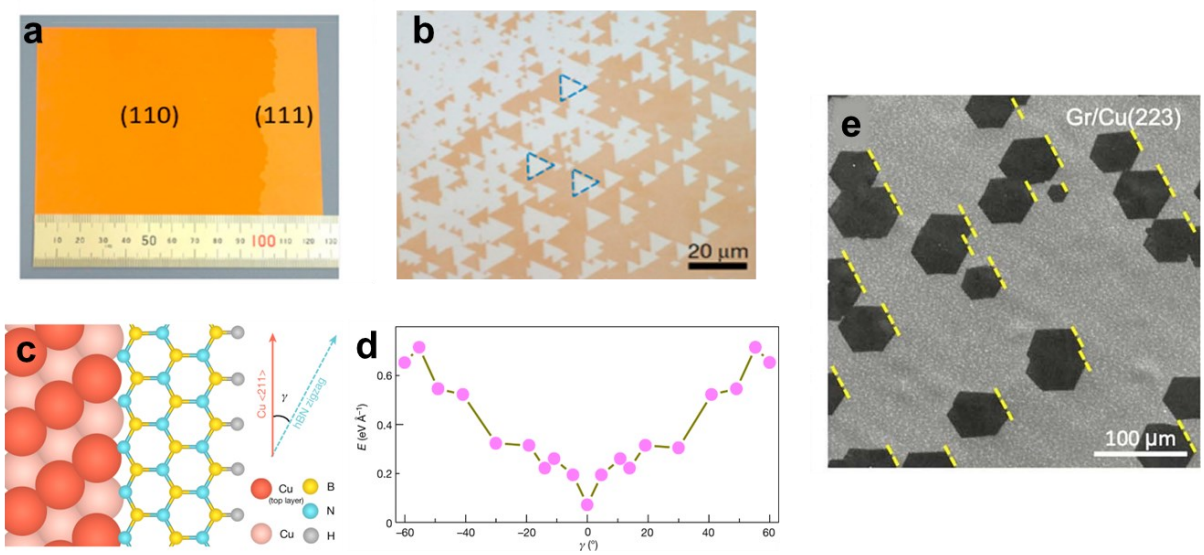


Figure 27; Substrate engineering for large single crystal growth. (a) OM image of the Cu growth substrate showing two regions of single crystal Cu after beinggrown with an artificial Cu(110) seed. (b) OM image of unidirectionally aligned hBN domains on Cu(110) facet. (c) Schematic of the Cu <211> and hBN edge orientation system analysed via DFT (d) Energy of hBN layer on Cu with respect of hBN domain rotation to the <211> edge of Cu. (e) Unidirectional graphene domains grown on a high index Cu facet. (a-d) reproduced from [123] and (e) from [111].

Precursors for CVD of hBCN

Growth of BCN materials via CVD typically involves using a combination of the precursors for synthesis of graphene and hBN. To date, the most common precursors for hBN growth have been amino-borane [126-131], a non-toxic solid which allows for safe handling, and borazine [113, 132-135], a pyrophoric liquid with low vapor pressure (Figure 28, a). Both precursors need to be heated to reach the gaseous phase and, typically, a carrier gas is used to introduce reactants to the CVD chamber. This can create difficulties in controlling their concentration which can affect reproducibility. Gaseous boron sources are available but are extremely toxic and, therefore, often avoided.. There are reports of diborane (B_2H_6) and boron trichloride (BCl_3) being used alongside ammonia (NH_3) as separate precursors in CVD of hBN, allowing for sequential deposition [107, 136]. However, using B_2H_6 and NH_3, thick hBN films (~100 layers) were realised and films were turbostratic and lacking in crystallinity [136]. For graphene growth, a gaseous carbon precursor, such as methane or acetylene, is typically used, controlled directly using mass flow controllers (Figure 28, b)[137, 138]. Reactants are often mixed with an etching gas, such as H_2, which has been shown to significantly affect the growth of graphene through activation of the catalytic surface, etching of defective growth regions and suppressing multilayer formation[139, 140].

The first reported 2D hBCN materials prepared by CVD were by Ci *et al.* in 2010, using ammonia borane and methane precursors. Here, they reported synthesising an atomic sheet of hybridised hBN and Gr domains through simultaneous introduction of growth precursors under LPCVD and high methane partial pressures [141]. Raman and UV-vis analysis is used as evidence of hybridisation in the hBCN sheet, although no characteristic E_{2G} peak of hBN is found in Raman analysis (only graphitic C) and no SEM images are shown, making it unclear exactly how this hybridisation might look at the microscopic level. Using the same precursors, hBN-Gr stacked heterostructures can also be grown [116, 142-144]. Wang *et al.* synthesised

graphene-on-hBN stacked hBCN structures by sequential growth of a hBN on Cu followed by graphene growth once full coverage of hBN had been realised [143]. Where full coverage is not reached [119, 120, 145], or gaps are etched in the first deposited layer [56, 146], lateral Gr-hBN heterostructures can be formed. BN co-doped graphene (BNGr) has also been realised though simultaneous introduction of a low ammonia borane flux during optimised graphene growth with methane [19]. In a similar fashion, C doped hBN was only recently been reported by Liu *et al.*, with methane introduced during an optimised hBN synthesis [23]. By employing separate BN and C precursors, control over relative concentrations can be achieved by their respective mass flows, resulting in tuneable physical properties in the overall structures [141].

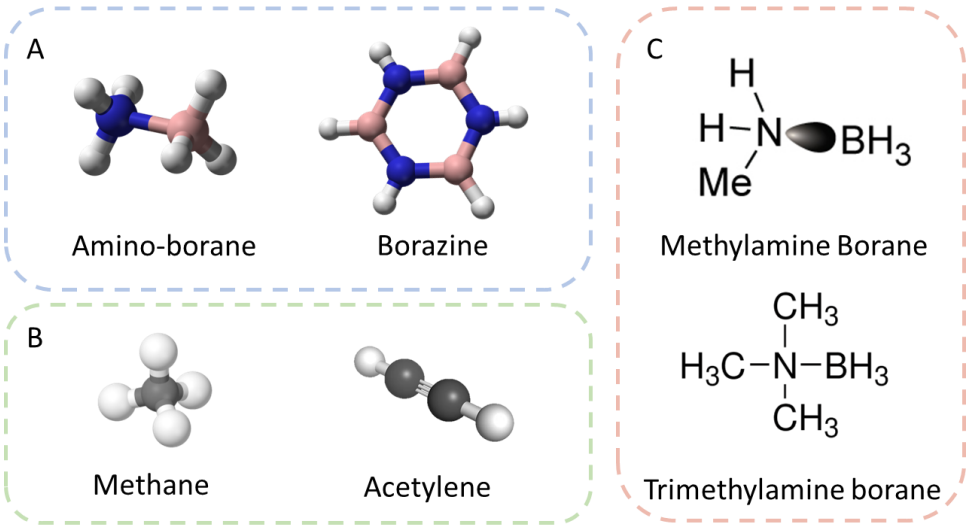


Figure 28: Common precursors used for hBCN growth via CVD. (a) hBN precursors amino-borane and borazine, (b) graphene precursors methane and acetylene. (c) hBCN single source precursors methylamine borane (MeAB) and trimethylamine borane (TMeAB).

Growth using single source precursors for hBCN synthesis via CVD has also been reported, using precursors such as methylamine borane (MeAB) and trimethylamine borane (TMeAB) (Figure 28, c) [18, 147-149]. These solid precursors already possess C-N bonds within their network, which increases the incorporation of N-C bonds into the BCN network, which are less energetically favourable, thermodynamically speaking, than B-N and C-C, and they can be a useful method of synthesising more alloyed BCN structures. While these pre-cursor sources

typically allow for stochiometric synthesis based on their relative B, C and N content, the tuneability is not available.

1.3.5.7 Limitations of the synthesis methods and challenges

To date, most 2D devices are manufactured in laboratories, fabricated using mechanical exfoliation from highly crystalline, bulk materials. However, with this approach, material sample size is often small, and the process is not time & cost effective, thereby limiting the scalability and economic cost of production. In response to this, the scientific community has turned to other methods of synthesising graphene, hBN and hBCN at a larger scale. These mainly comprise of pyrolysis techniques [5, 14, 100, 101, 150], which allow for large-scale production of the material. Unfortunately, these techniques have drawbacks of their own that limit certain applications of the 2D material, primarily the low crystal quality, crystallite size and defect control. Bottom-up approaches, such as molecular beam epitaxy (MBE) [25, 43, 151], pulsed laser deposition (PLD) [52, 152] or IBSD [25, 153] can surpass some of these issues, allowing for more precise control over synthesis conditions, resulting in higher quality films. However, they are costly and require complex synthesis protocols. The CVD method, used in this thesis, is a well-known and scalable route for synthesis of high-quality 2D materials, and for a fraction of the cost of these higher-end operating techniques. In particular, the catalyst-assisted (CA) CVD method has shown exceptional promise and has already succeeded in growing centimetre-scale, single crystal films of both graphene and hexagonal boron nitride [111, 123, 154]. Given the maturity of graphene and hBN growth, interest is now being cultivated in growth of mixed BCN materials via CVD. This work uses low-cost and non-toxic precursors, ammonia borane and methane, and a simple synthesis protocol, atmospheric CVD, to produce hBCN materials with tuneable properties in a scalable and cost-effective manner.

Chapter 2

Characterisation Methods

The following chapter will briefly discuss the various characterisation techniques used in this thesis and how they apply to the study of 2D materials. The basic principles of operation will be introduced as well as information that can be gathered from each technique as it pertains to the study of 2D materials.

2.1. Scanning Electron Microscope

The Scanning Electron Microscope (SEM) is one of the more convenient techniques for sample characterisation during the synthesis optimisation process, alongside optical microscopy. A schematic of the SEM is shown in Figure 29 (a). In SEM, A stream of collimated electrons generated via thermionic emission or field emission gun are accelerated towards a sample under voltages of the order of tens of kV. Electrons are focused by electromagnetic lenses onto a sample such that they interact. A detector then collects the emitted electrons which are interpreted to give an image.

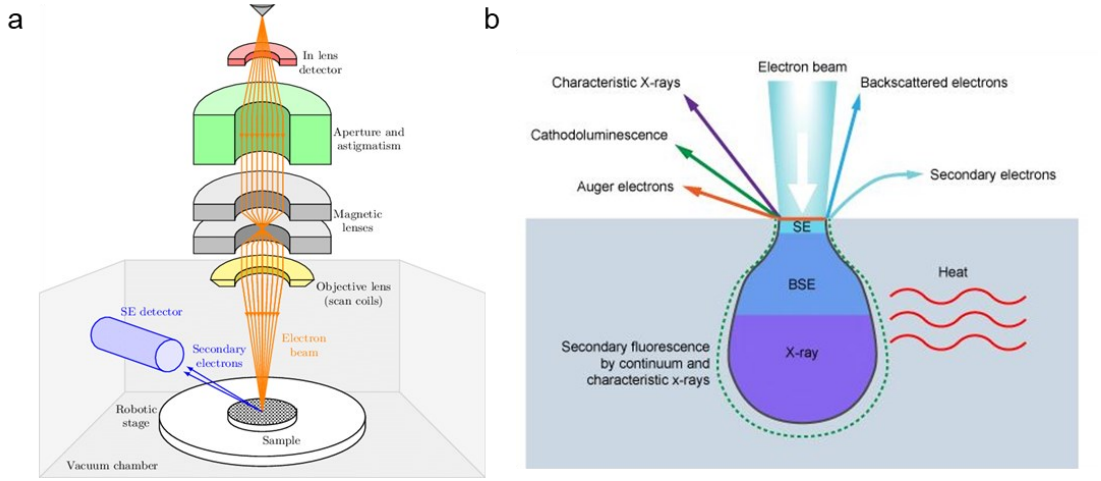


Figure 29, Scanning electron microscopy (SEM) working principles. (a) Schematic of a SEM showing how the beam is collimated and collected. Reproduced from *[155]*. (b) Diagram of an electron beam interacting with the sample, showing the various processes that can occur. Some electrons are able to penetrate deeper into the bulk (backscattered electrons) while others are scattered closer to the surface (secondary and Auger electrons).*[156]*

There are several ways in which the electrons can interact with the sample. They can be transmitted (in the cases of very thin samples), reflected or cause ionisation within the sample. These electron-matter interactions can be divided into two classes;

- **Elastic scattering**; the electron trajectory within the specimen changes, but its kinetic energy and velocity remains essentially constant. The result is generation of *back-scattered electrons* (BSE) shown in Figure 29, (b). These electrons are high in kinetic

energy and carry information about the atomic composition of the sample. For example, regions with varying atomic masses and thickness will show enhanced contrast in the BSE detector.

- **Inelastic scattering**; Here, energy of the incident electron is lost through the transfer to the specimen. The result is the generation of:
    - *Secondary electrons*: electrons are released from ionization on the surface caused by the beam of primary electrons. The mean free path of electrons in most materials is of the order or 1 nm. Therefore, only electrons created near the surface are detected. These electrons carry information about the topological details of the material's surface and are detected with the secondary electron detector.
    - *Characteristic x-rays*; High energy photons are produced when electrons from the inner shells of the atom are ejected after collisions with the electron beam and their vacancy filled by outer shell electrons. The energy spectrum of these photons is characteristic of the element involved. These photons are detected in EDX analysis.

In this thesis, SEM is used to detect material growth via the contrast between regions of graphene or hBN coated and the bare Cu (Figure 30 a). Beam attenuation arises from 2D layers on Cu, reducing the intensity and offering contrast between the regions. Similarly, with more layers, less electrons escape towards the detector and, thus, SEM can also be used to analyse multilayer coverage (Figure 30 b). For heterostructure growth, hBN and graphene have different transparencies with the electron beam and these regions can be distinguished under SEM analysis (Figure 30 c). For full coverage on the growth substrate, additional considerations are often needed for characterisation, as no contrast, such as that in Figure 30 (a), is available. Therefore, secondary features like wrinkles and folds (seen in Figure 30 d) are

used to characterise the material. In the case of hBN and graphene, their thermal expansion coefficients differ significantly to that of a metal like Cu (which expands significantly at elevated temperatures), such that, upon cooling after growth, wrinkles and folds form in the adlayer to accommodate the shrinking of the metallic growth substrate below. In this thesis, scanning electron microscopy (SEM) images are obtained using a JEOL-840F, Zeiss EVO and Zeiss Merlin microscopes with resolution limits of 1-5 nm.

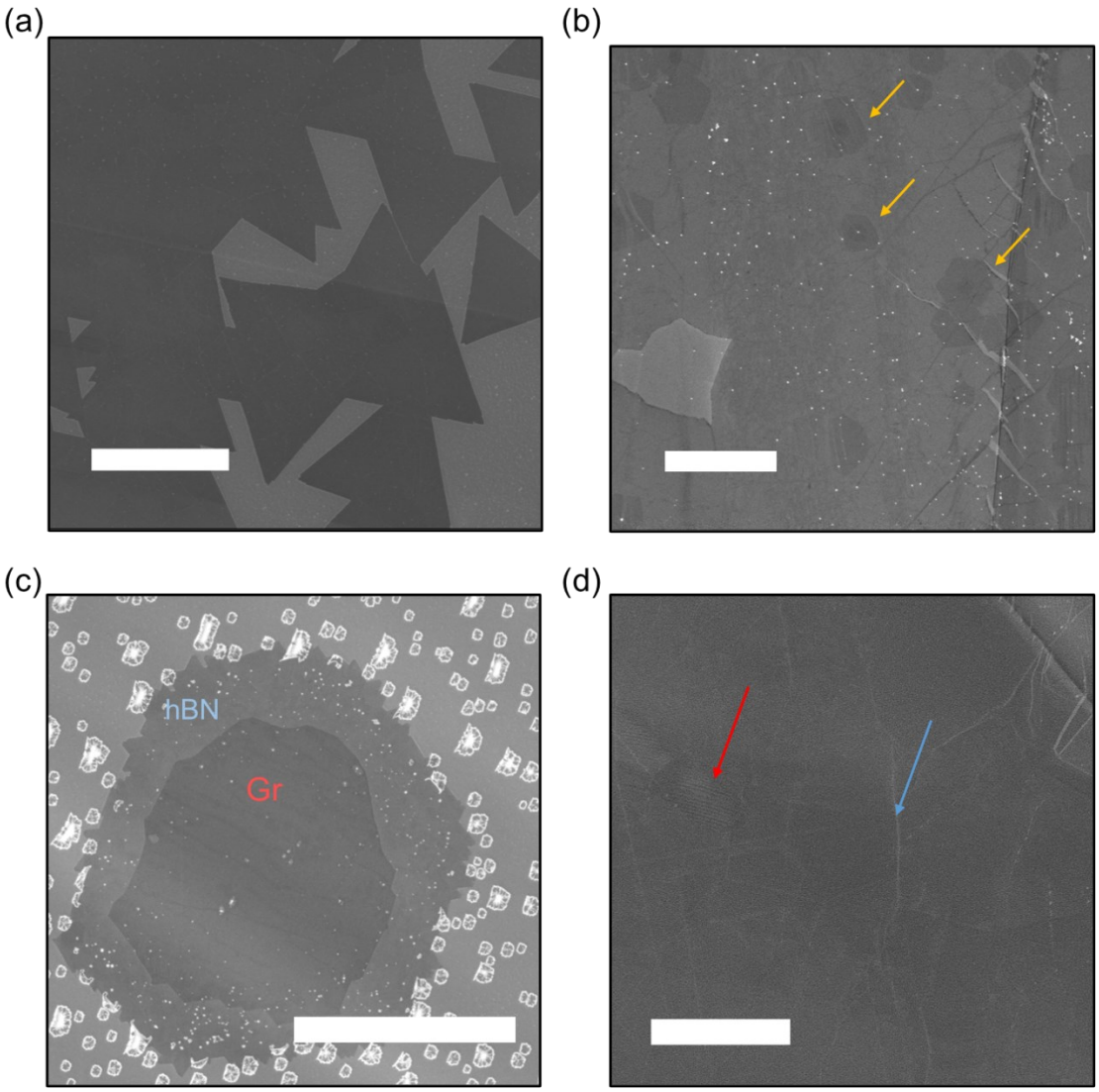


Figure 30; Contrast between 2DM and underlying substrate and imaging features. (a) SEM image of individual hBN domains on Cu. Islands can be easily distinguished due to the contrast between the signal coming from the Cu and hBN regions (scalebar is 40 μm). (b) SEM image showing intensity contrast from multilayer regions (yellow arrows) of graphene on Cu. (c) hBN and graphene have different transparencies with the electron beam and these regions can be distinguished under SEM analysis. (d) Fully converged region of hBN film on Cu. Without any contrast from the underlying substrate, it is difficult to distinguish if there is deposition. From features such as wrinkles (red arrow) and folds (blue arrow), we can infer that there is hBN present (scalebar is 20 μm).

2.2. Energy dispersive x-ray spectroscopy

Energy dispersive x-ray spectroscopy (EDX) is a technique which analyses the x-rays emitted from the sample under irradiation from the SEM electron beam. As these emitted x-rays are characteristic of the element involved, and their intensity is proportional to their concentration, EDX can be used to quantitatively measure the atomic composition of a region of the sample. Figure 31 (a) shows a schematic of the x-ray generation process.

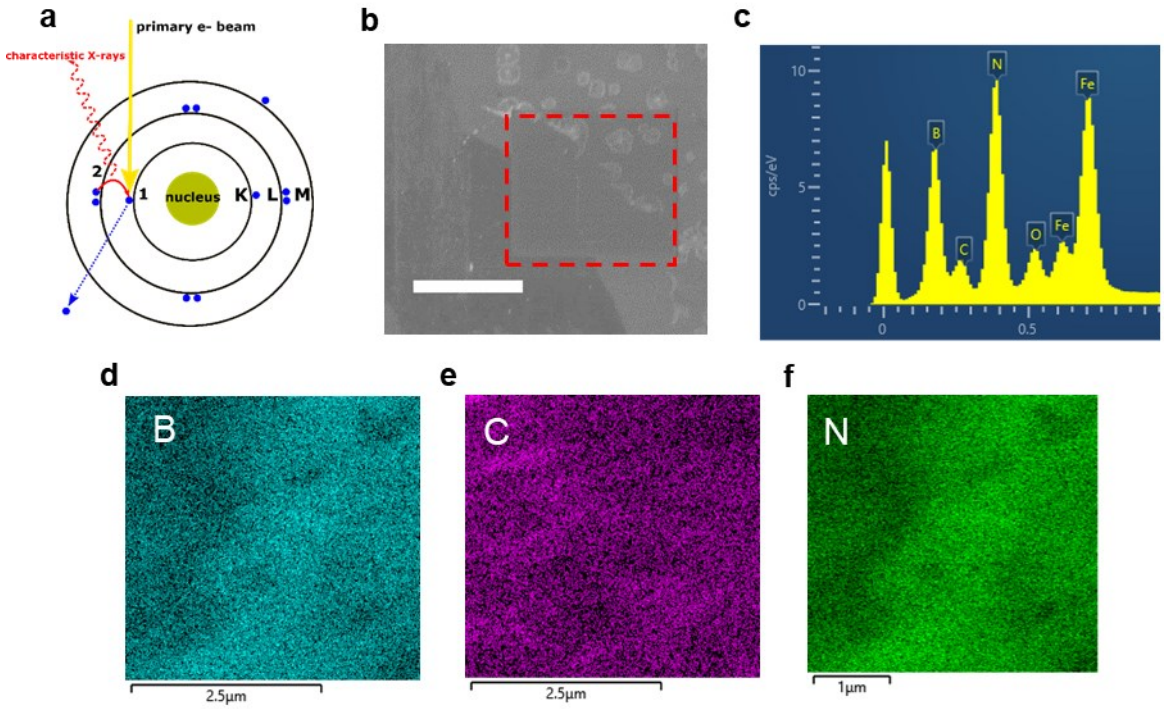


Figure 31; Energy Dispersive X-ray Spectroscopy (EDX). (a)Schematic of the x-ray generation process when an electron beam interacts with the inner shell electrons in the sample *[157]*. (b) SEM image showing a region of a Gr-hBN heterostructure that has been damaged by the electron beam (scalebar is 15um) (c) A typical EDX spectrum identifying the elements present in a typical BCN structure grown on Fe. (d-f) Elemental maps which show the spatial elemental composition of B, C and N.

As EDX requires high-energy electrons to generate x-rays through core electron interactions, it is difficult to use this technique for few-layered materials. Figure 31 (b) shows a region of a few-layer hBN/Gr heterostructure synthesised on Cu which has been damaged by the electron beam after an attempted EDX analysis. As well as this, light elements such as B, C, N, O are difficult to detect in thin samples as their low photon energies are positioned close to the electronic noise of the detection system, and they also generate lower x-ray yields. For thicker

samples, EDX can be a useful tool for identifying and quantifying atomic composition in the BCN sample. An EDX spectrum of multilayer BCN layers grown on Fe is shown in Figure 31 (c). EDX elemental mapping may provide insight regarding the qualitative distribution of elements in the material. These maps are generated based on the peak intensities at each point, shown in Figure 31 (d-f), corresponding to boron, carbon and nitrogen, respectively. In this thesis, energy dispersive X-ray (EDX) analysis was conducted by John Ballentine using a Zeiss Merlin SEM equipped with an EDX detector (Oxford Instruments). EDX data was analysed using AZtec EDX Analysis software.

2.3. Transmission electron microscopy

Transmission electron microscopy (TEM) provides an accurate way of characterising 2D materials at the nanoscale, measuring things like layer number and electron diffraction, which can reveal the stacking order and lattice features of the 2D film. A schematic of a TEM is shown in Figure 32 (a). Like SEM, TEM generates images using a high voltage electron beam (in TEMs case, however, it is a much higher voltage) produced by an electron gun at the top of the apparatus and travels down towards the sample under the strong electric field. Electromagnetic lenses to focus the electron beam onto the sample. The electron beam then passes through the sample where its path is influenced by the atoms in the thin sample. By allowing the beam to go through the sample, imaging at higher resolution (~ 0.2 nm) is possible due to the reduced interaction volume. More lenses are used to focus the transmitted beam onto a fluorescent screen at the bottom of the microscope, where an image is generated. The image can be studied directly in operating mode or else captured using a CCD for further analysis using image processing software.

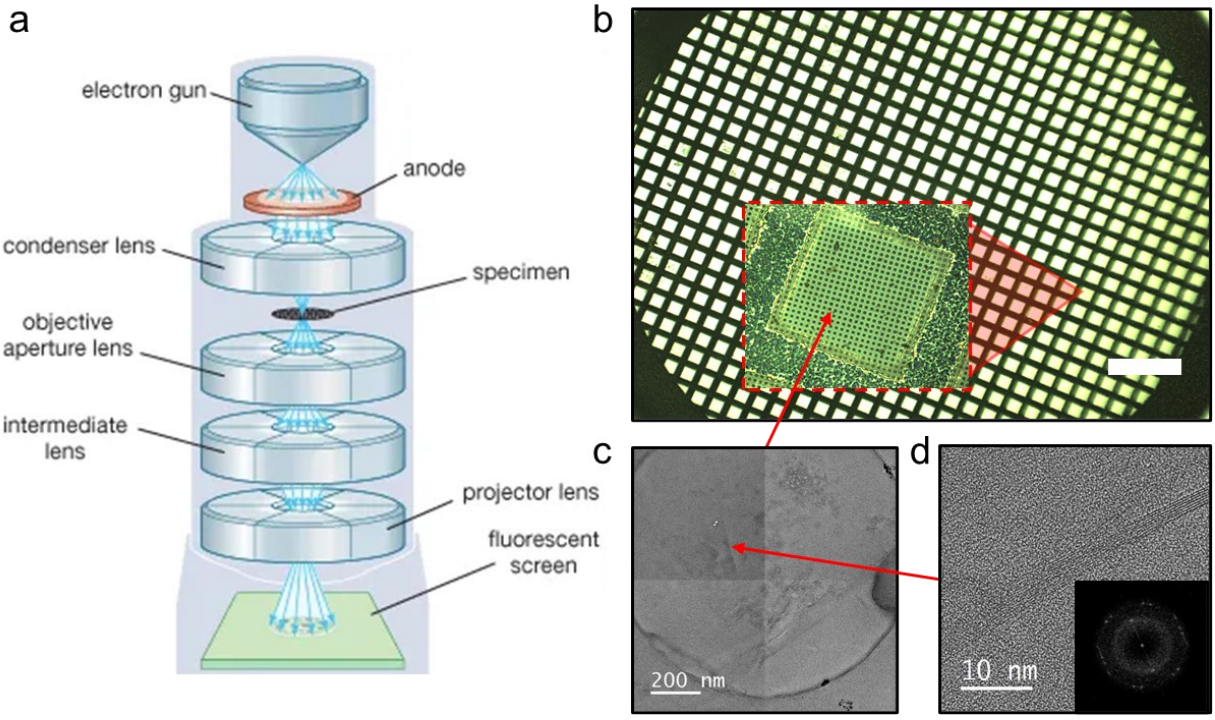


Figure 32; Transmission Electron Microscope - apparatus and experimental details. (a) diagram of TEM with main components labelled, taken from *[158]*. (b) OM image of Quantifoil Au TEM grid with patterned carbon membrane visible from the inset image. The patterned carbon support foil with defined hole size, shape and arrangement allows for easy sample preparation, as the 2DM is well supported, and high-resolution EM data collection due to negligible z-height variations across the supported sample. Scalebar is 0.3mm (c) TEM image where hBN film is suspended over vacuum on the circular patterned carbon foil. (d) A fold in the hBN film can be used to deduce the layer number. The FFT inset shows two rotated six-fold diffraction spots, characteristic of rotated layers.

A JEOL TEM-3000F (field emission gun) is used in this thesis, operating at 200 kV. TEM images are processed using the software Digital Micrograph 3. Figure 32 (c,d) show two TEM images at different magnification. In Figure 32 (d) edge or fold features in the hBN film are used to deduce the layer number. Inset in Figure 32 (d) is the fast Fourier transform (FFT) which gives information about interlayer rotation and stacking.

2.4. Optical Microscopy

Optical Microscopy (OM) is a useful tool to quickly evaluate the quality of the prepared growth substrate before synthesis as well as the quality of the growth post-synthesis. Post-growth graphene and hBN are not readily visible on metallic substrates due to their high reflectivity.

For assessing growth quality, metal foil was oxidised to enhance contrast between regions covered and free of 2DM deposition (Figure 33, b). OM was also used to assess the quality of 2DM transferred onto Si substrates (Figure 33, c). Due to the low light absorbance of monolayer hBN (~0.1%), it is much more difficult to distinguish than graphene (2.3%). However, at higher layer numbers, it can be readily used.

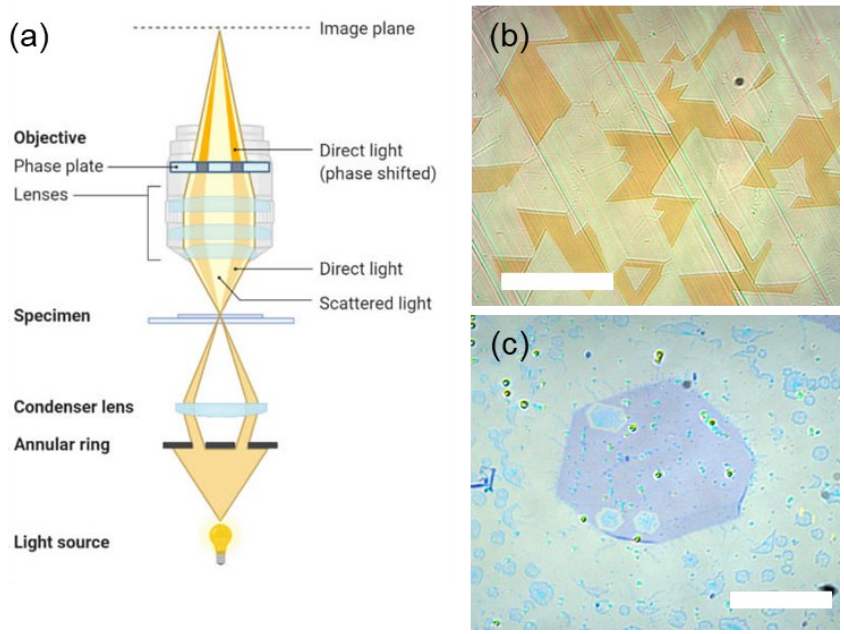


Figure 33; (a) Schematic of an optical microscope, similar to that used in this thesis. (b) OM image of hBN domains on Cu foil. The bare Cu regions have been oxidised to enhance contrast between the regions of covered and uncovered hBN on Cu. Scalebar is 50 µm (c) OM image of a hBN/Gr heterostructure transferred onto SiO_2/Si substrate. Graphene shows a much higher absorption than hBN and is readily observed on the SiO_2 substrate. hBN has an absorbance of < 0.1% and is difficult to observe it on SiO_2 via OM. Scalebar is 25 µm.

2.5. Optical Profilometry

Optical Profilometry is a useful tool for analysis of film thickness in 2D layers as well as characterising surface roughness of growth substrates. A schematic of an optical profilometer is shown in Figure 34, (a). Light beams are split, reflecting from a reference (known distance, reflectivity) and the test material and both beams are recombined at the photodetector. The path difference between the reference and test sample creates a phase difference between them, creating an interference pattern between the initially identical light waves. This interference

beam is focused into the digital photodetector, which sees the constructive interference areas as lighter, and the destructive interference areas as darker. Through analysis of this interference pattern at each point, the path difference can be deduced, and a 3D topological map constructed.

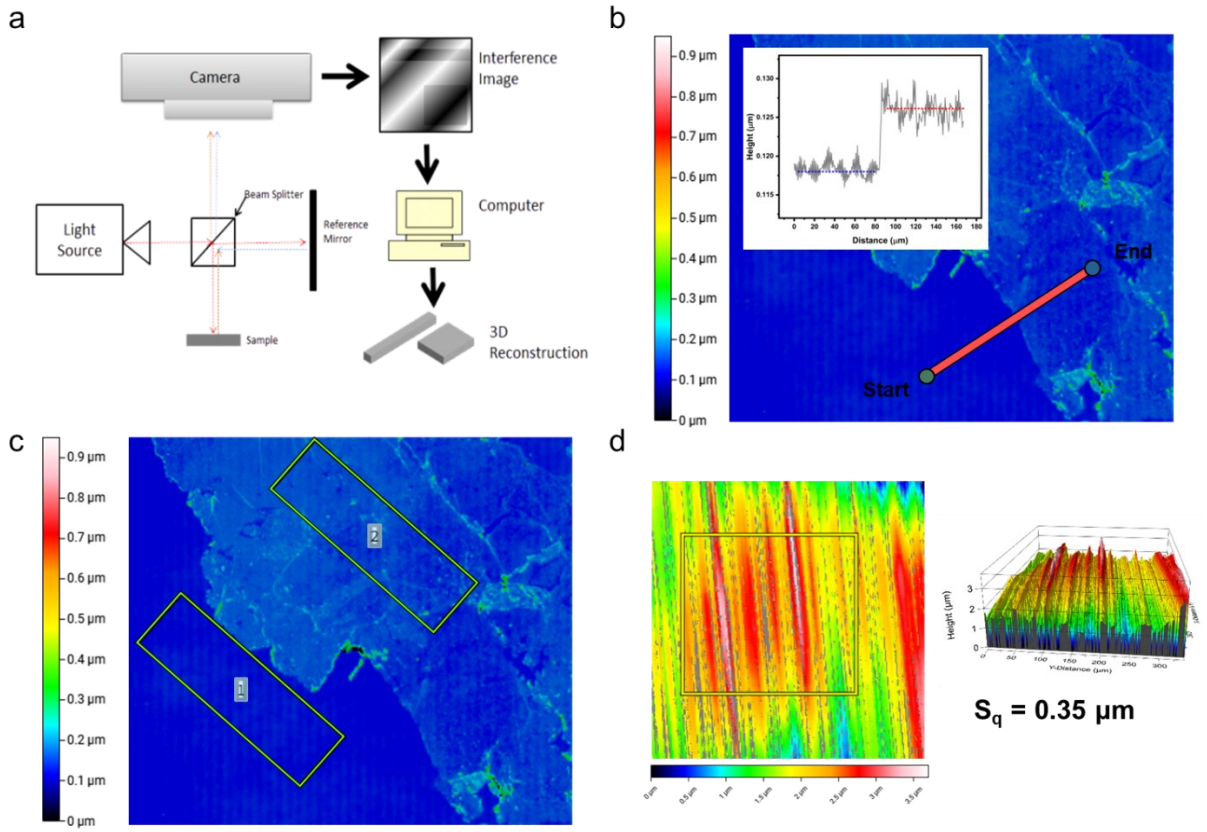


Figure 34; Optical profilometry working principle and examples of data analysis. (a) diagram of optical profilometer set-up. A white light source is used to illuminate the sample, collimated by a condenser lens. A beam splitter splits the light into a 'measurement' and 'reference' beam. The reference beam is reflected by a mirror of known path length while the measurement beam is reflected or scattered by the sample. Both returning beams are detected at the CCD sensor, forming an interference pattern of the measurement and reference beam at that point. Combining these across the xy-plane gives a spatially resolved interference image which can be reconstructed, using computational software, to give a 3-D surface. (b,c) Profilm3D software offers several methods to analyse the step height of 2D films. (b) shows a line profile of the film while, in (c), average heights differences across the two rectangles are used to give an estimate for film height in multi-layered hBN films grown on Fe. (d) Average roughness of surfaces can also be obtained as is done for 'as received' Cu foil.

In this study, the ProFilm 3D optical profilometer is used in PSI mode, which has a vertical resolution of 1 nm [159] making it useful for easy characterisation of multilayer hBN films and silica structures. Line profiles can be generated for the mapped area (Figure 34 b) as well as average height difference between two areas (Figure 34 c) which can be used to estimate the

film thickness in multilayer hBN films. The surface roughness of substrates can also be deduced using optical profilometry, as shown in Figure 34 (d).

2.6. X-ray Photoelectron Spectroscopy

X-ray Photoelectron Spectroscopy (XPS) is an analytical tool based on the photoelectric effect, where a photon of sufficient energy can eject electrons from a surface when it impinged upon it. The technique uses an x-ray source to produce high energy photons that interact with atoms and eject electrons from different electron shells. The ionised electrons are attracted towards the energy analyser where their kinetic energies are measured, and a spectrum created via the machines software. A schematic of the XPS apparatus is shown in Figure 35, (a). Because of the short mean free path of electrons ionised in the XPS process, the technique is very surface sensitive and only allows for the detection of elemental species and their bonding environments in the top few nanometres. The probe size is much larger due to difficulties with focusing x-rays, typically around 30 – 400 μm. The sample is always in electrical contact with the spectrometer system so that both have a common reference for measuring the electron's energy. With a common reference value, measuring the kinetic energy of the electron emitted allows for the binding energy to be determined once the photon's energy is known;

$$h\nu = E_{binding} + E_K \qquad (3)$$

An XPS spectrum is typically measured as intensity vs. binding energy. In the XPS spectrum, elements have characteristic peaks due to their electronic structure (1s 2s 2p 3s 3p 3d etc.) and bonding configurations (Si and SiO_2, for example) and thus E_b will vary between elements and also the elements different bonding environments. Figure 35 (c) shows a survey spectrum of Cu foil, showing large quantities of Si and O contamination. Through analysis of the peak areas as well as relative sensitivity factors (RSF) for each element, which are unique to the XPS machine, one can estimate the atomic composition of the sample surface. Through high

resolution scans of peaks in the survey spectrum (Figure 35, d-e), the chemical bonding environments can be deduced via peak fitting and matching peak centres and FWHM to literature values and those available in XPS databases such as NIST XPS database [160].In Figure 35 (d,e), two peaks are fitted for each spectrum corresponding to two different bonding environments of B in spectrum (d) and Si in spectrum (e).

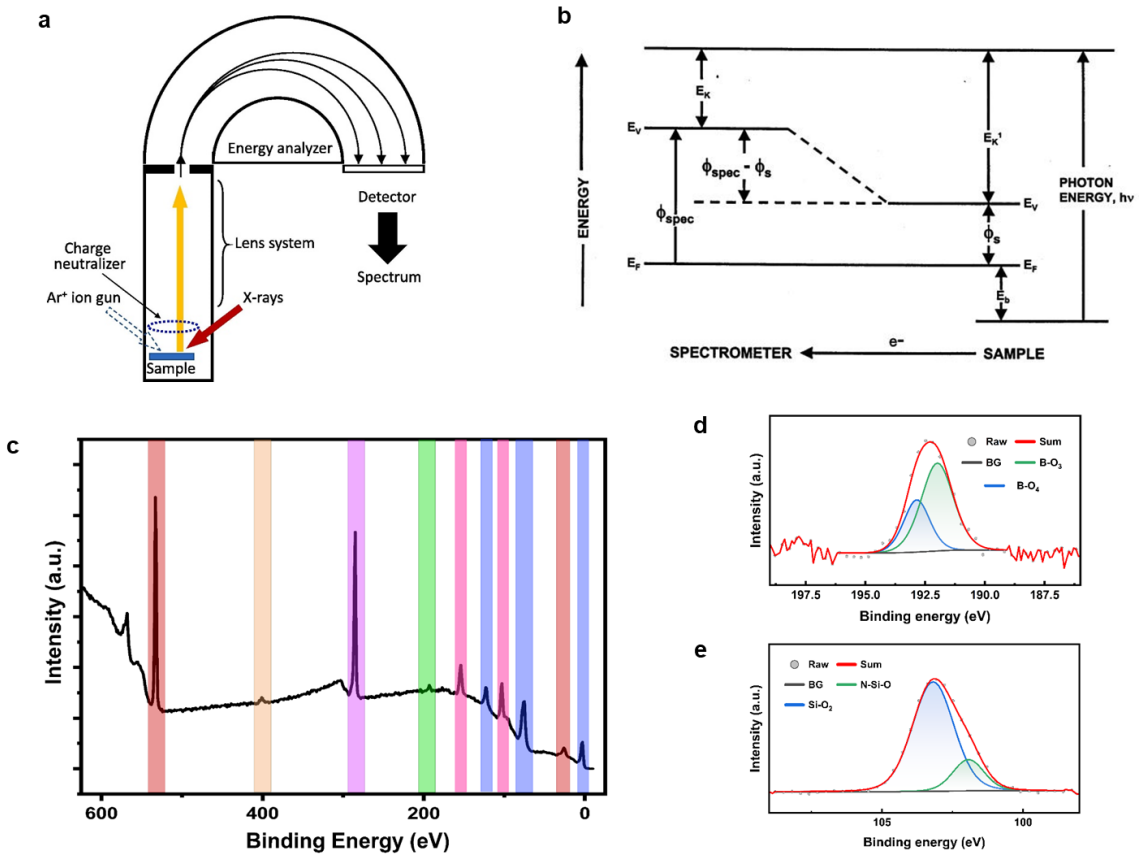


Figure 35; XPS working principle and examples of data analysis (a) Diagram of XPS apparatus. Photoelectrons are directed towards the director via the energy analyser which can separate the electrons based on their energy. The photo-detector can then measure the electron current as a function of their energy. (b) Energy level schematic for binding energy, E_b, measurements, reproduced from *[161]*. (c) Typical XPS survey scan showing the surface of Cu foil after a contaminated hBN synthesis. Copper (blue), carbon (purple), boron (green), nitrogen (orange) are seen as well as the contaminants, silicon (pink) and oxygen (red). (d,e) High resolution XPS of (d) Si 2p and (e) B 1s which have been deconvoluted to show the different bonding environments present.

Figure 36 shows the binding energies of deconvoluted peaks in the B1s, C1s and N1s spectra of reports concerning $B_xC_yN_z$ materials which are used to evaluate XPS data in this thesis.

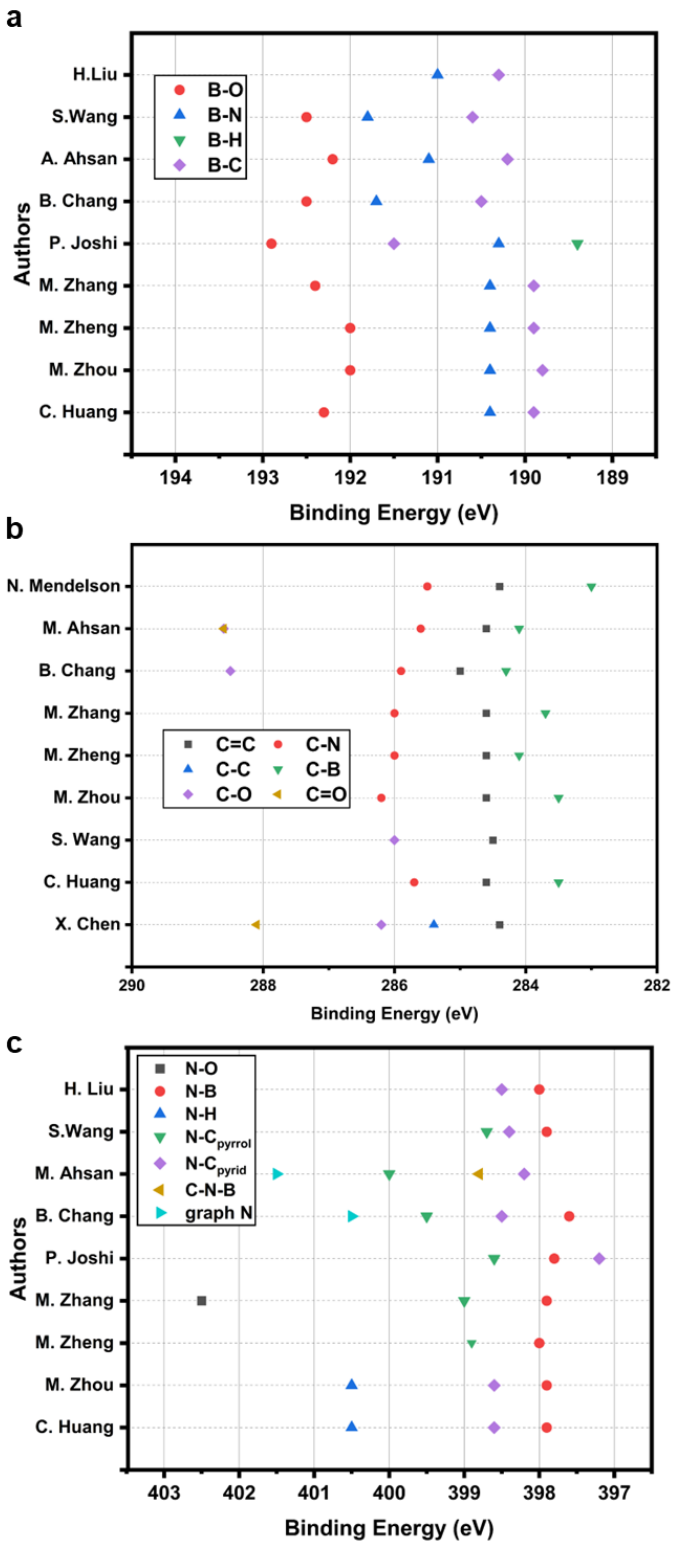


Figure 36; XPS energy values observed in literature and used as reference points for the bonding states of BCN materials in the (a) B1s, (b) C1s and (c) N1s spectrum. *[7, 9-11, 13, 17, 22, 23, 142, 150, 162]*

In this work, XPS was performed by Dr. Philip Holdway, using a K-Alpha X-ray photoelectron spectrometer with a monochromated Al K irradiation source. The source was operated at 12

keV and a 400 μm spot size was used. The analyser operates at a constant analyser energy (CAE) 200 eV for survey scans and 50 eV for detailed scans The raw data was used for peak deconvolution, fitted using CasaXPS software.

2.7. Raman Spectroscopy

Raman spectroscopy is a form of vibrational spectroscopy, much like IR spectroscopy. When light is scattered from a molecule most photons are scattered *elastically* through a process known as *Rayleigh scattering* or elastic scattering. However, a small fraction of the photons (~ 1 in 10^7 photons) are scattered at frequencies different from the frequency of the incident photons, a phenomenon known as the *Raman effect.* The Raman effect arises from an oscillating induced dipole caused by light waves interacting with the electron cloud around the sample. During Raman scattering, a partial transfer of energy occurs between the photon and sample, shifting the vibrational state of the sample. The photon emitted thus has an energy that has been shifted by the value of this energetic state change. Rayleigh and Raman scattering in terms of energetic states are represented in Figure 37.

Raman spectroscopy measures this energy loss (Stokes) or gain (anti-Stokes) in photon energy known as "Raman shift". Every material has a unique Raman spectrum with a certain number of expected peaks. Measuring the output spectra of Raman scattering as a function of wavenumber yields information about the structure of the material being irradiated. For Raman spectroscopy, the wavenumber is defined as;

$$wavenumber = \frac{1}{\lambda_{incident}} + \frac{1}{\lambda_{scattered}} \quad (4)$$

The intensity at each wavenumber gives rise to the Raman spectrum, which can be used to identify materials, as well as assess their quality, crystallinity, and defect densities.

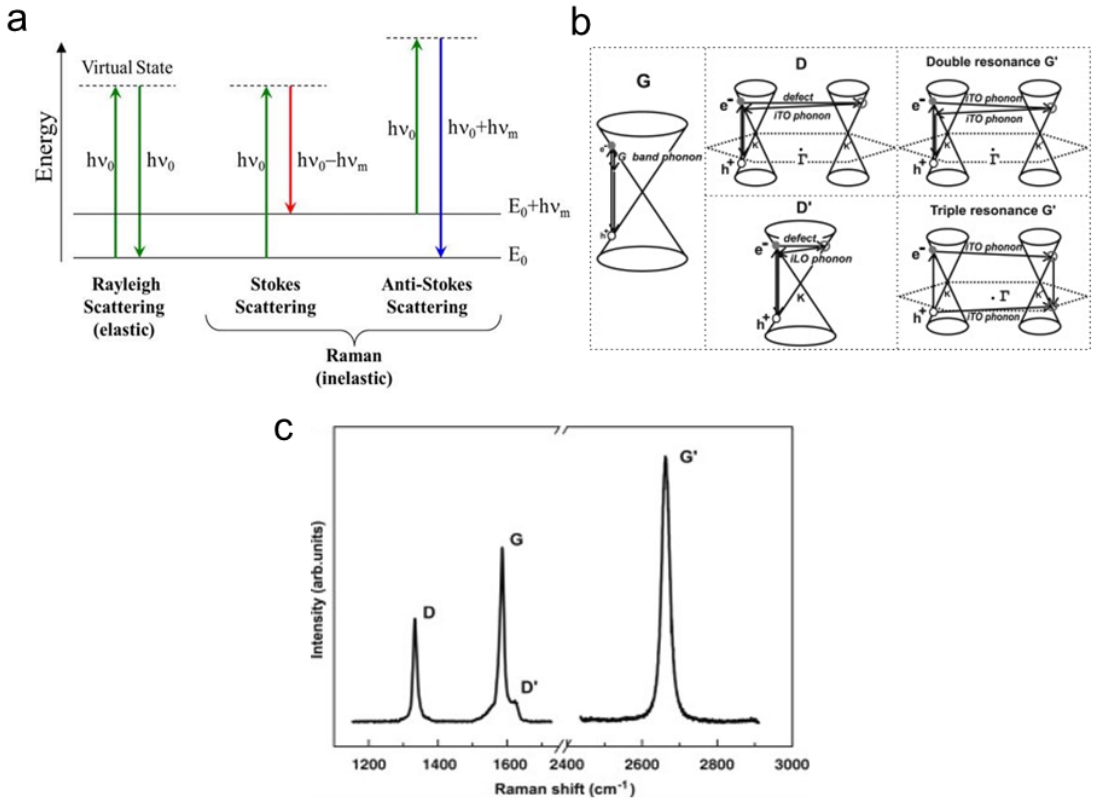


Figure 37; (a) Schematic of Rayleigh and Raman scattering processes. Reproduced from *[163]* (b) Characteristic Raman scattering in graphene materials. The cones represent the electronic bands near the edges of the Brillouin zone corners. (c) shows an exemplar Raman spectrum of graphene, exhibiting how resonance features in (b) appear in the spectrum.(b) and (c) are both reproduced from *[164]*.

Figure 37 (b) shows the band structure of graphene near its BZ edges and the Raman oscillations that may occur. Some resonances require the presence of a defect to scatter the electron before recombination (D and D') which can be used to detect and quantify defect concentrations in the material. The double and triple resonance processes (G' or 2D) are very sensitive to layer numbers as the electronic band and phonon band structures are no longer a Dirac cone in multi-layered (or even doped) graphene and thus the Raman response is reduced. This peak can be used to infer layer number of the graphene sample, as well as doping effects [165]. These resonance features in graphene manifest themselves at characteristic wavenumbers, shown in the Raman spectrum in Figure 37 (c).

The Raman activity of pristine hBN is shown in Figure 38. hBN has the E_{2G} mode at low frequency with stokes (S) and anti-stokes (AS) peaks at 52.5 cm^{-1} and -52.5 cm^{-1}, respectively,

and at high frequency with stokes peak at 1365 cm^{-1}. The low frequency peaks are not typically observed due to the limits of Raman detectors to detect it. The high frequency peak at 1365 cm^{-1} has good intensity and is used to identify and characterise hBN. This mode is caused by in-plane displacements of B and N atoms in the lattice, as seen in Figure 38.

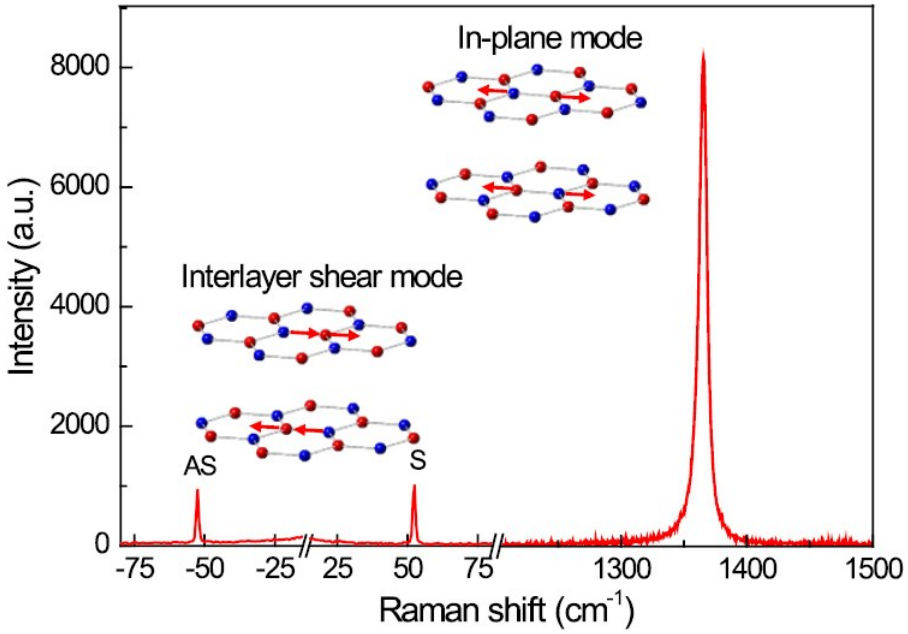


Figure 38; Raman spectrum of hBN crystal taken by Stenger et al. *[166]*. In this spectrum, both the low frequency Stokes (52.5 cm^{-1}) and anti-Stokes (-52.5 cm^{-1}) are observed, as well as the high frequency Stokes peak at 1365 cm^{-1}.

Raman activity of hBCN often resembles either that of hBN or graphene, depending upon composition. Inferences regarding crystallinity of a material can be made using Raman spectroscopy. Highly crystalline materials will exhibit intense resonances with low FWHM. As crystal structure is degraded, the intensity is reduced and the FWHM increases. Wang *et al.* systematically doped intrinsic hBN and observed a broadening of the E_{2g} peak of hBN at 1365 cm^{-1} and, at highest C doping, broad D and G peaks of graphene, as shown in Figure 39 (a). In cases where high flux of carbon were used, mainly peaks from graphene were observed in the Raman spectrum. Ci *et al.* synthesised BCN with high methane and ammonia borane flows and suggested that segregated hBN and graphene layers had formed [141]. However, Raman analysis showed only regions of defective graphene, as shown in Figure 39, (b). A spectrum of

CVD graphene is included below for comparison. Highly disordered 2D BCN is often synthesised via pyrolysis. Wang *et al.* observed that the 2D peak was suppressed in BCN samples with higher B/N starting ratios, shown in Figure 39 (c) [3]. As such, BN incorporation into the graphene system is seen to (1) significantly increase the intensity of the defective peak and (2) suppress the intensity of 2D peak.

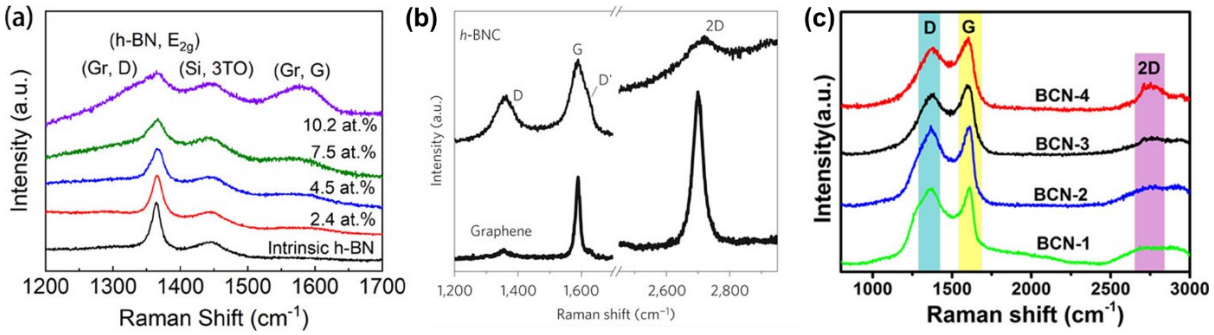


Figure 39; Raman characteristics of 2D BCN (a) Raman spectra of hBN doped with varying levels of carbon [25] (b) Raman spectrum of hybridised domains of hBN and C synthesised under high methane flux and a comparison spectrum of CVD graphene below. *[141]* Raman spectra for highly defective BCN sheets synthesised via pyrolysis. In the sample with highest C content, the 2D is more readily observed. [3]

In this thesis, a LabRAM Aramis Raman confocal microscope was used to record Raman spectra. Raman spectroscopy was performed with a 100× objective lens, a green laser (532 nm) using laser power of ~ 1 mW with acquisition times < 25 s to prevent sample damage from the laser.

2.8. UV-vis Spectroscopy

UV-Vis spectroscopy is an characterisation method that measures the intensity of UV or visible light absorbed by or transmitted through a sample at each wavelength in comparison to a reference sample. It can be used to estimate the band gap energy of materials using the Tauc method where UV-Vis absorbance data can be used to extrapolate for the samples band gap, E_g. The Tauc method is based on the assumption that the absorption co.efficient, α, can be expressed by the following equation;

$$(\alpha . h\nu)^{\frac{1}{\gamma}} = B(h\nu - E_g) \quad (5)$$

where hν is the energy of the photon, E_g is the band gap energy, and B is a constant. The factor γ depends on the nature of the transition which is ½ and 2 for direct and indirect transition band gaps, respectively. From the straight line plot of the absorption peak, the band gap (E_g) can be deduced. Bulk hBN has recently been reported as having an indirect band gap (γ = 2) [42], however, at the few-layered scale, this is often treated as a direct transition (γ = ½) [43, 51, 167, 168]. Figure 40 (a) shows a Tauc plot for BCN samples prepared via MOVPE where γ = ½ is used. A clear reduction in the band gap is observed with increasing carbon content (from 5.8 eV to 5.3 eV) [169]. In hBCN materials, where sizeable domains of hBN and graphene are present, the optical absorption is a combination of their relative concentrations [141]. With increasing C %, the absorbance peak from graphene located at ~300 nm increases in intensity, shown in Figure 40, (b). The hBN absorption peak located at ~220 nm also increases in intensity with increasing C at. %, likely due to few-layer formation. In semiconductors and insulators, broadening of the sub band gap absorption tail is often observed with introduction of defects to the lattice, caused by this increased disorder within the structure [170]. This sub-band gap absorption tail can be expressed by the Urbach equation;

$$\alpha = \alpha_0 e^{(\frac{h\nu}{E_U})} \quad (6)$$

where where α_0 is a constant and E_U is the Urbach energy. By plotting the ln(α) vs *hν*, the Urbach Energy can be determined from the inverse of the slope. Figure 40 (b) shows the Urbach plots for deducing E_U in C doped hBN samples [25]. In this thesis, UV-Vis absorption spectra were recorded using a Cary 5000 UV-Vis spectrophotometer with samples prepared on z-cut quartz substrates which is also used for the reference.

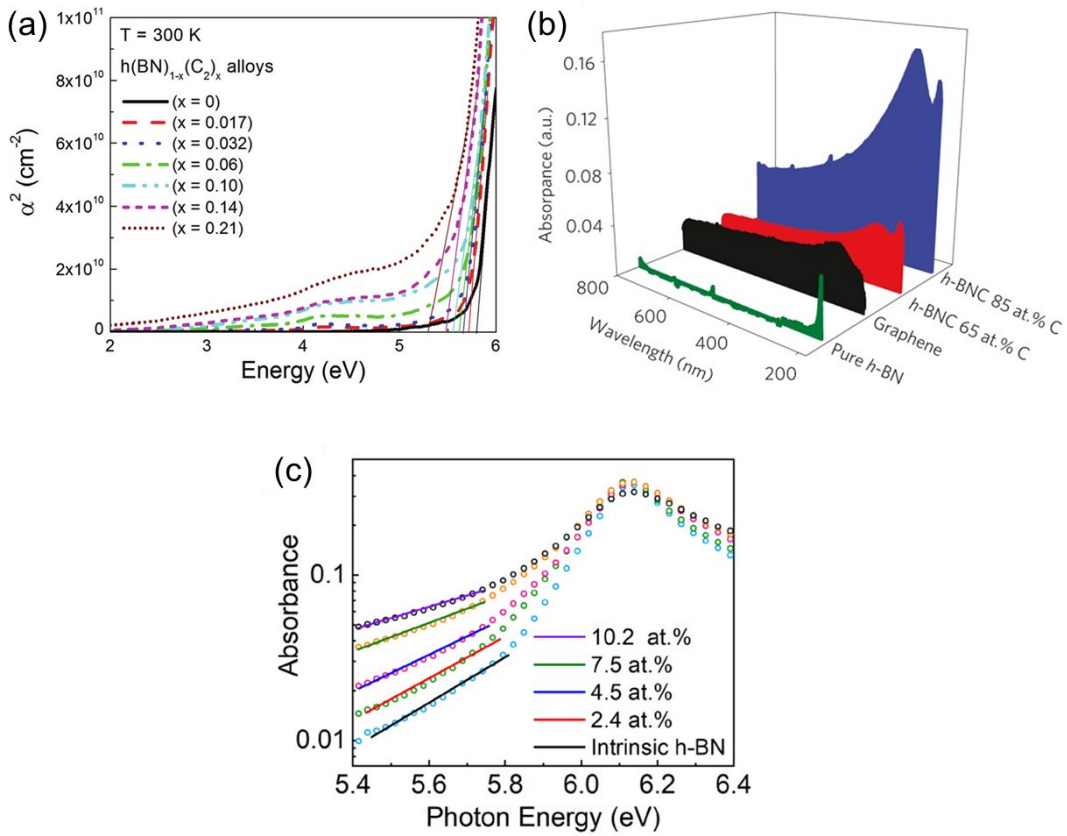


Figure 40; (a) Tauc plot used to calculate E_g for BCN materials with varying atomic ratios of B-C-N. Reproduced from *[169]*. (b) UV-vis data of hBCN films composed of segregated hBN and graphene domains. With increasing C content, the π-plasmon peak of graphene becomes more prominent, yet the hBN absorption peak is still present *[141]*. (c) Urbach plots to determine the Urbach energy, E_U, for C doped hBN layers, reproduced from [25].

2.9. Materials Modelling

In materials science, computer simulations are carried out for a variety of purposes, such as predicting new materials and their properties, interpreting, and understanding experimental data, as well as guiding future experimental work by defining the most suitable parameter ranges. Using mathematical models, they aim to describe the physical processes at the atomic scale. In these simulations, there is a trade-off between accuracy of results and the resources required. For accurately simulating the electronic structure of materials, methods such as density functional theory (DFT) are usually applied. However, the computational costs associated with this method restrict its application to small systems and short time scales.

Approaches like Molecular Dynamics (MD) and Kinetic Monte Carlo (KMC) modelling allow for simulation of larger systems and at longer timescales but do not accurately describe the electronic behaviour as they rely on approximating atomic behaviour with empirical potentials [171]. Results presented in Sections 3.3.3 and 3.3.6 of Chapter 3 in this thesis are obtained via atomistic computer simulations using DFT methods. More details behind the theory associated with this computational approach can be found in the Appendix.

2.9.1. Ab-initio theory

In theoretical chemistry, the properties and characteristics of a system of atoms are often investigated using *ab initio* quantum mechanics [30, 171]. This theory postulates that for a system of N electrons, M nuclei, it has a wavefunction, Ψ, that fully describes the system, and follows the Schrödinger equation;

$$i\hbar\frac{\partial\Psi}{\partial t} = H\Psi \tag{7}$$

where $\hbar$ is the reduced Planck constant and H is the Hamiltonian operator that corresponds to the total energy of the system. For stationary systems, the time-independent solution can be separated out;

$$H\Psi = E\Psi \tag{8}$$

In atomic units, the Hamiltonian can be expressed as;

$$H = -\sum_{i=1}^{N}\frac{1}{2}\nabla_i^2 - \sum_{A=1}^{M}\frac{1}{2M_A}\nabla_A^2 - \sum_{i=1}^{N}\sum_{A=1}^{M}\frac{Z_A}{r_{iA}} + \sum_{i=1}^{N}\sum_{j>1}^{N}\frac{1}{r_{ij}} + \sum_{A=1}^{M}\sum_{B>1}^{M}\frac{Z_A Z_B}{R_{AB}} \tag{9}$$

∇_i^2 and ∇_A^2 are kinetic energy operators for the i^{th} electron and A^{th} nucleus in the system, respectively, M_A is the mass-ratio of nucleus A to an electron, Z_A and Z_B are atomic numbers of nuclei A and B, respectively, r_{iA} is the distance between the i^{th} electron and A^{th} nucleus, R_{AB} is the distance between the A^{th} and B^{th} and nuclei r_{ij} is the distance between the i^{th} and j^{th} electrons. These five terms represent; the kinetic energy of the electrons (1^{st}) and nuclei (2^{nd}),

the coulomb attraction between electrons and nuclei (3rd) as well as the coulombic repulsion between electrons (4th) and nuclei (5th).

2.9.2. Born-Oppenheimer Approximation

For large systems, this Hamiltonian can become incredibly complex. In order to make these computations mathematically feasible, the Born-Oppenheimer approximation was proposed [30]. This approximation treats nuclei as being fixed and the electrons are free to move under an electrostatic field. As such, the new Hamiltonian, H_e, is written as;

$$H_e = -\sum_{i=1}^{N}\frac{1}{2}\nabla_i^2 - \sum_{i=1}^{N}\sum_{A=1}^{M}\frac{Z_A}{r_{iA}} + \sum_{i=1}^{N}\sum_{j>1}^{N}\frac{1}{r_{ij}} + V \quad (10)$$

Where V refers to the potential coming from the nuclei. The time-independent Schrodinger equation (TISE) is now;

$$H_e\Psi_e(R,r) = E_e(R)\Psi_e(R,r) \quad (11)$$

Where the electronic wavefunction $\Psi_e(R,r)$ is a solution describing the motion of electrons in the system and is a function of the nuclear coordinates.

2.9.3. Hartree-Fock theory

Hartree-Fock (HF) theory is an approach to solving the TISE under the above approximation, and it does so by approximating an N electron wavefunction with a single Slater determinant [30, 171]:

$$\Psi_{SD} = \frac{1}{\sqrt{n!}}\begin{bmatrix}\Phi_1(1) & \cdots & \Phi_n(1)\\ \vdots & \ddots & \vdots \\ \Phi_1(n) & \cdots & \Phi_n(n)\end{bmatrix} \quad (12)$$

Φ_i is a single electron spin orbital function and n is the total number of electrons in the system. According to Wolfgang Pauli, the wavefunction describing the electron system must be antisymmetric with respect to the interchange of any pair of electrons [172]. A Slater

determinant is antisymmetric and satisfies Pauli's exclusion principles [30, 171]. Within HF theory, electron correlation is not included as the motion of an electron is only described in an *average* Coulombic field of all other electrons. Therefore, the HF wave-function will always have an energy ≥ the true wave function. Using the variation principle, the set of orbitals Φ_i that give the most accurate total wavefunction Ψ_{SD} and, thus, the lowest energy, can be found. In practice, the orbitals Φ_i are approximated by a linear combination of atomic orbital basis functions;

$$\Phi_i = \sum_j C_{j,i}\chi_j \quad (13)$$

The Slater determinant is then calculated using the Roothaan-Hall equations [173];

$$F_i \sum_j C_{ji}\chi_j = \varepsilon_i \sum_j C_{ji}\chi_j \quad (14)$$

Where F is the Fock operator and ε is the orbital energy. If all coefficient for the atomic orbitals (C_{ji}) are known, this is then written as;

$$FC = SC\varepsilon \quad (15)$$

S is the orbital-orbital overlap matrix, F contains the matrix elements of the Fock operator and ε is the matrix of orbital energies. Solving this equation involves finding a set of coefficients, C, that minimises the energy of the electronic system, and it is solved iteratively until the set of molecular orbital coefficients, C, do not vary significantly from one iteration to the next and the process is said to have 'converged'. This process is often referred to as the HF self-consistent field (SCF) procedure [30].

2.9.4. Electron Correlation

Within the HF approximation, the motion of an electron is correlated with the *average* field created by all other electrons in the system. This is not the whole picture - in reality, each electron is correlated dynamically to that of each other electron in the system. There is always

a difference between the exact energy, i.e. the exact solution of the TISE, and the HF energy. This difference is known as the HF limit and it defines the electron correlation energy such that [171];

$$E_{exact} = E_{HF} + E_{correlation} \quad (16)$$

For computational chemistry calculations, correlation energy does not vary significantly in molecules where bonding in the system does not change much. For calculations on conformational properties, such as calculating the rotational barrier in a molecule, this can be carried out with acceptable accuracy at the HF level. However, where bonding in a molecule changes, the correlation energy changes drastically. HF method performs poorly for calculations on the forming or breaking of chemical bonds. To address this limitation, techniques such as DFT, estimate this $E_{correlation}$ more accurately via calculating the energy of the system as a function of the electron density.

2.9.5. Density Functional Theory (DFT)

The wave function of a system of N atoms is a complex function, depending on 3N spatial and spin variables. DFT circumvents this obstacle by treating energy as a unique functional of the electron density, n, which can be approximated by the square of the wave function, such that it is only a function of the position, r, depending on only three spatial coordinates [30]:

$$n(r) = \int \Psi^2(r) dr = 1 \quad (17)$$

P. Hohenberg and W. Kohn [174] proved that the electron density of any system determines all ground state properties of the system, such that the total energy of the system is a unique functional of the electronic density, n(r). Under Hohenberg-Kohn (HK) theory, the energy functional for the system is thus [30];

$$E[n(r)] = T_s[n(r)] + E_{ext}[n(r)] + E_H[n(r)] + E_{XC}[n(r)] \quad (18)$$

Where T_s is the kinetic energy of the electrons, E_{ext} relates to the external potential (caused by external field, e.g fixed nuclei in the lattice), E_H is the Hartree energy (related to Coulomb potentials between electrons) and E_{XC} is the exchange-correlation energy which makes up the remaining contribution to the total energy.

Work by W. Kohn and L.J. Sham [175] introduced spin-orbital functions into the HK theorems, opening a way for practical calculations of the electron density. Using this method, a comprehensive, many-body system of interacting electrons is converted into a system of non-interacting electrons in the presence of an effective potential. With this, one can solve the many-body problem of interacting particles iteratively by solving a series of Kohn-Sham (KS) equations, which are essentially one-particle Schrodinger equations;written as;

$$\left[-\frac{1}{2}\nabla_i^2 + V_{eff}(r)\right]\Psi_i = \varepsilon_i\Psi_i(r) \tag{19}$$

Where ε_i are the orbital energies of the KS orbitals, Ψ_i, and the effective KS potential V_{eff} is expanded as;

$$V_{eff}(r) = V_{ext}(r) + V_H(r) + V_{XC}(r) \tag{20}$$

The KS equations can be solved in a similar fashion to those of the HF method, self-consistently (SCF), after which the electron density can be calculated.

For the exchange-correlation potential (V_{XC}), the exact form of this is unknown and many approximations have been developed to model this potential. The list of these approximations with varying levels of complexity in tackling V_{XC} is known as Jacob's ladder [176], illustrated in Figure 41. The lowest rung of the ladder and most basic of the approximations is the local density approximation (LDA) [171]. Here, the electron density is treated as a homogenous electron gas. LDA is sufficient for systems with uniform or slowly varying electron densities. It describes well bulk systems but fails at accurately predicting properties for strongly correlated systems.

On the next step of the ladder, we find generalised gradient approximations (GGAs), which improve on LDAs by including the first derivative (spatial alteration) of the density as an additional value [171]. In this thesis, the GGA introduced by Perdew, Burke and Ernzerhof (PBE) is used in simulations of B, C and N on the Cu facet and also the formation energy of dopants in a graphene sheet, carried out in Chapter 3 [177].

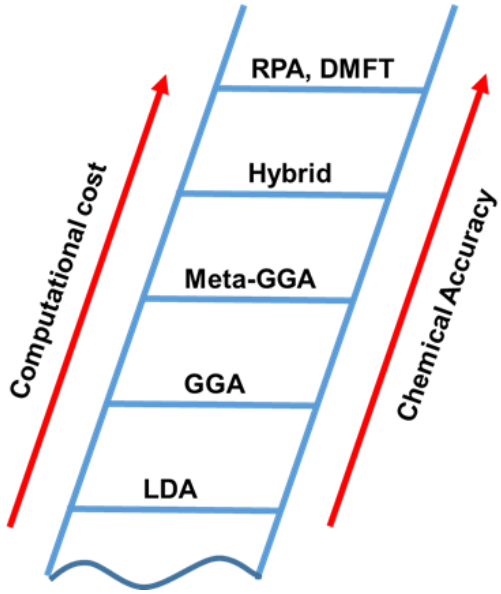


Figure 41; Schematic illustrating Jacob's Ladder in DFT. Each rung on the ladder represents an approximation for the exchange-correlation energy. As one increases in step height, the chemical accuracy of the approximation increases but so too does the computational cost.

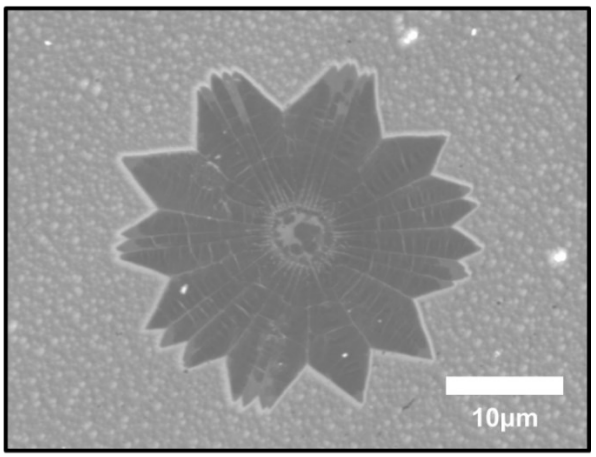
The approach used by these approximations whereby the electron density is considered as a homogenous electron gas results in an unphysical interaction of an electron with itself through the effective potential. The consequence of this is a 'self-interaction' error, which results in the energy band gaps calculated within LDA and GGA being *underestimated*. 'Self-interaction' is avoided in the HF method, as each electron experiences the potential created by the other electrons [171]. However, with this method, correlation effects are ignored, resulting in *overestimated* band gaps. Thus, hybrid density functionals, composed of an exact exchange part from the HF method and a correlation part from DFT within GGA-PBE, more accurately describe band gap values than either method in isolation [178]. The drawback of

using this method is that calculations are computationally more expensive. The hybrid density functional developed by J. Heyd, G. E. Scuseria and M. Ernzerhof (HSE06) [179, 180] is used in Section 3.3.6 of Chapter 3 to accurately determine the opto-electronic properties of 2D BCN materials.

Chapter 3

Synthesis of 2D Borocarbonitride Materials on Pristine Metal Foils





"hBN-templated Graphene flower"

3.1 Introduction

In this chapter, I use both theoretical and experimental techniques to investigate the growth and properties of hBCN 2D materials formed on pristine metal substrates of copper and iron.

I begin by looking at the atomic processes of B, C and N on Cu(111) via DFT calculations, to give insight into precursor behaviour on the growth substrate. Following this theoretical investigation, an atmospheric pressure, catalyst-assisted CVD protocol for the growth of hBN and 'C doped' hBN (hBN-C) structures on copper, is derived. This is done using low-cost and easy-to-handle precursors, ammonia borane and methane. To synthesise quality hBCN materials, I first optimise growth parameters for intrinsic hexagonal boron nitride towards crystalline 2D layers, before tailoring the processes towards hBN-C. Specifically, I focus on 'C doped' hBN synthesis, starting from low carbon chemical potential , $\mu_B = \mu_n >> \mu_C$, and increasing μ_C systematically, and analyse the changes to morphology of the film as well as opto-electronic changes in Raman and UV-vis spectroscopy.

On copper substrates, weak interactions with the substrate and B/C/N precursors and low solubilities ensure growth is *surface-mediated* and self-limiting. This means that growth of hBN and hBN-C films are limited in height to a few layers. Iron, on the other hand, has a higher solubility of B, C and N at growth temperatures > 750 ˚C and so, multi-layer growth can be realised via *precipitation-mediated* growth [113, 167, 181, 182]. Such a synthesis method is useful in applications where a thicker and more robust active layer is required. First hBN growth is optimised on Fe substrates before conducting 'C doped' hBN synthesis through methane introduction. The effect of carbon inclusion on the opto-electronic properties of the films is characterised in a similar fashion to growth on Cu.

'C doped' hBN has recently found applications in opto-electronics via enhanced single photon emission [22, 23] and DUV detection [25], in electronics via active layers in 2D memristors

[87] and reduced current injection into hBN crystals [86]. These methods have typically employed costly and complicated synthesis methods such as MBE of IBSD to synthesise high-quality crystals. As such, the synthesis protocol investigated here may provide an alternative low-cost, non-toxic and industrial scalable process for growth of 'C doped' hBN.

3.2. Materials and Methods

Materials

Cu foil (Alfa Aesar - 46986RG, 0.025mm thick, annealed, uncoated, 99.8% metals basis), Fe foil (Goodfellow – 99.8%, 0.1mm thick). Ammonia borane (Sigma Aldrich - 682098 , ≥97%), 250 ppm methane mix (BOC Ltd., 250 ppm balanced in Ar, ≥99.995%) pure methane (BOC Ltd., ≥99.995%), Argon (BOC Ltd., ≥99.995%), hydrogen 2.5% mix (BOC Ltd., 2.5% balanced in Ar) and pure hydrogen (BOC Ltd. ≥99.995%), Chlorobenzene (99.8%, anhydrous – PN:284513), ammonium persulfate (98%, reagent grade – PN:215589), Acetone (ACS reagent, ≥99.5% - PN:179124), IPA (ACS reagent, ≥99.5% - PN:190764), Acetic Acid (glacial, ACS reagent, ≥99.7% - PN: 695092), potassium hydroxide (ACS reagent, ≥85%, pellets – PN:221473), Poly(methyl methacrylate) (M_w 350,000 and 15,000 – PN: 445746 and 200336). Phosphoric acid (85% in H2O - Alfa Aesar, PN:33266). Si/SiO2 wafers (300nm SiO2 layer) were purchased from MicroChemicals GmbH. For optical studies, z-cut quartz substrates (13.0mm Ø x 2.0mm) were used, purchased from CRYSTRAN.

Methods

Pre-synthesis substrate treatment;

• Copper: As-received copper foils have rolling lines present from production. Rolling lines serve as nucleation sites for 2DM growth. Therefore, to increase the domain size of the synthesised material, the foil is first treated via electo-polishing (EP). To do this, copper foils are first washed with acetone, IPA and DI water to remove any organic contaminants that may interfere with the electro-polishing process. Cu foils are polished in 85% H_3PO_4 aq. solution. A positive potential is applied to the Cu foil (1.8 V for 30 minutes). Afterwards, Cu foil is washed in 5% acetic acid in H_2O followed by rinsing in DI water, IPA and drying with N_2 gun. A schematic of the EP set up, as well as surface characterisation of the Cu foil pre and post EP, can be found in Appendix Section 8.1.1.

• Iron: Similarly, the surface of the as-received Fe foils have rolling lines from production which can influence the uniformity of the grown material and can produce a non-uniform film. Electro-polishing of Fe typically requires harsher chemicals such as sulfuric acid [183], and so mechanical polishing was carried out Al_2O_3 paper up to 2000 grit and SiC at 2400 and 4000 grit, followed by polishing with Brasso™ and a cloth to allow a smooth finish to the surface of the foil.

Synthesis of hBN and hBN-C structures on Cu via APCVD; Films were grown on copper foils using a modified CVD furnace at atmospheric pressure. The APCVD system was composed of a stainless-steel gas mixing manifold connected to gas lines with Ar, H_2, 2.5% H_2 in Ar, Ar, CH_4 and CH_4 in Ar (250 ppm) mix. Each gas line is controlled with its own MKS gas flow meter connected to a centralised digital power supply and display module. Gas lines fed into a precursor evaporation chamber, through to a fused silica tube (26 mm diameter) and a high

temperature furnace (schematic shown in Figure 42). An electrical heater and electrical tape were used to heat the precursor chamber containing the ammonia borane complex (AB) external to the high temperature furnace. Electropolished copper foil was washed with acetone, IPA and dried under N_2, before being placed in the substrate holder. The substrate holder was comprised of two fused quartz plates separated by a gap of 6 mm. A confined reaction space has previously been shown to improve the growth of 2DM via catalytic assisted CVD by increasing the local concentrations of reactants in the confined space, while also suppressing evaporative loss of Cu, ensuring smoothness of the substrate, reducing nucleation, and increasing domain sizes [184-187]. The substrate holder and Cu foil were then placed in the centre of the CVD furnace. Before synthesis, the reaction chamber was vacuum purged with argon three times to remove any organic contaminants present in the chamber. This vacuum purging step was introduced as it was found to reduce the occurrence of irregular, isosceles hBN domains during CVD growth. Further characterization and discussion on these irregular growth structures can be found in Appendix Section 8.1.2. The vacuum pump was used only for purging the system of any potential contaminants and all syntheses were carried out at atmospheric pressure. After this, annealing of the Cu foil was carried out in 4 % H_2 in Ar mix at 1050 ºC for 60 minutes to remove any impurities on the surface and allow for enlarging of the copper grains. All synthesis were carried out at 1050 ºC to allow for high quality deposition and faster synthesis times. For pure hBN samples, ammonia borane was sublimed at a set temperature, T_{AB}, and carried into the reaction chamber using total 400 sccm of 4 % H_2 in Ar (16 sccm H_2, 384 Ar). For carbon doped samples, various partial pressures (p.p) of CH_4 were introduced during optimised hBN synthesis to achieve doped growth. Once an experiment had finished, the furnace was moved via a runner track so that the sample could be rapidly cooled to room temperature (200 ˚C min^{-1}).

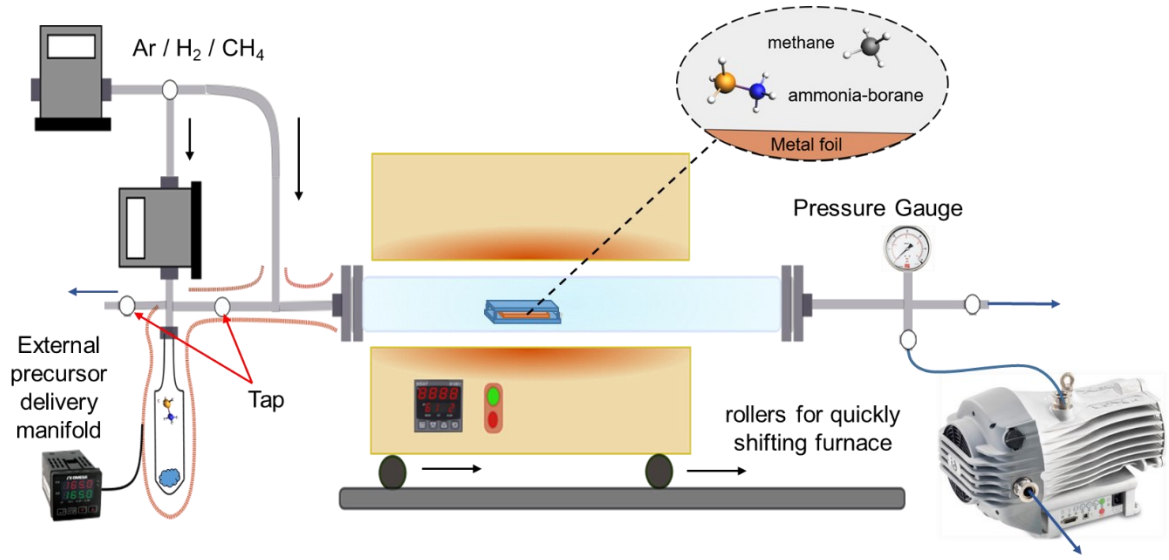


Figure 42; Schematic of the APCVD set up used in this thesis. The Cu substrate is placed within a confined channel in the quartz substrate holder.

Synthesis of hBN and hBN-C on Fe via APCVD; Films were grown on copper foils using a modified CVD furnace at atmospheric pressure as described in the previous section. The mechanically polished Fe foil was washed in acetone, IPA and dried under N_2, before being placed, uncovered, on a quartz substrate at the centre of the CVD furnace. Before synthesis, the reaction chamber was vacuum purged 3 times with argon to remove any organic contaminants present in the chamber. After this, annealing of the Fe foil was carried out in H_2 in 1100 ºC for 60 minutes to remove any impurities and allow for enlarging of the Fe grains. 300 mg of AB precursor was used for each run and T_{AB} set to 80˚C. For synthesis, the temperature of the furnace was held at its set value for 60 minutes with precursors introduced with 10% H_2 in Ar at 400 sccm. After this, the furnace was cooled at a set rate until a temperature of 725 ˚C had been reached and then, the flow of AB was shut off and the furnace shifted via a runner track and allowed to cool. For pure hBN samples only AB was introduced. For carbon doped samples, CH_4 was introduced with AB to achieve 'C doped' hBN growth. Here, the holding temperature and cooling rate were set at 950 ˚C and 5 ˚C min^{-1}, respectively.

Film transfer procedure for APCVD grown films; An overview of the transfer process is shown in Figure 43. PMMA (Mw 15,000) 4% wt. in chlorobenzene was spin coated onto the 2DM grown atop of the copper foil at 2400 RPM for 60s (acceleration 200RPM/s). The sample was then baked on a hot plate at 120 ˚C for 90 seconds, after which it was placed in under a UV Ozone lamp at irradiance 30 mW cm^3 at 253.7 nm for 10 minutes. UV exposure has been shown to decrease the adhesion strength of PMMA and facilitate better polymer residue removal at the end of the transfer process [188]. A second coating of PMMA (Mw 350,000) 4% in chlorobenzene was coated on the stack with the same spin coating parameters. This second higher Mw coating has been shown to increase the structural durability of the film after it is removed from the metal substrate, enhancing the ease of transfer [189]. Again, the sample was baked on a hotplate at 120 ˚C for 90 seconds before floating the stack in a solution of 0.1M ammonium persulfate until the metal substrate had etched away. The PMMA/2DM stack was then cleaned by floating in deionised water for 15 minutes, three times, changing the solution each time. Afterwards, while the stack is floating in DI water, it is picked up by the target substrate. The new PMMA/2DM/target substrate stack is dried and heated at 60 ˚C to relax the polymer and enhance the contact of the 2DM with the surface of the target substrate. The stack is then placed in acetone at 50 ˚C for 2 hours to remove the PMMA polymer from the surface of the 2DM, after which the residual acetone + PMMA is washed away in IPA before drying with a N_2 gun.

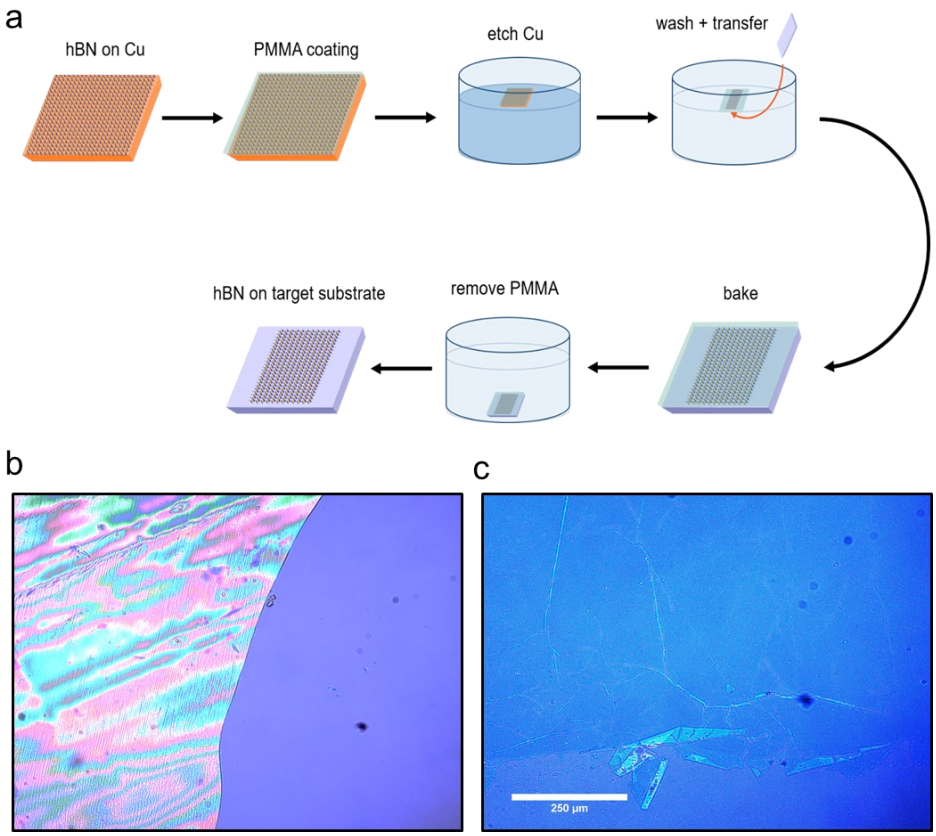


Figure 43; 2D material film transfer using PMMA support layer. (a) Schematic of the transfer process for a 2D material such as hBN grown on Cu. (b) OM image of a PMMA/2DM stack transferred onto SiO_2/Si substrate. The PMMA layer shows thin-film interference while the bare SiO_2/Si substrate is purple (c) OM image of 2D hBN film on SiO_2/Si after PMMA layer is dissolved away. Only slight contrast can be seen between hBN and the Si substrate. Wrinkles and folds are observed in the film, which are common from the wet transfer process.

Computational details for investigating the behaviour and atomic processes of B, C and N on Cu(111) – Section 3.3.1; Ab-initio calculations were performed with the BAND code implemented in SCM [190, 191]. Electron exchange and correlation was managed by the generalized gradient approximation of the PBE level of theory and a TZ2P basis set. The in-plane periodicity of the supercell is c (2 × 4) or p (2 × 4), corresponding to 8 Cu atoms per layer. The (111) facet of copper is chosen as it is the most stable and dominant low-index surface for polycrystalline copper, as predicted via the Wulff method [192], and is frequently used as the substrate in experimental studies of hBN, graphene and BCN growth [126, 141, 147, 148, 193]. The k-points were sampled with 5×3×1 Monkhorst–Pack grids. Geometry optimizations were performed where all atoms except for the bottom 2 layers of the Cu slab

were relaxed until the force on an each atom is less than $1x10^{-3}$ Hartree $Å^{-1}$. To calculate the adsorption energy (ΔE_{ads}) of an adatom on the Cu surface, the following equation was used;

$$\Delta E_{ads}=E_{slab+mol}-E_{slab}+ E_{mol} \quad (21)$$

Where $E_{slab+mol}$ is the energy of the adatom adsorbed on the Cu surface, E_{slab} is the energy of the Cu slab and E_{mol} is the energy of the isolated adatom. The nudged elastic band method (NEB) within the SCM software is used to calculate the energy barriers of diffusion for atoms on and under the surface [194].

Computational details for determining the relative energies of formation of doped graphene;

DFT calculations were performed via the Amsterdam Modelling Suite licensed by SCM. Geometric optimisations of the structures were performed with the BP86 functional with D3 dispersion correction and all electron STO ZORA – DZP basis set.

To evaluate the stability of these BCN structures, their formation energies (E_{form}) were calculated. E_{form} helps to estimate whether a substitution is energetically feasible or not and it is defined as;

$$E_{form} = E_{Gr-doped} - E_{Gr} \pm N(X)\mu(X) \quad (22)$$

Where, $E_{Gr\text{-}doped}$ is the total energy of the doped structure, E_{Gr} is the total energy of the graphene layer, N(X), is the numbers of atoms of species X that have been added (N(X) < 0) or removed (N(X) > 0) from the system, and μ(X) is the chemical potential defined as the single-atom energy of atom X.

3.3. Results & Discussion

3.3.1. Theoretical Insights into the Atomic Processes of B, C and N on Cu(111)

Before introducing results from the experimental CVD investigations, I use this first section to elucidate the behaviour of BCN's constituent atoms on the surface of the copper growth substrate via *ab initio* methods. While the chemisorption and diffusion of each individual atom in the BCN system is likely to have been studied with DFT, no reports carry out a comparative study. As each study uses different approximations, XC functionals and basis set, it is not possible to make accurate comparisons across studies. As such, here we report the first DFT study on the comparative energetics of the atomic processes of B, C and N adatoms on the Cu(111) surface, the most energetically favourable facet of copper [192]. These calculations compare the relative energies of the processes of adsorption diffusion and penetration are the prelude to BCN growth and allow for insight into the relationship between the precursor and the growth surface.

Adsorption of B, C and N on Cu(111)

Figure 44 shows the positions of the adsorption sites calculated. Top, bridge, fcc (F), and hcp (H) sites are on the surface of Cu(111), while F' and H' are in the sub-surface.

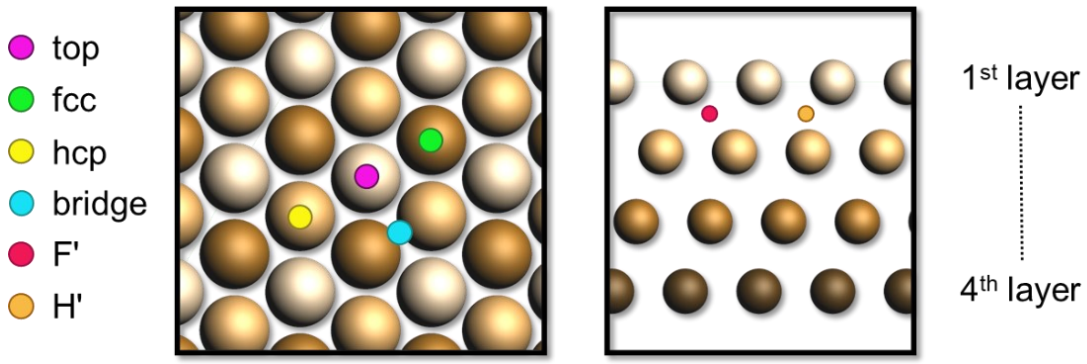


Figure 44; Schematic showing the positions of the calculated adsorption sites, top, fcc, hcp, bridge, F' and H' on and in the Cu lattice.

Table 1 summarises the relative energies (w.r.t. the fcc site) and calculated adsorption energies of B, C and N atoms at the various adsorption sites on the face of Cu(111). The most stable sites for adsorption are those with the lowest ΔE_{ads}. Energies in brackets are the calculated adsorption energies as defined in the methods section (equation 21 in Methods Section 3.2). A negative adsorption energy means that the atomic configuration is stable. For ease of comparison, energies are referenced relative to the fcc surface site. At the surface, boron and carbon atoms are most stable at the bridging sites of copper whereas nitrogen is most stable at the fcc site. We find that all sites analysed are stable for all three atom types except for the on-top site for carbon. For B and C atoms, the most stable adsorption sites are in the sublayer.

Table 1; Relative energies of the B and N atoms at various adsorption sites on the Cu(111) surface, exhibiting the relative stabilities of the precursor atoms at each site. All energies here are in eV and are referenced to the fcc site adsorption energy. The absolute energies are in brackets.

Atom	fcc	hcp	top	bridge	F'	H'
B	- (-4.210)	0.026 (-4.185)	1.257 (-2.954)	-0.096 (-4.306)	-0.938 (-5.149)	-0.932 (-5.142)
C	- (-4.847)	0.052 (-4.794)	6.300 (1.657)	-0.1225 (-4.969)	-0.667 (-5.513)	-0.28 (-5.127)
N	- (-3.662)	0.102 (-3.560)	2.027 (-1.635)	0.182 (-3.480)	0.204 (-3.458)	0.333 (-3.329)

We observe a significant energy decrease of 0.93 eV (relative to the surface) when the B atom is in the sub-surface layer of Cu and there is a possibility that boron atoms mix with the copper layer. Here, the boron atom is found to form a seven-coordinate complex with Cu, in the form of a mono-capped octahedral/mono-capped trigonal prism structure (Figure 45). The bond lengths between Cu and B here are in the range 1.94 - 2.31 Å, in agreement with calculations of copper boride structures calculated previously (2.04−2.35 Å) [195]. The B atom relaxes to this structure from both *F'* and *H'* sites, and so, they are equivalent. We call this site *br'*. In a

similar fashion, C atoms prefer to locate in the sublayers of Cu(111) and are most stable at the F' site. Here, C occupies an octahedral (O_h) site, coordinated with six Cu atoms. Notably, N atoms are more stable on the surface than in the subsurface, by around 0.2 - 0.3 eV.

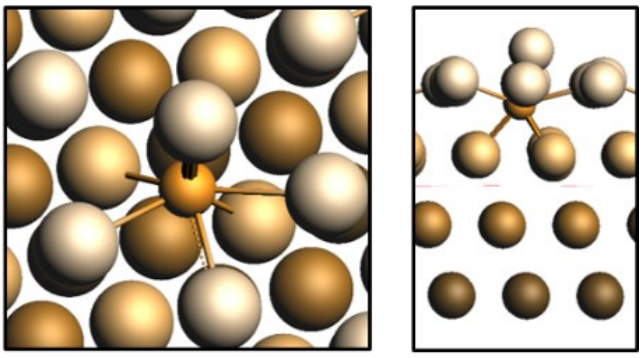


Figure 45; Boron is most stable in the sublayer of Cu(111); co-ordinated with seven Cu atoms at the br' site, forming a monocapped octahedral/monocapped trigonal prism structure.

Due to N atoms being more stable on the Cu(111) surface and B/C atoms preferring to reside in the sublayers, one could reason that a 1:1:1 precursor flux would result in a higher concentration of N at the Cu(111) surface, provided the energy barriers for diffusion into the subsurface were low enough. Such a concentration gradient could explain experimentally observed equilibrium shapes of hBN grown on Cu; N -terminated zig-zag (ZZ) domains (Figure 46, a). A nitrogen-rich environment at the surface of Cu promotes a higher chemical potential of N (μ_N) than B (μ_B) and the formation of these traditionally observed shapes (Figure 46, b) [134, 196]. In hBCN synthesis using AB and CH_4, this could favour C-N bond formation over C-B. In the next section, we analyse the diffusion and penetration barriers for B, C and N on Cu(111) and shed further light on this.

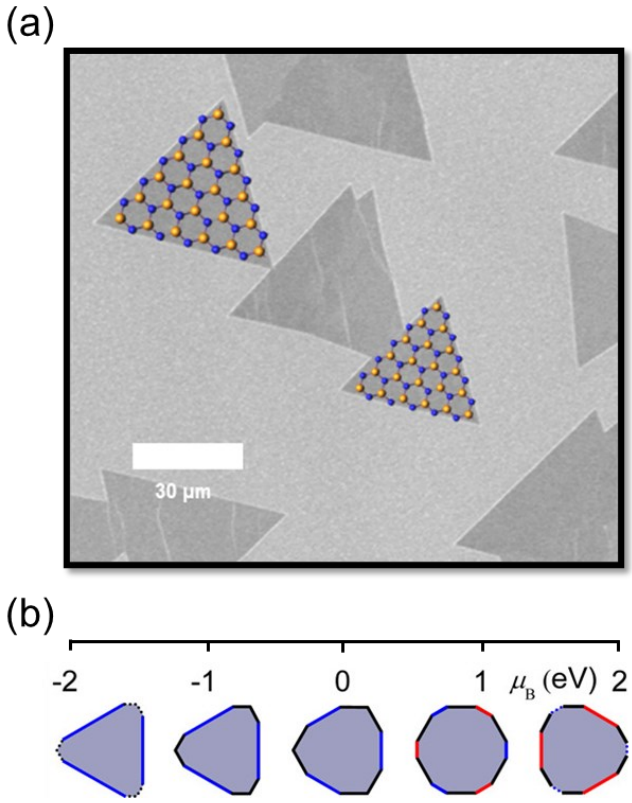


Figure 46; (a) SEM image of hBN domains on Cu with an overlay of N-terminated, zig-zag atomic domains, which are the equilibrium shape of hBN on Cu *[196]*. Overlayed hBN domains not to scale, for visualisation purposes only. (b) Equilibrium shapes of h-BN on Cu at various chemical potentials of boron, μ_B. Blue lines represent N-terminated edges while red lines represent B-terminated edges. (b) is adapted from *[196]*

Diffusion and penetration of B, C and N on Cu(111)

Having been adsorbed onto the Cu surface, the adatoms can move from site to site on the surface and also penetrate the substrate's sublayers. Understanding the energies barriers for these atomistic processes is important in being able to predict the behaviour of B, C and N at the initial growth stages of BCN on the growth substrate, Cu. Figure 47 summarises the energetics barriers for diffusion and penetration of B, C and N atoms *on* and *into* Cu(111). All atoms show low energy barriers to diffusion on the surface of Cu. Furthermore, B and C show low barriers to penetration into the sublayer and large barriers in the reverse direction. In contrast, N atoms experience larger barriers to penetration and thus likely reside on the surface of Cu.

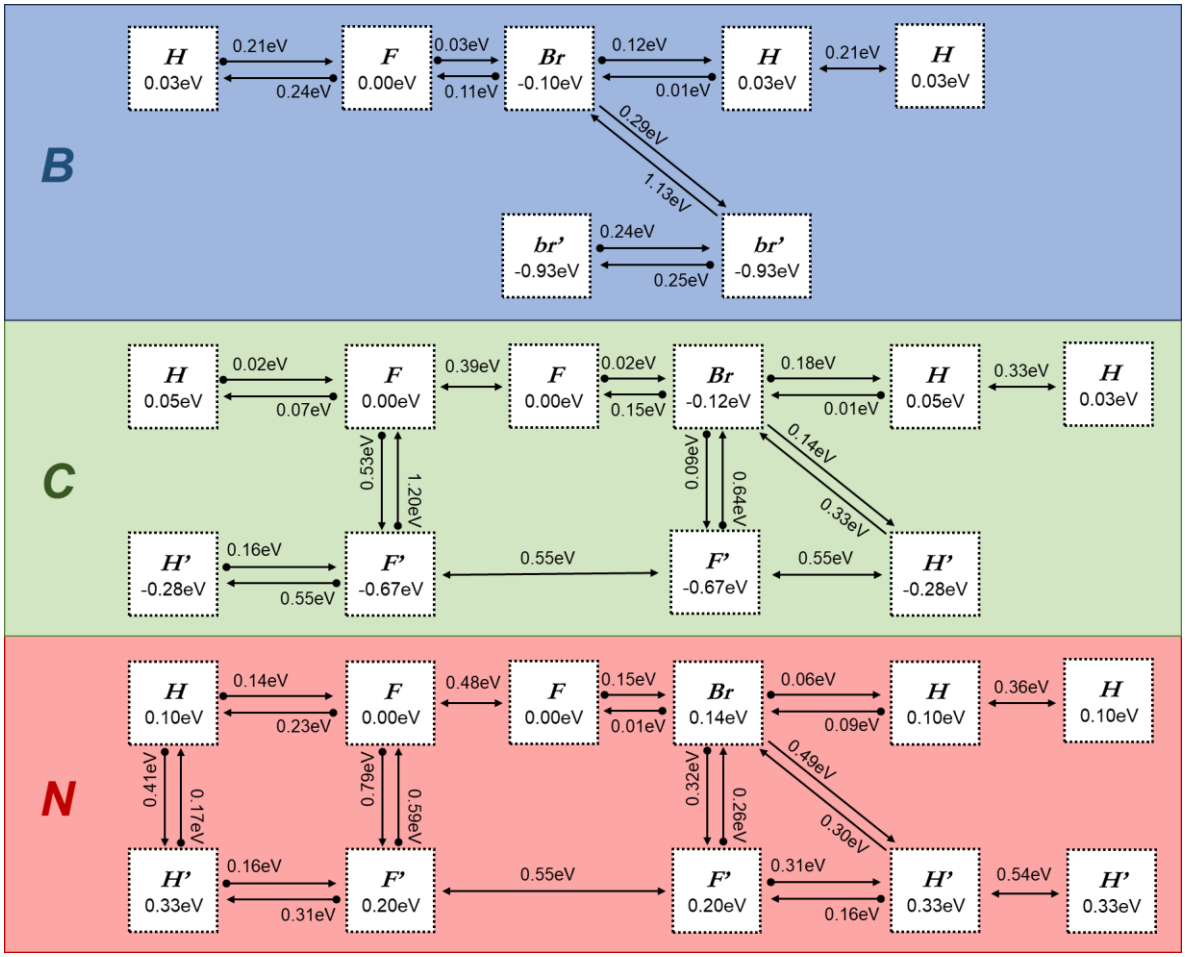


Figure 47; Energies of diffusion (horizontal arrows) and penetration (vertical/diagonal arrows) of B, C and N atoms on the Cu(111) surface. All atoms show low energy barriers to diffusion on the surface of Cu. B and C show low barriers to penetration into the sublayer and large barriers in the reverse direction. N atoms experience larger barriers to penetration and likely reside on the surface of Cu.

Figure 48 shows the potential energy surfaces for the most likely diffusion processes of B, C and N on the Cu substrate. B is most stable at the bridging site and moves along the surface through other low energy sites. Thus, possible paths for B might be *br* → *H* or *br* → *F*. For these processes, the energy barriers are quite low at ~0.1eV. This means that boron can diffuse readily on the Cu(111) surface moving through these sites. Processes that do not move through this low energy bridging site are faced with an increased energy barrier to diffusion (e.g. *F* → *H*, 0.24 eV). All energy barriers for diffusion towards the bridging site are low and thus the B atom will tend towards this location. On the surface, B atoms experience low resistance to diffusion, with all diffusive steps below 0.25 eV. At synthesis temperatures of ~1000˚C (k_BT ~ 0.1 eV), these energy barriers are readily surmountable and surface B atoms are highly

mobile. As the B atom shows increased stability below the surface, we also investigated the atomic barriers to penetration. Interestingly, B atoms would only diffuse into the sublayer via the bridging site. The energy barrier involved in the *br → br'* process is calculated to be 0.29 eV in the *forward* direction and a much larger 1.13 eV in the *reverse* direction. This suggests that B atoms readily penetrate the interior of Cu(111) and experience a much larger resistance in returning to the surface. This reiterates our previous hypothesis on B preference to first fill the Cu sublayers. In the sublayer, B atoms are again quite mobile, with the *br' → br'* process calculated to be 0.24 eV. The most likely migration paths for B on Cu(111) are *F/H → br* on the surface which then readily penetrates into the sublayer the (*br → br')*. All three processes related to the most stable surface site, *br*, are compared in Figure 48 (a).

For the C atom, the diffusion barriers for processes on the surface are also low and the atom is highly mobile. The migratory processes related to the most stable surface site of C, *br*, are compared in Figure 48 (b). From the bridging site, C readily diffuses into the subsurface at the F' site, with an energy barrier of 0.09 eV in the *forward* direction and a larger barrier of 0.64 eV in the *reverse* direction, similar to the B atom. Notably, the energy barrier for penetration is lower than that of diffusion on the surface. While in the subsurface, C atoms experience a barrier to diffusion of 0.55 eV, larger than that of B. Thus C is less mobile when dissolved in Cu than B. Similar to the case of B, the most likely migration paths for C atoms are *F/H → br* on the surface of Cu(111) which then penetrates into the sublayer via *br → F'*.

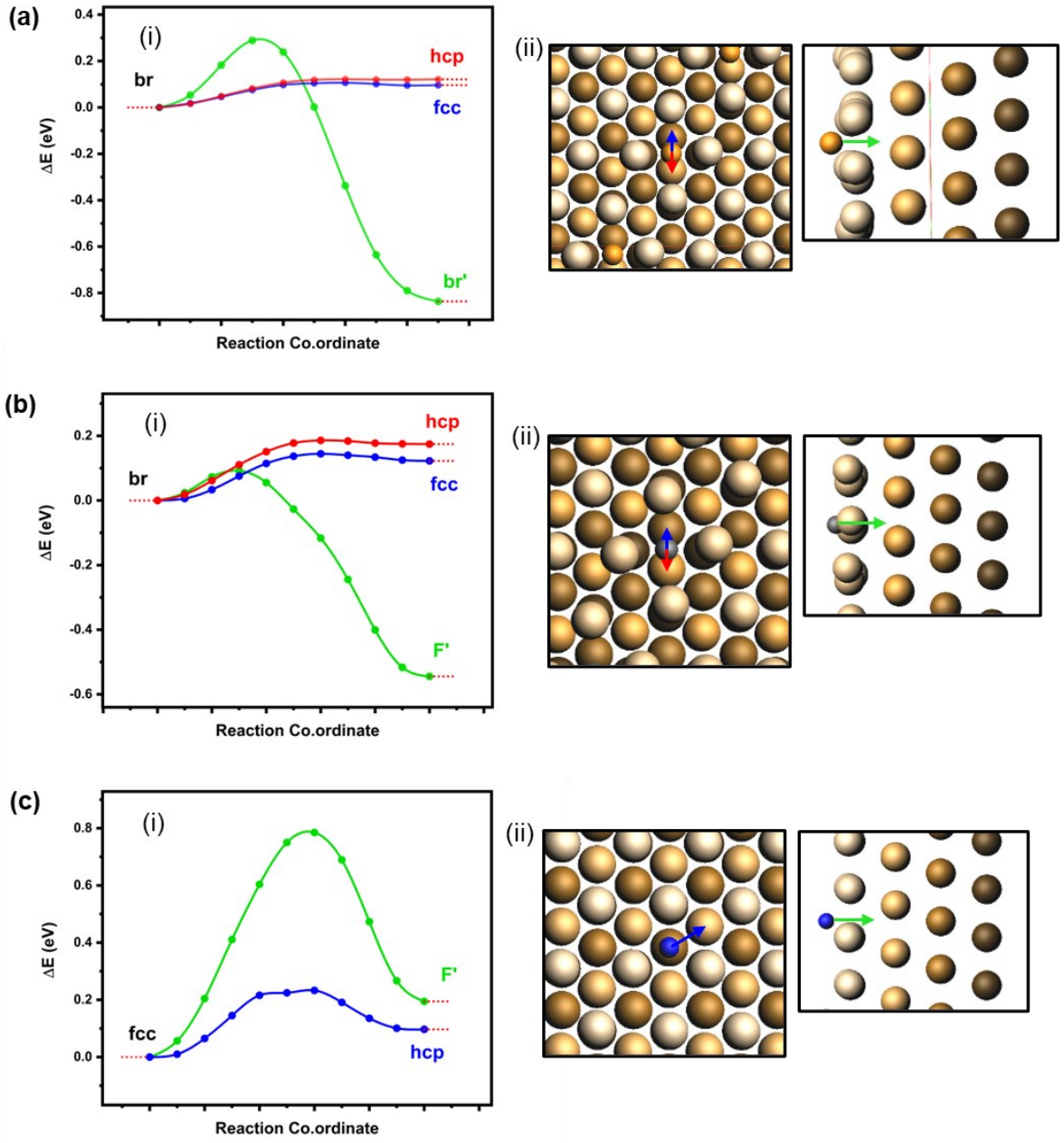


Figure 48; (i) Potential energy surfaces of the (a) boron (b) carbon and (c) nitrogen atom along diffusion paths on the surface (red,blue) and into the sublayer (green) (ii) Schematic showing the direction of migration of the atom. The arrow colour corresponds to the reaction coordinate in (i). Boron and carbon clearly show a preference to enter the sublayers while nitrogen prefers the surface of Cu.

For the N atom, the diffusion barrier is 0.23 eV for the $F \rightarrow H$ process. To penetrate the Cu surface, a large barrier of 0.79 eV is required (Figure 48, c). Therefore, the N adatom is expected to migrate mainly on the surface of Cu(111). There exists a lower energy route into the sublayer via the bridging site of N ($br \rightarrow F'$; 0.32 eV). However, energy barriers in the reverse direction are lower, thus N will tend to reside on the surface.

Overall, the small diffusion barriers for the B, C and N atoms on Cu(111) implies that they are all highly mobile at temperatures typically used during CVD growth (T = 1000 ˚C, k_bT = 0.11 eV). The crystallites of hBN and graphene are more stable than highly entropic alloys of BCN. The hierarchy of energetic stability of the bonds is B– N > C– C > C– N > C– B > B– B > N– N [74]. With highly mobile atoms on the surface (low energetic barriers to surface diffusion) and high temperatures (large thermal energy), the atoms can readily diffuse on the Cu surface and find the lowest energy site, i.e. a crystallite of hBN or graphene, where they are most likely to reside. This results in domains that are segregated into hBN and graphene regions, rather than homogeneously alloyed, something observed in several experimental studies [141, 193].

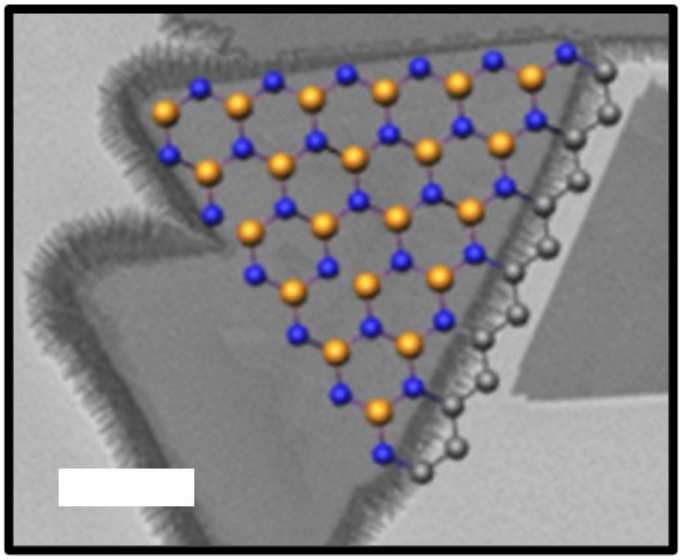


Figure 49; SEM image of hBCN material grown on Cu. Overlayed BCN structure not to scale, for visualisation purposes only (B – orange, N- blue, C -grey). Due to the propensity for graphene and hBN to segregate, carbonaceous regions are observed precipitating from the hBN domain. N-terminated, zig-zag atomic domains, which are the equilibrium shape of hBN on Cu, may form N-C bonds with this carbon region at the edge of the hBN lattice. Scalebar is 10 μm.

Figure 49 shows a schematic of such a structure, where edges of the hBN domain are bonded with carbon (full characterisation of these structures available later in this chapter). For penetration into the Cu sub-surface, B and C experience low energy barriers at 0.29 eV and 0.09 eV, respectively. In exiting the sublayer, B experiences a much larger barrier (1.13 eV)

than C (0.64 eV). We would expect B and C atoms to first fill the sub-layers of Cu before a concentration is built on the surface. N, on the other hand, experiences a higher penetration barrier into the bulk (0.79 eV) and lower energies towards re-entering the surface, so, we would expect it to reside on the surface. Therefore, it could be reasoned that for growth conditions where the precursor stoichiometry of B:N is 1:1 (such as those using ammonia-borane), there would exist a concentration difference at the surface where N > B. As the lowest energy structure of the hBN domain on Cu is the N-terminated equilateral triangle, particularly in environments where $\mu_n > \mu_b$ [196, 197], and carbon is bonded at these regions, there likely exists more N-C bonding than B-C bonding in these structures. I will draw on these observations later in the chapter to explain some of the characterisation of hBN-C growth on Cu.

3.3.2. hBN Synthesis on Pristine Copper

In order to synthesise quality hBN-C structures on Cu, the synthesis of hBN was first optimised. To do so, I considered three aspects of the hBN growth process: the precursor heating profile, the precursor loading and synthesis time.

Literature on hBN growth using the ammonia borane precursor is widely available, with 2D deposition on Cu first achieved in 2010 by L Song et al. [198]. However, specifics about the parameter space surrounding the precursors loading and temperature profile vary widely and are sometimes not even reported [199, 200]. Typically, small amounts of ammonia borane are used (<20 mg) as high partial pressure of B and N precursors can often result in amorphous and adlayer growth [126, 129]. There are some reports where high quality hBN films are achieved on Cu with ammonia borane amounts exceeding 100 mg, although these are in the minority and typically adopted a ‘free molecular flow’ or ‘Cu pocket enclosure’ set-up, where

access to the Cu surface by the precursor is severely restricted, leading slow mass transport [130, 131, 201].

Heating profiles for the AB precursor typically fall below 100 ˚C due to asymmetric concentration profiles for N and B that occur when ammonia borane is heated at higher temperatures [126], as well as the presence of polymeric BN particles on the growth substrate at elevated precursor heating temperatures [202, 203]. Higher heating profiles result in the formation of structurally different N_xB_y-containing species, and as such, the precursor decomposition profile is not constant, which can impact quality and reproducibility [126, 130]. As such, AB heating is restricted to below 80 ˚C. Pristine hBN synthesis employing a high ammonia borane heating temperature (T_{AB}) is possible, but these reports have typically used a liquid catalyst method of growing hBN, where temperatures above the melting point of Cu are employed. This enhances the ability of Cu to dissociate and decompose any larger polymeric particles that often result [204].

Another parameter which influences the growth of hBN is the gas composition. Typically, a combination of argon and hydrogen is used with the partial pressures varying from study to study. To visualise these reports, a parameter space was constructed for CVD hBN growth on Cu using ammonia borane. Figure 50 shows a plot of the ammonia borane heating temperature and loading with respect to Ar:H_2 ratio for various CVD studies on hBN. Many of the studies included in Figure 50 synthesise hBN with H_2 in Ar in the region of 10% up as far as pure H_2 (0% Ar). For safety precautions and ease of scalability in industrial cases, in our study, hydrogen concentrations are kept at the flammability limit of 4% during growth. As well as this, previous work has shown that higher hydrogen partial pressures, the edges of the hBN domains can be etched away which allows additional layers to grown underneath [205, 206]. As such, in our study, H_2 concentrations are diluted significantly in Ar to prevent excessive etching, whilst also promoting layer-by-layer growth.

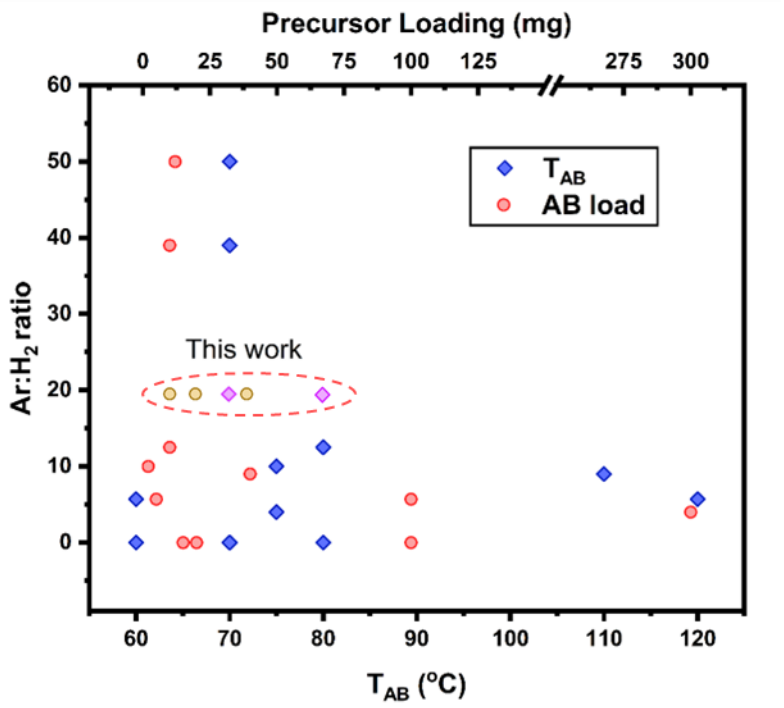


Figure 50; Growth parameters for APCVD hBN synthesis studies on Cu *[124, 126, 127, 129-131, 201, 204, 207-209]*. Circular dots refer to AB loading and correspond with the top x-axis while triangular dots refer to the temperature at which AB is heated and correspond with the bottom x-axis.

AB loading optimisation

The precursor loading for hBN growth was investigated to optimise growth towards layer-by-layer growth. Three amounts were chosen; 40, 20 and 10 mg. Synthesises were carried out at 1050 ˚C for one hour (T_{AB} = 80 ˚C) and samples analysed via Raman and SEM, shown in Figure 51. With the highest loading capacity, full hBN coverage on Cu is achieved during the 1 hour of growth. A broad peak centred around ~1370 cm^{-1} is observed in the Raman spectrum, suggesting a hBN film with poor crystallinity. This is also evidenced in SEM analysis (Figure 51 b (i)), where lots of nucleation points are seen. Lowering the amount to 20 mg, full coverage is again observed and the ML nucleation has been suppressed significantly, although still present. The Raman spectrum shows a clear peak at 1366 cm^{-1} with a narrow FWHM of 13 cm^{-1}, indicating good crystallinity. At 10 mg precursor loading, individual domains of hBN are

observed after growth for one hour, and Raman analysis shows a peak at 1368 cm^{-1} with FWHM of ~13 cm^{-1}. While there is no significant increase in crystallinity as evidenced by the Raman FWHM, lower precursor loading allows for a gradual filling of the catalyst bulk reservoir and build-up of reactants at the surface of Cu. This translates to reduced nucleation densities and larger individual domain sizes [129]. As such, the precursor loading was set at 10 mg.

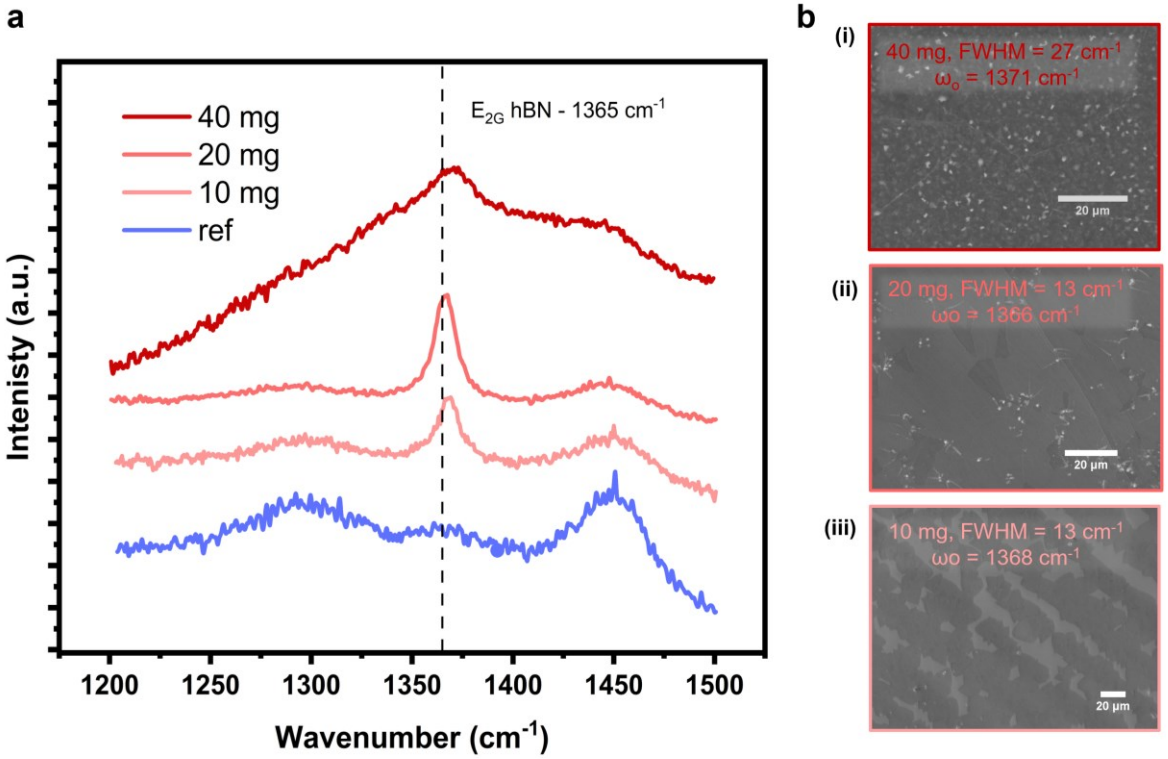


Figure 51; hBN film quality using different loading mass of AB. (a) Raman spectra of the various hBN films grown under different AB loading amounts and transferred onto SiO_2/Si substrate. The reference spectrum in blue is the bare SiO_2/Si substrate (b) SEM images for samples grown with (i) 40 mg AB (ii) 20 mg AB and (iii) 10 mg AB. Raman values extracted from (a) are overlayed. The white contrast in SEM images (b, i and ii) signify multilayer nucleation on the surface of Cu.

AB heating temperature, T_{AB}, optimisation

Two heating temperatures were trialled for hBN deposition; 70 ˚C and 80 ˚C. Figure 52 shows results of two synthesis where the heating profiles of the precursor are different. Looking at the heating profile for ammonia borane, it was found that a low heating temperature of 70 ˚C was best to produce triangular hBN domains. This is important when synthesising extended hBN

films as irregular shaped domains will increase the number of boundary effects as they converge.

Figure 52 (a) shows an SEM image for hBN grown with T_{AB} at 80 ˚C. hBN domains are observed as having positive curvature along their edges. These shapes have been observed experimentally and are formed when the chemical potential of the boron species is higher than that of the nitrogen ($\mu_B > \mu_N$), as depicted previously in Figure 11 c). When the profile is decreased by 10 ˚C to 70 ˚C, triangular hBN islands are formed (Figure 52, b), which are typically observed when $\mu_N > \mu_B$. These observations are supported by previous studies on the decomposition profiles of ammonia borane which found that at higher heating temperatures, B species showed a higher relative contribution to the overall flow [126]. As well as this, a lower nucleation density of hBN domains was observed in the sample grown with T_{AB} = 70˚C. As such, the heating profile for ammonia borane decomposition was set at 70 ˚C.

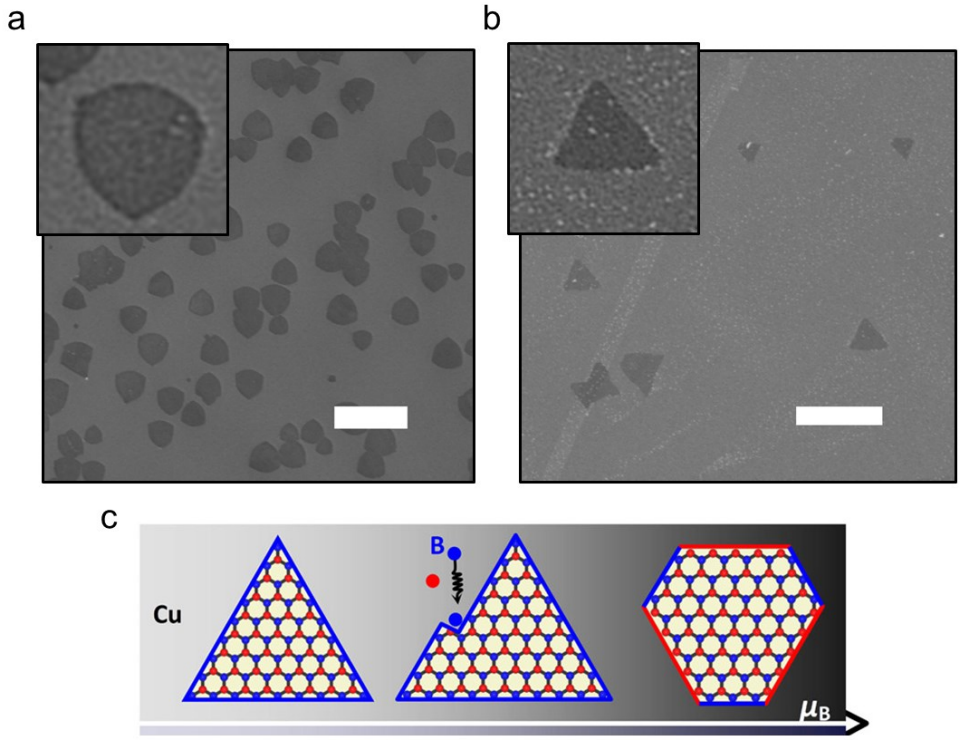


Figure 52; Effect of heating temperature of AB. (a) SEM image of hBN growth with T_{AB} = 80 ˚C. Inset is a magnified domain showing the rounded edges of hBN. (b) SEM image of hBN growth with T_{AB} = 70 ˚C. Inset is a magnified domain showing the straight line edges of hBN. Both scale bars are 20 µm. (c) Domain shape of hBN with increasing boron chemical potential. At higher boron chemical potentials, rounded hBN edge form. Adapted from *[196]*

These results also illustrate how sensitive the growth of hBN is to the decomposition profile of ammonia borane. An increase of just 10 ˚C can significantly increase (1) the domain shape and (2) the nucleation density of hBN. A thermal PID controller is used to supply power to the heating tape surrounding the AB container. This fluctuates through OFF/ON as it maintains the set temperature resulting in fluctuations in thermal energy delivered to the AB precursor, which can affect the flow profile. Furthermore, the sublimation of BN species from ammonia borane is often not stochiometric and can produce various gaseous B and N species upon heating . The use of a solid and non-toxic precursor such as ammonia borane allows for safe handling, however, the drawback is that it can be difficult to accurately control the reactant concentration in the CVD chamber. This is why using gaseous sources is so valuable, as growth parameters can be more accurately controlled and are less susceptible to variance in reactants and fluctuations in their relative concentration. Unfortunately, a non-toxic boron gaseous source is yet to be reported.

Optimised growth of hBN on copper

Optimised hBN growth was carried out at 1050 ˚C, with 10 mg of ammonia borane precursor heated at 70 ˚C. Figure 53 shows hBN growth at several stages using the optimized synthesis parameters. After 2 hours, the copper substrate is almost completely covered with hBN. Domain sizes were measured after 60 minutes of optimised growth, after which domains become converged and difficult to differentiate. After 60 minutes growth, domains with lateral sizes as large as 56 um were observed with an average domain size of 43.9 +/- 6.3 μm. Further SEM characterization of hBN growth is available in Appendix I, Section 8.1.3.

Reported domain sizes and growth rates of other hBN synthesis studies on Cu are listed in Table 2. LPCVD techniques show larger domain sizes than traditional APCVD methods, due to the growth system operating in a molecular flow regime (APCVD is viscous flow and thus

mass transfer limited), where the mean free path of reactants is large and growth is surface reaction rate limited, resulting in reduced nucleation density and larger single crystals of hBN [201, 210]. High-end CVD techniques such as those using substrate facet engineering [123] and H_2O assisted etching [211] have been able to improve the APCVD process and synthesise very large single crystal domains of hBN. The method used here, employing a confined channel for growth, has previously been shown to reduce nucleation and enhance the domain sizes in APCVD studies on graphene[184-187], and we observe similar results in this study, whereby slightly larger hBN domain sizes are achieved compared with typical APCVD [209, 212].

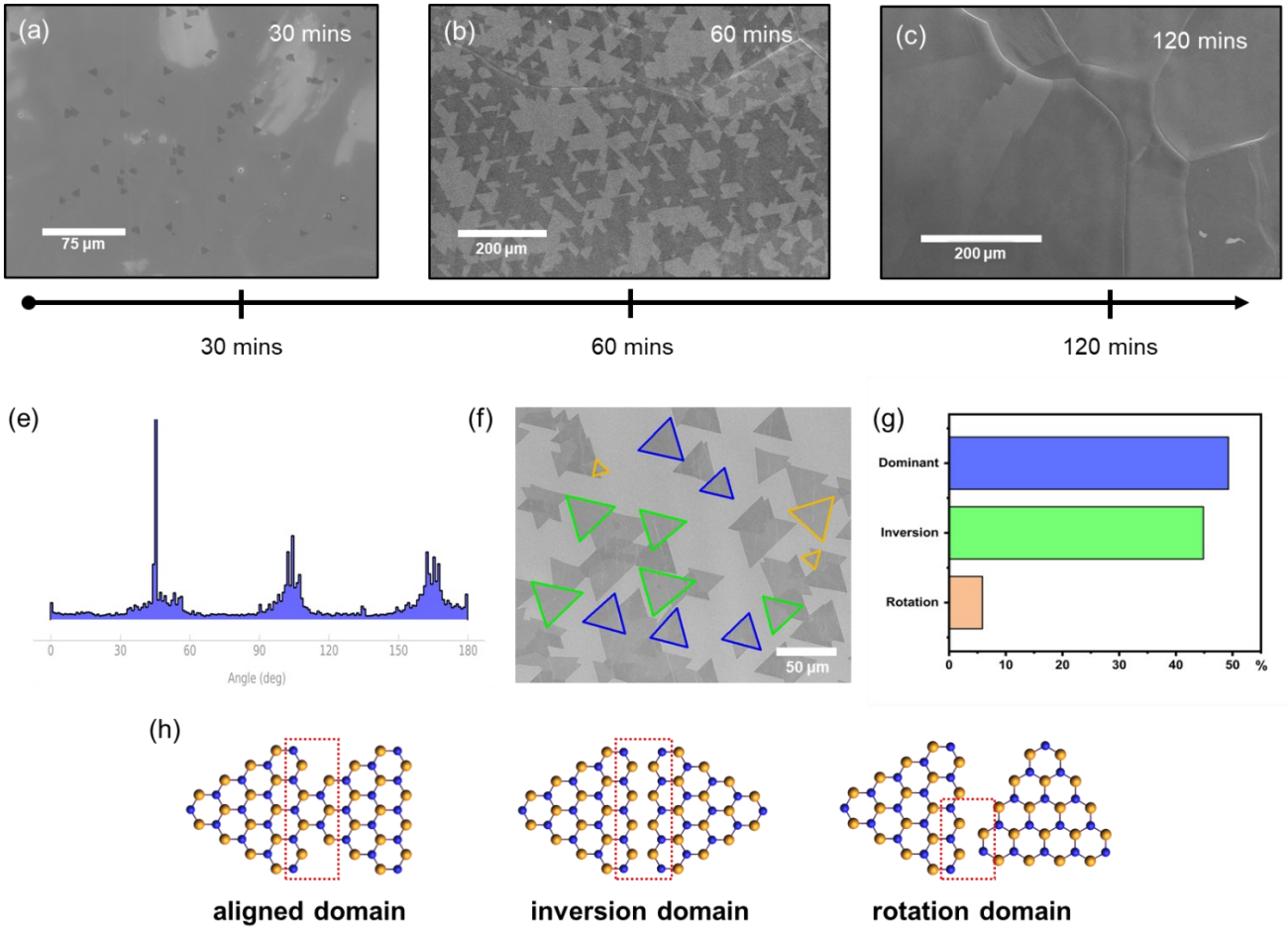


Figure 53; Optimised growth of hBN. SEM images of optimised hBN growth after (a) 30 minutes, domain sizes are still quite small, suggesting a long incubation period is required at T_{AB} = 70˚C (b) 60 minutes, lots of nucleated domains showing good alignment, (c) 120 mins, almost total coverage of Cu by hBN. (e) Sobel filter of the edge orientations of hBN domains on Cu, analysed using the GrapheneResQ tool. Domains show a periodicity of 60˚ with good alignment. Due to the di-atomic structure of hBN, inverted domains still form grain boundaries. As such a statistical analysis was carried out. (f) shows an SEM image where dominant (blue), inversion (green) and rotated (orange) domains are highlighted. (g) shows the result of the statistical analysis of each type of domain. There is no preference between dominant and inverted domains, indicating many twin boundaries may exist. A small amount of rotated domains are also observed. (h) Schematic showing how the di-atomic crystal structure can result in inversion grain boundaries and defects that arise from rotated domains.

From the wide-angle SEM view of hBN growth after 60 minutes in Figure 53 (b) and SEM image (f), domains are highly aligned on the surface of copper, with their growth directions tied to the facet of copper on which they grow. The alignment of these domains is analysed using the Graphene ResQ tool [213], an open-source suite of tools to allow for fast, automated, processing of SEM images. The domains show great alignment along the 45˚, 105˚and 165˚ directions (Figure 53, d), showing an epitaxial relationship of 60˚ periodicity with the copper substrate. Unfortunately, the program does not consider the inversion grain boundaries that form when domains are rotated by 60º with respect to each other, due to the polar structure of h-BN with alternating boron and nitrogen atoms. When these misaligned domains merge, a defect line with B-B and N-N bonding can be generated at the interface. These defect lines are depicted in Figure 53 (e). Aligned (blue), inversion (green) and rotated (orange) domains are observed in our hBN growth, depicted in the SEM image, Figure 53 (c). Statistical distributions of the domains orientation shown in Figure 53 (d) reveal that there is little preference between the aligned and inversion domains, with the percentage of inverted domains at 44.9% and 5.9% for rotated domains, indicating that many twin boundaries may exist in the converged film.

Table 2; Reported domain sizes of CVD hBN on Cu (* denotes LPCVD)

Author	CVD Method	Growth Rate (um/min)	Size (um)
Yijing Stehle [212]	Typical	0.7	20
Grace Wood [209]	Typical	0.25	5
Kamal Sharma [208]	Typical	0.4	25
Xiujiu Song [214]	Pocket *	0.6	72
Yanxin Ji [201]	Pocket *	0.5	300
Roland Tay [215]	Resolidified Copper	-	10
Ren-Jie Chang [216]	Oxygen assisted CVD	0.33	20
Mohammad Malik [210]	Oxygen assisted CVD *	3.6	180
Weijun Wang [207]	Free mol. Flow *	0.7	80
Hongwei Liu [129]	LMCat	0.5	15
Lifeng Wang [211]	H2O assisted LMCat	3.67	330
Li Wang [123]	Substrate facet engineering	55.56	10,000
This work	Confined channel	0.7	44

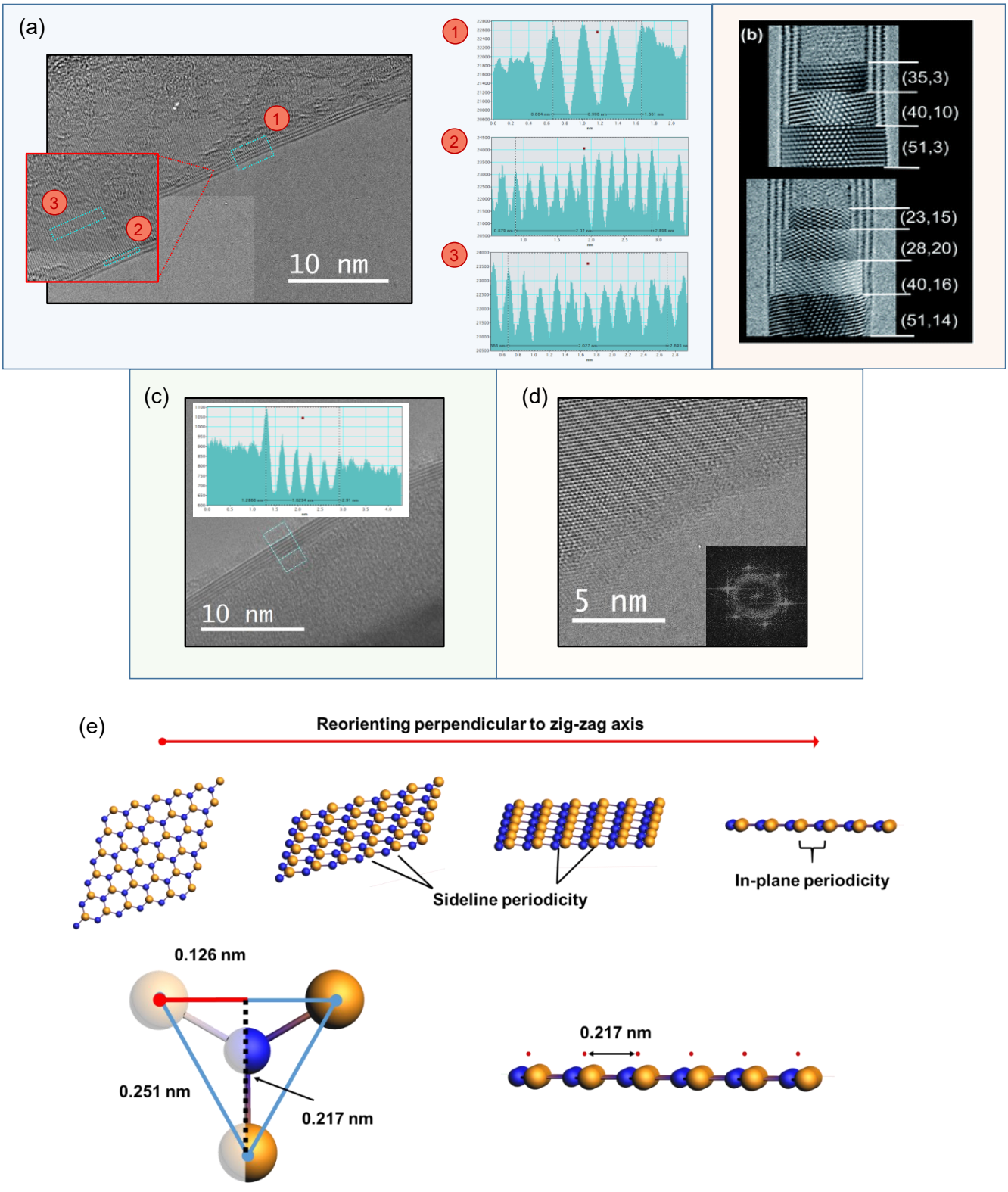


Figure 54; TEM analysis of optimised hBN film. (a) TEM image showing regions of different periodicity, labelled 1-3. Point 1 refers to the interlayer distance of hBN, determined at 0.33 nm. Point 2 refers to the periodicity along the hBN plane, measured at 0.202 nm. Point 3 refers to the sideline periodicity observed in the film, which we attribute to out of plane interaction of the film with the electron beam. This is measured at 0.203 nm. (b) Sideline periodicity has been observed previously in curved carbon structures such as nanotubes. Adapted from *[217]*. (c) Area of multilayer hBN growth (6 layers). (d) Area of monolayer hBN growth. Inset is FFT image showing a six- fold hexagonal pattern. (e) Schematic showing the in-plane and sideline periodicity of the hBN lattice that becomes apparent as the lattice is gradually tilted.

TEM characterisation is carried out on the hBN films to determine the number of layers and confirm crystallinity. Figure 54 shows TEM images of film edges, illustrating how the number of hBN layers varies between monolayer and up to 6 layers in (Figure 54, a, c, d). Layer spacing was determined to be between 0.32 – 0.33 nm, consistent with the theoretical c-spacing for hBN. Periodicity along hBN planes was observed in the TEM image shown in Figure 54 (a), measured at 0.202 nm. This value is consistent with the calculated spacing of the (01-10) zone axis of 0.217 nm (compared to 0.213 nm in graphene). The deviation from the theoretical spacing might arise from out of plane distortion with the electron beam. Similarly, periodicity is observed along the sidelines of the film (region 3 in Figure 54, a), measured at 0.203 nm. This sort of additional contrast has previously been reported in graphene as well as CNTs where it is attributed to out of plane distortion of graphene and the curvature of the nanotubes (shown in Figure 54, b) [217, 218]. A similar situation could be arising here, where the area of the lattice is changing in orientation with respect of the TEM e-beam. Figure 54 (e) gives a schematic of how these types of contrast might arise in the TEM image and derives their spacing. FFT analysis of various regions of the hBN film showed both rotated and AA' stacking in hBN samples (available in Appendix Section 8.1.3).

Few-layered growth of hBN on Cu is something that has previously been observed in many APCVD studies of hBN growth on Cu [134, 198, 219]. The varying layer number in the hBN film suggests that, for our system, more control over the synthesis is needed for monolayer hBN growth. Factors such as sample smoothness, Cu grain boundary size and reservoir effects have been already reduced via the pre-synthesis steps of electro-polishing and annealing. To achieve further control, carrying out synthesis at low pressures could promote monolayer growth, as growth dynamics shift from mass transport limited to surface reaction limited regimes at low pressures [199]. However, it adds another level of complexity in the CVD process and brings with it issues of its own (increased Cu evaporation rates, longer synthesis

times). As monolayer growth is not a prerequisite for this study, few-layered growth of hBN on Cu is sufficient.

Optoelectronic characterisation was carried out on the hBN films via UV-vis spectroscopy. The Tauc plot shown in Figure 55, (a) measures the bandgap of hBN to be 5.95 eV. Raman spectroscopy confirmed good crystallinity of the material with FWHM value of 17.2 ± 2.3 cm^{-1}, similar to other reports on crystalline hBN layers grown on Cu via CVD [199, 220]. Figure 55 (b) shows an exemplar spectrum of the hBN film on SiO_2.

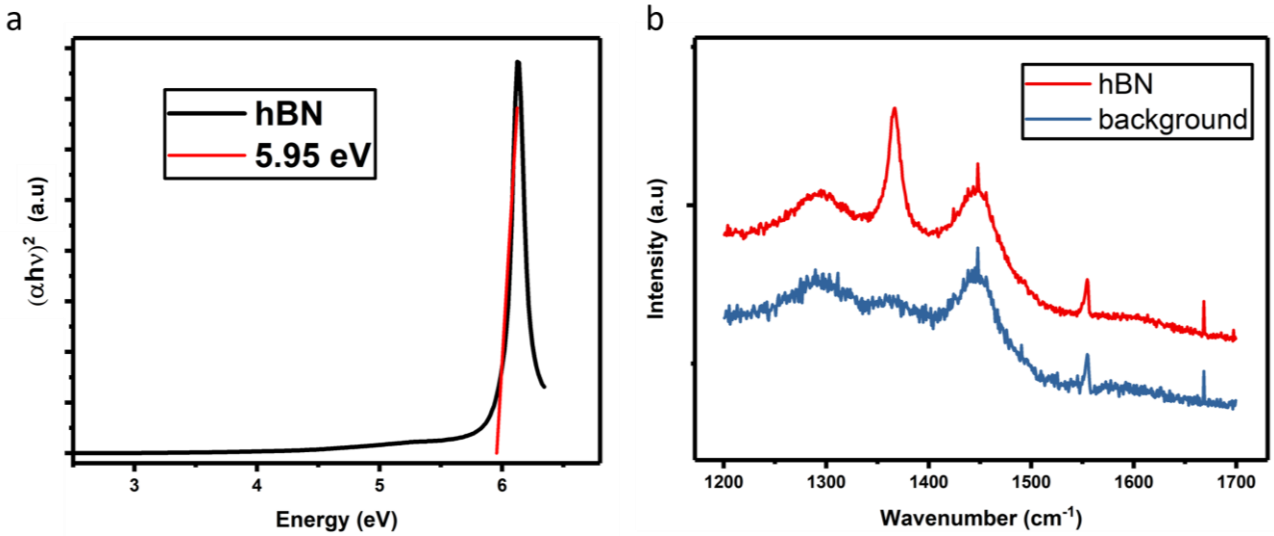


Figure 55; Opto-electronic characterisation of optimised hBN film. (a) Exemplar Raman spectrum of hBN film showing a clear E_{2G} peak. (b) Tauc plot of hBN sample showing exhibiting a band gap of 5.95 eV.

In summary, this section details the synthesis of few layer hBN films on copper foil via APCVD. An initial analysis of the parameter space for hBN growth indicated that low precursor loading and heating profiles were optimum for hBN growth. This was verified through a series of experiments which suggested that a 10 mg load and 70 ˚C heating profile was optimum for growth of well aligned, triangular domains of hBN on the Cu substrate. Using a confined channel set up, the average domain size of hBN was determined to be ~44 µm with a growth rate of 0.7 µm/min, higher than typical APCVD set ups reported in literature.

In SEM analysis, domains typically showed good alignment with two preferential growth directions, aligned and inverted, which may result in many twin boundaries in the fully

converged film. Regions of varying layer number and stacking sequence were observed across the one film under TEM analysis, characterising the films as few-layered. TEM analysis also revealed several edge contrast features whose occurrence have been explained as resulting from a change in orientation of the film with respect to the beams z-axis. The hBN film was characterised as highly crystalline via Raman spectroscopy, with a FWHM of 17.2 cm^{-1}, similar to other reports on CVD hBN layers grown on Cu [199, 220]. Finally, the optical band gap of these few layered hBN was determined to be 5.95 eV.

Having optimised the synthesis protocols for hBN on Cu, I next move to synthesise carbon doped hBN (hBN-C) structures, through *in situ* doping with CH_4 during optimised hBN growth.

3.3.3. Carbon doped hBN grown on Cu metal foils

Incorporating carbon into the lattice of hBN, and producing C doped hBN (hBN-C), can modify the material properties in various ways, as highlighted in Section 1.3.4 of Chapter 1. However, varying growth methods can incorporate the atomistic carbon differing ways; ion implantation of C in hBN produces point defects in the hBN lattice [22], whereas techniques like IBSD can result in mixed phase hBCN growth [25]. As such, it is beneficial to carry out research into each synthesis method and its relationship with the resulting hBN-C material. Only very recently has C doped hBN synthesised on Cu via APCVD been reported in the literature [23]. Starting from an optimised hBN synthesis, Liu *et al.* introduced methane during hBN growth on Cu and reported the first effective approach for modulating SPEs in hBN grown via CVD. With methane introduced at a fixed partial pressure, Liu *et al.* used the synthesis temperature to control the concentration of C incorporated into the flake and their results showed a clear correlation between SPE density and the temperature of growth. At temperatures above the melting point of Cu, no enhancement to SPE density was observed, which they attributed to C

sequestration into the Cu liquid substrate and thus preventing incorporation into the hBN flakes. However, below the melting point of Cu, they observed a significant increase SPE density, due to the increased concentration of carbon at the surface of Cu which is effectively incorporated into hBN. As such, they conclude that C doping of hBN films synthesised on Cu via CVD should be carried out below the melting temperature of the substrate to enhance the effects of C incorporation.

With this in mind, this work builds on Liu *et al.*'s study *[23]* and looks at C doping of hBN below the melting point of Cu, using methane partial pressure as the variable parameter to investigate the effective doping of hBN. Currently, no studies have looked at the role of methane partial pressure during "C doped" hBN growth on Cu foils. Specifically, we report on the effects of methane partial pressures on growth morphology and opto-electronic material properties of the resultant hBN-C films, starting from low partial pressures of methane ($\mu_{BN} > \mu_c$) and increasing this parameter systematically. Analysis of the growth is carried out via SEM, TEM and Raman characterisation and conclusions drawn about the mechanism for growth. XPS is used to probe the chemical bonding profile in each hBN-C sample by looking at the B 1s, C 1s and N 1s core electrons. Finally, UV-vis spectroscopy is used to analyse the optical properties of the samples and understand the effect of increased C doping on the films.

Using the previously optimised parameters for hBN growth, methane is introduced during hBN synthesis with the following gas flow parameters. CH_4/H_2 ratio is also included as this has been shown to be a relevant parameter in CVD studies of graphene [221].

Table 3; Gas flow composition for growth of $hBNC_x$ samples

Sample	CH_4 sccm	H_2 sccm	Ar sccm	CH_4/H_2 ratio
hBN	0	16	384	-
$hBNC_1$	0.0075	16	384	1 : 2133
$hBNC_2$	0.0125	16	384	1 : 1280
$hBNC_3$	0.020	16	384	1 : 800
$hBNC_4$	0.096	16	384	1 : 167

From analysis of the hBNC samples, I separate the growth regimes into three sections;

(i) low partial pressures of CH_4 resulting in C doped hBN (H_2:CH_4 > 800)

(ii) partial pressures of CH_4 resulting in hBN-templated graphene growth (H_2:CH_4 = 800)

(iii) high partial pressures of CH_4 resulting in mixed phase growth (H_2:CH_4 < 800)

The morphology and structural quality of each sample is initially characterised via electron and optical microscopy methods in combination with Raman spectroscopy, before then carrying out a comparative analysis of chemical composition via XPS and opto-electronic properties via UV-vis spectroscopy at the latter stage of this Section.

(i) Low partial pressures of CH_4 forming C doped hBN

Introducing the lowest concentration of methane during the synthesis did not observably influence the growth of hBN domains, as seen in the SEM images of the $hBNC_1$ sample in Figure 56. Similar to optimized hBN growth, equilateral, triangle domains with good alignment are realised on the Cu substrate and no observable difference under full film coverage. This is similar to growth reported in Liu *et al.*'s study, where no distinct observations could be made between hBN and C doped hBN morphologies under optical microscopy analysis [23].

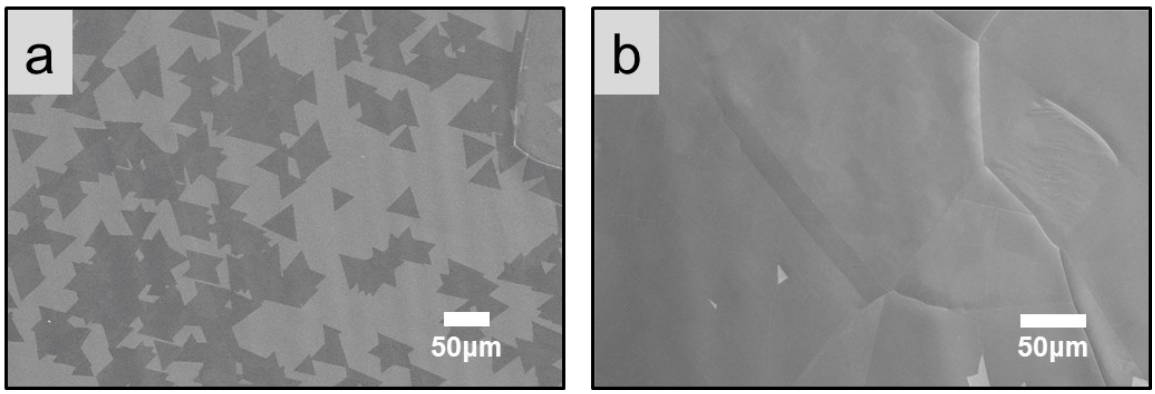


Figure 56; SEM of $hBNC_1$ growth at (a) t = 60 mins and (b) t =120 mins. Traditional triangular shapes of hBN are observed until film converges.

With increasing partial pressure of CH_4 in sample $hBNC_2$, regions of contrasted deposition along the edges of the hBN domains are observed, shown in SEM images Figure 57, a-b. This deposition is needle like in its morphology and surrounds the edges of the exposed hBN domains. Figure 57 (c) shows a wide-view OM image of hBN domains distinguishable against the oxidised Cu substrate, with edge deposition features visible via the contrast along several hBN edges. Raman analysis carried out on these edge features to determine their composition (Figure 57, d) revealed that they were comprised of highly disordered, graphitic carbon. From analysis of the I_{2G}/I_G ratio (0.42), these regions are multilayered in nature. These graphitic regions exhibited an I_D/I_G ratio of 2.6, D' peak at 1615.4 cm^{-1} and an $I_{D'}/I_G$ ratio of 0.22, which corresponds to vacancy and boundary type defects in graphitic strucures [222]. This correlates with the morphology of the carbon structures, which are dendritic in nature and thus possess many boundary defects. Dendritic growth typically occurs under diffusion-controlled growth, *i.e.* where the "adatom C flux" on Cu is significantly lower than the rate of 'edge attachment' of C species [154, 223-225]. In particular, Hao *et al.* observed that by lowering the edge attachment energy barrier through O activation on oxidised Cu surfaces, growth was shifted towards dendritic graphene domains. At fast edge attachment rates, flux of C species becomes the important parameter for domain shape and a low flux of C resulted in dendritic patterns of graphene [154]. In a similar fashion, BN edge-activation could shift the kinetics of graphene

nucleation and growth towards dendritic growth by reducing the energy of the edge-attachment barrier.

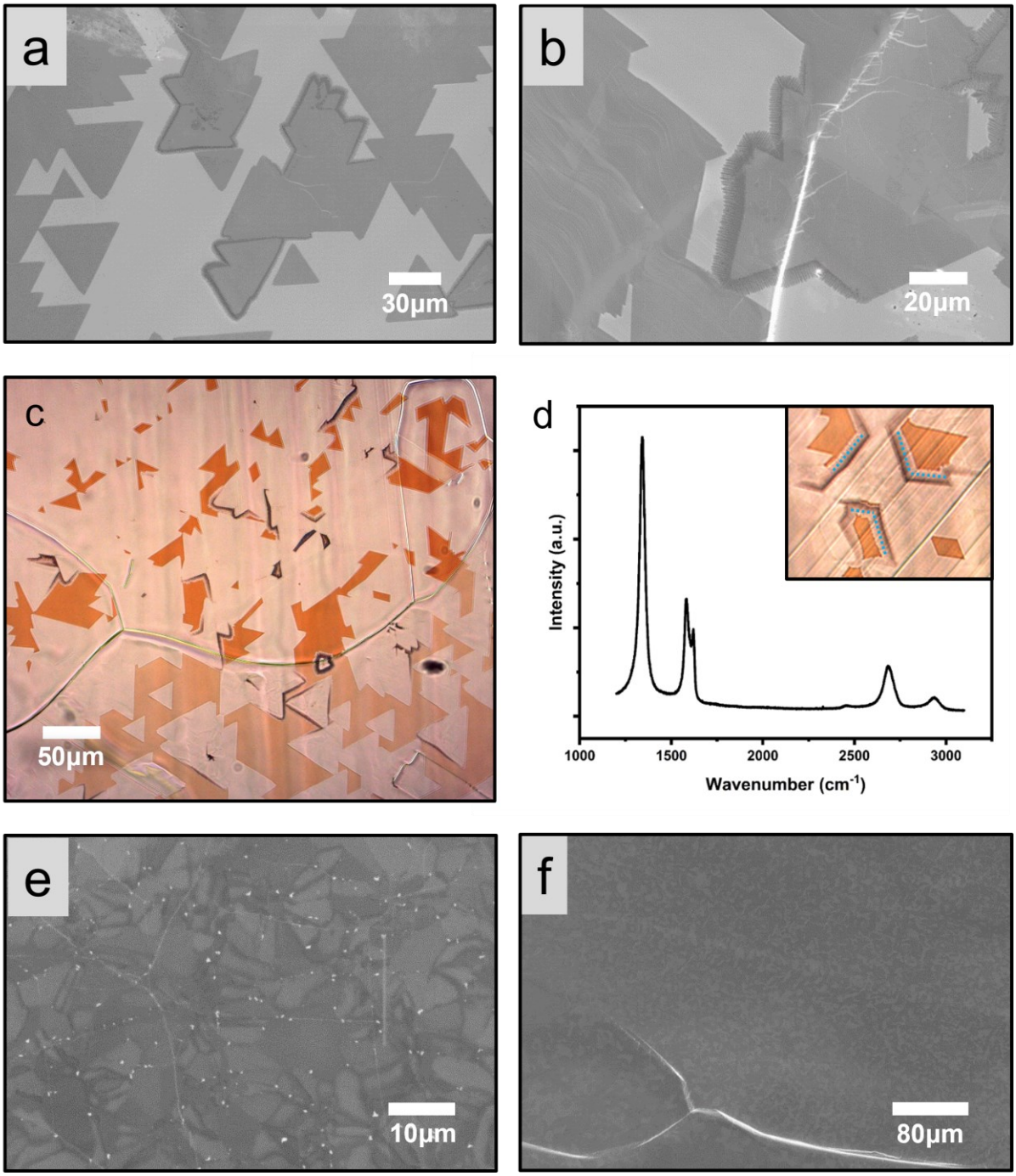


Figure 57; SEM of $hBNC_2$ growth (a-b) at t = 60 mins. Individual domains of hBN are observed with dendritic growth structures extending from their edges. (c) Wide view OM image showing contrasted regions along the hBN domain edges (d) Raman analysis of these edge regions reveal they are comprised of highly defective, graphitic carbon. Here, the I_D/I_G and I_{2D}/I_G ratios are 2.60 and 0.42, respectively. Inset shows a close-up OM image of the hBN domain and dendritic edge structures analysed in Raman. (e-f) SEM of $hBNC_2$ at film convergence. As growth continues, domains converge and the dendritic edge patterns are encompassed in the film, exhibited by the darker contrasted domain edges in (e).

Increasing the deposition time to allow for film convergence, regions of varying contrast in the hBN film are observed, as seen in Figure *57* (e-g). hBN domains continue to grow towards these C capped regions, encompassing them within the hBN film. The material is likely comprised of hBN with defective domain edges, whereby C is intercalated both as point defects within the hBN domain and as graphitic edge defects along converging domain channels.

TEM characterisation was carried out to investigate the structural effects of carbon inclusion at the nanoscale for sample $hBNC_2$ (Figure 58). TEM analysis showed regions of good crystallinity across the sample, as determined via FFT analysis, yet the $hBNC_2$ sample also contained significant regions of amorphous material on the surface of the film. The amorphous regions still exhibited FFTs with a hexagonal pattern, but at a lower intensity, suggesting that these regions lay on the surface of the crystalline film. Amorphous regions were not observed under TEM analysis of intrinsic hBN samples, suggesting they were unlikely PMMA residues from the transfer procedure, instead resulting from the needle structures along the edges of

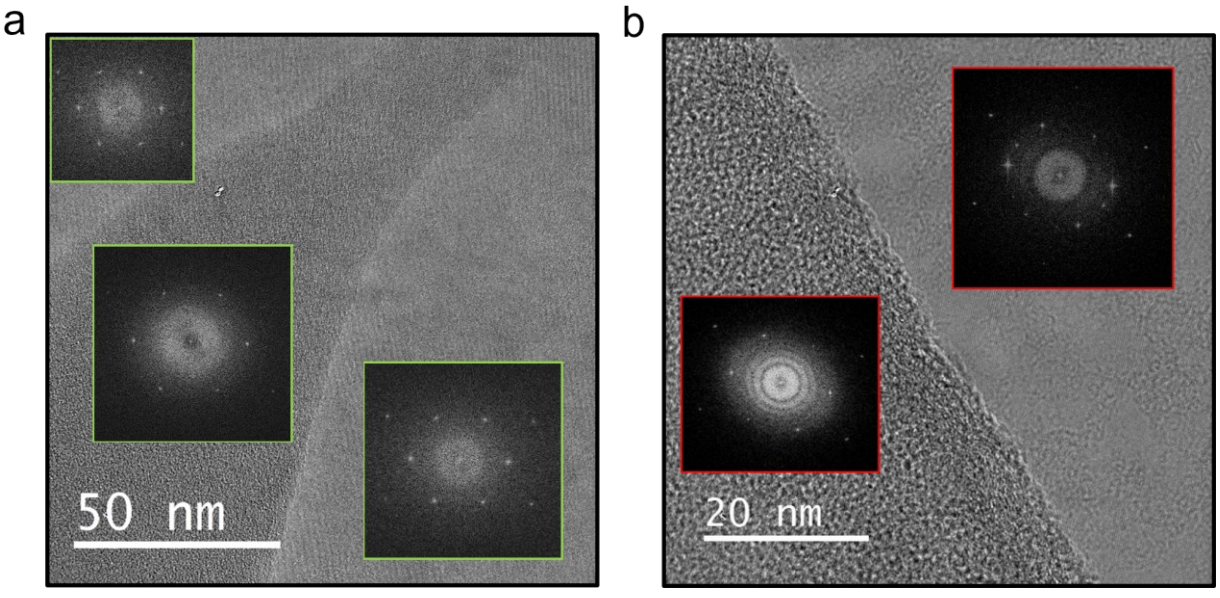
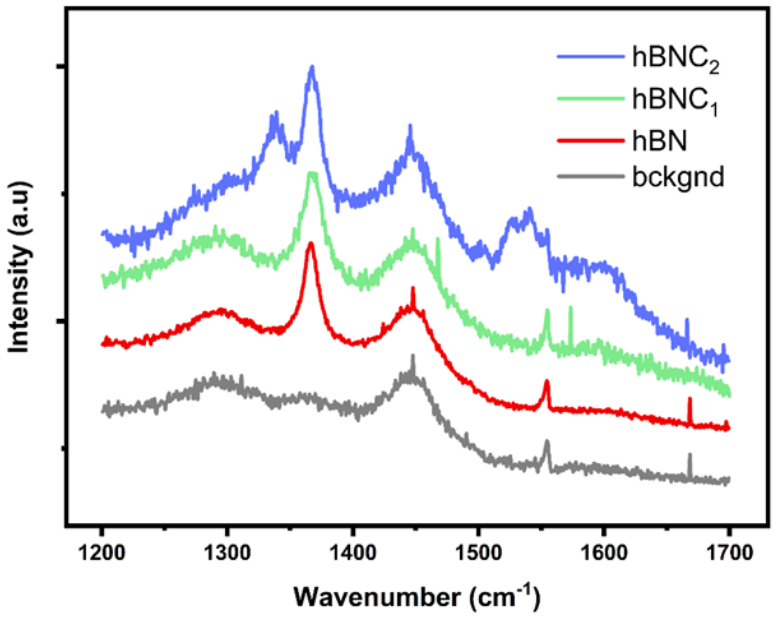


Figure 58; TEM images of $hBNC_2$ sample with amorphous regions observed. (a) FFTs inset from top, middle, and bottom of film show the six-fold crystallographic pattern associated with hexagonal systems, exhibiting good crystallinity in the sample. The same FFT is observed across the three sections but with varying intensity, as the amorphous regions disrupt the electron beam, suggesting that amorphous regions lie atop the crystalline regions of the film (b) FFTs inset show the reflections observed from the LHS and RHS of the image. The same FFT pattern is observed, but with varying intensity, suggesting that the dendritic growth structures form on the hBN film and are possibly amorphous.

hBN which are degraded during the transfer process. Dendritic graphene will possess lower crystallinity in comparison to compact graphene domains due to the irregularity in its fragmented, geometric shape and has been previously shown to possess lower oxidation resistance than single crystal graphene domains [226].

Raman specroscopy was carried out on samples of the converged films, results of which are seen in Figure 59. A slight increase in the E_{2G} peak of hBN is observed between the hBN and $hBNC_1$ sample, with no observable carbon related peaks. In sample $hBNC_2$, however, the emergence of a shoulder D peak of carbon is observed, centred at 1338 cm^{-1} as well as a small, broad G peak at ~1600 cm^{-1}. Two peaks are also observed at 1525 cm^{-1} and 1540 cm^{-1}, which we assign to defective N-H and C-H vibrations within the film [227].

a



b

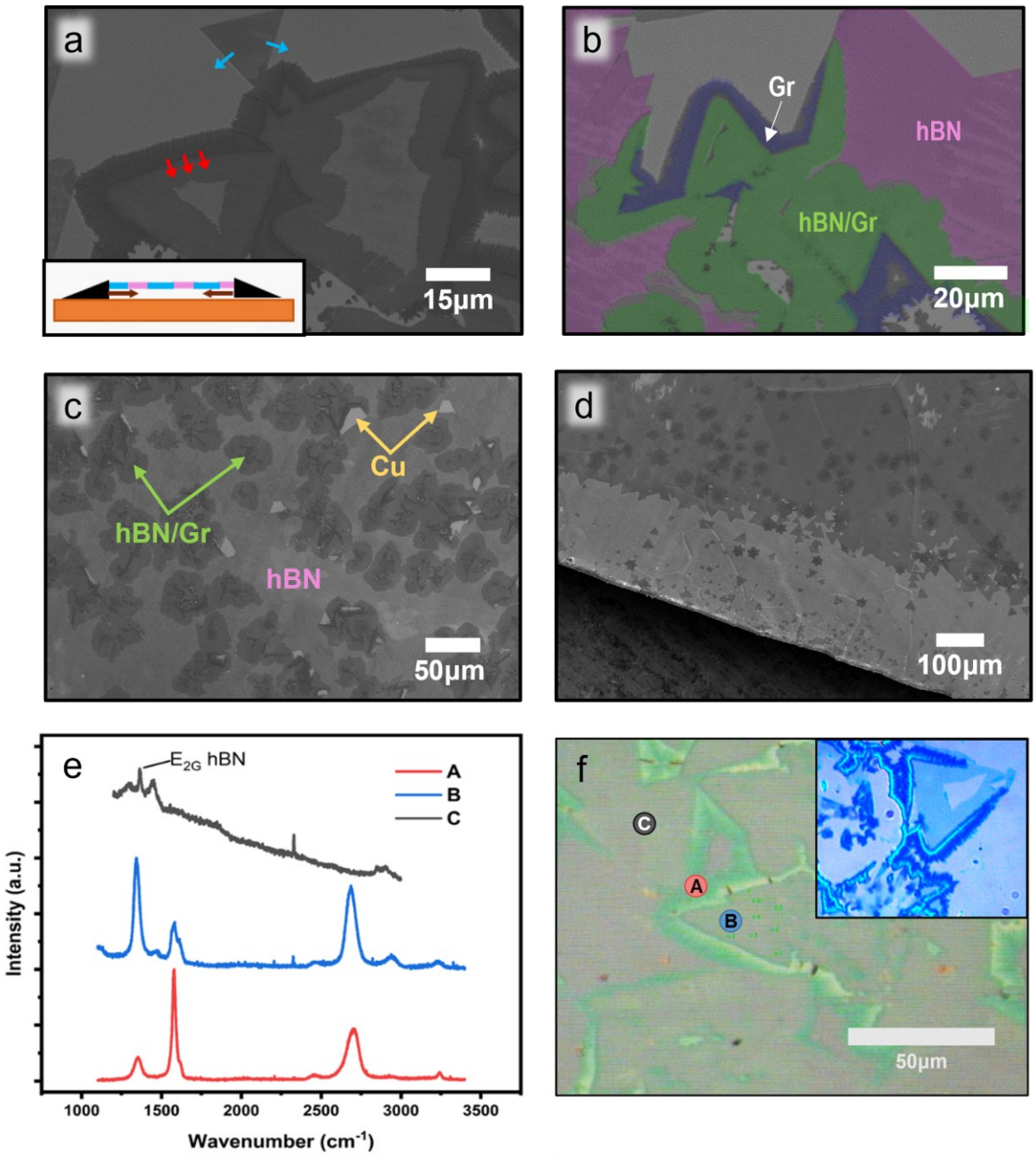
Spectrum	E2G peak (cm^{-1})	D peak (cm^{-1})	G peak (cm^{-1})	E2G FWHM (cm^{-1})
hBN	1366.5	-	-	15
$hBNC_1$	1367.6	-	-	22.5
$hBNC_2$	1367.4	1337.6	1596.5	14.7

Figure 59; Raman characterisation of samples synthesised under low p.p methane. (a) Raman spectra for each sample exhibiting the characteristic E_{2G} peak of hBN. Grey spectrum is the reference substrate SiO_2/Si. $hBNC_2$ sample also exhibits small D and G peaks of graphitic carbon. (b) Table exhibiting the fitted peak values for spectra in (a).

(ii) hBN-templated Graphene nucleation

By further increasing the partial pressure of methane, graphene nucleation was observed, with growth congruent with hBN domains, *i.e.* template assisted growth of graphene domains by hBN. These structures are shown after 60 minutes of synthesis in Figure 60 (a-b). Again dendritic structures are observed along the edges of the hBN domains, from where the graphene regions congruently grew along nucleated hBN, suggesting that these structures are a prelude to the graphene growth beneath hBN and that the hBN edge acts as a low energy site to facilitate their nucleation. The outward growth direction of hBN is highlighted via blue arrows in Figure 60 (a), whereas the inward growth direction of the graphene is shown by the red arrows. A cross-sectional schematic of this growth is also depicted, inset of Figure 60 (a); graphitic carbon regions, (shown as the black triangles) first nucleate along the hBN domain edges (pink and blue layer). As growth proceeds, the concentration of carbon grows until it reaches a crititcal point, whereby congruent graphene domains (brown arrows) can nucleate below the hBN domain and in contact with the Cu substrate, with C species supplied by surface diffusion of C adatoms from decomposed gaseous methane species on Cu, as well as C atoms that detatch and diffuse from the low-crystallintiy (and thus stability [226]) dendritic graphitic edge regions. Based on the principle of minimum energy, and under the influence of a hydrogen environment and high thermal energies, atoms belonging to the metastable dendritic graphitic regions may detach as free atoms, and find a lower energy site, forming stationary atoms in a growing graphene lattice below hBN. As graphene growth on Cu is surface-mediated and catalytically activated, the graphene domains most likely nucleate beneath the hBN domain and not on its surface. Underneath the hBN domain, the growing graphene is protected from the hydrogen environment and congruent graphene grows inward from the hBN edge [228].

Figure 60 (b) uses colouring to further distinguish the various regions of growth; the blue region highlights the dendritic graphitic regions, while green shows the regions of templated graphene



g

Spectrum	D peak (cm^{-1})	G peak (cm^{-1})	2D peak (cm^{-1})	2D FWHM (cm^{-1})	D/G	2D/G
Blue (B)	1342.7	1578.7	2687.0	60.9	2.86	2.312
Red (A)	1352.5	1578.9	2698.6	81.1	0.21	0.48

Figure 60; $hBNC_3$ sample (a) SEM image of the sample at mid growth stage (t = 60 mins). Red arrows show the direction of graphene growth inwards from the hBN domain edges, nucleating from the graphitic edge deposits. hBN domains continue to grow, as shown by the blue arrows, which eventually envelop the graphitic regions. Inset shows a cross-sectional schematic of growth (b) Colourised SEM image discerning the various regions; blue – dendritic, graphene deposits, pink – hBN islands, green – hBN / graphene stacked heterostructure. (c-d) SEM images of $hBNC_3$ sample at film convergence (t=120 mins). Graphene domains are non-traditional and highly irregular in shape, due to the edge-nucleated growth. (e) Raman spectra for spot regions A, B and C, seen in image (f). (f) OM image taken by Raman microscope during analysis. Inset is OM image with enhanced contrast features that show the three distinct regions; dendritic growth at the edges of the hBN domains (A), congruent graphene domains templated by hBN (B) and intrinsic hBN region (C). (g) Table exhibiting the fitted peak values for spectra in (e).

growth bounded by the hBN domain, and purple represents the hBN-only region. Increasing the synthesis time and allowing growth to growth proceed towards a fully converged film, the graphene domains exhibit non traditional shapes, as seen in Figure 60 (c-d), due to the anisotropic growth directions templated by the converging hBN domains. Differences in contrast of the graphene domains suggest that the templated graphene is non-uniform on the growth substrate, in terms of layer number. Further SEM characterisation of the $hBNC_3$ sample is available in Appendix I, Section 8.1.5.

Raman characterisation of the $hBNC_3$ sample was carried out, shown in Figure 60 (e-g). Three regions are observed with distinct Raman spectra; dendritic, needle like-graphene grown at the edges of the hBN domains (spectrum A), congruent graphene domains below hBN's surface (spectrum B) and intrinsic hBN region (spectrum C). The raman spectrum for the dendritic growth at the edges of hBN domains shows a relatively low I_D/I_G ratio in comparison to the previous $hBNC_2$ sample of 0.21 ($hBNC_2$ - 2.6) and a similar I_{2D}/I_G ratio of 0.48 ($hBNC_2$ – 0.42). This is a significant reduction of defect density, suggesting an increased graphitisation of this region with increased C adatom "flux", as has been observed in other experiments on graphene CVD [154, 224]. Analysis of the graphene domains grown beneath hBN exhibit raman features of highly defective, monolayer graphene. Here, the I_D/I_G and $I_{D'}/I_G$ ratios are 2.86 and 0.2, respectively, similar to the case of the highly defective edge regions in sample $hBNC_2$ (2.60 , 0.22), which corresponded to vacancy type defects [222]. The I_{2D}/I_G is different, however, at 2.31 ($hBNC_2$ – 0.42), suggesting a monolayer graphene structure. This graphene layer is highly defective, likely due to vacancy defects resulting from the slow diffusion of C adatoms at the hBN/Graphene/Cu interface, as well as possible substitutional dopants in the Gr sheet from the more soluble B adatom from the AB precursor (as highlighted in Section 3.3.1).

TEM analysis carried out on the $hBNC_3$ sample showed it to be highly crystalline, as evident in the FFT patterns in Figure 61. Also observed was the presence of amourphous regions on

the film, similar to that of $hBNC_2$ (available in Appendix Section 8.1.3). TEM analysis of the film exhibited regions of rotated adlayer growth, seen in Figure 61. FFT analysis is used to distinguish the rotated adlayer. Figure 61 (a, i) shows a wide view image of the TEM sample. Figure 61 (a, ii) shows the FFT corresponding to the blue box in (i) and exhibits two sets of hexagonal diffraction patterns, circled in yellow and blue. In the region below Figure 61 (a, iii), only one set of hexagonal spots are observed. Notably, this set of diffraction spots, circled in yellow, is present in both regions, demonstrating the presence of adlayer growth.

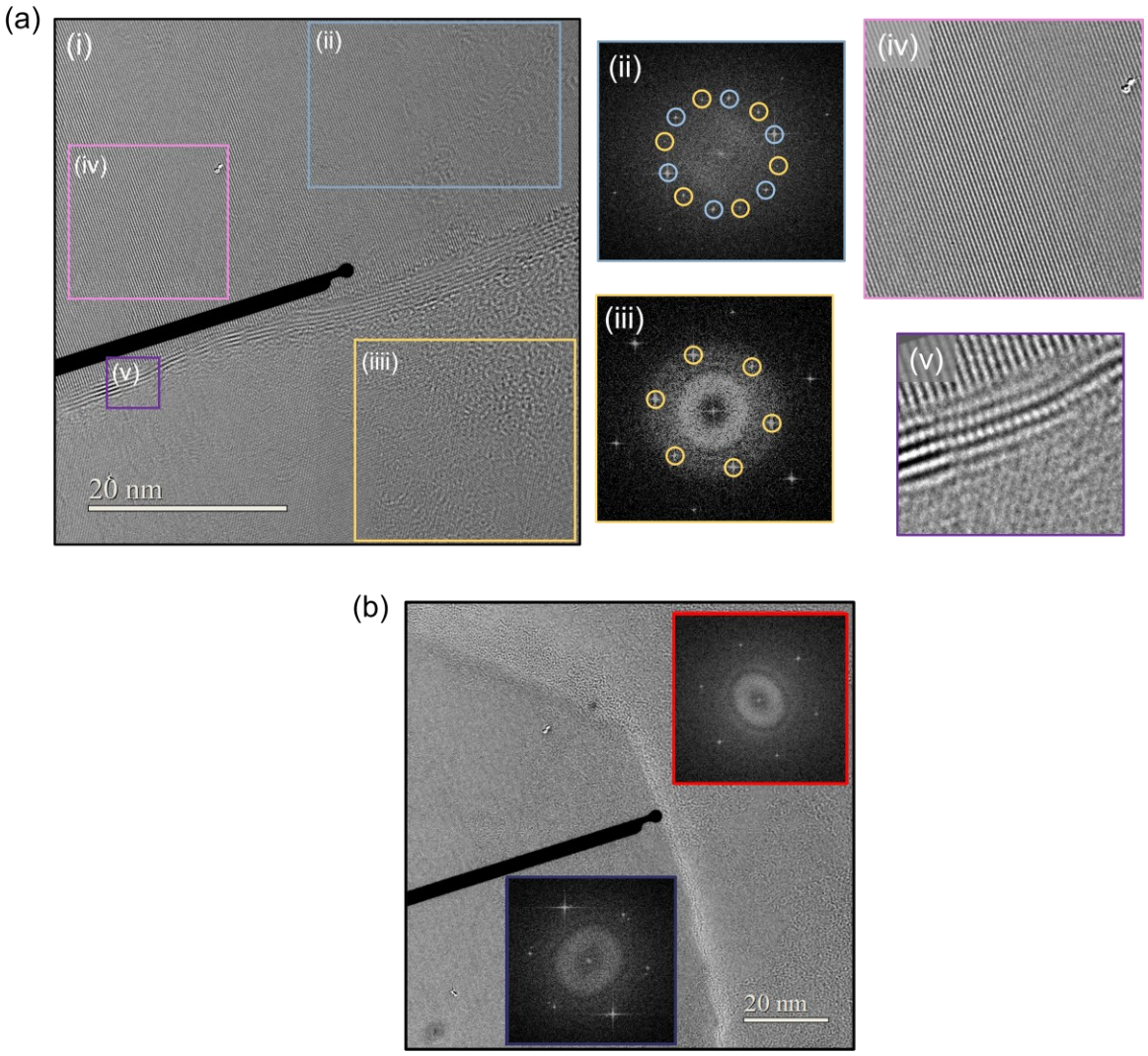


Figure 61; TEM analysis of $hBNC_3$ showing additional regions of rotated adlayer growth. (a), (i) TEM image of $hBNC_3$ sample exhibiting two FFT patterns across layers. (ii) FFT pattern of the blue box in (i) showing two sets of hexagonal diffraction spots, circled in blue and yellow. (iii) FFT pattern of the yellow box in (i), showing one set of hexagonal diffraction spots, circled in yellow. These diffraction spots are also present in (ii), demonstrating the presence of an adlayer. (iv) region showing sideline periodicity, suggesting the region is raised and out of plane with the electron beam (v) The adlayer is multilayered, explaining the observed distortion in (iv). (b) Region of adlayer showing a smaller rotation angle in the FFT analysis than in (a). As such, the interlayer angles are not uniform across the sample.

Sideline periodicity is observed in Figure 61 (a, iv), shown in the pink, suggesting the region is raised slightly, and out of plane distortion occurs between it and the electron beam, similar to that observed in hBN TEM analysis. The layer below lacks this periodicity. This adlayer is multilayered (Figure 61 a, v – purple box), resulting in the out of plain distortion observed. Furthermore, rotation of the adlayer is not constant across differing regions in the sample, as evidenced in Figure 61 (b). Here, we see from the FFT patterns that the relative rotation between layers is smaller than in (a). Rotated domains could also be observed by overlapping grain boundaries in hBN growth [206], however, here, distinct regions of adlayer growth are observed under TEM. It is difficult to precisely distinguish whether these regions are graphitic or hBN via FFT analysis due to the very similar lattice parameters of hBN and graphene. Tools such as HRTEM and TEM-EELS should be used in future to determine the atomic make up of the adlayer. Unfortunately, due to pandemic shut-downs and restricted access, these were unavailable during this study.

Here, we show that vertically stacked heterostructures can form via hBN-templated growth using a *one-step* synthesis protocol (introducing the C precursor, methane, during hBN growth), which has not been reported in the literature. Instead, CVD-synthesised vertically stacked Gr/hBN heterostructures similar to those reported here have typically employed *two-step* processes and techniques like co-segregation of C from substrates with a higher C solubility, such as Ni, coated with hBN [144, 229]. Raman features of heterostructures synthesised via this method, also show defective graphene, with high $I_{D/G}$ intensity ratios, which they ascribe mainly to hybridisation between graphene and hBN that occurs during the high temperature growth process which was supported by XPS observations [229].

Other studies of heterostructure growth on Ni substrates found that the interaction between the first grown layer and the Ni growth substrate heavily influences the growth of the adlayer, that

is, that adlayer growth only occurrs beneath domains with a weak interaction with the substrate [230, 231]. This supports our observations on Cu, which is weakly interacting with hBN and graphene domains [232-234], and likely allows for the diffusion of C atoms beneath the hBN domain, leading to the nucleation of graphene. Work by Lu *et al.,* on hBN-Gr heterostructures synthesied on Cu-Ni alloys similarly observed graphene adlayers underneath already formed hBN domains, facilitated through nucleation along the hBN-Gr boundaries (Figure 25, d-i) [116] . This is similar to growth observed in our study, where graphitic material nucleated first on the outer domains of hBN before extending underneath to form an in-plane heterostructure, and adds further evidence to the hypothesis that the hBN edge reduces the energy of the edge-attachment for graphene growth. In the case of Lu's work, they manage to synthesise defect-free graphene heterostructures, which they attribute to the use of Cu-Ni substrate rather than Cu [115]. Adding Ni content to Cu, increases its capacity for dissolving carbon into the bulk and thus, its diffusion below the hBN domain. With a higher rate of diffusion, C atoms can reach the growth front of the graphene domain at a faster rate allowing for attachment-limited growth. Graphene grown under this regime is typically isotropic, resulting in a higher quality domain [235].

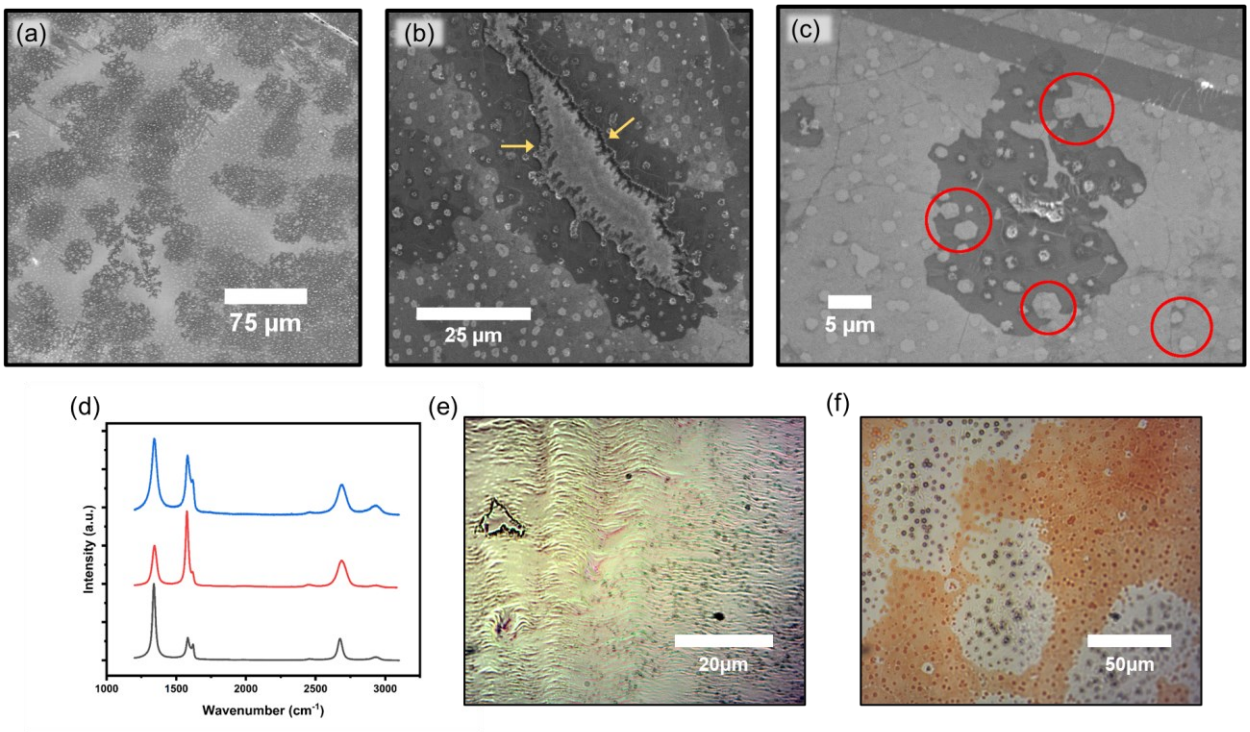
A recent report of intercalation growth of graphene domains beneath hBN on Cu substrates, using *acetylene*, did realise high quality graphene domains [142]. Here, depositions were separated (*two-step* process) and acetylene was only employed following hBN deposition, not during growth [142]. As a precursor for graphene growth on Cu, acetylene has increased surface diffusivity and mobility on Cu in comparison to methane [137, 138]. As such, no diffusion limited growth was observed and high quality hBN-Gr stacked heterostructures were formed. Importantly, acetlyne allowed for a quick graphene deposition time, such that the hBN domain was not etched [142].

With the high level of defects detected in Raman analysis of the $hBNC_3$ sample, the often desirable electrical properties of graphene on hBN stacked heterostructures, such as its high electron mobility and thermal conductivity [236], is likely degraded. Still, defects are beneficial in certain appplications. Previous work on vacancy defects in graphene have shown they provide enhanced, stabilised binding sites for adatoms such as Pt [237], Li [238, 239], Cu and Fe [240]. Similarly, substitutional doping of B and N into the lattice has previously also been shown to improve the properties of graphene materials in sensing [19], catalysis [241] and energy [3] applications, with the adatoms providing new bonding functionalities, modified electronic charge densities and even opening up a band gap in the graphene sheet. However, while the results presented in this section do provide an understanding of hBN-templated graphene growth on Cu using a *one-step* synthesis protocol, the economic viability of these stacked heterostructures is low. The highly defective nature of graphene has little use for the typical electronic applications of stacked Gr-hBN [242-244]. Highly doped or defective graphene does have applications in catalysis but can be synthesised from less costly and technical processing techniques than CVD, such as pyrolysis [2, 9, 10, 14, 17, 100-102] liquid phase exfoliation [21] or chemical exfoliation [245, 246]. By employing novel CVD techniques such as substrate alloying, or using a more mobile and reactive precursor such as acetlyne, the quality of graphene could be improved to increse the viability of this *one step* synthesis protocol towards electronics grade appications.

(iii) High partial pressures of CH_4 – Highly anisotropic, mixed-phase growth.

Upon further increase of the CH_4 partial pressure during synthesis, highly anisotropic growth is observed on the Cu substrate. SEM analysis of these structures can be seen below in Figure

62. Various phases with different contrast are observed, with the many competing growing domains. In Figure 62 (b), non- converged growth fronts of the film show irregular, dendritic growth at the edges, highlighted by the yellow arrows. The highly heterogeneous contrast of the region suggests many different forms of growth within the BCN system have occurred. The increased methane concentration likely allows for direct graphene deposition on the surface of Cu, which had previously been mediated from edge structures of hBN.



(g)

Spectrum	D peak (cm^{-1})	G peak (cm^{-1})	2D peak (cm^{-1})	2D FWHM (cm^{-1})	D/G	2D/G
Blue	1342.2	1583.2	2688.1	70.7	1.39	0.54
Red	1343.9	1578.2	2688.5	66	0.55	0.37
Black	1334.6	1580.8	2680.7	39.8	3.79	1.17

Figure 62; $hBNC_4$ sample - highly heterogeneous, mixed-phase character after 60 minutes of growth. SEM image (a) shows the variable composition of $hBNC_4$ on the Cu substrate. The darker contrasted regions are typically associated with being predominantly graphitic and carbon-based with hBN regions being lighter in contrast (b) Non- converged growth fronts of the film show similar dendritic growth at the edges (yellow arrows). The highly heterogeneously contrasted region suggests many different forms of growth within the BCN system have occurred. (c) brightly contrasted hexagonal domains are observed, highlighted by the red circles, suggesting some form of epitaxial relationship exists. (d) Raman spectra acquired at different regions of the $hBNC_4$ film could be grouped into three regions; highly defective, multilayered (blue), defective, multilayered (red) and highly defective, few-layered (black). (e,f) OM imaged of the $hBNC_4$ film on Cu pre (e) and post (f) oxidation. Different regions of the film oxidise at different rates, as seen by the varying contrast in colours from, yellow to dark orange, in (c). (g) Table showing the fitted peak values for spectra in (d).

Competing growth fronts between the graphene and hBN, disrupts the formation of crystalline hBN domains as well as the B,N precursors disrupting isotropic graphene growth. However, hexagonal domains are also seen, evidenced via the red circles in Figure 62 (c), suggesting that some epitaxial growth exists. The darker contrasted regions are typically associated with being predominantly carbon-based, as has been with previous samples, with regions comprised of hBN being lighter in contrast, however Raman spectroscopy showed no characteristic signs of hBN (Figure 62 d). Raman characterisation of the films showed a highly heterogenous character exhibiting regions of defective graphene with varying levels of defect density and layer number. Figure 62 (d) shows three spectra collected from different regions of the film on SiO_2. The spectra exhibit I_D/I_G and I_{2D}/I_G ratios varying from 0.55-3.79 and 0.37-1.17, respectively, showcasing various defect concentrations and heterogenous nature across the same film. No E_{2G} peak of hBN was observed during the analysis. At large enough methane partial pressures, graphene becomes the dominant growth, as characterised by Raman spectroscopy. These results are similar to those reported by Ci *et al.* where layers of hybridized boron nitride and graphene were synthesised under a pure methane and amino-borane environment (no H_2 or Ar) [141]. There, highly defective graphene regions were observed under Raman (shown in Figure 39, b), which they attributed to disorders and boundaries in the carbon network induced by hBN domains, and no hBN E_{2G} peak evident, similar to our results. Similar structures were also observed via SEM of hBCN structures grown via CH_4 flow and IBSD deposition from a hBN target [153], under the highest methane partial pressures. There, raman characterisation exibited a similar, highly defective nature. The mixed phase character of the film is also observed through analysis of the films resistance to oxidation. Figure 62 (e-f) shows OM images of the film on Cu before and after oxidation at 200°C for 2 minutes. The film is seen to oxidise preferentially under certain domains, which is likely to occur at sites with a higher density of grain boundaries and point defects [247].

TEM analysis of the film exhibited regions of widely contrasting layer numbers, shown in Figure 63. FFT analysis shows one section with three rotated hexagonal diffraction patterns, one of which is much higher in intensity than the others (red boxes). Other regions show FFTs with a multitude of rotated 6-fold diffraction patterns (orange, green), signifying a multilayered structure with high disorder and turbostratic nature. A magnified section of the layer boundary (blue) shows the moiré patterns formed on both sides of the adlayer growth. This is something also observed in Ci *et al.*'s study, where multiple adlayers were reported, also in turbostratic stacking [141], adding support to our observations, that the growth at higher methane partial pressures is comprised of highly heterogenous hybridized domains of boron nitride and graphene.

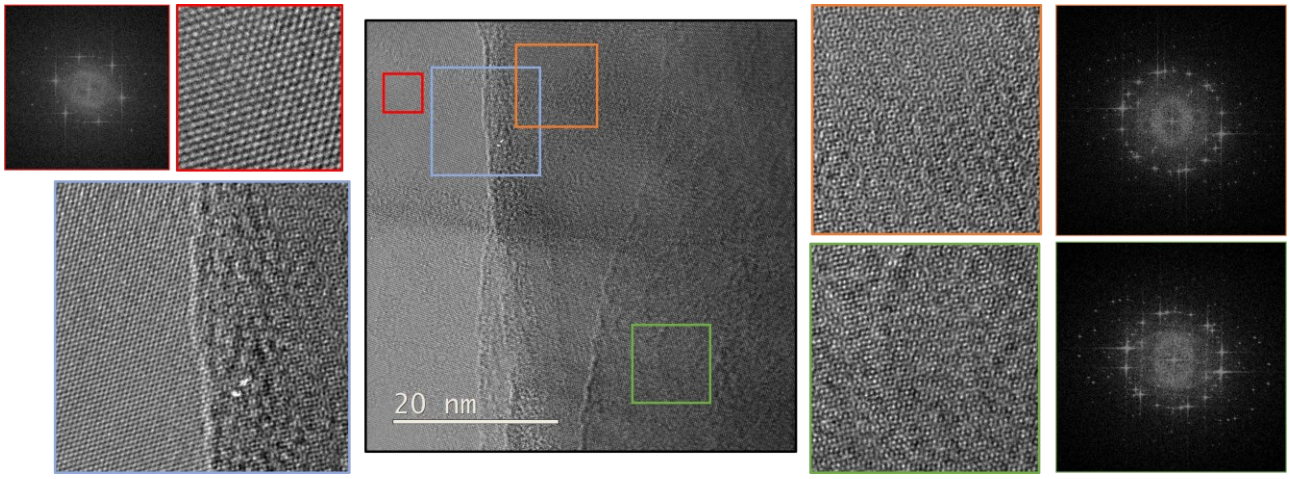


Figure 63; TEM analysis of $hBNC_4$ sample. Regions of multi-layered island growth are observed, indicated by the FFTs of each region. The red ROI produces an FFT with a single hexagonal pattern. Green and orange ROIs reveal FFTs with a multitude of hexagonal diffraction patterns, signifying highly turbostratic, layer-plus-island growth. The blue ROI shows the interface between the layer and 'island' growth.

XPS Chemical analysis of $hBNC_x$ samples

Chemical analysis of the films was carried out via XPS. The few-layer nature of the grown $hBNC_x$ sample makes XPS results extremely challenging to extract the atomic percentage of C doping in the film. The C peak, mainly comprised of the adventitious C signal, largely overshadows the B and N peaks in comparison and the few-layered nature of the samples

prohibits precleaning methods, such as ion sputtering of the material with an Ar beam, as this can introduce additional defects and dopants to thin films, making results unrepresentative [248]. However, this does not affect the general trend observed in the high resolution XPS spectra, where through peak fitting, changes in chemical environment can be distinguished and their relative contributions discerned.

The results of this analysis are summarised in Figure 64 below. The N1s, C1s and B1s spectra for each sample are overlaid in their respective plots to discern variations across samples in Figure 64 (a-c). Evidently, peak broadening is observed with increasing C precursor flow in each of the XPS spectra. This suggests the samples are less homogenous and crystalline with increasing methane partial pressures, as has been observed in our SEM results. By fitting peaks in each individual spectrum, the chemical bonding environments present in the sample can be distinguished. An example of fitted N 1s, C 1s and B 1s spectra for the $hBNC_2$ sample is shown in Figure 64 (d-f), respectively. In the N1s spectra, peaks are fitted as follows; N-B peak at 398 eV, N-$C_{pyrolic}$ peak at 399.5 eV. In the C1s spectra, the C-C peak is centred at 284.8 eV, C-B at 283.4 eV, C-N at 286 eV and C-O at 288.6 eV. The B1s spectra are fitted with peaks at 190.1 eV for B-N, ~191.2 eV for O-B-C related bonding, and 189.2 eV for B-C bonding [7, 9-11, 13, 17, 22, 23, 142, 150, 162]. All fitted XPS spectra for the samples can be found in Appendix Section 8.1.7.

Results of analysis of peak contributions, which together make up the whole spectrum of each sample, are summarised in bar charts in Figure 64 (g-i). Bonding in the N1s spectra show a clear increase in N-$C_{pyrolic}$ bonding upon carbon inclusion during synthesis, which increases with increasing methane partial pressure. In the highly anisotropic sample, $hBNC_4$, we also observe a peak for N-$C_{graphene}$. We see a more significant increase in % contribution from the N-C bonding peaks in the N1s spectra compared to the B-C peak % contribution in the B1s spectra, supporting our theoretical observations in Section 3.3.1, that the tendency of N atoms

to reside on the Cu surface and form N-terminated hBN islands may lead to increased N-C bonding in the structure. This observation holds for low CH_4 partial pressures, where no graphene nucleation occurs. At higher CH_4 partial pressures, for samples $hBNC_3$ and $hBNC_4$,

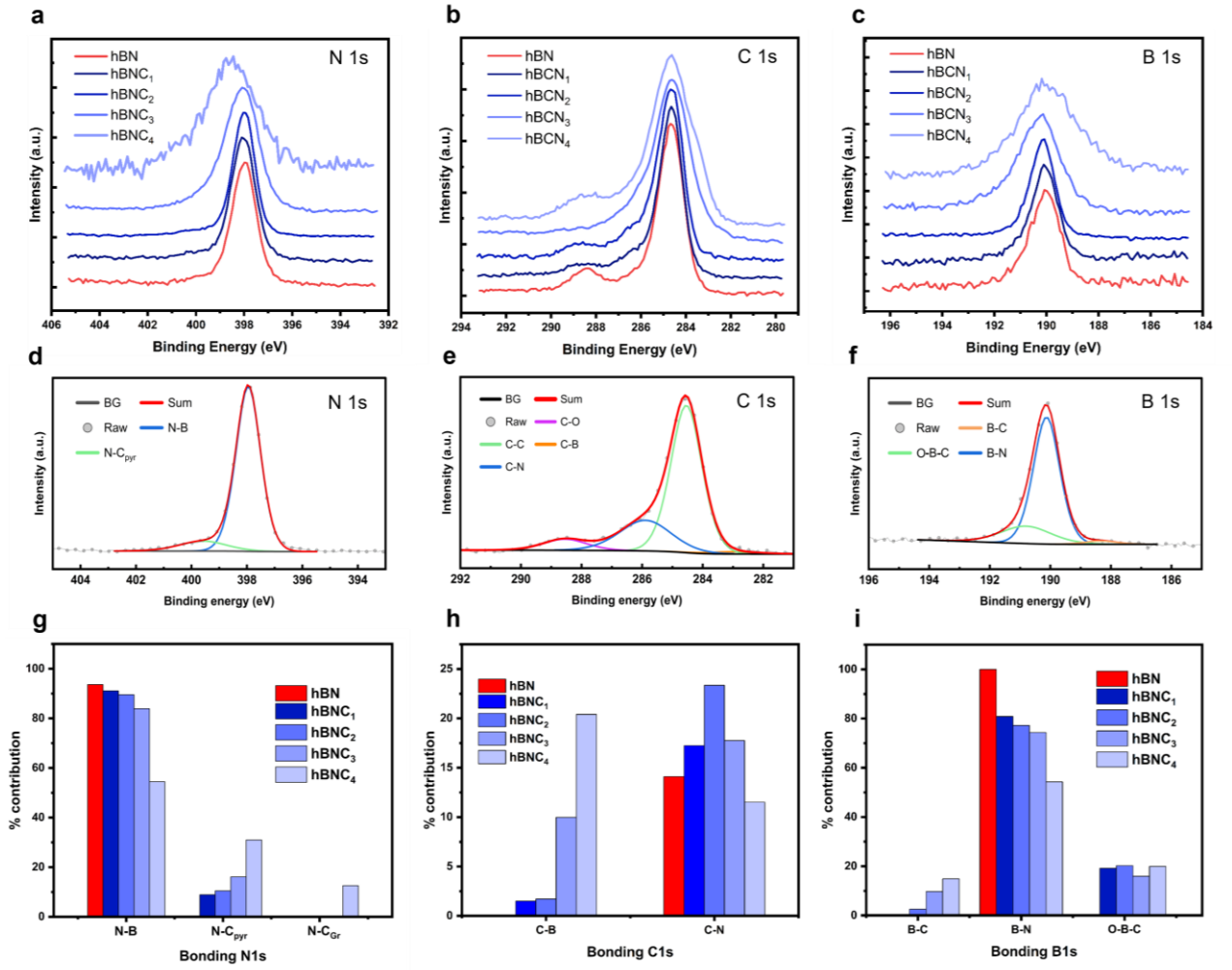
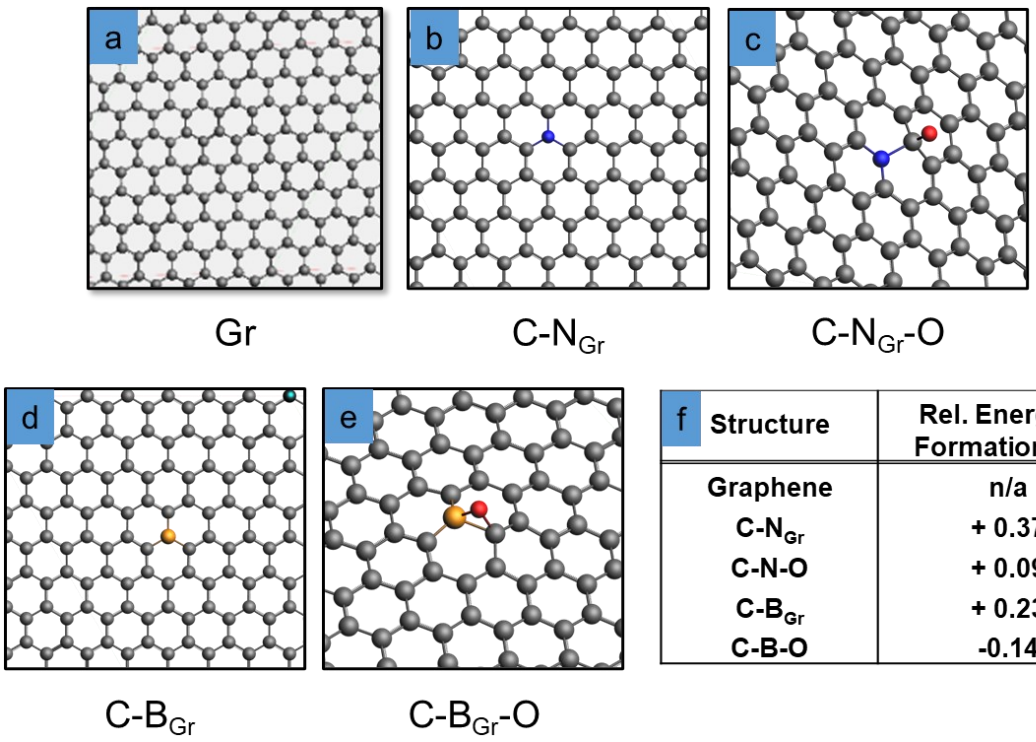


Figure 64; XPS characterisation of hBN and $hBNC_x$ samples. (a-c) Overlaid high resolution XPS spectra of the (a) N1s (b) C1s and (c) B1s regions for all samples. (d-f) Peak fitting of $hBNC_2$ sample (d) N 1s, (e) C 1s and (f) B 1s spectra. (g-i) Bar charts depicting the bonding contribution towards the overall spectra for bonding peaks in the (g) N1s (h) C1s and (i) B1s regions.

we observe considerably more B-C bonding, evident in both the C1s and B1s spectra, which suggests that the graphene domains observed are B doped. Conversely, the relative % contribution from the C-N peak in the C1s spectrum decreases as more B is incorporated. The reason for this is as follows; the initial edge-attachment of C structures to the N-terminated hBN domain leads to an increased N-C signal. At higher CH_4 partial pressures, graphene domains begin to nucleate and grow below hBN (as seen in Figure 60). From our DFT study

in Section 3.3.1, we know that N atoms preferably reside at the surface of Cu, while B and C atoms tend to penetrate the sub-surface. B and C atoms can thus more readily diffuse under hBN and form B-C structures in the growing graphene domain, leading to a larger B-C contribution in these samples. At highest methane flow, $hBNC_4$, we also observe a $N\text{-}C_{Graphene}$ peak contribution. Here, the methane concentration is high enough for graphene domains to deposit freely on the Cu surface, interacting with mobile surface N species, resulting in N-doped graphene, as well as B species, forming co-doped structures.

Another observation from the XPS analysis is the presence of oxide species in the doped hBN films, evident from the C-B-O bonding peaks in samples synthesised under methane flow. These peak positions in the B1s spectra do not match pure B-O bonding peaks ($\geq$ 192 eV [7, 13]) and are ascribed to C-B-O bonding peaks [9]. Such peaks are not found in the intrinsic hBN case, suggesting that B-C doping may introduce oxygen-related doping. The tendency for the boron moieties in hBN to react with oxygen and form boron oxide species has been discussed in Section 3.3.2 (in relation to irregular isosceles hBN growth), and this is likely enhanced with the introduction of other dopants and defects in the hBN film. In the case of graphene doping, DFT calculations on the enthalpy of formation of B and N doped graphene sheets (Figure 65) were carried out to better understand their relative stability in comparison to graphene, calculated using equation 22 in the methods section. Results show how boron doped structures form a stable oxide (- 0.14 eV w.r.t graphene) more readily than nitrogen dopant sites (+ 0. 09 eV w.r.t. graphene). Furthermore, in N-doped structures, the oxygen atom does not bond with the nitrogen, and instead bonds with the neighbouring carbon atom (N-C-O bonding not C-N-O). As such, it is believed that B-C related moieties in hBCN structures have a stronger tendency to react with oxygen species than N-C ones, as is evidenced also in our XPS studies.



f

Structure	Rel. Energy of Formation (eV)
Graphene	n/a
C-N$_{Gr}$	+ 0.37
C-N-O	+ 0.09
C-B$_{Gr}$	+ 0.23
C-B-O	-0.14

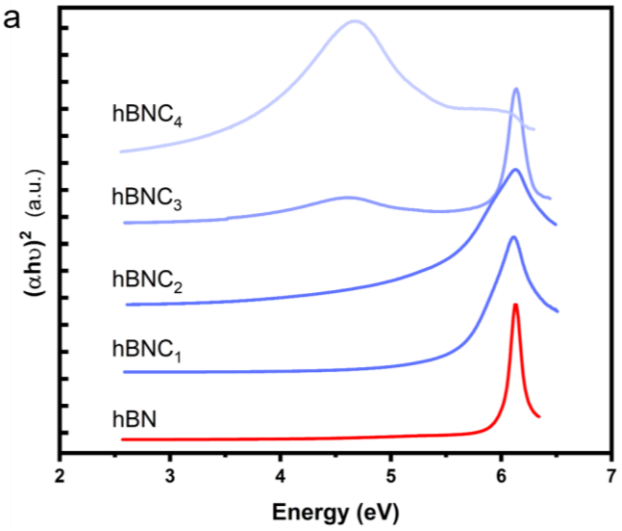
Figure 65; Geometry optimised structures of simulated (a) graphene, (b) N doped graphene (c) oxygenated N doped graphene (d) B doped graphene (e) oxygenated B doped graphene. (f) A table showing the relative energies of formation for each of the structures in comparison to graphene. In the case of N doped graphene, the oxygen atoms binds only with the neighbouring C atom, whereas in B-doped structures, the oxygen atom forms a stable structure bridging the B-C bond

Optical properties of hBNC$_x$ samples

After analysing the chemical composition of the hBCN films, their optical properties are investigated via UV-vis spectroscopy, with results shown in Figure 66. The Tauc plots are left in relative units only, as film thickness is not well specified for the samples, which still allows for the optical band gap to be determined [249]. The bandgap of intrinsic hBN is observed at 5.95 eV. With samples synthesised under low methane concentrations, the band gap is reduced significantly, by ~0.3 eV to 5.60 eV in sample hBNC$_1$ and ~0.5 eV to 5.42 eV in sample hBNC$_2$. This substantial reduction of the bandgap is observed alongside peak broadening, suggesting hBN crystallinity is reduced in these samples. In sample hBNC$_3$, where we observe graphene nucleating, a restoration of the bandgap of hBN to 5.90 eV is found, as well as the

emergenge of a peak around 4.6 - 4.7 eV, corresponding to the excitonic peak of graphene [250]. This is further enhanced in the sample with highest pp_{CH4}, $hBNC_4$, which is composed of a major excitonic graphene peak at 4.7 eV and a minor hBN peak whose bandgap is fitted at 5.41 eV (deconvolution of these peaks can be found in Appendix Section 8.1.6), indicating that this sample is primarily comprised of graphitic material with the presence of some segregated hBN domains. These results suggest that, initially, C introduced at low partial pressures is incorporated into the hBN lattice as point defects, reducing its crystallinity and its optical band gap. However, once μ_C is large enough for graphene domains to nucleate, these graphene domains acts as a carbon sink, preventing C adatoms' incorporation as point defects, and instead attaching to the growing carbon lattice, which is a more energetically favourable arrangement. This is supported by DFT observations made previously in this Chapter, whereby low energetic barriers to diffusion for B/C/N adatoms and high thermal energy at CVD synthesis temperatures result in highly mobile C adatoms that tend to find the most stable energy configuration on Cu; forming graphene structures instead of C point defects in hBN.

a



b

Sample	E_g (eV)	E_U (eV)
hBN	5.95	0.269
$hBNC_1$	5.60	0.823
$hBNC_2$	5.42	1.532
$hBNC_3$	5.89	0.613
$hBNC_4$	5.41	0.455

Figure 66; UV-vis spectroscopic characterisation of hBN and hBNC samples. (a) Tauc plots for all samples described in this section. (b) Table exhibiting the band gap energies and Urbach energies for each sample. Individual Urbach plots can be found in the Appendix. Samples synthesised under low pp_{CH4} show a significant reduction in bandgap and increase in Urbach energy.

This is also reflected in our analysis of the Urbach Energy which quantifies the level of energetic disorder in a sample [25, 170], as outlined in Section 2.8 of Chapter 2. These plots can be found in the Appendix Section 8.1.6 and their results are shown in Figure 66 (b). From these results, it is seen that Urbach energy increases with moderate C doping, below the graphene nucleation threshold, and that the incorporation of C atoms causes significant disorder (E_U of hBN is 269 meV whereas for $hBNC_2$ it is 1.532 eV). For samples $hBNC_3$ and $hBNC_4$, the Urbach energy is reduced upon graphene nucleation, suggesting that low quantities of C doping results in a significant degradation in crystallinity through point defect introduction, whereas concentrations resulting in graphene nucleation are less impactful with regards structural disorder in hBN. It should be noted that E_U for sample $hBNC_4$ is determined from the fit of the hBN absorbance peak, modelled using a Voigt function, (Appendix Section 8.1.6) and therefore the peak broadening might not be truly representative. It is also worth mentioning that the Urbach energies listed in Figure 66 (b) are significantly larger than those reported for traditional semiconductors (<100 meV). However, these are in line with other reports on E_U for BN and BNC materials [25, 251].

Conclusions on *in-situ* C doping of hBN on Cu

This is the first study to look at the effect of methane partial pressure during C doping of hBN. CH_4 was introduced during optimised hBN growth in an attempt to produce C doped hBN. Samples were synthesised with varying partial pressures of CH_4 flow to modulate the film properties. Results reveal that methane partial pressures must be carefully controlled and optimised for C doping of hBN. At low $p.p._{CH4}$, C doped hBN was synthesised and it is shown that the optical absoprtion properties of hBN could be effectively modulated. Through SEM analysis, samples with low pp_{CH4} were not seen to have drastically impacted morphology of the individual hBN domains, except for the observed nucleation of needle-like defective

graphene structures along hBN domain edges. Significant narrowing of the bandgap was observed in these samples (up to 0.6 eV), as well as well as broadening of the sub-band gap absorption tail.

However, there is a limit to the concentration of carbon that can achieve C doped hBN on Cu through point defect introduction. Above a certain threshold of $p.p._{CH4}$, graphene nucleation occurs and C adatoms are instead consumed by growing graphene domains. The hBN bandgap is unaffected by CH_4 inclusion, due to nucleated graphene acting as C sink for C adatoms and thus reducing the quantity of hBN point defects. Graphene structures extend inwards from needle-like growth regions nucleated along the hBN edges, suggesting that these are the first structures to form before templated growth occurs. These adlayers were characterised as defective graphene via Raman spectroscopy, likely due to vacancy defects resulting from the slow diffusion of C precursor below the hBN domain, as well as the presence of B dopants in the sheet, which is supported by XPS observations. Such a structure could have beneficial catalytic properties through introduction of functional defects. However, the economic viability of this synthesis method in comparison to other defect rich hBCN synthesis, such as pyrolysis, is low. Improvements could be made to the synthesis, such as the use of alloyed templates (Cu-Ni), or more mobile and reactive precursors, such as C_2H_4, to improve the quality of the graphene adlayer towards electronic grade applications. Typical procedure for stacked heterosturcture growth have employed *two-step* stages of growth. Here, templated growth of graphene on hBN domains was observed for the first time using a *one*-step process; simultaneous flow of BN and C precursors, aminoborane and methane.

At highest pp_{CH4}, highly anisotropic, mixed-phase growth is observed. Films consited of defective graphene with varying levels of defects and layer numbers, as determined via Raman spectroscopy and TEM. XPS analysis also showed this sample to have the largest B-C and N-C bonding contributions likely due to doped graphene depositing directly on the Cu surface.

At higher pp_{CH4}, there are several additional competing growth factors, such as individual graphene domain nucleation on Cu as well as the increased likelihood for multilayer nucleation, and a highly defective, heterogenous BNC sample is produced. Such a film is unlikely to have any attractive advantages over highly defective BNC formed via pyrolysis due to the higher cost and enginering controls required for the CVD process.

To conclude, C doped hBN is grown on Cu with a tunable optoelectronic character, as shown through our UV-vis observations. However, careful considerations are needed to employ this synthesis method in future – namely controlling carbon concentration at the surface of Cu in order to suppress graphene nucleation and thus promote C point defect inclusion. Future work could look at alloying the catalystic substrate to suppress graphene nucleation by increaseing C solubility and allow for enhanced point defect intercalation. Furthermore, the emission properties of such C doped hBN films should be investigated to validate observations made by Liu *et al*. [23], which reported enhanced SPE emission for C doped hBN. However, their study only looks at one data point for C doped hBN and so, further work is needed to establish a trend. C doped hBN has emerged as an interesting material to produce optically stable single photon emission (SPE) for quantum light generation but has traditionally been synthesised usind MBE methods or by ion implantation [22, 23, 55]. It would therefore be interesting for future work to use photoemission spectroscopy to look at the emission properties of C doped samples here, below the graphene nucleation threshold, as the UV-vis characterisation clearly identifies a trend in the modulation of the opto-electronic properties of hBN with increased carbon doping.

3.3.4. Multilayered hBN Synthesis on Pristine Iron

For many applications, thicker 2D materials are preferred over single layered growth. In the case of hBN, applications in electronic devices often require thicker hBN layers as a dielectric substrate, as too thin a layer can result in uncontrollable leakage currents [252]. Similarly, thicker hBN results in enhanced chemical resistivity and stability, in cases where hBN films act as protective coatings [253], and enhanced emission intensity in opto-electronic applications [254]. The low solubility of BCN precursors in Cu means growth is surface limited, and high quality, nm-thin 2D films are unachievable. Here, we investigate a different approach to avoid the surface mediated, self-limited growth by using a different growth substrate, iron (Fe), one with an enhanced solubility of B, C and N, and can mediate a precipitation growth mechanism, allowing for growth of thicker hBN and hBN-C films.

Iron is a cost-effective and widely available transition metal. Figure 67 gives details on some of its physical properties. At room temperature, it is found in the alpha phase and its unit cell is body centred cubic (bcc). Above 900˚C, the material undergoes a phase transition to its gamma phase, which is face centred cubic (fcc) and possess a much larger unit cell size. In this phase, iron possesses a much higher solubility towards B, C and N, by almost two orders of magnitude [255]. Another factor which plays an important role for segregation growth is the lattice mismatch between the grown adlayer and metal substrate. hBN and graphene show a minimal lattice mismatch with gamma iron, calculated as 0.87 % and 2.45 %, respectively (Appendix Section 8.1.7 shows this calculation). With alpha iron, the lattice mismatches are similarly small, at 0.77 % for hBN and 0.85 % for graphene. As such, Fe makes for an interesting substrate for multilayer hBN and hBN-C growth via APCVD.

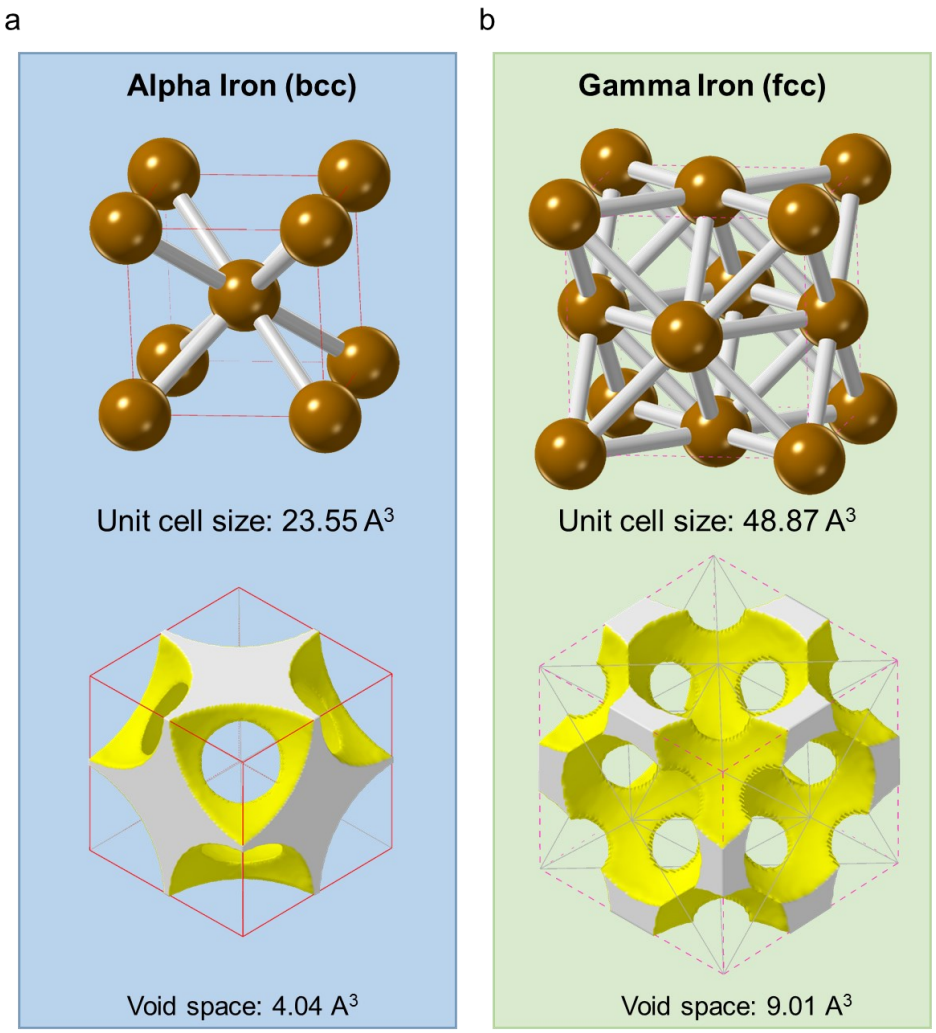


Figure 67; Structural properties of iron allotropes. (a) The unit cell of alpha iron is body-centred cubic (bcc) and is the phase found at RT (b) Above 910˚C, the crystal structure of iron changes to face-centred cubic (fcc), known as gamma iron. With this, there is a significant increase in unit cell size (24 vs 49 A^3) and void space (4 vs 9 A^3) which results in a significant increase in interstitial atom solubility.

Previous studies involving this growth substrate have focused on controlling the bulk reservoir of Fe to allow for *monolayer* growth. Caneva *et al.* studied the effect of H_2 and NH_3 pre-annealing on hBN growth and found that H_2 pre-annealing resulted in multi-layered hBN growth through the formation of iron borides (FeB_2) whereas NH_3 pre-annealing resulted in monolayer growth through the formation of iron nitrides [135]. Similar work on multi-layered hBN growth, this time using a $Fe_{82}B_{18}$ alloy found, through *in-situ* XRD analysis, that the formation of Fe_2B is the initial step in the synthesis of hBN products [168].

Currently, no studies have looked at hBN-C growth on Fe foils via segregation. A carburising *pre-treatment* on the Fe foil was studied by Babenko *et al.*, where C_2H_4 was introduced *prior*

to hBN growth with borazine. Their study found that carburising the Fe substrate allowed for enhanced hBN domain sizes, from 5 um to 25 um, which they attribute to the partial filling of Fe foils with C that reduces B and N solubilities and allows for enhanced surface mediated growth [256]. In contrast to our work here, the study does not introduce a carbon precursor *during* the synthesis to dope hBN and, as such, C doping of the hBN is likely quite low. Furthermore, the study does not characterise any chemical doping or opto-electronic effects of the C pre-treatment on hBN, only the effect of hBN domain size.

For the first time, a segregation-mediated growth method is used to synthesise multilayer hBNC films on Fe foils via APCVD using methane and ammonia borane as C and B/N precursors, respectively. Initially, the protocol for the growth of hBN films is optimised before then introducing the carbon precursor during growth. C introduction is interpreted via XPS and EDX analysis before characterising the opto-electronic properties of the films via UV-vis absorption measurements. I adopt another simple APCVD synthesis process, the stages of which are outlined in Figure 68; (1) the H_2 annealing stage to purify the Fe substrate and remove impurities like oxygen. This is carried out above the γ transition temperature of iron to ensure the substrate is in the γ-phase. (2) Exposure of Fe to the B/N/C precursors, ammonia borane and methane. The holding temperature at which this is carried out determines the relative solubility of the precursors which has implications on the final thickness of the film. (3) Controlled cooling of the substrate to 725 ˚C to allow for segregated growth of continuous films on the Fe surface.

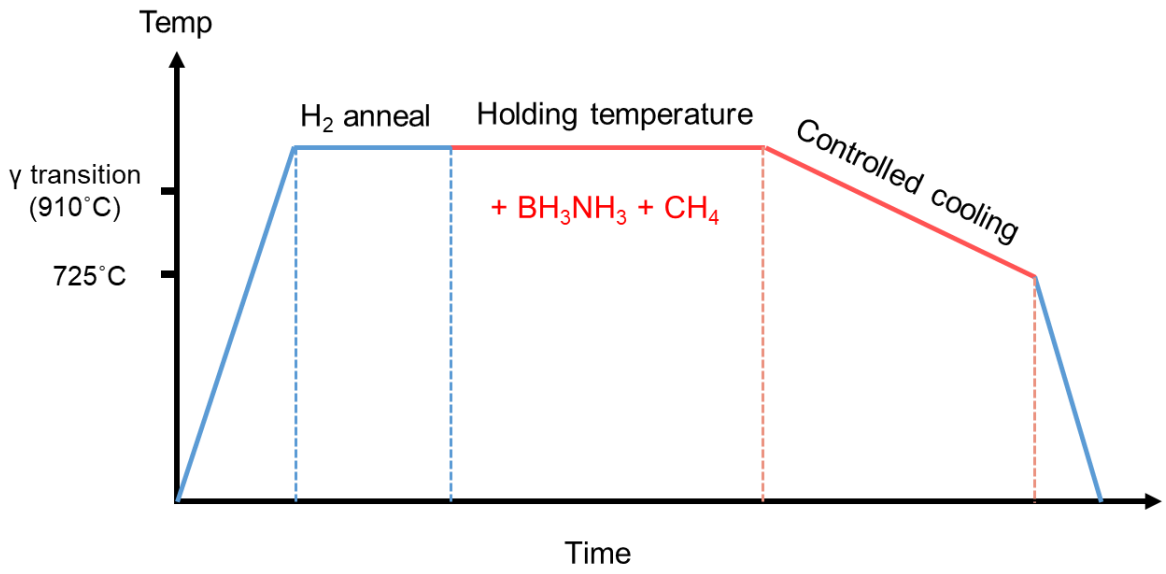


Figure 68; Schematic of the CVD process for segregated growth. Annealing the substrate above the γ transition temperature is carried out in H_2 prior to growth to ensure substrate is in the γ-phase, enlarge domains and also remove impurities from the growth substrate. Precursors are introduced at the set holding temperature for a set period. Afterwards, the substrate is cooled to 725 ˚C at a set cooling rate to allow hBN to precipitate on the surface of the Fe foil.

Cooling rate optimisation

Initially, the cooling rate was investigated for the growth of multilayer hBN, which has previously been shown to drastically affect hBN deposition on Fe [113, 114]. It was found that fast cooling rates resulted in the formation of individual hBN domains. By rapidly cooling the substrate, the interstitially doped atoms have little time to precipitate to the surface and form extended domains and are essentially 'frozen' in the substrate. Figure 69 (b) shows a schematic of the precipitation process. Controlling the cooling process at a lower rate allows for atoms to diffuse and precipitate more readily at the surface and growth of a continuous hBN film can be achieved [113]. Figure 69 (a) shows SEM images of hBN coverage from a cooling rate of (i) 200˚C min^{-1} (furnace shifted) (ii) 25˚C min^{-1} (iii) 10˚C min^{-1} (iv) 5˚C min^{-1}. The percentage coverage of hBN on the Fe surface increases from below 40% to almost 100% when a slow cooling rate of 5˚C min^{-1} is applied. This cooling rate was then chosen for the remaining experiments. Figure 69 (d) shows an exemplary spectrum of the hBN sample grown on Fe, with a clear E_{2G} peak of hBN visible.

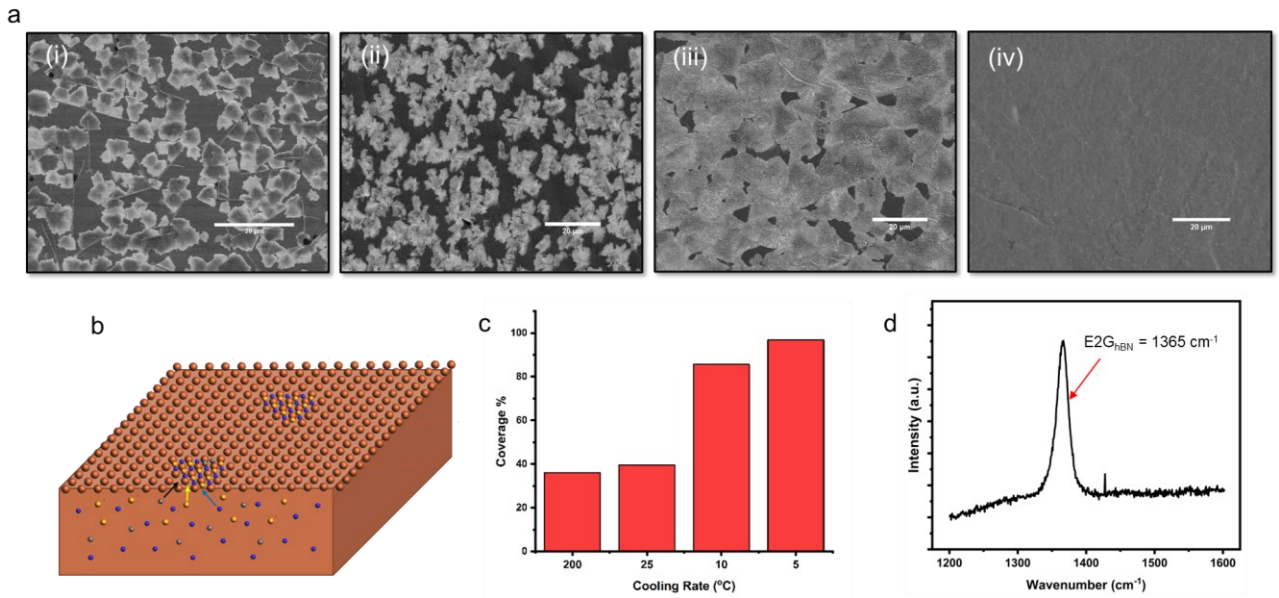


Figure 69; Influence of cooling rate on film coverage. (a) SEM images showing the effects of cooling rate on growth coverage (i) 200˚C min^{-1} (furnace shifted) (ii) 25˚C min^{-1} (iii) 10˚C min^{-1} (iv) 5˚C min^{-1}. (b) Schematic of the segregated growth process for multi-layered films on the surface of Fe. Islands form as interstitial atoms are forced out from the bulk upon cooling. (c) Chart showing the percentage coverage of the Fe surface with hBN for the various cooling rates. (d) Exemplary Raman spectrum for hBN samples grown on Fe showing a clear E_{2G} peak of hBN at 1365 cm^{-1}.

Holding rate optimisation

The effect of the holding temperature at which Fe is exposed to ammonia borane is also investigated (Figure 70). At higher temperatures, the solubility of precursors is increased, allowing for increased filling of the bulk reservoir of Fe. As cooling proceeds, there are essentially more atoms being expelled towards multilayer growth and thicker hBN films are achieved. Four holding temperatures were investigated: 1100 ˚C, 1000 ˚C, 950 ˚C and 900 ˚C. At higher temperatures of 1000 ˚C and 1100 ˚C, thick 200 – 300 nm hBN films were realised which shown a large variation in height across the film (Figure 70, a-b). Due to the enhanced structural stability of the thicker films, no PMMA scaffold was needed during the removal of the Fe growth substrate, and large area, continuous hBN films were easily delaminated via etching (shown in Appendix Section 8.1.8). At 950 ˚C, a dramatic decrease in film thickness was observed, as films of <20 nm were formed. A lower holding temperature means a lower

solubility of hBN precursors in the bulk, resulting in thinner films. Films here were measured with a thickness of 15.9 +/- 4.2 nm.

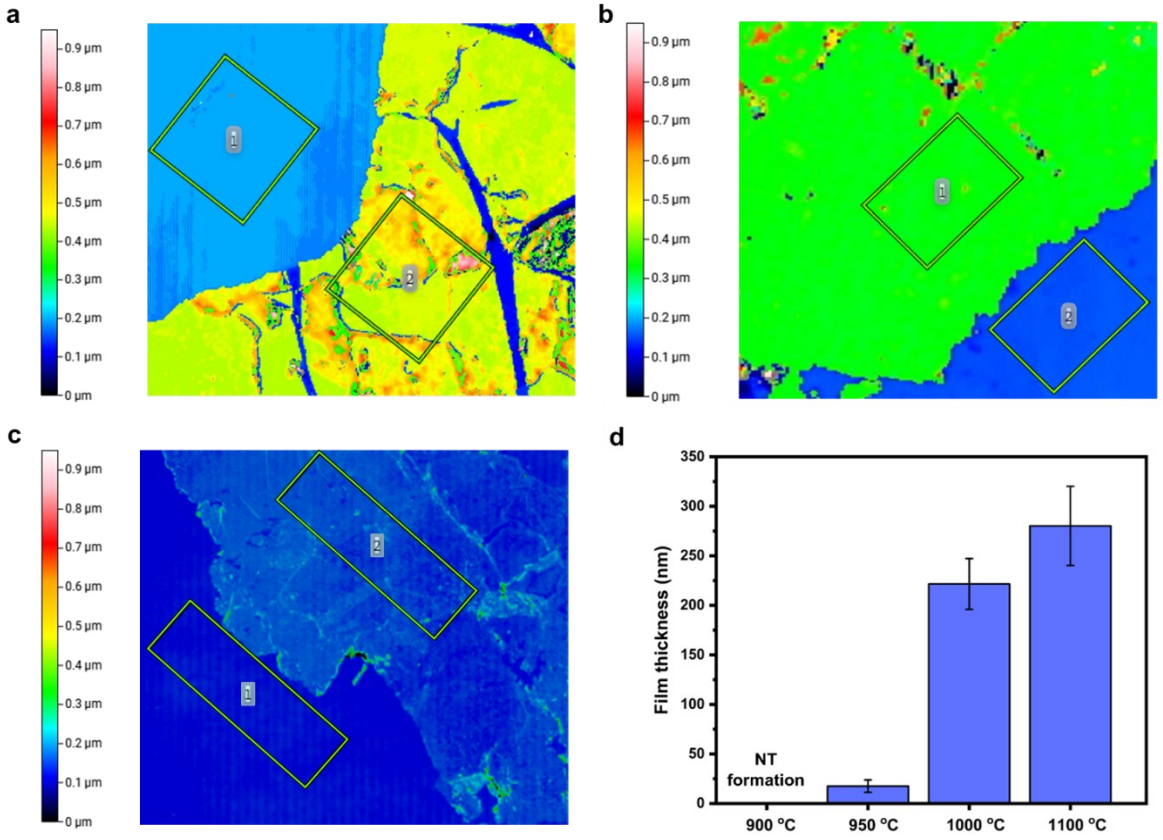


Figure 70; Influence of holding temperature on film thickness. (a) Optical profilometry measurements on hBN films transferred onto SiO_2/Si substrates for films synthesised using holding temperatures (a) 1100 ˚C, (b) 1000 ˚C, (c) 950 ˚C.

Interestingly, at temperatures of 900 ˚C, 1D nanotubes of hBN were grown on the Fe surface. At this temperature, Fe is just below the transition temperature for the formation of γ-iron. As it comprised mostly of α-iron, which has different unit cell properties, resulting in the nucleation of 1D structures rather than 2D films, shown below in Figure 71. Figure 71 (a) shows an SEM image of the Fe foil surface coated with nanotubes. Tubes do not show any preferred growth orientation and exhibit a buckled morphology. A clear signal form the E_{2G} peak of hBN is observed at 1365 cm^{-1} in Raman spectroscopy and the band gap of the nanotubes was calculated to be 5.46eV via UV-vis characterisation.

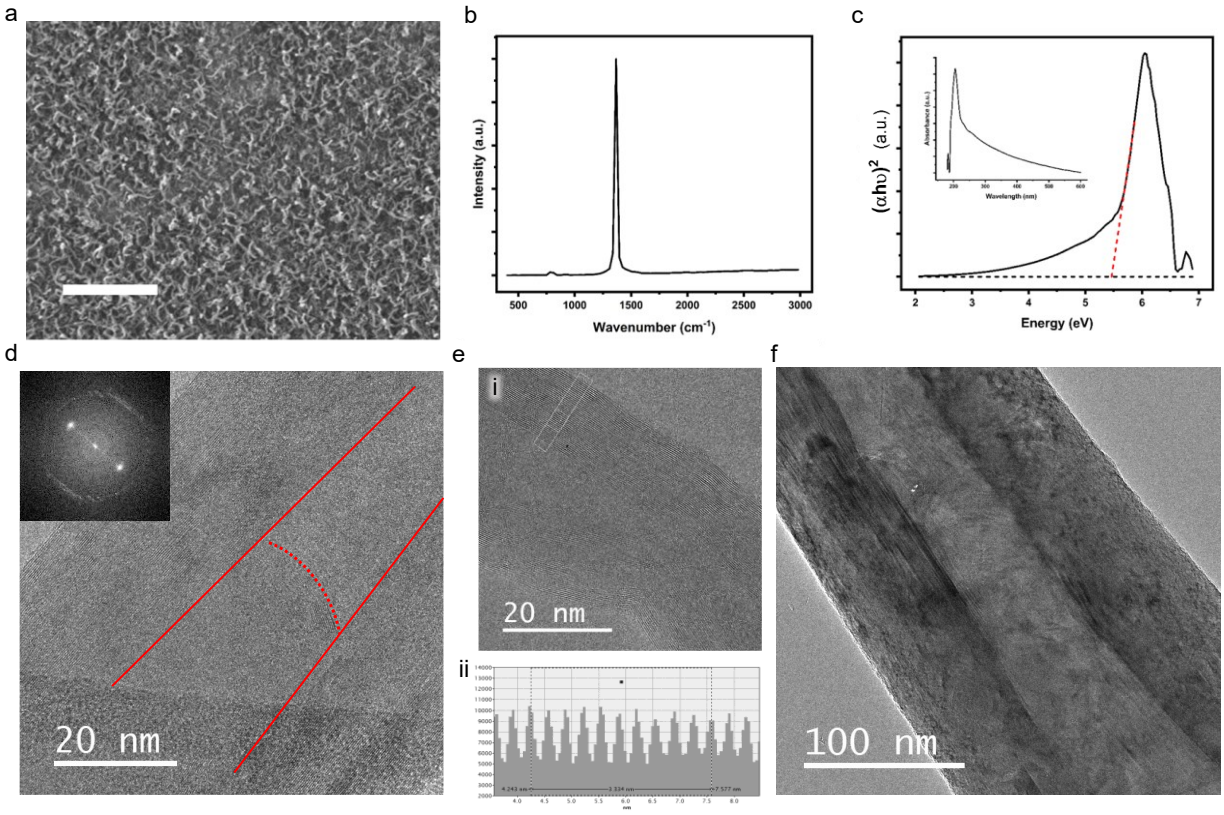


Figure 71, Characterisation of BNNTs formed on Fe foil. (a) SEM image showing the bundles of nanotubes formed on the surface of the Fe foil at 900 ˚C holding temperature. Scale bar is 10 µm. (b) Raman spectrum of material collected in (a). The E_{2G} peak of hBN is clearly identified and shows a strong signal. (c) UV-vis characterisation of BNNTs; the Tauc plot shows a bandgap of 5.46 eV with a broad absorption tail. Absorption plot is inset. (d) TEM characterisation of BNNT formed on Fe foil. Tubes show a bamboo morphology where 'caps' form periodically in the centre of the tube. Inset is the FFT pattern, where distinct spots are observed from reflections along the hBN c-axis. (e) Interlayer spacing of BNNT tubes is calculated at 0.333 nm. (f) Large multilayer tubes of the order of 200 nm were also observed, suggesting growth is not homogeneous and uniform.

TEM analysis revealed the tubes possess a multi-layered structure and bamboo morphology. A wide variance in tube diameter was also observed, with tubes ranging from 80 – 200 nm in diameter. At 900 ˚C, Fe is is still partially in its α phase, and solubility is thus low. This likely resulted in nanotube nucleation on the surface of the foil rather than diffusion into the substrate and controlled sequestration to form layered growth. Previous reports on BNNT growth using an iron growth substrate used similar synthesis temperatures of ~900 ˚C but required the use of toxic and difficult to handle precursors such as B_2H_6 and NH_3 or high end techniques such as MBE [257]. Here, we report a non-toxic method for MW BNNT growth on Fe foil substrates using ammonia borane as the precursor.

3.3.5. Carbon doping of hBN films grown on Fe

Having tailored the synthesis parameters to achieve continuous, multilayer-thick hBN films, we then focus on introducing carbon during the synthesis, in the form of CH_4, to dope the hBN structure and modify its properties. Table 2 details the gas flow composition for these experiments. Samples were first annealed at 1100 ˚C under pure H_2 for 1 hour. For each run 300 mg of ammonia borane was used, heated at T_{AB} = 80 ˚C. The holding temperature and cooling rate were set at 950 ˚C and 5 ˚C min^{-1}, respectively. In contrast to the distinctive graphene and hBN regions observed in C doping of hBN on Cu, SEM analysis showed no observable differences in hBN-C films grown on Fe (SEM micrographs can be found in Appendix Section 8.1.9).

Table 4; Gas flow composition for C doped hBN samples synthesised on Fe foil

Sample	CH_4 sccm	H_2 sccm	Ar sccm	CH_4/H_2 ratio
hBN	0	40	360	-
$hBNC_3$	3	40	357	1 : 13.3
$hBNC_6$	6	40	354	1 : 6.7
$hBNC_{10}$	10	40	350	1 : 4

XPS analysis was carried out to investigate the chemical composition of the samples. Figure 72 shows a stacked plot of the high-resolution spectra for the (a) B1s, (b) C1s and (c) N1s regions for each sample. What is immediately noticeable is the overall peak broadening in the B1s and N1s spectra, for the C doped samples in comparison to the intrinsic hBN sample suggesting a reduction in hBN homoegeneity and crystallinity. From peak fitting of the individual spectra of sample $hBNC_6$ (Figure 72, d-f), we can deconstruct the various bonding environments present in the sample. Three peaks can be identified in the B1s spectrum, located at 189.8 eV, 190.3 eV and 191.4 eV, which we attribute to B-C, B-N and O-B-C bonding in the sample [7, 9, 13, 150, 258]. The O-B-C bonding peak falls below that of pure boron oxide (>192 eV) and so we attribute this peak to O-related defects of B-C which arise under increased

methane flow [258]. Five peaks are used to fit the C1s spectrum; peaks at 288.6 eV, 286.2 eV, 285.6 eV, 284.8 eV and 283.9 eV, which are attributed to C=O, C-O, C-N, C-C and C-B bonding resectively in the samples [7, 9-11, 13, 17, 22, 23, 142, 150, 162]. In the N1s spectra, three peaks are fitted; N-B peak at 398 eV, N-$C_{pyridinic}$ peak at 398.8 eV and an N-$C_{pyrrolic}$ peak fitted at 400.1 eV [10, 11, 23, 150]. Individual peak fitting for each sample is available in Appendix Section 8.1.10.

Relative contributions of the deconvoluted peaks in the various XPS spectra are summarised in Figure 72 (g-i). In the B1s spectrum, broadening is attributed to contributions from B-C and O-B-C peaks which tend to increase with increasing CH_4 flow. Similarly, in the N1s spectra, N-C and oxide related N-C bonding sites contribute to the broadening. The * mark above the N-$C_{pyrrolic}$ peak of hBN is to note that this peak can also be ascribed to N-H bonding, which may explain why hBN contribution for this peak is larger than the $hBNC_3$ and $hBNC_6$ samples [150]. The C1s spectra show a significant contribution from C-B and C-N bonding peaks, increasing with relative CH_4 flow, signifying C doping in the hBN network. At the same time, C-O and C=O bonding peaks decrease, likely due to increased signal from intercalated carbon regions rather than adventitious C species (adventitious carbon is generally comprised of a variety of relatively short chain hydrocarbons with small amounts of both singly and doubly bound oxygen functionality). Due to the nature of the hBN films being thicker, atomic % of B, C, N and O in sample could be more accurately determined via XPS (Figure 72, d). With increasing CH_4, more carbon is detected in the samples. Across all samples, atomic % of B is larger than that of N, even in the intrinsic hBN case, suggesting a material with many N vacancies. This is further supported by the more apparent trend in increased B-C and O-B-C bonding in the deconvolution of the B 1s spectra with increasing CH_4 flow, which is less apparent in the N 1s spectra. Overall, the incorporation of C is not linear with increasing CH_4 flow; significant incorporation of C is achieved with the lowest methane flow profile, which

increases only slightly with increasing methane partial pressures. Furthermore, a larger atomic % of oxygen is detected with higher methane flows and C doping. In the deconvoluted spectra, we see how O defects species are likely B-related, similar to XPS analysis of hBN-C on Cu in Section 3.3.3.

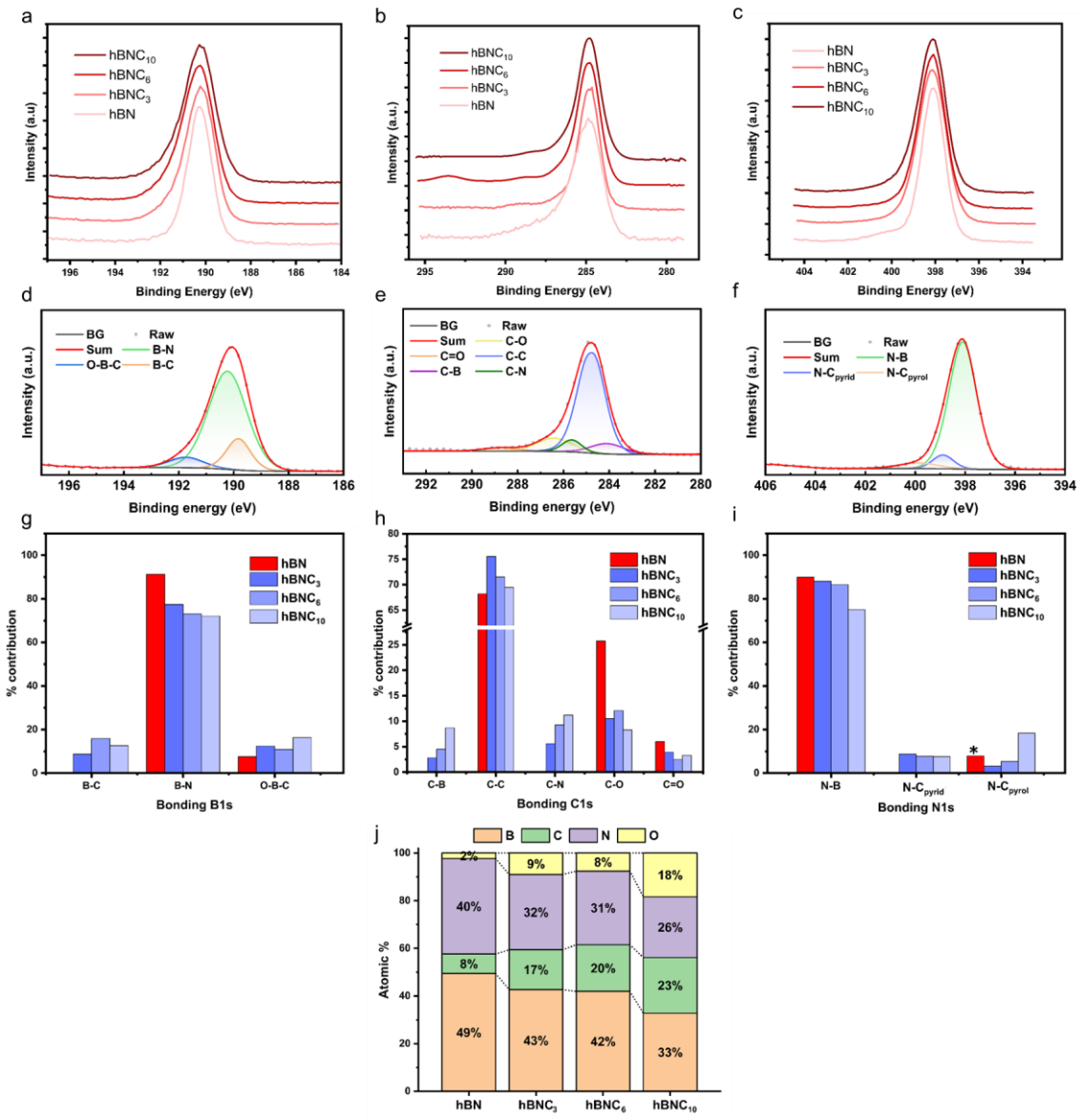


Figure 72; XPS analysis of hBN-C grown on Fe. (a) B1s (b) C1s and (c) N1s overlaid spectra of hBNC samples synthesised on Fe. (d-f) Peak fitting of $hBNC_6$ sample (d) N 1s, (e) C 1s and (f) B 1s spectra. (g-i) Summary of bonding contributions of the (g) B1s (h) C1s and (i) N1s peaks for each sample. (j) Atomic % of elements in each sample as determined by XPS

EDX analysis on the intrinsic hBN sample vs the $hBNC_6$ sample was also carried out to verify some of our XPS observations, shown in Figure 73. The EDX spectrum of each sample is

available in Appendix Section 8.1.11. In both samples, aluminium and oxygen is detected, presumably Al_2O_3 impurities that precipitate from the Fe substrate. Boron is more difficult to detect via EDX and so its relative atomic % is lower than that of N, converse to our XPS results. We observe an increase of C atomic % of 4.9 % to 16.1% from the hBN to $hBNC_6$ sample, an increase of 11%, similar to the atomic % deduced from XPS analysis. The at. % of oxygen in the C doped hBN sample does not increase between samples, differing from our XPS analysis, suggesting oxygen impurities detected via XPS are located at the surface of the film.

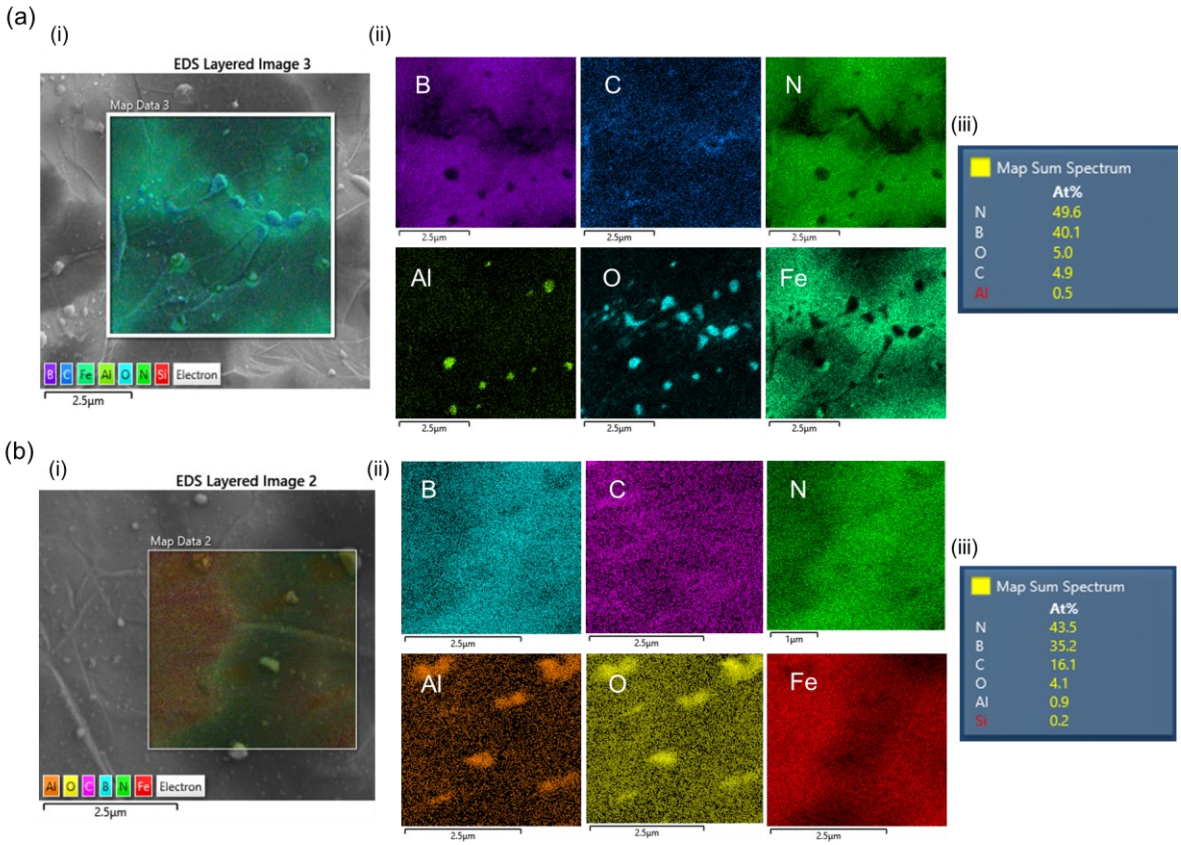


Figure 73; EDX analysis of (a) hBN and (b) $hBNC_6$ on Fe. (i) Region of interest taken for EDX maps. (ii) Atomic map data for B, C, N, Al, O and Fe for the ROI in (i). (iii) EDX calculated atomic % data with the Fe content removed. Al and O impurities are observed in both samples, presumably coming from the Fe foil. Relative C content increases by ~ 11% in the C doped sample.

Such surface defects could be beneficial in catalysis applications. Previously, B_xO_y defects on the surface of a Fe/BN catalyst have been harnessed to tune the activity in the Fischer-Tropsch reaction [259]. In this study, calcination in air for 12 hours was carried out to prepare the

material with B-O surface defects. Here, a simple CVD method could be used to introduce surface defects into hBN during its synthesis.

TEM characterisation was carried out on the same samples to look for any structural variation and loss in crystallinity after carbon doping. Both samples exhibited turbostratically stacked regions as determined via FFT analysis (Figure 74, a, c). Edge analysis of the hBN sample (Figure 74, b) showed regions of thickness ~ 6 nm with lattice spacings characteristic of hBN (0.34 nm). Figure 74 (d) shows a fold in the $hBNC_6$ sample, of size 13 nm, suggesting a similar thickness in the film of ~ 6 nm. As such, samples of hBN and carbon doped hBN show similar thickness and crystallinity at the nanoscale, as determined by TEM.

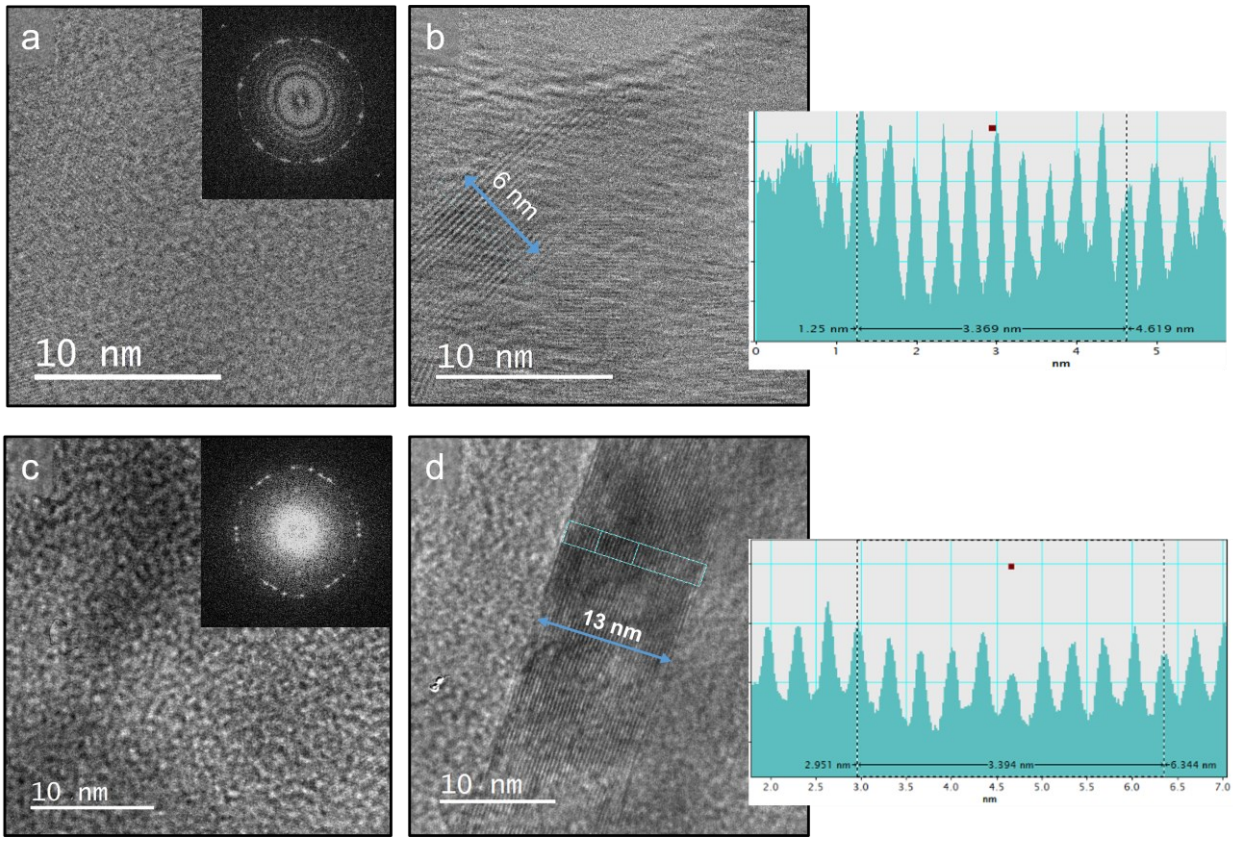
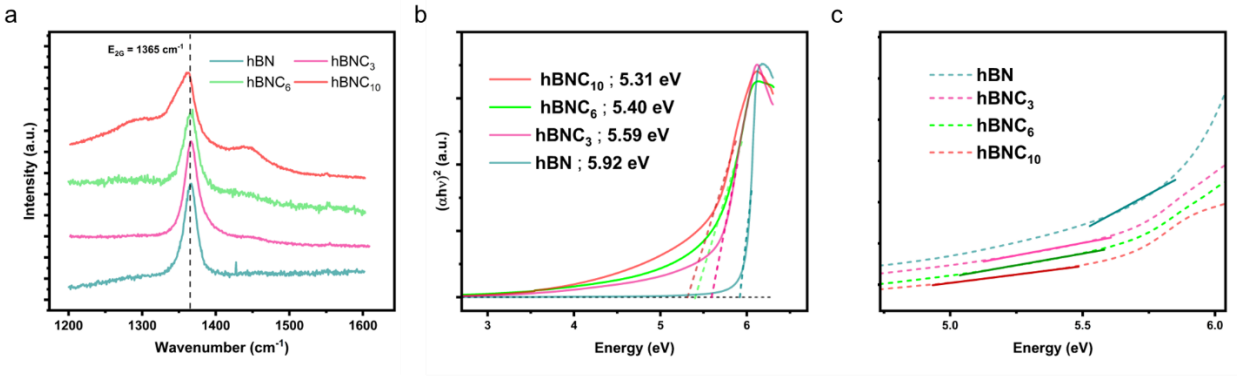


Figure 74; TEM analysis of hBN and $hBNC_6$ samples. (a) TEM image of the hBN sample with FFT inset showing a region of the film with turbostratic stacking. (b) Edge analysis of the hBN film showing a thickness of 6 nm. The line profiles of the ROI is inset below and shows an interlayer distance of 0.34 nm. (c) TEM image of the $hBNC_6$ sample with FFT inset showing turbostratic stacking (b) TEM image of a fold in the $hBNC_6$ film, measured at 13 nm. Inset is a line profile of layers in the fold. The interlayer spacing is measured to be 0.34 nm.

Raman spectroscopy of the intrinsic and C doped hBN films on SiO_2/Si was performed to study the effects of C introduction on the microstructure of the hBN films. Figure 75 (a) shows the Raman spectra for each of the samples, with peak centres and FWHM reported in Figure 75 (d). The typical E_{2G} peak of hBN is observed in all samples, centred around 1365/1366 cm^{-1} apart from the highest doping $hBNC_{10}$, where the peak is red-shifted to 1359 cm^{-1}. Similarly, the FWHM of the E_{2G} peak show little variance apart from the $hBNC_{10}$ sample whose FWHM increases by 10 cm^{-1}. Our Raman analysis reveals little degradation in crystallinity in samples $hBNC_3$ and $hBNC_6$. However, sample $hBNC_{10}$ shows deviation from the rest with significant red-shifting of the E_{2G} peak centre and increased FWHM, suggesting degradation of crystallinity in the material. Similar broadening and red-shifted features were observed in carbon doped hBN devices grown via IBSD with highest CH_4 flow rate, which they attribute to the reduction of crystallinity from C incorporation (shown in Figure 39, a) [25].



d

	Bandgap (eV)	Urbach Energy (eV)	E_{2G} ω_o (cm^{-1})	E_{2G} FWHM (cm^{-1})
hBN	5.92	0.58	1365.4 ± 0.4	17.7 ± 0.4
$hBNC_3$	5.59	1.67	1366.4 ±0.9	18.7 ± 1.8
$hBNC_6$	5.40	1.77	1365.3 ± 0.3	18.3 ±2.6
$hBNC_{10}$	5.31	2.453	1359.1 ± 6.8	25.2 ± 4.1

Figure 75; Opto-electronic characterisation of hBNC samples synthesised on Fe foils. (a) Raman spectra for hBNC samples. The dashed line shows the E_{2G} wavenumber of hBN at 1365 cm^{-1}. (b) Tauc plot used to determine the optical bandgap of each sample. A clear trend of lowering of the bandgap with increased CH_4 flow is observed. (c) Urbach energy plots showing the straight line regions used to determine E_U. Urbach energies for the samples rise with increasing C doping (d) Table exhibiting results of the opto-electronic characterisation of hBNC samples grown on Fe.

UV-vis spectroscopy was carried out on films transferred onto z-cut quartz optical substrates to determine the optical absorption of the materials. Figure 75, (b) shows the Tauc plot for each

sample. All samples exhibit a similar sharp absorption peak around 200 nm with almost no absorption within the visible range (1.5 – 3.1 eV). Peak broadening is observed in all C doped samples, comparable to the lightly doped hBN samples in the previous section on C doped growth on Cu. Significantly, no π-plasmon absorption peak of graphene is observed, as was the case for higher pp_{CH4} synthesis of C doped hBN on Cu. A reduction in the overall bandgap is also observed from 5.92 eV for the intrinsic hBN sample down to 5.31 eV in the $hBNC_{10}$ sample. Increased peak broadening is also observed with increasing carbon content. The Urbach energy was calculated to assess the structural and compositional disorder of each sample, the plots of which are shown in Figure 75 (c). As can be seen from table in Figure 75 (d), with increasing carbon concentration, there is an increase in Urbach energy, suggesting once more that the inclusion of carbon reduces both the band gap and crystallinity of the hBN material.

In previous reports on C doping of hBN synthesised via IBSD, a similar reduction in bandgap and increase in Urbach energy is observed which resulted in a significant improvement of the DUV photo-detection properties of the hBN-C device [25]. Similarly, C implantation in hBN has been shown to introduce single photon emitters (SPEs) via MBE, MOVPE and ion implantation techniques[22, 23, 260]. This synthesis method demonstrates a simple and cost-effective method of producing C doped, multilayer hBN in a controlled manner via APCVD using non-toxic and readily handled precursors, ammonia borane and methane. Notably, graphene nucleation is not observed with sysnthesis on Fe, suggesting that this is suppressed, allowing for a more tractable method of synthesising C doped hBN films. Furthermore, films synthesised on Fe are thicker, meaning they are more durable than mono or few layered hBN, and have an enhanced absorption cross section, properties which have implications when applying this material in optoelectronic devices.

3.4. Conclusion, summary and outlook;

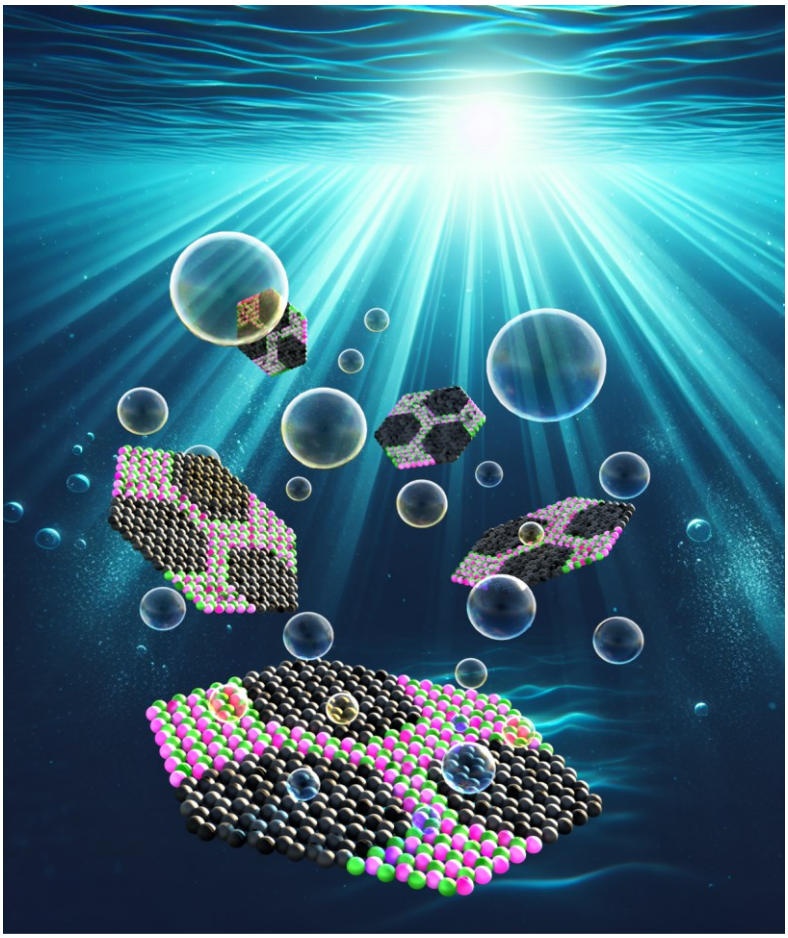
The main objectives of this chapter were to investigate APCVD growth of 2D "C doped" hBN (hBN-C) materials on Cu and Fe metal foils. A versatile method for producing 2D hBN-C structures is presented based on non-toxic, safe to handle precursors and industry scalable CVD processes. On Cu, this work reported different forms of nucleation and growth of hBN-C structures under increasing C precursor flow. At low methane partial pressures, C doping of the hBN film could effectively be achieved, and its electronic band gap was reduced by up to 0.5 eV. We attribute this to a loss of crystallinity in the structure with C point defects introduced to the hBN lattice. At higher pp_{CH4}, graphene domains intercalated below hBN were observed, nucleating from the dendritic graphene regions at hBN edges and extending underneath the hBN domain. The graphene is characterised as being highly defective via Raman analysis. This is likely due to vacancy defects arising from the slow dissociation and diffusion of C species below the hBN domain, as well as the occurrence of B doping. Boron can dope the growing carbon domain due to its enhanced ability over N to penetrate and diffuse in the Cu sublayers (similar to C), as determined via DFT calculations. As such, vertically stacked defective graphene / hBN heterostructures on Cu are reported for the first time by *simultaneous* introduction of BN and C precursors, aminoborane and methane. However, the highly defective nature of the graphene likely limits the economic viability of this synthesis method. Future work could consider the choice of precursor and substrate engineering to improve the graphene quality towards electronics grade application. More reactive and mobile C species like C_2H_4 would reduce the occurrence of vacancy-like defects due to its enhanced mobility on the Cu substrate. In a similar vein, alloyed substrates, such as Cu-Ni, allow for tailorable properties of the growth catalyst, such as precursor solubility and diffusivity, extension of the synthesis

temperature range to improve reaction times, as well as the overall catalytic activity of the growth substrate, which can improve the quality of heterostructures grown.

Fe foils were also trialled as a growth substrate for C doped hBN, allowing for multilayer films to be synthesised. Synthesis of hBN on Fe was strongly dependent on the cooling rate - to ensure extended coverage, a slow cooling rate was necessary, which allowed for slow precipitation of interstitial interstitial atoms from the bulk. The holding temperature for bulk reservoir filling was also an important parameter, influencing the thickness of the resulting films. C doping of hBN on Fe was investigated by means of CH_4 introduction during optimised hBN synthesis. In contrast to growth on the Cu substrate, no graphitic precipitation was observed via SEM, Raman and UV-vis analysis, even under highest methane flow, suggesting a more tractable method of synthesising C doped hBN using this substrate. Analysing the optical properties, incorporation of C resulted in a lowering of the materials bandgap from 5.92 eV to as low as 5.31 eV at highest methane flow, with no optical signature of graphene being observed, unlike with growth on Cu. These results are the first to report modulation of the hBN bandgap by C doping of hBN films synthesised on Fe substrates. These observations also suggest that graphene nucleation is suppressed in segregation-mediated growth on Fe, making it an attractive growth substrate for hBN-C material system for future optoelectronic devices.

Chapter 4

2D Phase Separated Graphene/hBN toward catalysis: a DFT Study



4.1. Introduction

hBCN as a catalytic material is still at an early stage of its development, with the relationship between atomic design and catalytic activity of the materials yet to be fully understood. This is partly due to the wide variety of bonding iterations the material can have, as well as the lack of practical knowledge regarding the distribution of B, C and N within synthesised hBCN materials. This wide range of permutations within the hBCN network also imparts a high degree of tunability with regards the material's physical properties, based on two principal factors: the atomic proportion of B, C and N in the structure and, secondly, the distribution of atoms throughout, giving various possibilities of B–C, B–N, C–C, and N–C bond formation.

To better understand the relationship between the structure of hBCN and its properties, theoretical investigations have focused on the atomic arrangement within the material, often exploring highly entropic and exotic 'homogenous' hBCN systems which offer exciting properties, such as ultra-low bandgaps [78, 82, 84, 88-90], but are difficult to realise experimentally due to the thermodynamics of the system. Chemical stability of hBCN is dependent upon the relative energy of the bonding interactions between B, C and N atoms in the structure. Looking at bond energies, which is a key factor in stability, the trend is as follows; B-N (4.00 eV) > C-C (3.71 eV) > N-C (2.83 eV) > B-C (2.59 eV) [74]. Therefore, by maximising the number of B-N and C-C bonds, the overall structure is increasingly more stable [77, 261]. Evidently, this theoretical observation is also found experimentally, with many hBCN synthesis studies concluding that the materials synthesised are comprised of segregated hBN and graphene nano-domains [141, 262, 263].

As graphene / hBN segregation is almost unavoidable, much effort has instead been focused on controlling relative domain sizes and concentration in the films. Novel CVD efforts in synthesising hBCN materials have resulted in centimetre scale, hBN-graphene

super-ordered arrays comprised of graphene domains in a hBN matrix [119, 264]. In particular, M. Li et al. recently demonstrated precise control over the domain sizes of hBN:C and their density, using the liquid metal catalyst growth method (shown previously in Figure 26, g-h) [119]. With such control over the domain sizes and array densities in these hBCN structures, it will soon be possible to create hBCN films with defined C:hBN domain sizes, such that structures with specific optical and electronic properties may be realised, tailored towards the application's needs. To guide this work, more investigation into the opto-electronic properties of these structures for various domain sizes of C and hBN is required. This DFT study attempts to bridge this research gap by investigating the opto-electronic properties of phase-separated structures of hBN and graphene, similar to those recently reported [119]. This novel work can inform system design in these quasi-crystalline arrays, identifying trends and potential structures suitable for further study. The finite flake model is used to analyse structures of 252 atoms, systematically exploring their optoelectronic properties under gradients of carbon concentration and domain size. Based on this, we then identify viable structures that show potential as efficient catalytic materials for use in the Hydrogen Evolution Reaction (HER), Oxygen Evolution Reaction (OER) and CO_2 reduction reaction. Seven systems are investigated, starting from pure hBN and increasing the C content of the carbon domain at the centre until a pure graphene domain is obtained. Properties of each system are analysed and discussed under the headings of *Structure & Stability*, *Band Gap and Density of States*, *Band Edge Potentials*, *Oscillator Strength & Absorption.*

4.2. Materials and Methods

Methods

Computational details for investigating the properties of 2-D Phase Separated Graphene – Boron Nitride Monolayers – Section 4.3.1; DFT calculations were performed via the Amsterdam Modelling Suite licensed by SCM. Geometric optimisations of the structures were performed with the BP86 functional with D3 dispersion correction and all electron STO ZORA – DZP basis set.

hBCN structures are constructed by doping the centre of a hexagonal hBN domain; initial carbon concentration is 0.9% (BN-C_2 - C dimer), 2.8% (BN-C_6 - six C ring) and then gradually increasing the size of the hexagonal C domain until a pure graphene flake is realised. We introduce a parameter, α, that represents the ratio of the area of the hBN domain to the area of the carbon one;

$$\alpha = \frac{A_C}{A_{hBN}} \tag{23}$$

where α = 0 signifies a pure hBN domain and α = 1 signifies a solely carbon domain.

To evaluate the stability of these BCN structures, their formation energies (E_{form}) were calculated. E_{form} is an important parameter that helps to estimate whether a substitution is energetically feasible or not and it is defined as;

$$E_{form} = E_{BCN} - E_{BN} - N(C)\mu(C) + N(B)\mu(B) + N(N)\mu(N) \tag{24}$$

Where, E_{BCN} is the total energy of the BCN monolayer, E_{BN} is total energy of a carbon-free BN domain, N(C), N(B) and N(N) are the numbers of C, B and N atoms, and μ(C), μ(B) and μ(N) are the single-atom energy of C, B, and N, respectively. As the number of B and N atoms is equivalent in each of our calculated systems, their chemical potentials can be obtained through the relation;

$$\mu(B) + \mu(N) = \mu(BN) \quad (25)$$

where μ(BN) can be derived from E_{BN}/N(BN). N(BN) in the intrinsic hBN structure is 108. μ(C) is defined as $E_{graphene}$/N(C), and where N(C) is the number of carbon atoms within the calculated graphene domain, in this case 216.

For electronic structure calculations, several XC functionals were tested for increased accuracy against BP86-D3 [265]. These include TPSS [266], TB-mBJ [267, 268], and HSE06 [180], the results of which can be found in Appendix Section 8.2.1. To determine which functional was the most accurate, we compared bandgap values obtained for the intrinsic hBN case with the experimental bandgap of hBN at ~ 5.9 eV [42, 47, 269, 270]. HSE06 is chosen as the appropriate functional as it most accurately models the opto-electronic properties of hBN.

4.3. Results and Discussion

Structure and Stability

The geometry optimised model systems are shown in Figure 76. Seven systems are studied. Starting from a hBN flake, the centre point is doped with increasing C atoms, retaining a symmetric structure throughout, until a graphene flake is realised. The maximum C doping of the BN-C structure is capped at BN-C_{96} as further C doping would result in only a linear aminoborane capping layer to the structure, rather than hexagonal borazine.

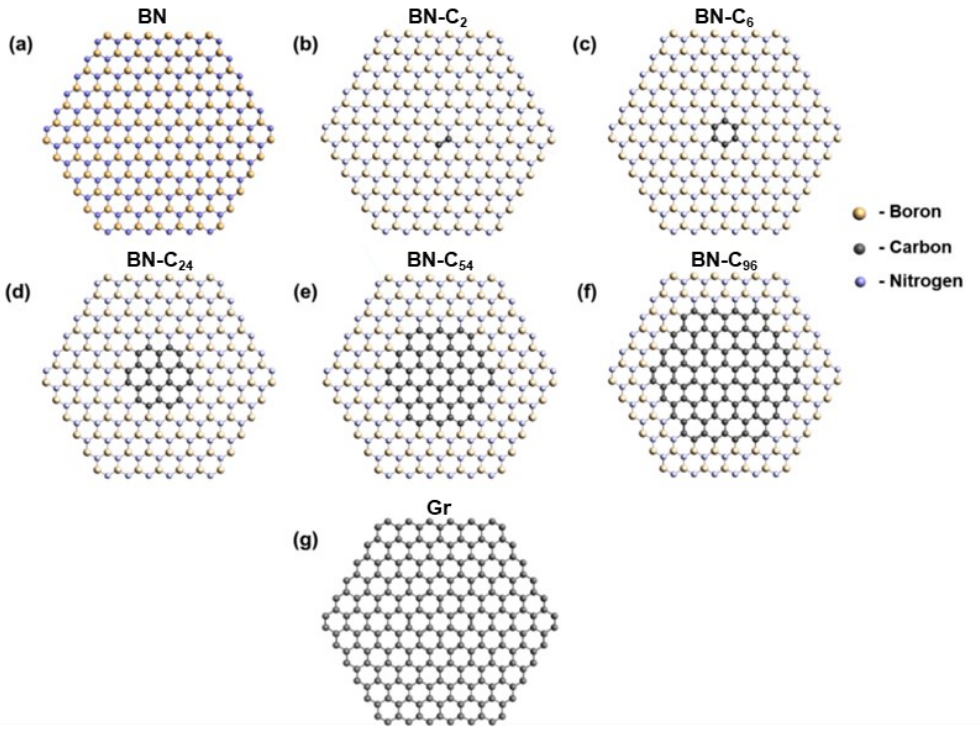


Figure 76; Atomic structures of calculated monolayer BN-C islands with C concentrations (a) 0%, pure BN, (b) 0.9%, BN-C_2 (c) 2.8%, BN-C_6, (d) 11.1%, BN-C_{24}, (e) 25.0%, BN-C_{54}, (f) 44.4%, BN-C_{96} and (g) 100%, Gr. Hydrogen edge atoms are not shown but are part of the calculated structure.

Table 5 shows the composition, α values and formation energy per C atom for each hBCN system. The α value is the ratio of the graphene domain to the total domain size. A clear downward trend for formation energy is observed for structures with increased C content. Calculated values of formation energies per C atom match closely with those calculated for similar BN_{C2} and BN_{C6} structures by Ren *et al.* (~1 eV per C and 0.5 eV per C, respectively) [85], validating the results obtained here.

Table 5; % C composition, domain size ratio parameter (α), formation energy per C atom and band gap values for the BN-C structures analysed in this study.

Structure	C at. %	α (A_1/A_2)	Formation Energy/ C atom (ev/C)	Bandgap Energy (eV)
BN	0.00	0	-	5.94
BN_{C2}	0.93	0.003	1.07	4.70
BN_{C6}	2.78	0.011	0.5	4.67
BN_{C24}	11.11	0.077	-0.168	3.04
BN_{C54}	25.00	0.209	0.2116	2.15
BN_{C96}	44.44	0.407	0.1724	1.61
Gr	100	1.000	-	0.95

Looking at Figure 77, formation energies per C atoms are high for systems with low C atomic % as disrupting the symmetry of the hBN lattice comes with a high energetic cost. In the case of the C dimer, the formation energy is 1.07 eV/C atom which drops to 0.50 eV/C atom with BN-C_6, as the π-conjugation in the C ring increases stability. For BN-C_{24}, the formation energy reaches a minimum and is negative (i.e. structure is more stable than intrinsic hBN sheet). At higher C atomic %, the formation energy is positive once more. This result suggests that there is an optimal structure that shows increased stability which occurs when α *ca.* 0.08, i.e. where the ratio of the hBN:C domain diameters is 3.6 : 1. Structures with larger carbon domains require an energetic cost, however, this value plateaus around 0.2 eV. These results also reflect experimental observations where graphene domains are preferred to point defects in hBN due to their higher stability.

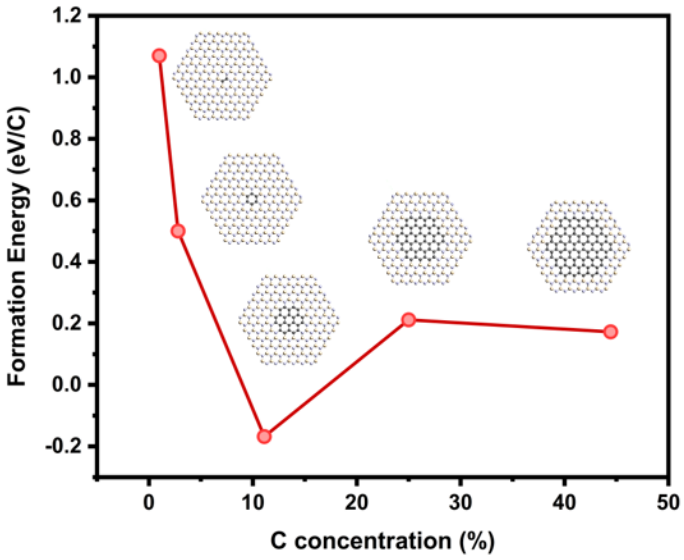


Figure 77; Formation energies per C atom introduced vs. the carbon concentration of the structure. At 10% C concentration, the relative energy of formation is negative, suggesting a structure more stable than hBN.

Band gap (E_g) and Density of States (DOS)

The band gaps of all hBCN structures determined with the HSE06 functional are found in Table 5. Evidently, the structures show a tuneable band gap, ranging from 5.94 eV eV in the hBN

flake down to 1.61 eV with highest C at. % (44%) proving the viability of these segregated hBCN systems as a tailorable electronic system. Figure 78 illustrates the lowering of the band gap, E_g, as the relative size of the carbon domain increases. A sharp decrease in E_g is observed upon first C inclusion as the symmetry of the BN lattice is broken. Upon further C introduction and enlargement of the C domain, the bandgap decreases gradually to 0.95 eV at $\alpha = 1$, for a pure carbon domain.

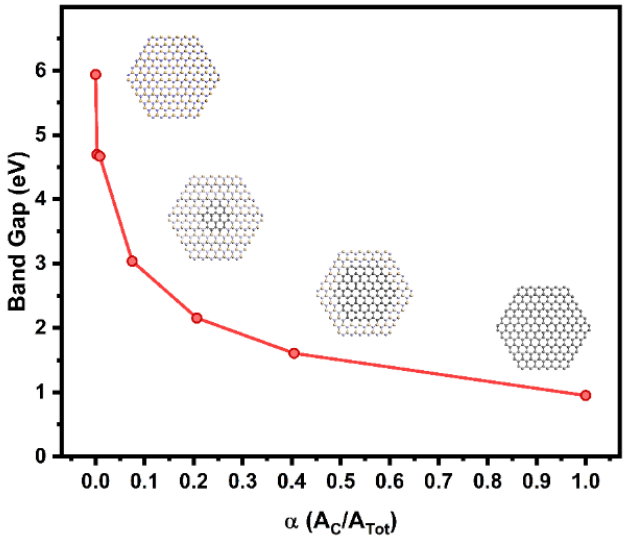


Figure 78; Electronic band gap vs α for various hBCN structures. A sharp decrease in E_g is observed upon first C inclusion as the symmetry of the BN lattice is broken. The bandgap decreases gradually as the graphene domain grows, to as low as 1.64 eV where C at. % is at 44%.

The band gap of a pure carbon flake is determined to be 0.95 eV, and not gapless as expected for a graphene sheet [271]. This is likely due to the finite size of the flake, i.e. it is not a repeating structure with C-C terminated edges. The HSE06 functional has previously been used to successfully model the gapless band structure of graphene [272]. Here, a periodic structure (3 x 3 cell) is used to simulate graphene [272]. Our system involves a finite flake size of 252 atoms (diameter ~ 2.4 nm) with hydrogen passivated edges in order to be able to accommodate the Gr-hBN heterostructure. Previous reports on hydrogenated graphene (e.g. graphane) have shown how C-H bonds in the structure can open up the band gap [273]. Wei Hu *et al.* reported on the band structure of similar hexagonal, hydrogen terminated flakes of graphene and found

that extended systems with diameters > 6.7 nm (~1500 C atoms) were required for a gapless band structure [274]. As such, the HSE06 functional here predicts a non-zero bandgap for the intrinsic carbon case.

Experimental data for the electronic bandgap of these hBCN structures can be found in [119], determined via STM measurements. Here, their structure has $\alpha \sim 0.14$ (around 18 at. % C) and E_g determined as 1.3 eV. This value for E_g lies below those calculated for structures with similar α value here (~2 eV). One possible explanation for this discrepancy is that the band gap has been over-estimated using the HSE06 functional. The HSE06 functional has been shown to improve accuracy for large bandgap materials and is viewed as one of the best available for modelling opto-electronic properties [178]. However, in some instances, it has been shown to overestimate the bandgap and modifications to the mixing parameters of the exchange functional are needed to improve accuracy [275]. To test the accuracy of the HSE functional in this system, more experimental references are needed, which are not available in our particular case.

Another possible explanation for the deviation between experiment and theory could be the experimental details of the STM method which have not been reported, such as the substrate on which the film rests – copper (its growth substrate) or silicon dioxide. Such a parameter would significantly affect the electronic properties of the layer and result in a reading of E_g different to that determined here in vacuum. For example, Nicholas Lanzillo *et al.* previously reported the band gap renormalisation of CNTs to smaller values on a hBN substrate from first principle calculations [276]. The decrease in band gap is the result of a polarisation-induced screening effect from the substrate which, in this case, altered the band gap by up to 0.5 eV. Other experimental data gathered on BCN films comprised of randomly distributed hBN:graphene nano-domains showed that at 60 at. % C, the optical bandgap was 1.61 eV as

determined via UV-vis spectroscopy, much closer to results gathered here for similar structures [141].

The DOS for the various structures are shown in Figure 79. For all C containing structures, we see that it is the C and N orbitals that contribute to the valence band levels whereas the conduction band levels are comprised mostly of B and C orbitals. It should be noted that states near the Fermi Level are composed solely of p orbital contributions (Appendix Section 8.2.2). The presence of C clearly influences the HOMO and LUMO states of the material as contribution to these states comes mostly from the C orbitals. An enlarged view of these band edges can be found in Appendix Section 8.2.3.

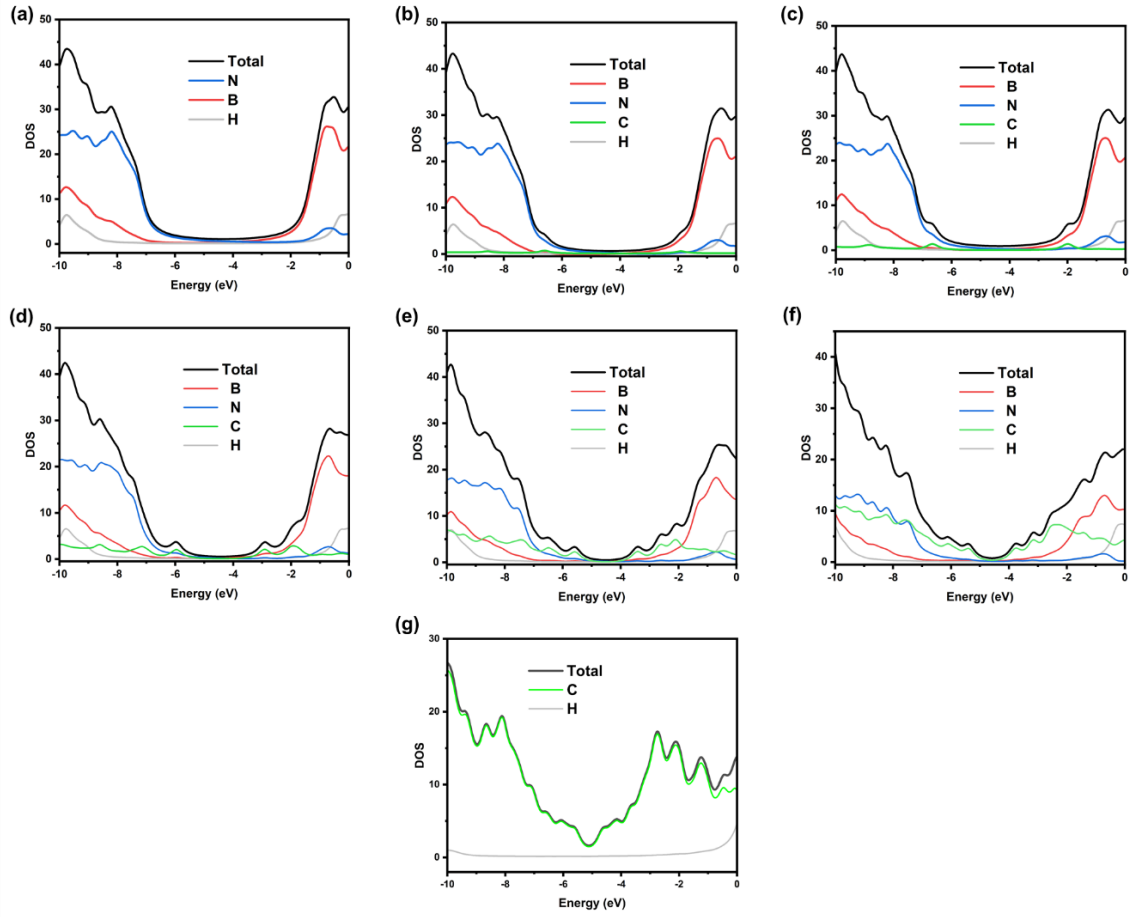


Figure 79; Graphs of the Density of States (DOS), showing the atomic contributions of B, C, N and H in the (a) BN, (b) BN-C_2 (c) BN-C_6 ,(d) BN-C_{24}, (e) BN-C_{54}, (f) BN-C_{96} and (g) Gr systems, at various energy levels with respect to vacuum. The inclusion of carbon introduces states within the bandgap of BN, lowering the electronic gap of the material.

This is further illustrated by the electron distribution depictions of the HOMO and LUMO orbitals for each structure, as seen in Figure 80. In the BN model, the HOMO is localised on each of the N atoms with no interaction with neighbouring B atoms. The LUMO is comprised of the outermost B atoms. As C is introduced the HOMO and LUMO are located at the C domain and charge transfer only occurs via the interior and domain boundary. Notably, in-phase interactions occur between C and B atoms and orbitals exhibit mixing, no longer localised as in the case of BN. This suggests that electron exchange likely exists between C and B atoms along domain boundaries. Conversely, little charge transfer occurs between C and N atoms at this boundary point. However, the C domain does induce delocalisation of

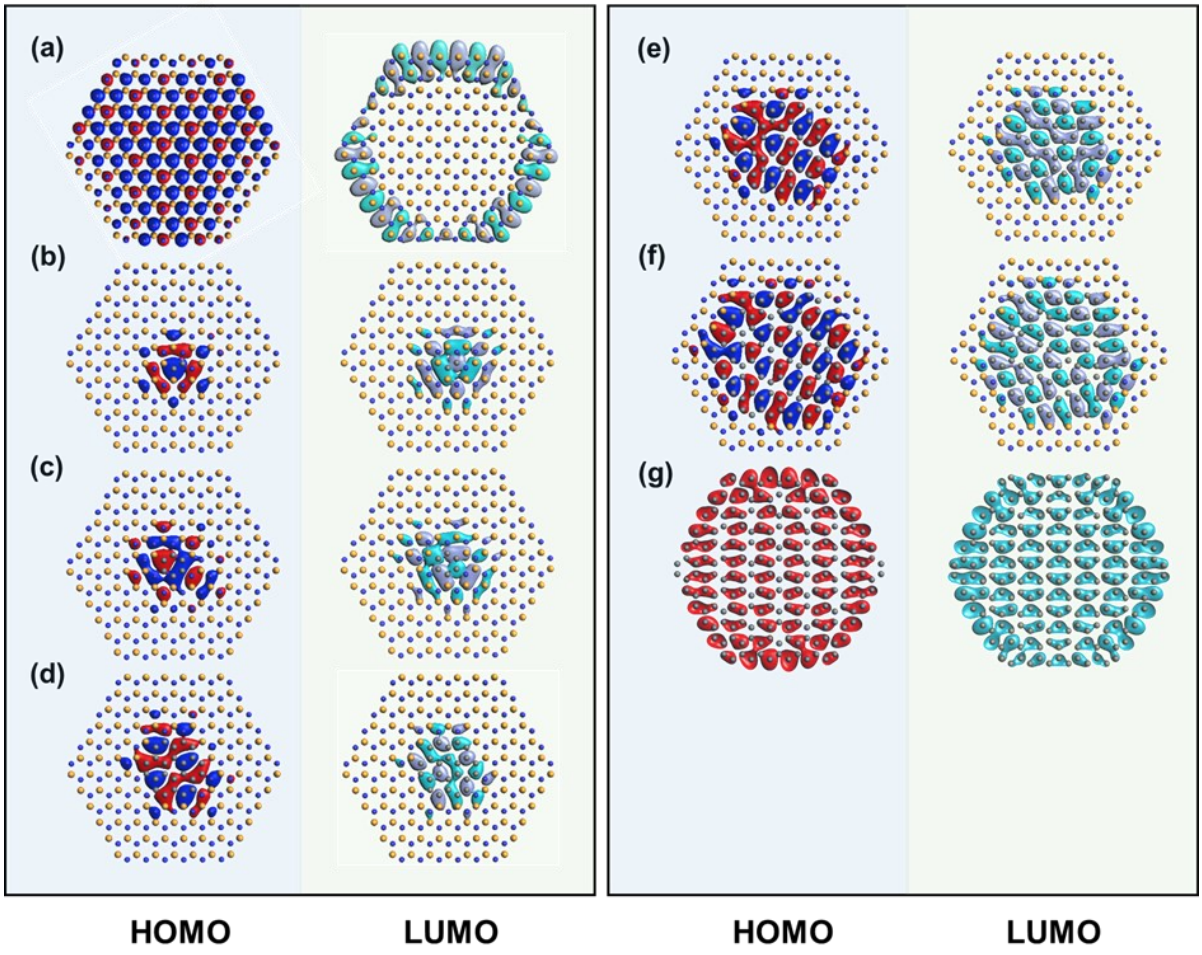


Figure 80; Highest occupied molecular orbital (HOMO) and lowest unoccupied molecular orbital (LUMO) for the various systems; (a) intrinsic BN, (b) BN-C_2 (c) BN-C_6 (d) BN-C_{24} (e) BN-C_{54}, (f) BN-C_{96} and (g) Gr. Clearly, the C bonding states are the dominant feature of the HOMO and LUMO of each structure. Red and blue orbitals are opposite in phase in HOMO, similarly for green and grey in LUMO.

electron density between B and N atoms in regions of hBN near the domain interface, something not observed in the intrinsic hBN case. In the pure carbon system, HOMO and LUMO orbitals reflect the delocalised nature of the graphene system as all orbitals are in phase with each other.

Band Edge Positions

In order to investigate the catalytic suitability of these hBCN structures for applications in technologically important reactions such as water splitting and CO_2 methanation, we observe the band edge potentials. To be suitable for redox catalysis, there are a few thermodynamic conditions the material must satisfy; the HOMO needs to be more positive than the oxidation potential of H_2O ($E° = 1.23$ V vs. NHE [277]) and the LUMO, more negative than the reduction potential of H^+ ($E° = 0.0$ V vs. NHE [277]) or CO_2 ($E_{CH4}° = -0.24$ V vs. NHE [278]). Figure 81 shows how the band edge potentials of the BN domain are modified by the inclusion of carbon in the lattice. Here, the left Y-axis signifies the potential difference with respect to Normal Hydrogen Electrode (NHE) potential, and the right Y-axis refers to the absolute energy with respect to vacuum. The relative positions of the band edges with respect to the NHE is calculated using the standard redox potential with respect to the vacuum potential, which is taken as -4.44 V for hydrogen reduction [277]. The potentials for hydrogen reduction reaction (H^+/H_2) at 0 V vs. NHE and Oxygen Evolution Reaction (O_2/H_2O) at 1.23 V vs. NHE are depicted by orange and blue horizontal dashed lines, respectively and the optimal ranges for the materials band edges are shown by the similarly shaded regions. Hoffmann *et al.* previously reported that for optimal catalytic performance, the material should have its conduction bands at a chemical potential of +0.5 to -1.5 V vs. NHE and its valence bands at a chemical potential of +1.0 to +3.5 V vs. NHE [279] and these intervals form the shaded regions in Figure 81. Furthermore, the green dashed line references the potential required for CO_2 methanation at -

0.24V vs NHE [278]. This can be extended to several other carbon species, depending on the reduction potential (HCOOH; -0.61 V, CO; -0.53 V, CH_3OH; -0.38 V, C_2H_4; -0.35 V, C_2H_6; -0.31 V) [278]

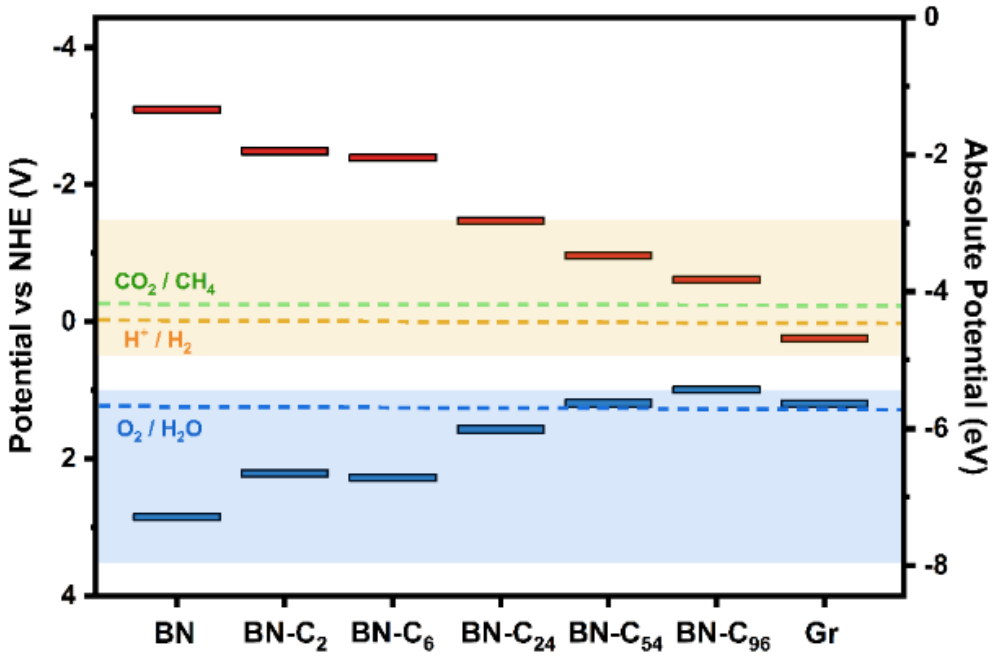


Figure 81; HOMO (blue) and LUMO (red) levels, i.e., band edges, of the BNC_x structures analysed in this work in comparison to optimal band edge positions for HER/OER and CO_2RR. The left Y-axis of the plot shows the potential difference with respect to Normal Hydrogen Electrode (NHE) potential, and the right Y-axis refers to the absolute energy with respect to vacuum. The potentials for HER (H^+/H_2) at 0 V vs. NHE, OER (O_2/H_2O) at 1.23 V vs. NHE and CO_2RR (CO_2/CH_4) at -0.24 V vs NHE are depicted by orange, blue and green horizontal dashed lines, respectively and the optimal ranges for the materials band edges are shown by the similarly shaded regions *[279]*.

Table 6 shows the HOMO, LUMO positions and offset potentials for each hBCN system investigated. In our calculated system, for intrinsic BN, the HOMO level already lies within the range for optimal oxidation energetics, as shown by the shaded blue region. However, with a bandgap of almost 6 eV, the LUMO level is significantly higher than the optimal reduction energies, making it an unsuitable choice material for catalytic reduction. As carbon is introduced to the lattice, there is an expected narrowing of the bandgap as both the HOMO and LUMO levels move towards each other.

Table 6; HOMO, LUMO levels for the various hBCN systems investigated, their chemical potential vs. NHE as well as voltage offset from their respective oxidation and reduction potentials.

System	HOMO (eV)	V vs. NHE (V)	Oxidation Offset (V)	LUMO (eV)	V vs. NHE (V)	H_2 Reduction Offset (V)	CO_2 Reduction Offset (V)
BN	-7.23	2.79	1.56	-1.3	-3.14	-3.14	-2.9
BN-C_2	-6.60	2.16	0.93	-1.91	-2.53	-2.53	-2.29
BN-C_6	-6.66	2.22	0.99	-2.00	-2.44	-2.44	-2.20
BN-C_{24}	-5.96	1.52	0.29	-2.94	-1.50	-1.50	-1.26
BN-C_{54}	-5.58	1.14	-0.09	-3.42	-1.02	-1.02	-0.78
BN-C_{96}	-5.39	0.95	-0.28	-3.78	-0.66	-0.66	-0.42
Gr	-5.59	1.15	-0.08	-4.64	+0.20	+0.20	+0.44

This trend continues even at the highest levels of carbon introduced. While BN-C_2 and BN-C_6 both satisfy the requirements for oxidising performance, their LUMO still lie outside the chemical potential interval for optimal reduction of H_2 and CO_2. This suggests that slightly doped BN, such as that irradiated with ions for C implantation or MOVPE grown samples [22, 23, 57], may not be suitable as catalytic materials in the HER/ORR. With BN-C_{24}, both requirements are satisfied as the LUMO enters the region for optimal reducing performance, particularly for oxidation of H_2O, as the HOMO approaches the theoretical potential for the OER at 1.23 V. Still, there is a significant reducing offset of about 1.5 V. In the case of BN-C_{54}, we find that the position of the HOMO is at 1.15 V vs. NHE, which just straddles that of the oxygen reduction requirements, and the LUMO is located at a more reasonable reducing offset of -1.01 V. Finally, with BN-C_{96}, the highest C at.% system, the LUMO is at -0.66 V vs. NHE, providing a reducing offset of 0.66 V for H_2 and 0.42 V for CO_2. The HOMO is located at a lower value of 0.95 V vs. NHE and is therefore slightly outside the optimal range. Despite good reducing performance, the absence of an oxidation offset here reduces the applicability of BN-C_{96}. The band edge positions for the graphene flake are also included. Both HOMO and LUMO levels lie outside the optimal range to provide a good oxidation and reduction offset for the OER and HER, respectively. Furthermore, the band gap of the system (0.95 eV) , i.e. the minimum energy of the photon harvested by the material, is below that required to drive OER (1.23 V). As such, the hydrogenated carbon nano-flake is not thought to be a good candidate for OER/HER catalysis. For systems BN-C_{24}, BN-C_{54} and BN-C_{96}, the band gaps are

suitable. However, their band positions are not ideal. In order to improve upon this, parameters such as pH and temperature of the reaction can be varied in order to alter the potentials required [90].

At T and pH > 0, energy levels are shifted by (k_BT ln10) x pH, where kB is Boltzmann's constant [280]. At room temperature (298 K) and pH 7, this provides a shift of 0.41 V. Other studies have focused on engineering strain in the lattice as a method of shifting band edge positions into the desired range [82, 88, 89]. Under conditions of room temperature and pH, Figure 82 shows how the HOMO and LUMO levels of the three optimal structures, BN-C_{24}, BN-C_{54} and BN-C_{96} shift in energy level. Here, all three structures satisfy the thermodynamic requirements for HER and OER. BN-C_{24} now straddles the oxidation potential with an offset of 0.70 V, while its LUMO lies 1.09 V and 0.85 V above the reduction potential for H_2 and CO_2, respectively. For BN-C_{54}, the HOMO is very well situated at 0.32 V below the potential for H_2O. Similarly, its LUMO has a reduction offset of 0.61 V for H_2 and 0.37 V for CO_2, potentially making this a material with good reducing and oxidation capabilities. With BN-C_{96}, we find that the position of the HOMO band now lies 0.13 V below the oxidation potential for H_2O, giving it an oxidation offset and improving its applicability in the oxygen reduction reaction. The LUMO now has a reducing offset of 0.25 V for H_2 and 0.01 V for CO_2, making it an attractive candidate for HER although its suitability for CO_2 reduction might be diminished as a small offset is generally required [281].

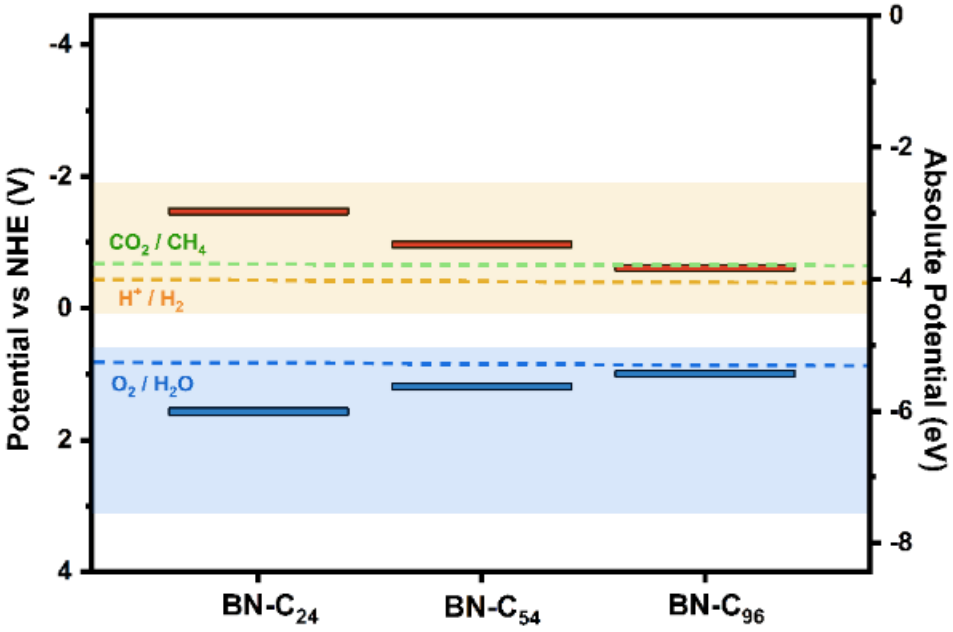


Figure 82; HOMO (blue) and LUMO (red) levels of the three optimal BN-C structures, BN-C24, BN-C54 and BN-C96, with the chemical potentials of HER, OER and CO_2 reduction shifted by 0.41 V when pH = 7.

Electrolysis in neutral pH presents a transformative way for environmentally friendly, cost-effective hydrogen production. However, the field is still developing with one of the biggest challenges being the lack of robust hydrogen evolution reaction (HER) catalysts that are active at this pH [282]. Interestingly, a recent study on hBN/Pt co-catalysts for HER have shown better hydrogen evolution performance than Pt/C for a seawater solution (pH ~ 8) [283]. Here, we have identified three hBCN candidate systems which show good bifunctionality in the overall water splitting reaction at RT and neutral pH.

Oscillator Strength and Absorption

Light absorption is an important factor if these materials were to be used in photo-catalysis. The oscillator strength of each systems excitations is calculated, a quantity that can be directly related to light absorption [284]. From this, we can infer the photo-activity of the material and its suitability in photocatalytic applications. Figure 83 displays the calculated excitation spectrum of the various BCN models over the range 0 – 7 eV. Results here were obtained via

time-dependent DFT (TDDFT) calculations, again, using the HSE06 exchange functional, implemented within the Amsterdam Density Functional program [285]. A watermarked spectrum of the solar spectral irradiance as a function of energy is included to guide the reader towards where the material is deemed 'photo-active' in a solar sense. Data for this spectrum was taken from an online database on the standard solar spectrum [286].

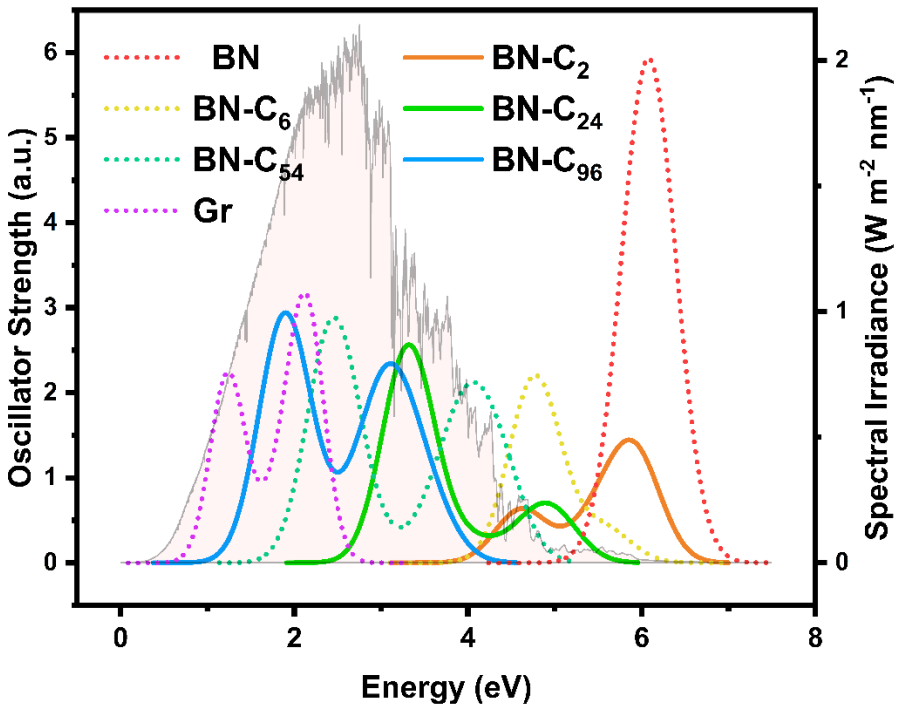


Figure 83; Oscillator strength with respect to excitation energy for the various BN-C structures showing their optical absorption properties. The solar spectral irradiance as a function of energy is watermarked in light orange to show the 'photo-active' regions. This particular plot is quantified by the right hand side y-axis.

For structures BN, BN-C_2, and BN-C_6, we observe the absorption edge outside of the solar spectral range and so cannot be considered as photo-active catalysts. With BN-C_{24}, its absorption peak lies on the just on the edge of the solar spectrum at around 3.2 eV. This means that, although some of the higher energy photons might excite the material, their intensity is low (solar irradiance is ½ its peak value) reducing its efficiency as a photo-catalyst. BN-C_{54} has its strongest excitation located in the middle of the solar spectrum, at 2.4 eV, making it a good candidate for photo-catalysis. At this energy, the absorbed photon will possess enough

energy to drive the catalytic reaction for the HER/OER process (1.23 V). The BN-C_{96} system also offers a material with good photo-active properties with two absorption peaks located within the solar spectral range, a major peak at 1.9 eV and a smaller one at 3 eV. Again, the minimum energy of the photon harvested by the material is greater than the energy required to drive the splitting of H_2O at 1.23 V. Thus, out of the three viable materials, BN-C_{54} and BN-C_{96} both show good optical response in the solar spectrum and, therefore, we propose them as potential candidates for environmentally friendly, photo-catalytic H_2O splitting. To comprehensively investigate their photocatalytic activity, future work should focus on systematically determining the mechanism of both water oxidation and hydrogen reduction half reactions on these structures, looking at various reaction sites at the BN-C interface. By looking at the energies of adsorption, reaction, and desorption of H_2O and its products, we can further evaluate the efficacy of these systems as photo-catalysts.

4.4.1. CVD of hBN/Gr lateral heterostructures

Synthesis of lateral graphene-hBN heterostructures similar to those described above were trialled on the Cu substrate using the experimental set-up and synthesis protocols previously derived for hBN (Section 3.3.2) and graphene (optimisation of synthesis described inn Appendix Section 8.4), employing *step-wise* APCVD deposition of graphene and hBN.

Experimental

Sequential deposition of graphene and then hBN was carried out on Cu using optimised synthesis parameters (T_{CVD} = 1050 ˚C, H_2:CH_4 = 2000, T_{AB} = 70 ˚C , 10 mg AB, 400 sccm 4% H_2 in Ar). CH_4 (0.01 sccm), H_2 (20 sccm) and Ar (380 sccm) were introduced for 25 minutes

to deposit graphene, followed by hBN deposition by heating 10 mg ammonia borane at 70 ˚C for 2 hours for full film coverage and 1 hour for isolated domains.

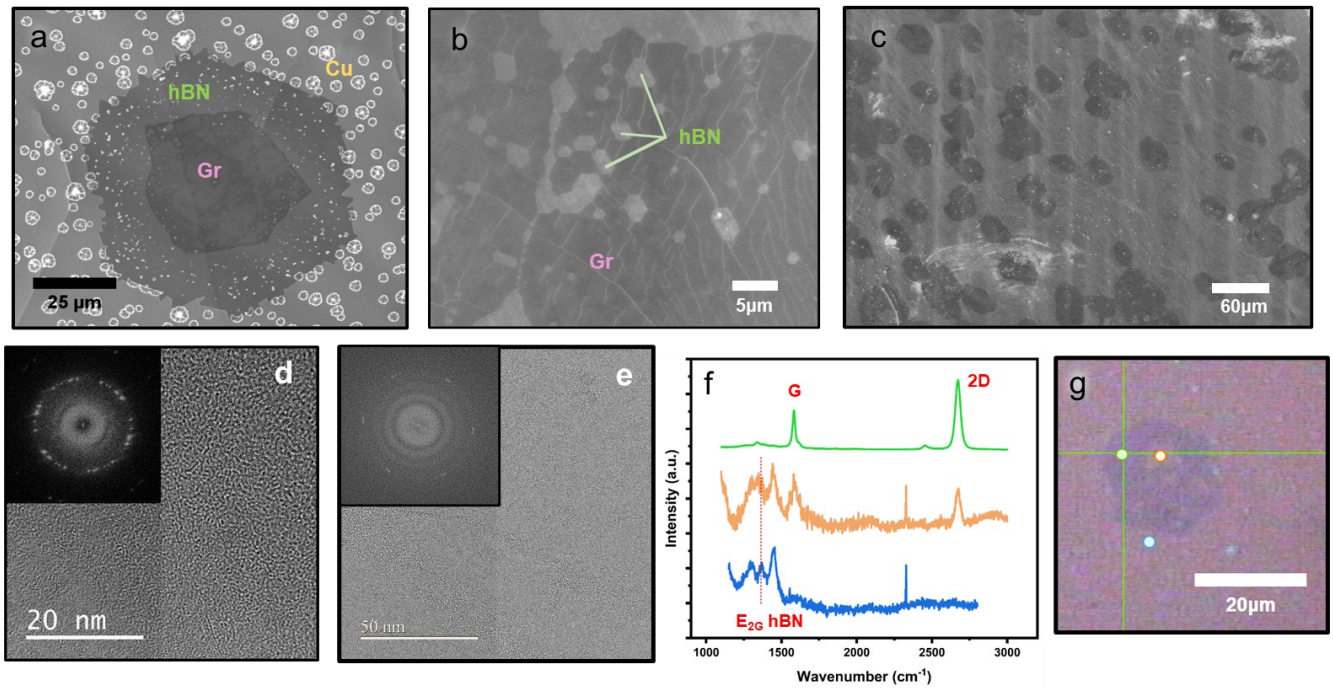


Figure 84, Characterisation of Gr-hBN lateral heterostructures grown on Cu. (a) SEM image showing an individual Gr-hBN flake on Cu. White particulates result from the degraded hBN precursor. (b) SEM image exhibiting the etched regions of graphene in the Gr-hBN heterostructure which have been filled with hBN. (c) Wide-view SEM showing non-homogenous nucleation density and domain sizes of graphene on Cu (d,e) TEM analysis showing (d) turbostratic and (e) crystalline regions within the same film. (f) Raman spectra of different regions in the Gr-hBN heterostructure, with regions shown in the OM image (g).

Gr-hBN heterostructures were realized on the Cu surface, shown in SEM images in Figure 84 (a-c). A clear interface between hBN and graphene regions can be observed from the contrasted regions highlighted in SEM image, Figure 84 (a). White deposits surrounding the hBN arise from aged ammonia-borane precursor, which will be addressed in the proceeding chapter. Etched graphene domains were also observed, likely occurring from H_2 etching during the incubation stage of B/N concentrations prior to hBN nucleation and slow rate of hBN deposition (Figure 84, b). Issues were also encountered with non-homogenous nucleation density and domain sizes of the graphene islands due to the epitaxial constraints of using a solid Cu substrate (Figure 84, c). TEM analysis showed that heterostructure films varied in

crystallinity, with some regions exhibiting a turbostratic nature (Figure 84, d) and others highly crystalline (Figure 84, e).

Raman spectra of various regions of the heterostructure showed that the graphene was of relatively high quality (green spectrum, Figure 84 f), with an I_D/I_G ratio of 0.21 and I_{2D}/I_G ratio of 1.73. Regions surrounding graphene domains exhibited the characteristic E_{2G} peak of hBN at ~1370 cm^{-1} (blue spectrum). Etched regions within graphene domains exhibited signatures of both hBN and graphene, as evidenced in the orange Raman spectrum in Figure 84 (f). As is to be expected, graphene here is more defective with I_D/I_G ration of 0.57 and I_{2D}/I_G ratio of 0.94. UV-vis analysis of the film also found signatures of defective graphene, available in Appendix Section 8.4. Two plasmon resonances are exhibited at 4.6 eV and 5.2 eV, which are attributed to graphene and defective graphene plasmon resonances, respectively.

A handful of studies have looked at sequential APCVD growth of lateral graphene / hBN heterostructures on the solid metal Cu substrate [287, 288], although full hybrid film growth is not reported, instead focusing on individual flakes. As such, hBN deposition times are shorter and graphene etching during the second stage of deposition (hBN growth) has not been reported. For full film growth, this should be a consideration as graphene quality can be significantly reduced by H_2 etching over the course of a full hBN film deposition, as was shown here. This etched and defective graphene reduces the overall quality of the heterostructure. Furthermore, with full hybrid film growth, the epitaxial constraints imposed by the Cu lattice impact the overall homogeneity of the film, as seen in Figure 84 (c). Graphene domains are not homogeneously spread across the growth substrate, but rather randomly located and often merging into one another. These results highlight how the slow deposition times and epitaxial constraint of growth on the solid Cu substrate are not well suited for the production of highly ordered Gr-hBN lateral heterostructures.

Recently, full hybrid film growth of Gr-hBN lateral heterostructure on liquid metal catalysts (LMCats) of Cu via APCVD were reported [119, 120], where epitaxial constraints were unapparent due to the liquid nature of the growth substrate. Figure 85 (c,d) shows results from Li *et al.*'s recent work on growth of graphene / hBN super-ordered arrays on liquid Cu [119], contrasted against results obtained in this study on the solid metal catalyst (Figure 85, a-b). The epitaxial constraints of the solid substrate mean that growing graphene domains are unable to move or rotate once nucleated resulting in randomly nucleated graphene domains in the heterostructure. Using the LMCat technique, the absence of crystalline structure on the surface of the metal allows for nucleated domains to move freely and rotate, during growth, and without any substrate induced strain. Instead of the epitaxial relationship driving the orientation of the graphene domains, it is the electrostatic potential of the graphene domains that becomes the dominant factor during growth. In this regime, individual graphene domains adjust their orientation to align with that of adjacent domains (Figure 85, c), resulting in remarkable order across mesoscopic length scales (Figure 85, d). Furthermore, due to the high temperature and enhanced catalytic activity of the LMCat substrate, reaction times for hBN growth are enhanced and graphene etching is thus avoided, leading to high-quality, homogenous and ordered heterostructures. As such, for extended hybrid film growth, future work should focus on employing the novel substrate technique of liquid metal catalysts (LMCats) to advance the production of super-ordered films of Gr-hBN lateral heterostructures.

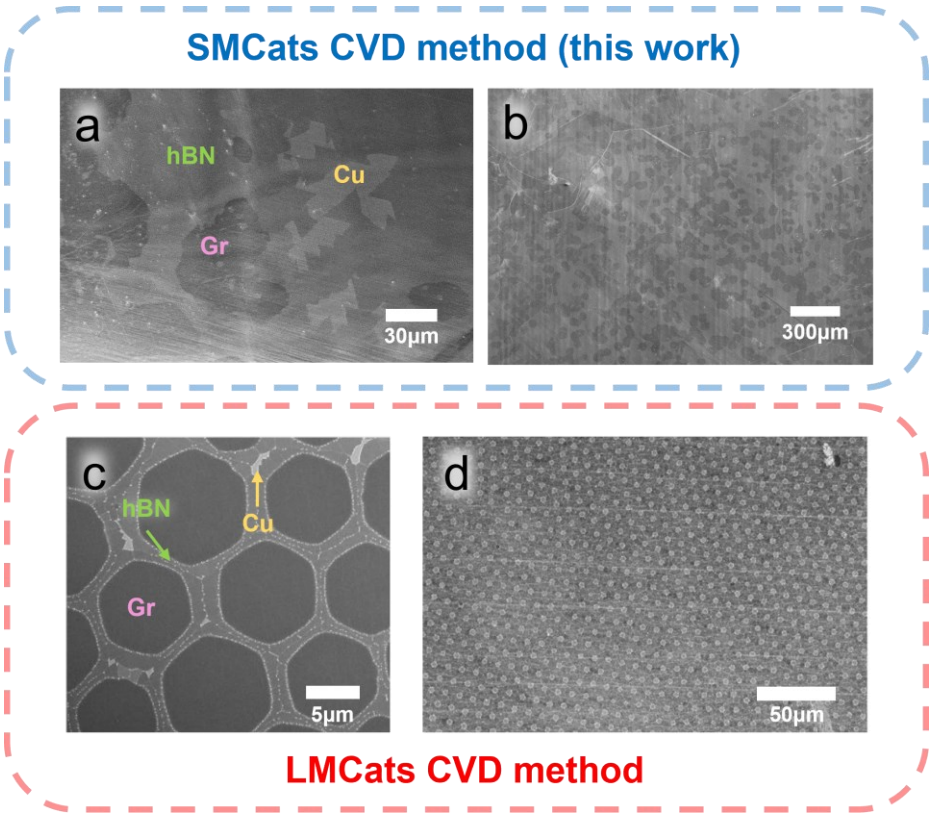


Figure 85, Comparison of Gr-hBN full-film heterostructures resulting from (a,b) Solid Metal Catalyst (SMCat) and (c,d) Liquid Metal Catalyst (LMCat) growth on Cu. SEM images (c,d) are adapted from [119]

4.4. Conclusion, summary and outlook;

Graphene / hBN lateral heterostructures are promising candidates for a wide range of applications, from optics [56, 91] to electronics [289, 290]. DFT investigations into the properties of phase-separated hBCN systems revealed that these materials may have applications in photo-catalysis, specifically in the HER and OER reactions for hydrogen generation via water splitting and also the CO_2 reduction reaction. Out of seven trialled systems, three candidates were identified as being potentially viable catalytic materials in water splitting and CO_2 reduction; BN-C_{24}, BN-C_{54} and BN-C_{96}. BN-C_{24} and BN-C_{54} showed band edge positions suitable for single semiconductor catalysis of HER/OER as well as CO_2

reduction, under conditions near room temperature and neutral pH. Absorption properties were also calculated via Time Dependent DFT. Out of the three viable materials, BN-C_{54} and BN-C_{96} both show good optical response in the solar spectrum. Therefore, we propose them as potential candidates for photo-catalytic H_2O splitting that should be considered for further study on hBCN structures as novel 2D photo-catalysts. Future work should focus on systematically determining the energetics and possible mechanisms of both water oxidation and hydrogen reduction half reactions on these structures, looking at various reaction sites at the BN-C interface.

Step-wise APCVD synthesis of graphene/hBN hybrid films on the solid metal Cu catalyst highlighted a number of important considerations that have been overlooked by previous experimental studies, which have focused on individual flakes rather than extended films; namely how the slow deposition times and epitaxial constraints of growth on solid Cu are not well suited for producing extended films of ordered and defect-free Gr-hBN lateral heterostructures. Graphene domains possessed random orientations and variable nucleation density on the solid Cu substrate, which affect the homogeneity and applicability of the material. Furthermore, poor hexagonality and etching was evident, due to the long incubation and deposition time for hBN growth, reducing the quality of graphene domains in the structure. Future work should adopt the LMCat method, synthesising structures at elevated temperatures above the melting point of Cu, such that epitaxial constraints are avoided, improving the homogeneity of the overall structure, and deposition rates are significantly enhanced, reducing the likelihood of graphene etching.

Chapter 5

Growth of B, N doped silica nanoplatelets on copper through low-purity ammonia borane activation

5.1. Introduction

A range of precursors have been utilised in the literature for hBN CVD synthesis; diborane/ammonia [136], boron trichloride/ammonia [107], and borazine [113, 132-135], among others. Most of these are toxic, spontaneously flammable, corrosive, or challenging to store, which are significant safety concerns for hBN synthesis. Consequently, ammonia-borane (AB), has been used as the preferred precursor for hBN synthesis due to its safety in handling (it is classified as a "non-hazardous substance or mixture") and stoichiometric B:N nature. However, the material is not without its drawbacks. The compound is highly hygroscopic, which results in degradation over time, even with careful handling. Previous studies which looked at AB as a hydrogen storage material showed how AB gets slowly hydrolyzed upon storage and the accumulating borates and boric acid impurities can significantly change its decomposition activity [291]. These changes to the chemical purity of the precursor which affect its decomposition profile can significantly affect the hBN synthesis and produce undesirable side reactions and particulate impurities in the film, deteriorating the overall quality of hBN. A few reports on hBN synthesis have drawn attention to this occurrence, and their formation has been proposed as a result of solid polyaminoborane byproducts forming on the growth surface [244, 292]. Figure 86 shows an example of impurities observed in CVD studies on hBN growth with AB. These studies link their occurrence only to the precursor AB. In this work, I show that particulate impurities in hBN growth can result from both the overall purity of the AB precursor and the experimental apparatus used in the CVD process.

Due to pandemic shortages, the precursor typically used for hBN growth, high purity (> 97%) AB, became unavailable for a period. During this time, a lower purity grade (> 85%) AB was trialed, which resulted in a completely different synthesis product. The figure of 85% refers to the percentage of crystalline monomeric ammonia borane present in the precursor, with the

remaining 20% not explicitly disclosed but likely being B/N/O derivatives, such as borates and polymerized aminoboranes.

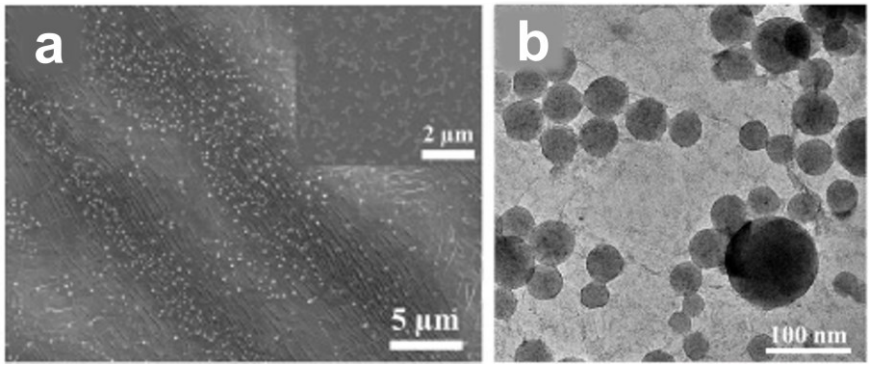


Figure 86; Particulate impurities observed in hBN CVD growth studies. (a) SEM image of hBN on Cu and transferred onto SiO2/Si (inset image) with particulates observed. (b) TEM analysis of particulates showed them to be spherical and non-crystalline. Both reproduced from [292]

This work is the first to report hBN synthesis with a low purity AB precursor, and the results obtained demonstrate the influence of atypical decomposition products on the synthesis product and quality of the hBN films. Many seminal CVD studies on hBN growth fail to explicitly identify the purity of their ammonia-borane precursor [120, 198, 202, 206, 288, 292, 293], which is a cause for concern, as my observations highlight significant differences in hBN growth using AB precursors of differing purity. The lower grade AB precursor preferentially forms doped silicate structures comprised of B-O and N-Si bonding groups, something that is not observed with high purity AB. The formation of these B, N doped silicate layers on the surface of Cu through ammonia borane activation has not been previously reported. As there are few robust precursors for hBN synthesis via CVD, particularly those with ease of safe handling, it is important to understand the precursor chemistry to improve synthesis protocols and avoid pitfalls in hBN CVD growth. As such, this chapter investigates the effects of low purity AB and the observed growth of doped silica structures, proposing a growth mechanism for their formation, and suggesting improved protocols to avoid their formation.

5.2. Materials and Methods

Materials

Cu foil (Alfa Aesar - 46986RG, 0.025mm thick, annealed, uncoated, 99.8% metals basis), ulta-pure Cu foil (Alfa Aesar – 10950, 0.025mm thick, Puratronic®, 99.999% metal basis) are used as growth substrates in this section and specified as 99.8% purity or UHP foil, respectively. High purity (Sigma Aldrich - 682098 , ≥97%) and low purity (TCI Ltd – B5082, ≥85%) ammonia borane used as a precursor for hBN growth, following synthesis protocols optimised in Chapter 3. KOH flakes (Sigma Aldrich, reagent grade 90%), acetic acid (Sigma Aldrich, ReagentPlus®, > 99%) were used for cleaning the copper foil of SiO_x impurities. NaOH pellets (Sigma Aldrich - 56730), tetrahydrofuran (THF) (Sigma Aldrich - 401757, anhydrous, ≥ 99.9%) were used in cleaning and recrystallising the low purity ammonia borane.

Methods

hBN growth on Copper foil; The same optimised hBN synthesis protocol was used as found in Chapter 3 of this thesis, only the AB precursor employed was either high purity (Sigma Aldrich, ≥97%) or low purity (TCI Ltd, ≥85%). Electropolished copper foil was washed with acetone, IPA and dried under N_2, placed in the substrate-holder, and centred in the CVD furnace. Before synthesis, the reaction chamber was vacuum purged with argon three times to remove any organic contaminants present in the chamber. Annealing of the Cu foil was then carried out in 5 % H_2 in Ar mix at 1050 ºC for 60 minutes after which 10mg of ammonia borane was sublimed at 70 ºC and carried into the reaction chamber using 400 sccm of 5 % H_2 in Ar.

Chemical treatment of Cu foil to remove SiO_x impurities; Cu foil (99.8% purity, uncoated) was immersed in 2M KOH for 10 minutes, followed by rinsing in DI water. Foil was then sonicated in acetic acid for 10 minutes before washing in DI water and drying under N_2.

Purification and recrystallisation of AB precursor; The procedure was adapted from previous reports by Komova *et al.* on AB repurification [294]. 2g of AB was dissolved in 50 ml of 20% aq. solution of NaOH before adding 170 ml of THF. The two-phase mixture was stirred in a closed flask for 30 minutes before separating out the organic phase using a separation funnel. Organic phase was then evaporated on a rotary evaporator at 40 ˚C to a volume of ~10 ml. To this, 25 ml of heptane was added, dropwise, at a rate of about 1 ml/min. The solution was cooled down in an ice bath and the precipitate, filtered off and washed first in heptane, followed three times by hexane, after which the material was dried in a vacuum box for several days.

Ball milling of AB/hBN powder; Ball milling of AB and hBN powder was carried out using the Emax high-energy ball miller. Water-cooled temperature control was enabled to ensure the sample remained < 50 ˚C during the milling process. Samples were prepared with a weight ratio AB/hBN powder of 1:6 and milled 1200 min^{-1} for 12 hours.

5.3. Results and Discussion

5.3.1. APCVD growth of hBN on copper using *aged* ammonia borane

During CVD studies of hBN growth on Cu, white particulates were sometimes observed on the surface of hBN films in samples synthesised using aged ammonia borane (high purity, Sigma Aldrich AB, > 6 months). These particulates were found to directly impact the shape of the hBN domains as evidenced in the SEM images in Figure 87 (a-c). Once the hBN fully converged, particles are found ubiquitously across the film. Attempts to remove these undesired particulates from the hBN film via hydrogen etching at 700 ˚C for 30 minutes were

unsuccessful and particles remained on the surface of the Cu. Instead, the hBN film is degraded, as can be seen in Figure 87 (e), where hBN domain boundaries have been etched away.

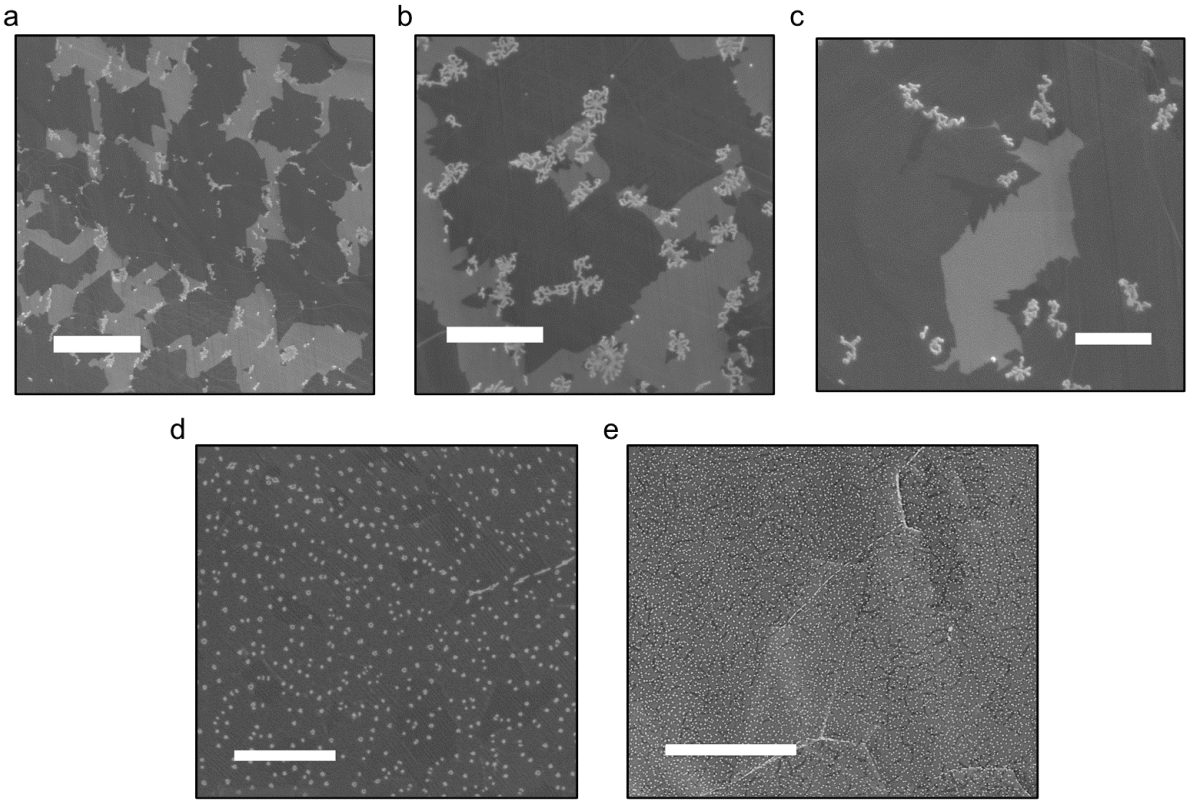


Figure 87; hBN synthesis carried out using aged ammonia borane precursor (Sigma Aldrich – 97% purity) after 6 months. SEM images showing the irregular growth observed when using aged ammonia borane precursor. White particles are seen on and between hBN domains (a-c).(d) After growth of a fully converged film, these contaminants still remain in the film. (e) Hydrogen etch preferentially removed hBN at grain boundaries rather than the contaminants, as seen by the dark domain edges. Scale bars for (a-e) are 20, 10, 5, 10, 50 μm, respectively.

It was believed that these particles originated from the degradation of the ammonia-borane precursor, due to its hygroscopic nature and a tendency towards spontaneous hydrolysis in air [291]. Figure 88 exhibits this degradation in the FTIR spectra of aged, Sigma Aldrich ammonia borane precursors (purple – 20 months, green – 16 months) alongside a fresh sample of TCI ammonia borane (black), all of which have been stored under vacuum when not in use. In the aged samples, all characteristic peaks are severely reduced in intensity with the N-H IR peaks almost unobservable. The B-H stretching peak has also changed in shape, signifying a change in structure. The B-N stretching peaks at around 750 cm^{-1} are no longer visible in the aged

spectra, signifying a significant change in the precursors overall structure. This evidently results in defects during hBN growth which are detrimental to its application as a 2D material.

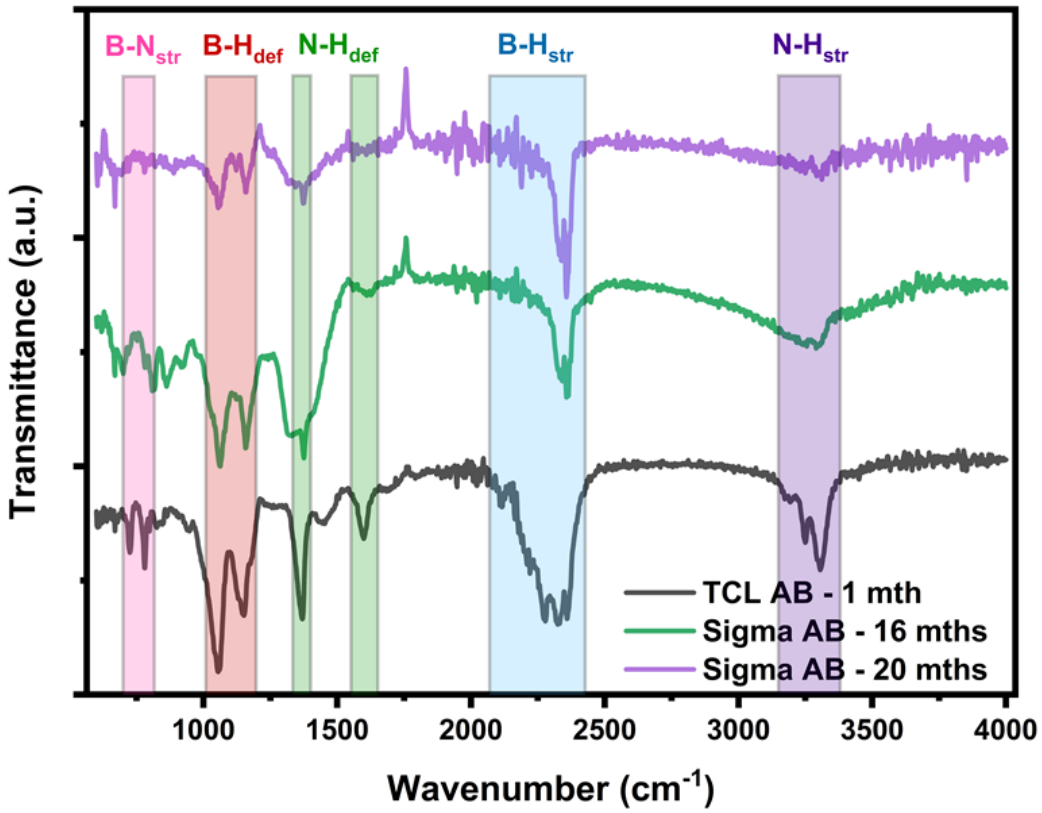


Figure 88; FTIR of ammonia borane precursor at various ages. Severe degradation is apparent in the aged samples with losses in intensity of almost all IR peaks, most significantly with peaks associated with B-N and N-H vibrations.

Similar structures have been reported in CVD studies of hBN growth, whose origin has been suggested to be from solid polyaminoborane solid byproducts forming from the very active monomeric aminoborane, resulting from decomposition of the AB precursor [244, 292]. As such, the remedy for this occurrence was to simply order fresh ammonia borane. Unfortunately, production of this chemical was severely impeded by external factors such as COVID-19. As a result, the "standard" precursor (97% purity, Sigma Aldrich) was unavailable and a lower grade source of ammonia borane was trialed as a replacement (TCI, 85% purity). This lower grade precursor significantly enhanced the formation of these defects which, in contrast to

previous reports, is shown to result from not only the purity of the ammonia-borane precursor, but also the experimental apparatus used in CVD synthesis, the quartz tube reactor.

5.3.2. hBN growth on copper using *low-purity* ammonia borane

Figure 89 shows SEM analysis of a hBN synthesis with the same experimental procedure as before, only using TCI ammonia borane. White particulates of 1.0 +/- 0.1 um in size were observed across the Cu surface with striking homogeneity. In some regions, larger particles were present, which stood out from the otherwise homogenous array of particles (Figure 89, c). It was observed that at grain boundaries of the copper foil, nucleation of the particles was higher, forming coalesced regions as seen in Figure 89 (d). As a control experiment, the synthesis procedure was carried out without introducing the ammonia borane precursor. As seen in Figure 89 (b), no particulates were observed on the Cu foil although some minor surface contrast can be seen, revealing that the structures result from use of the low purity ammonia-borane precursor.

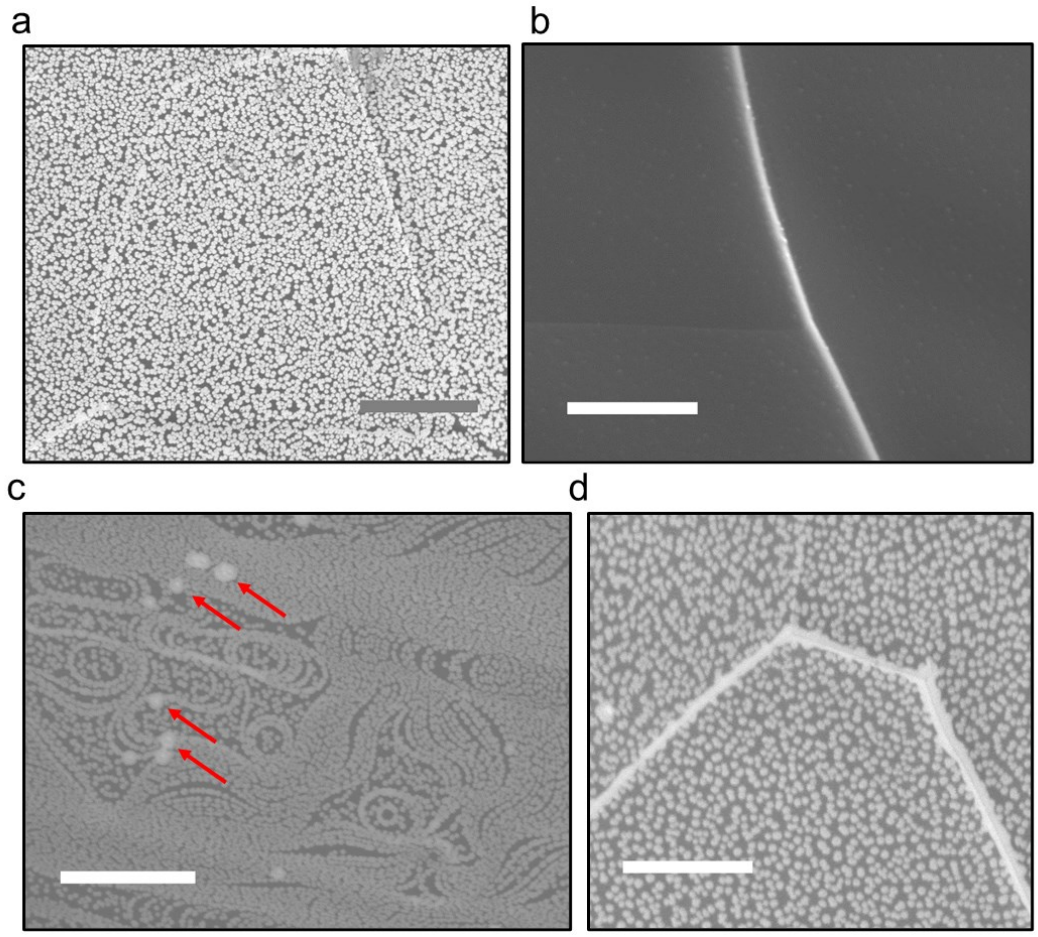


Figure 89; Results of hBN growth using previously optimised parameters except using lower purity AB, (TCL - 85% purity). (a) Large amounts of white particulates are seen on the surface, homogenous in size, and covering almost the entirety of the Cu foil. (b) Cu foil after using the same experimental parameters as in (a), except no flow of AB is introduced. (c) Larger particulates are also observed (red arrows). (d) Growth of these structures is enhanced at the grain boundaries of Cu, where coalesced regions are observed. Scale bars in images a-d are 80, 10, 30 and 15 µm, respectively.

EDX analysis was carried out on these samples to confirm the source of the contaminant, results of which are shown in Figure 90. Evidently, the source of the particles is Si and O contamination. Furthermore, on the EDX spectrum, there exists slight shoulder peaks to the left of the C and O peaks, where B and N are respectively found, suggesting some B and N content is present (inset in Figure 90, d). These results suggest that defects observed are mainly Si_xO_y related but are activated by the low purity precursor.

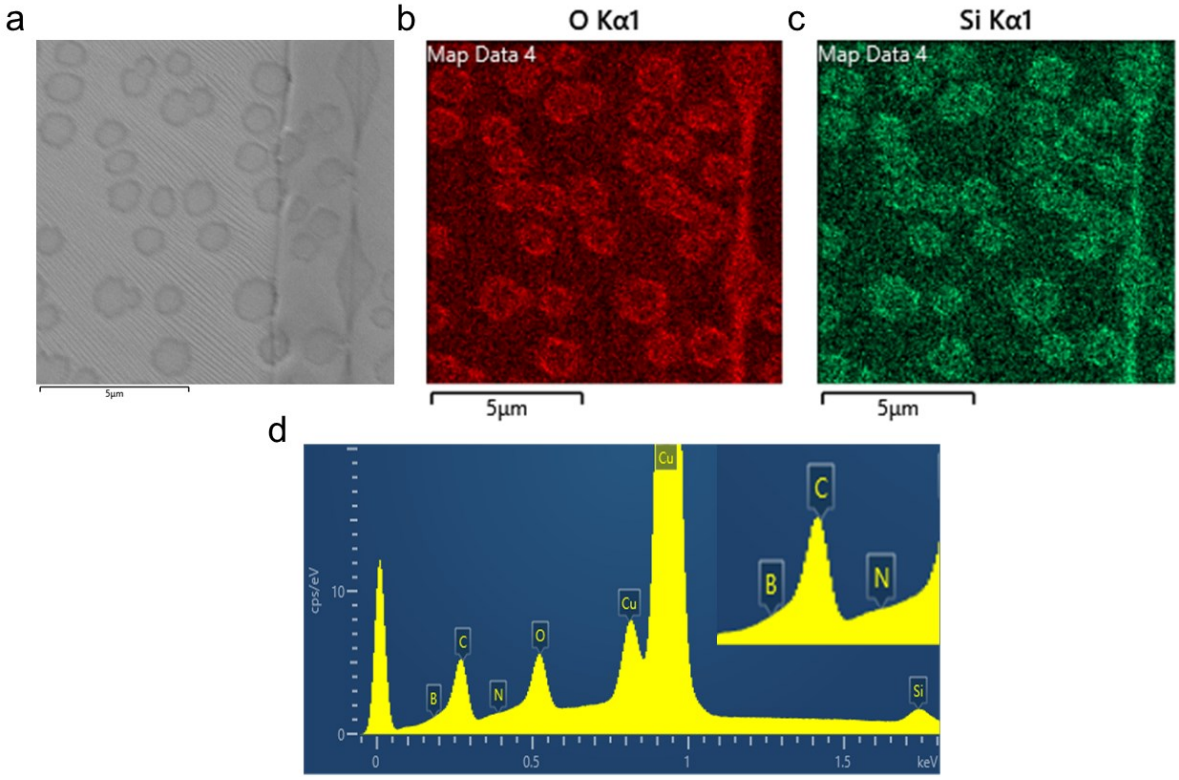


Figure 90; EDX analysis of growth structures resulting on Cu foil. (a) SEM image of contaminant on Cu foil. Wrinkles are seen in the image suggesting that some hBN growth may be present, alongside the growth of the contaminants. (b) Oxygen and (c) Si mapping of (a) showing the presence of oxygen and silicon at the particle and throughout the two growth fronts. (d) EDX spectrum for the map data (a-c). The energy range for B and N is enlarged on the inset image.

Further characterization was carried out via XPS spectroscopy. N1s, B1s and Si2p XPS spectra of the structures are seen in Figure 91 (a-c). In the N1s spectrum, two peaks are observed. Peaks at 400.9 eV and 398.6 eV are attributed to Si-N-O bonding and N-Si bonding, respectively [295, 296]. The peak at 398.6 eV could be interpreted as a N-B bonding peak, however, no accompanying B-N peak was observed in the B1s spectrum (B-N is typically observed at 190 eV). As such, we ascribe this peak to N-Si bonding [296]. The B1s spectrum is deconvoluted into two peaks, at 192.8 eV and 192.0 eV, ascribed to various B-O-Si and B-O-B bonding networks [297, 298] Finally, the Si 2p spectrum is resolved into peaks centred at 103.1 eV and 102.1 eV which we attribute to SiO_2 and SiO_xB/N_y, respectively [295, 299, 300]. These results suggests that structures of boron, nitrogen doped silica is present on the surface of Cu. Figure 91 (d) illustrates some of these structures, where regions of borosilicate and silicon oxynitride

have formed within the SiO_2 network. It is likely that there is some hBN formation on the surface of the copper, as evidenced by the wrinkles on the surface of Cu in the SEM image Figure 90 (a). However, this signal is overshadowed by that coming from the borosilicate and silicon oxynitride structures, and as such, it is not seen in the fitted HR-XPS spectra.

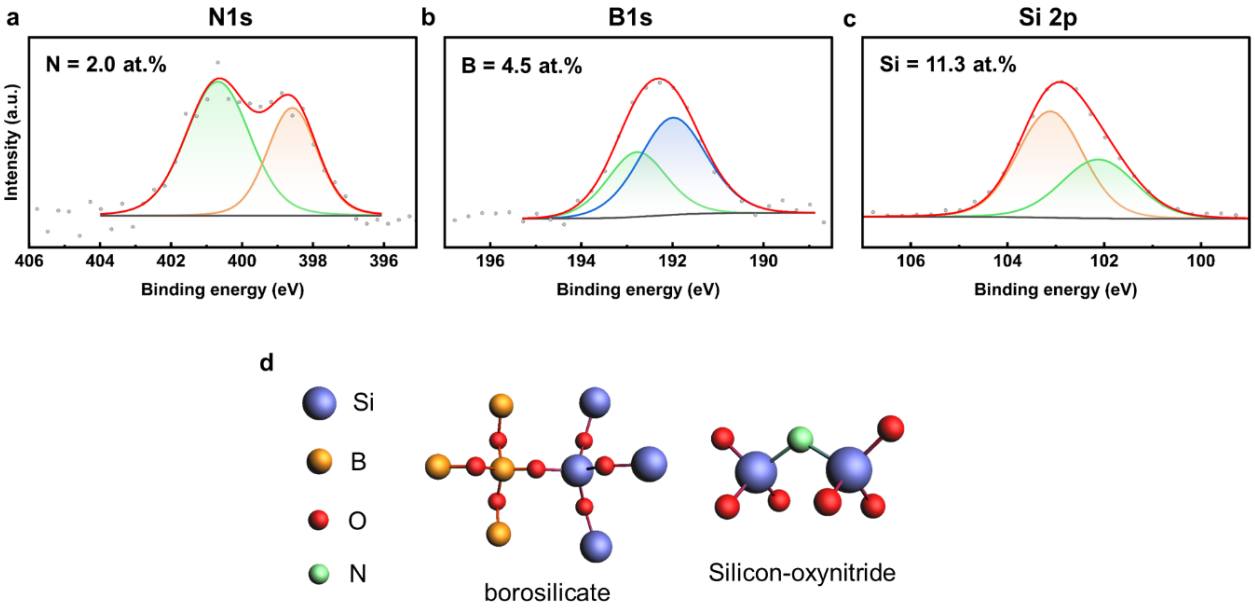


Figure 91; Interpretation of the growth structures as determined via XPS. (a) N1s spectrum of SiO_x structures on Cu foil. Two peaks are observed at 400.8 eV and 398.6 eV, which are attributed to Si-N-O bonding and Si-N-Si bonding, respectively. (b) B1s spectrum of the same sample, exhibiting peaks at 192.8 eV and 192.0 eV, ascribed to B-O-Si and B-O-B bonding networks, respectively. (c) The Si 2p spectrum is deconvoluted into two peaks, at 103.1 eV and 102.1 eV which we attribute to Si-O and doped Si-O-N, respectively. (d) Depiction of the proposed doped structures in the SiO_x structures formed, where B-O-Si and N-Si-O networks are formed.

To shed light on the origin of Si_xO_y in these structures, XPS analysis was also carried out at various stages of the overall synthesis procedure. Figure 92 shows results from the XPS analysis on the pre-synthesis foil (Figure 92, a), a control synthesis where no hBN precursor was introduced (Figure 92, b) and the post-synthesis foil (Figure 92, c). Silicon is detected in all three samples, however their chemical environments are slightly different. The Si 2p spectrum for the pre-synthesis foil shows peaks for organo-Si and SiO_2 at 102.1 and 103.1 eV, respectively [301]. In the control sample, a broad peak centred at 103.1 eV is observed, which we attribute to SiO_2 bonding. Finally, in the post-synthesis sample, a large SiO_2 peak at 103.1 eV and a smaller peak at 102.3, which we ascribe to the formation of O-Si-N / Si-O-B networks.

Looking at the O 1s spectra, the pre-synthesis sample shows peaks for O-Si and O-Cu bonding, at 532.3 and 531.3 eV, respectively [302, 303]. In the control sample, there is an O-Si peak as in the pre-synth sample, while the O-Cu peak has disappeared, likely from hydrogen annealing. In the O1s spectrum of the post-synthesis sample, there is a strong O-Si (bridging oxide) peak at 532.2 eV, as well as a smaller O-Si (non-bridging oxide) peak at 530.3 eV [304]. At 534.0 eV, there is a small peak signifying O-B bonding [298]. The structure of bridging (BO) and non-bridging oxides (NBO) is depicted in Figure 92 (d). BOs link two SiO_x units, providing strong bonds between the smallest structural units of the silicate network. NBOs provide a comparably weak bond between Si and one or more network modifier ions (B/N) that are not part of the silica network [305]. These results reveal that Si_xO_y is present in the control sample yet is not activated, producing no observable particulates on the surface of Cu (as seen in Figure 89, b). These observations further support the claim that Si_xO_y impurities are activated by the low-purity precursor.

Looking at the atomic composition % of the XPS characterization (Figure 92, e), we observe a relative decrease in Si:Cu from the pre-synthesis sample to the control sample, suggesting that organo-Si is removed in the heating process, supported by the disappearance of the organo-Si peak in the Si 2p spectrum of the control sample (Figure 92, b – ii). There still exists a significant amount of Si in the sample, suggesting that inherent silicate impurities exist in the foil or are introduced from the reaction chamber. Interestingly, in the post-synthesis sample, there is a significant increase in Si at. %, by as much as 5 at. %. This result indicates that the ammonia borane precursor is reacting with silicon contaminants, either already present as impurities in the Cu foil (and drawn to the surface during annealing) or from the quartz reactor itself. Since XPS is a surface sensitive technique, as these Si based structures form and cover the Cu surface, their interaction area increases within the XPS spot size and thus their relative at. % increases. In the control sample, no discernible contaminants are visible on the Cu surface

via SEM analysis (Figure 89, b), indicating that the B-N precursor facilitates the growth of these extended structures from Si_xO_y contaminants.

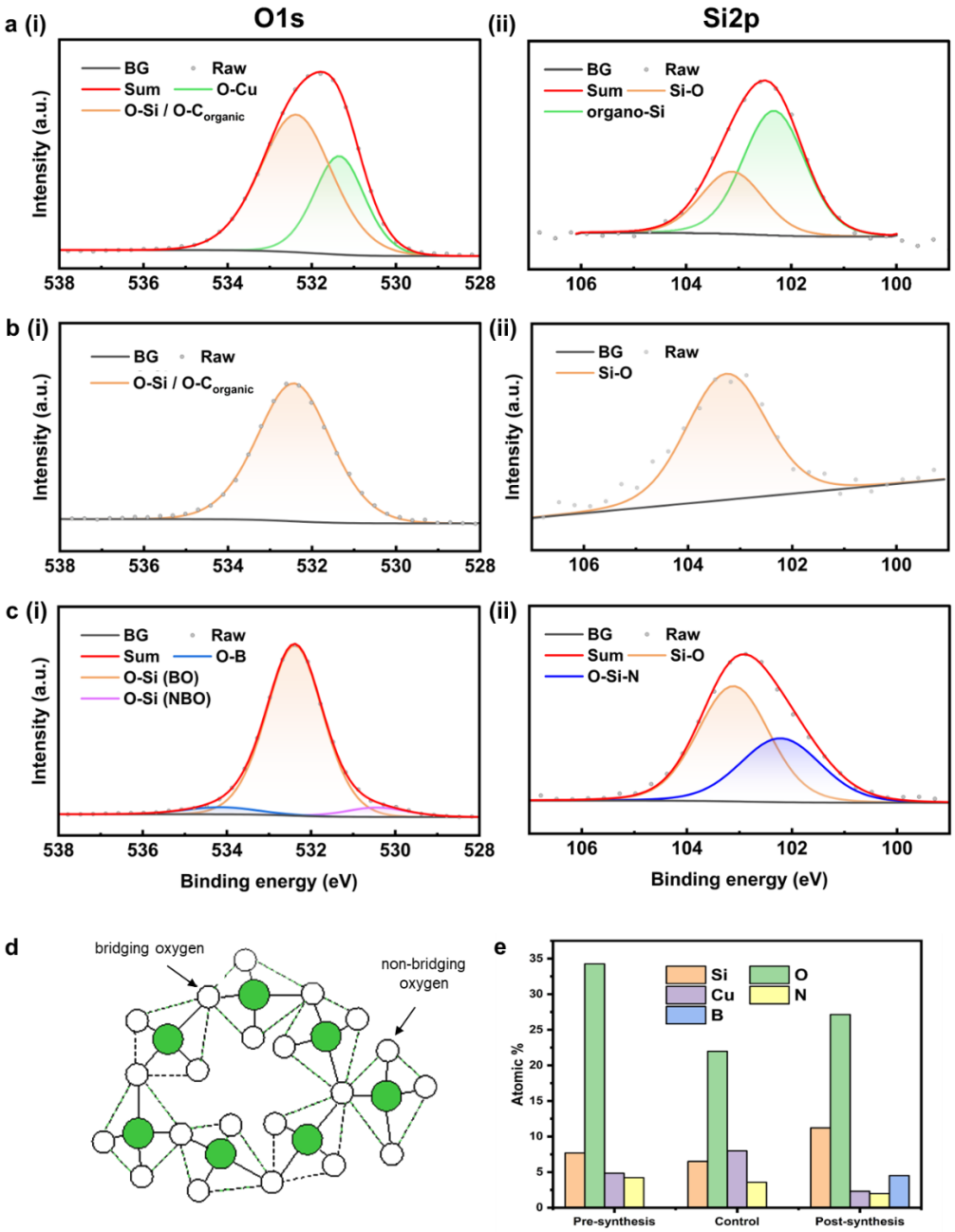


Figure 92; XPS analysis of silicon content in Cu foil pre-synthesis, post synthesis and in the control experiment. (i) O1s and (ii) Si 2p XPS spectra for the Cu foil (a) pre-synthesis (b) control experiment and (c) post-synthesis. (d) Depiction of bridging oxygen (BO) and non-bridging oxygen (NBO) in a silica network. (e) Atomic % composition in samples a, b and c.

This Si_xO_y contaminant can be introduced through a variety of ways; through the quartz tubing / substrate holder [306-308] or through impurities in the Cu foil [309], both of which have been documented in the literature.

Nonetheless, to eliminate other potential sources of contamination, such as the substrate holder, the experiments were repeated using Al_2O_3 plates as the substrate holder and cover. However, this did not eliminate the SiO_x contamination and doped silica structures were still observed after carrying out the hBN synthesis procedure.

To test if Si_xO_y contamination arises from Si already present on the Cu foil, cleaning was carried out using potassium hydroxide (KOH) and acetic acid. KOH is already known to dissolve silicon and silicon dioxide structures [310] and has previously been used to remove silicon based impurities from graphene and its growth substrates [309];

$$SiO_{2(s)} + 2KOH_{(aq)} \rightarrow K_2SiO_{3(aq)} + H_2O \quad (28)$$

Similarly, acetic acid is often used to prepare Cu foil for graphene growth [311] and it is used here as an additional treatment step to remove any copper oxide or silicon oxide particulates from surface of the foil. To do this, Cu foil (99.8% purity) was immersed in 2M KOH for 10 minutes, followed by rinsing in DI water before sonication in acetic acid for 10 minutes. Figure 93 shows XPS analysis of the foil after each processing step. Large O-Cu peaks are found in the O1s spectra of the cleaned foil as KOH heavily oxidises the Cu surface. Looking at the Si 2p spectra, we see that no Si-O peak exists in the KOH washed sample (Figure 93, a). A small peak is observed at 102.1 eV, assigned to organo-silicons. Following KOH + acetic acid cleaning, no silicon is detected via XPS. Ultra-pure Cu foil (99.999% purity) was also analysed via XPS for its silicon content and no presence of Si impurities were found (Figure 93, c).

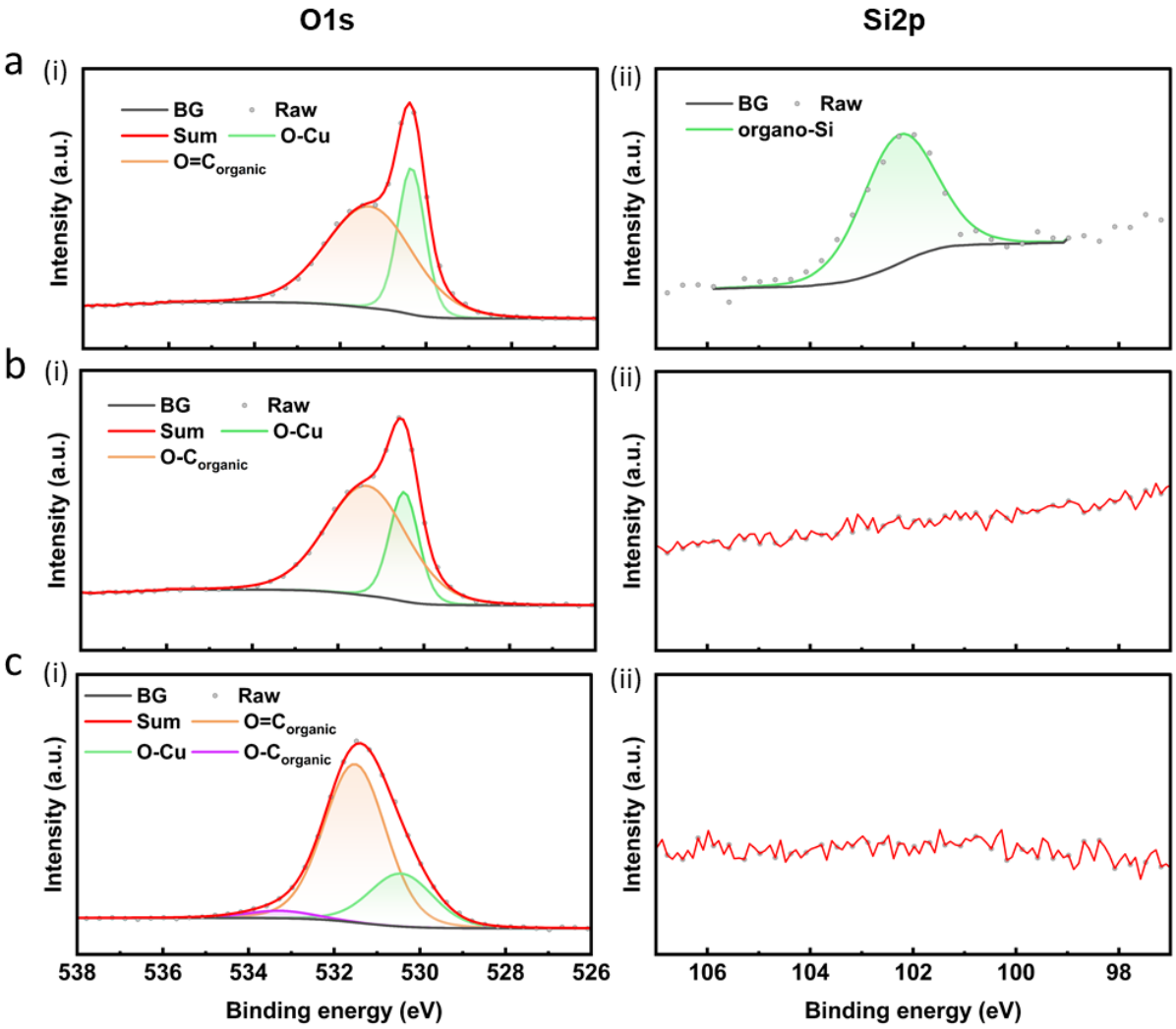


Figure 93; XPS analysis of Cu foil treated with various processing steps and of ultra-pure Cu foil (99.999%). (i) O1s and (ii) Si 2p XPS spectra for 99.8% purity foil after (a) KOH clean, (b) KOH + acetic acid clean and (c) 99.999% ultra-high purity foil.

The Si-free samples were used to determine if the growth of the silicon structures resulted from intrinsic impurities or those introduced by the growth chamber itself. Figure 94 shows SEM images taken from control and synthesis experiments carried out on cleaned 99.8% Cu foil and UHP 99.999% Cu foil. The same trend is observed, where silica growth structures are found on the Cu surface, triggered by the decomposition species of the AB precursor.

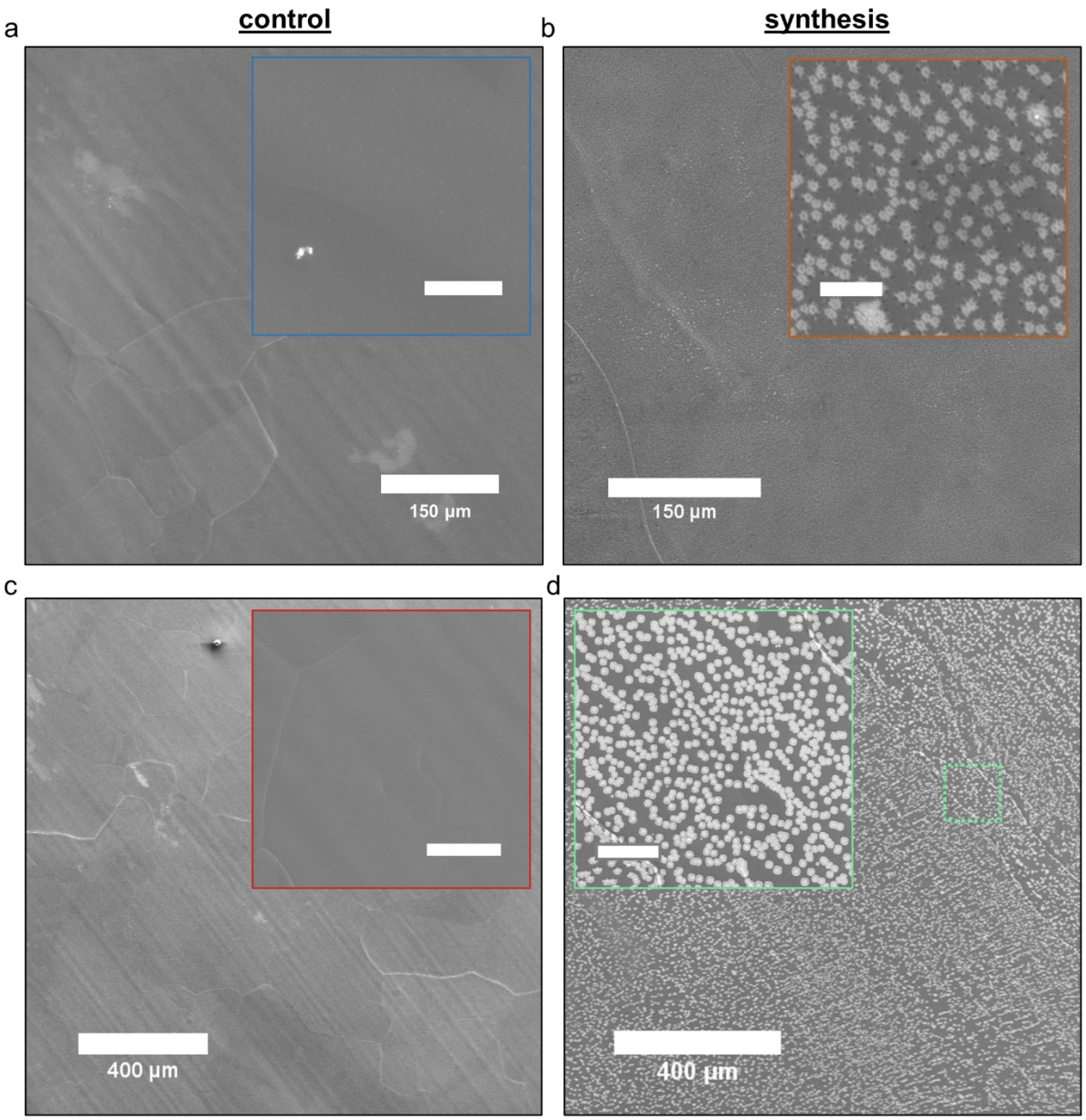


Figure 94; Results of hBN synthesis carried out on KOH + acetic acid cleaned 99.8% purity Cu foil (a, b) and ultra-high purity Cu foil (c, d). (a) SEM of cu foil after a control experiment with no AB introduced where cleaned Cu foil was used. Inset image scale bar is 10 um. No readily distinguishable growth structures are observed, however, the Cu surface shows signs of particles. (b) SEM image of synthesis carried out on cleaned Cu foil with AB introduced. Small deposits are observed. Inset image scale bar is 5 um. (c) SEM of cu foil after a control experiment with no AB introduced where UHP. Inset image scale bar is 50 um. Similar to the case of (a), no large growth structures are observed, however, the surface of the Cu shows some signs of some blemishes. (b) SEM image of synthesis carried out on UHP Cu foil with AB introduced. Circular deposits are again observed. Inset image scale bar is 40 um.

In the KOH + acetic acid cleaned foil, growth is slightly altered, smaller in size and less homogenous, likely due to a change in the surface topology and chemistry after the chemical cleaning process. In the UHP foil, homogenous growth of the structures is still observed (Figure 94, b), again with striking homogeneity. As such, no evidence is found to support that copper

foil was the source of the contamination. This indicates that the Si contamination is occurring not from impurities in the substrate, nor the substrate holder, but from the synthesis chamber itself. In the SEM images of the control samples, no large growth structures are observed. However, the Cu surface is not pristine and small blemishes are observed. These are likely Si nanoparticles that are deposited on the Cu foil from the quartz reaction chamber but have not been "activated" by the flow of AB. It is evident from this contamination, that quartz reactor tubes are not ideal for use in hBN synthesis using ammonia borane, especially with degraded or low-purity precursor. Undesirable, secondary species are produced using the low-purity or degraded precursor, which activate Si_xO_y contaminants from the quartz reactor to form extended doped, silica structures, inhibiting high-quality hBN growth.

As such, there are two drivers behind the growth of the observed doped silica structures; the Si_xO_y impurities arising from the reactor itself and the reactants arising from the low purity ammonia-borane. Since the growth of these structures observed is unavoidable through tackling the Si in the substrate, efforts were made to improve the quality of the precursor, in hope that the doped silicate structures might be suppressed and hBN growth would be promoted.

5.3.3. Washing and recrystallization of AB precursor

It was thought that by improving the purity of the precursor (~85%), close to that of the initial source used (< 97%), a reduction in the formation of the doped silica structures might occur. The ammonia borane precursor was washed and recrystallized as outlined in the methods section of this chapter. FTIR spectra of the as-received (black) and washed product (blue) are seen in Figure 95. The peaks associated with ammonia borane are more pronounced and small

peaks around 800-900 and 1500 cm^{-1}, associated with organic solvents left over from the synthesis procedure, have disappeared, suggesting an increase in precursor quality.

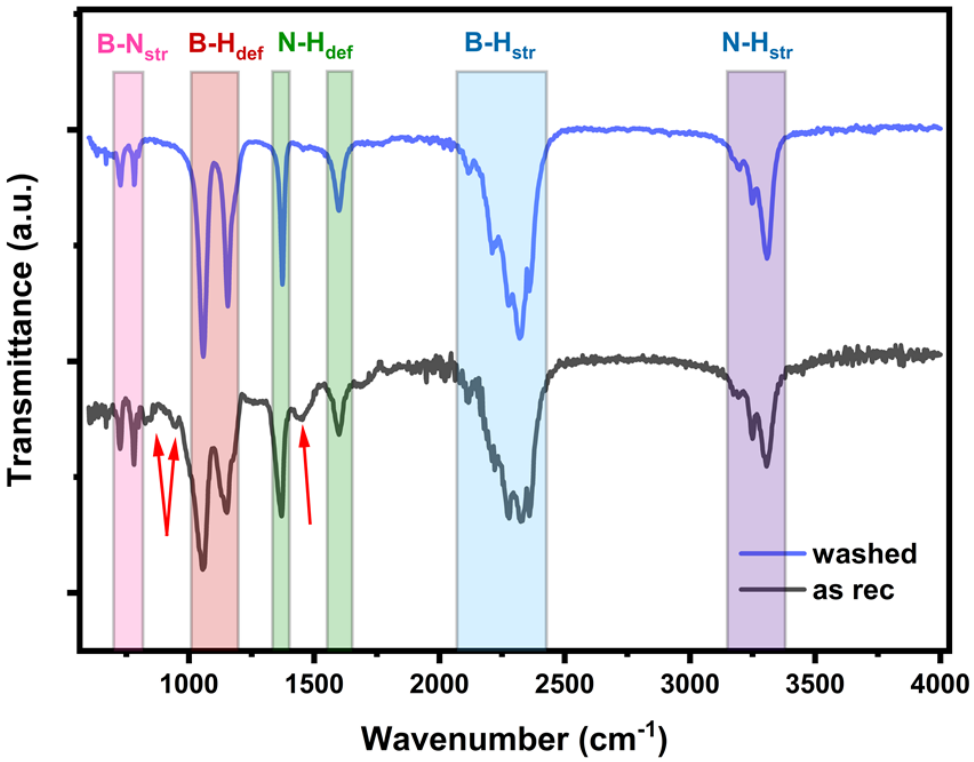


Figure 95; FTIR analysis of as received (black) and washed (blue) AB precursor. Peaks highlighted by red arrows are associated with C-H and C-C vibrations and are as a result of impurities in the AB. After washing and vacuum drying, these peaks are no longer apparent.

Growth was then carried out using the washed AB, following the procedure set out in Section 5.2. SEM analysis is shown in Figure 96 where silica structures are still present on the surface. However, the growth is enhanced in some cases and two distinct growth features are observed; large, globular deposits (10 – 40 um), often with a particle at the centre of their growth (Figure 96, c), as well as smaller, more homogenous structures which cover the entirety of the Cu foil. At the edge of the Cu foil, a fully converged, silicate layer is observed, as domains coalesce on the Cu substrate. This is likely due to the increased probability of silica particles falling on the Cu substrate from the walls of the quartz chamber at these regions. Washing of the AB precursor, evidently, *enhanced* the size of the observed silica structures in comparison to previous results.

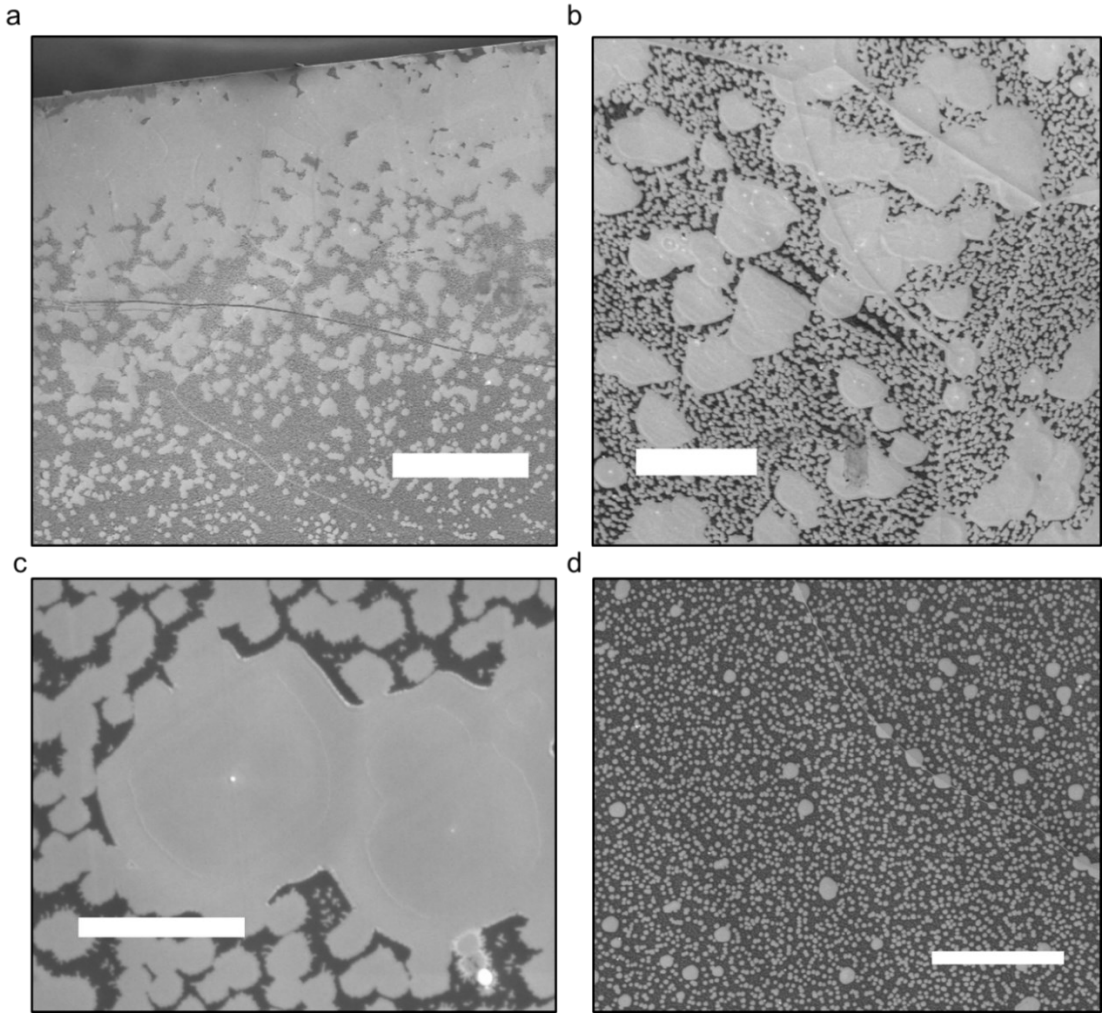


Figure 96; SEM results of hBN growth procedure using washed and recrystallised AB precursor. (a) Wide view SEM image of Cu substrate. Enhanced growth is observed at the edges of the foil where fully coalesced regions can be seen. (b-d) Two different forms of growth are observed across the substrate– large globules, many of which have an observable central locus point (as seen in image c), and smaller, homogenous deposits. Scale bars for SEM images (a-d) are 300, 50, 10 and 60 um.

5.3.4. Ball milling of ammonia borane with hBN powder for enhanced borazine selectivity

Previous studies on AB have found that certain treatments to the precursor can result in enhancement in the generation of borazine, the active component in hBN synthesis, and suppress non-stoichiometric release of molecules like ammonia and diborane [312, 313]. In particular, the mechanical activation of AB via ball milling with hBN powder has seen borazine

yield increase threefold [312, 313]. Ball milling of the ammonia borane precursor with hBN powder (1:6 ratio) was carried out, in an attempt to promote borazine release during hBN synthesis with the lower purity AB. Using this ball milled AB, hBN synthesis was attempted, the SEM results of which can be seen in Figure 97. Again, SiO_x 2D structures are observed on the growth substrate. These SiO_x domains are larger (16.6 +/- 3.0 um in size for trapezoidal deposits, 12.3 +/- 1.1 um for hexagonal deposits) and, more interestingly, show a clear epitaxial relationship with the underlying growth substrate, as observed in Figure 97 (a-c). The domains show different growth orientations on different facets of Cu, typically arranging themselves in a hexagonal or isosceles trapezium/kite shape, as exhibited in Figure 97 (c) and (d), respectively. The alignment of the silica structures across the substrate is extremely homogenous, only altering their orientation between individual copper domains (Figure 97, a). At the edges of the Cu growth substrate, domains converge to form films (Figure 97, e). Figure 97 (f) shows an SEM image of the growth front of the film.

Blue arrows highlight the lattice artefacts in the film, all of which seem to be oriented parallel to one another. Red arrows highlight small holes in the film. Enhancing the generation of borazine from AB through ball milling with hBN resulted in growth of highly aligned domains of SiO_x with increased domain size. Furthermore, in some parts, these aligned domains converged to form films of B,N-doped SiO_x on Cu.

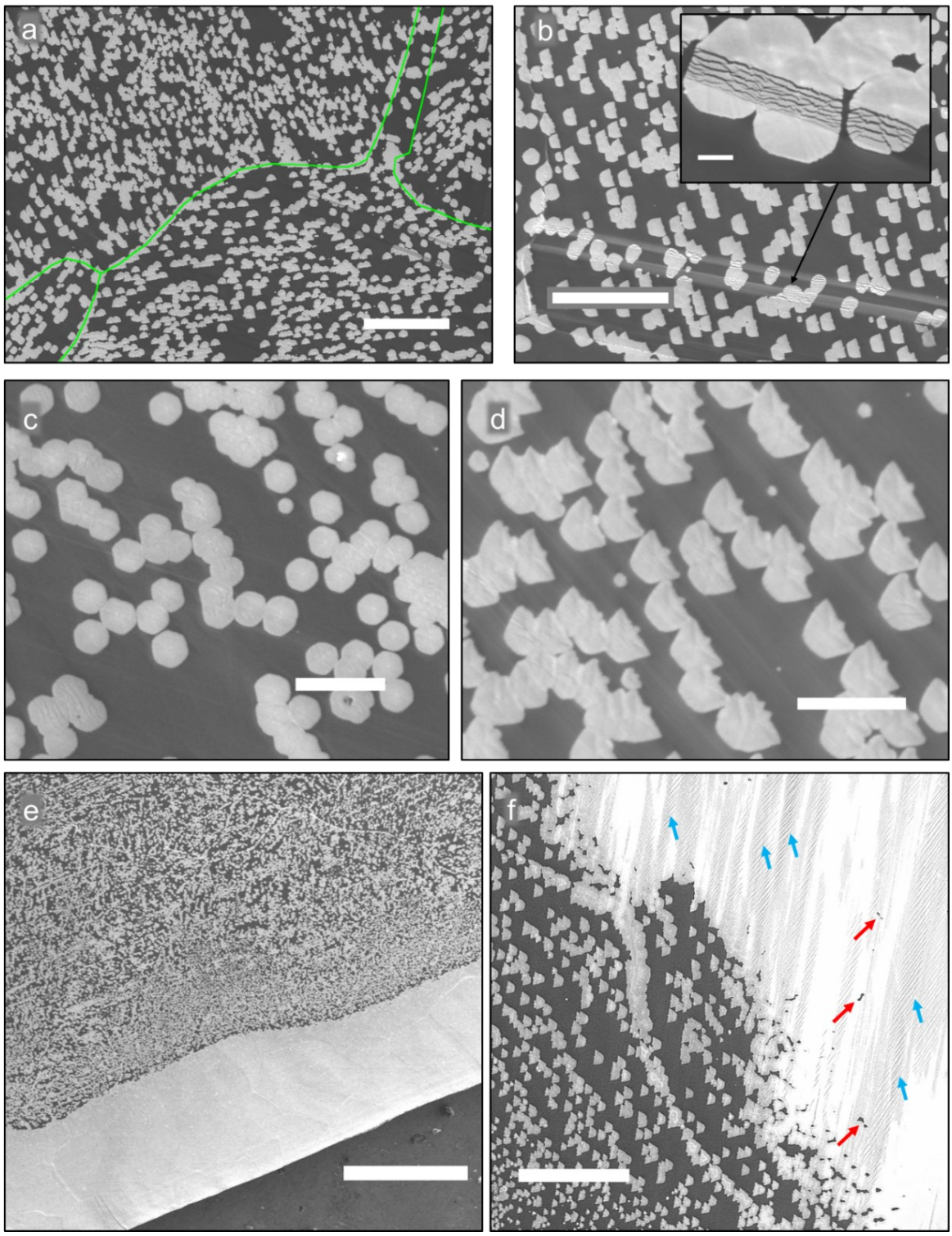


Figure 97; Results of hBN synthesis procedure using AB precursor ball milled with hBN powder. (a) Wide view SEM image showing different grains of Cu. Silica domains are aligned, showing a clear epitaxial relationship with the growth substrate. Scale bar is 150 um. (b) Facet of Cu showing step edges. The silica domains exhibit cracking along these edges. Scalebar is 75 um. Inset image shows a close-up of a similar region (scalebar is 5 um). (c,d) domains show different growth shapes yet highly homogenous domain sizes and alignment. Both scale bars are 30 um. (e) Wide view SEM image showing the edge of the Cu substrate. Increased nucleation has resulted in the formation of a converged silica film. Scale bar is 500 um. (f) Close up of the edge of the growth front of the silica film. Domains still show remarkable alignment. Red arrows show holes in the silica film whereas blue arrows highlight stepped lattice features in the film. Scalebar is 80 um.

Samples transferred onto flat Si/SiO_2 substrates were analysed via optical profilometry, results of which are displayed in Figure 98. Both individual domains and converged films show a height of ~ 20 nm, suggesting that the formation of the converged silica film is self-limiting on Cu. Folds are also observed in the converged film, as seen in Figure 98 (b).

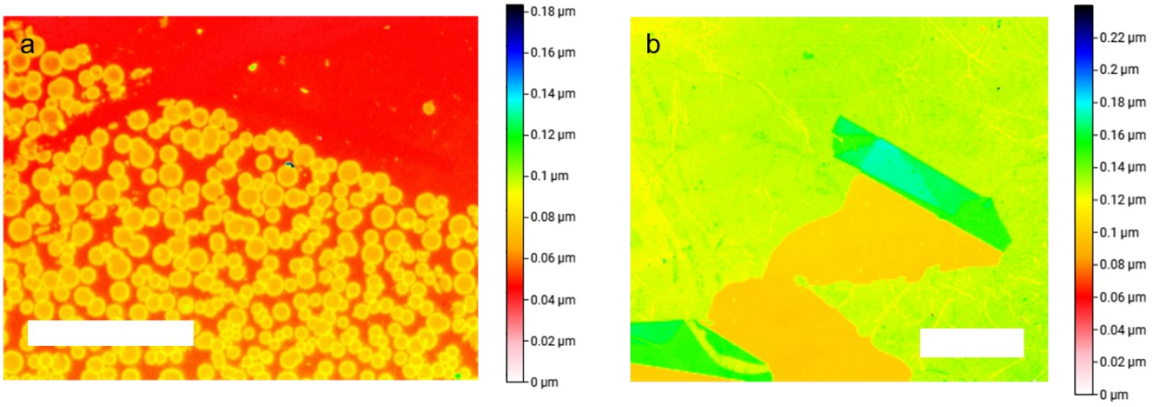


Figure 98; OP measurements of B,N doped SiO_x structures transferred onto Si/SiO_2 substrate. (a) Individual domains of the doped silica showing a circular domain shape and heights of ~20 nm. Scale bar is 50um (b) Fully converged film of doped silica transferred onto Si/SiO_2 substrate. Film heights were also measured to be ~20 nm. Scale bar is 100 um.

Due to the high degree of alignment and homogeneity of domain shape in the silica domains on Cu, it was thought that some degree of crystallinity may exist within the structures. TEM analysis was carried out to investigate this. Figure 99 shows results of this study. On the contrary, the structures show an amorphous structure, as seen in the FFT, inset in Figure 99 (b), where diffuse annular rings are found. Nanoparticles of size ~50 nm were also observed in the sample, transferred from the Cu growth substrate. Silica domains are seen to have a network of branches which converge and grow into one another (Figure 99, a-c). These types of structures are observed in many diffusive pattern-forming systems, such as those observed in electro-deposits of zinc, grown around a point cathode in an electrochemical cell [314, 315], shown in Figure 99 (e). In this study, similar structures were observed at low concentrations of the growth material and high voltages (driving force of the reaction). Here, the regularity of the structure is explained by the large difference in resistance at the interfaces of the electrolyte and zinc deposits, forming drift currents of drifting ions that can readily diffuse in the

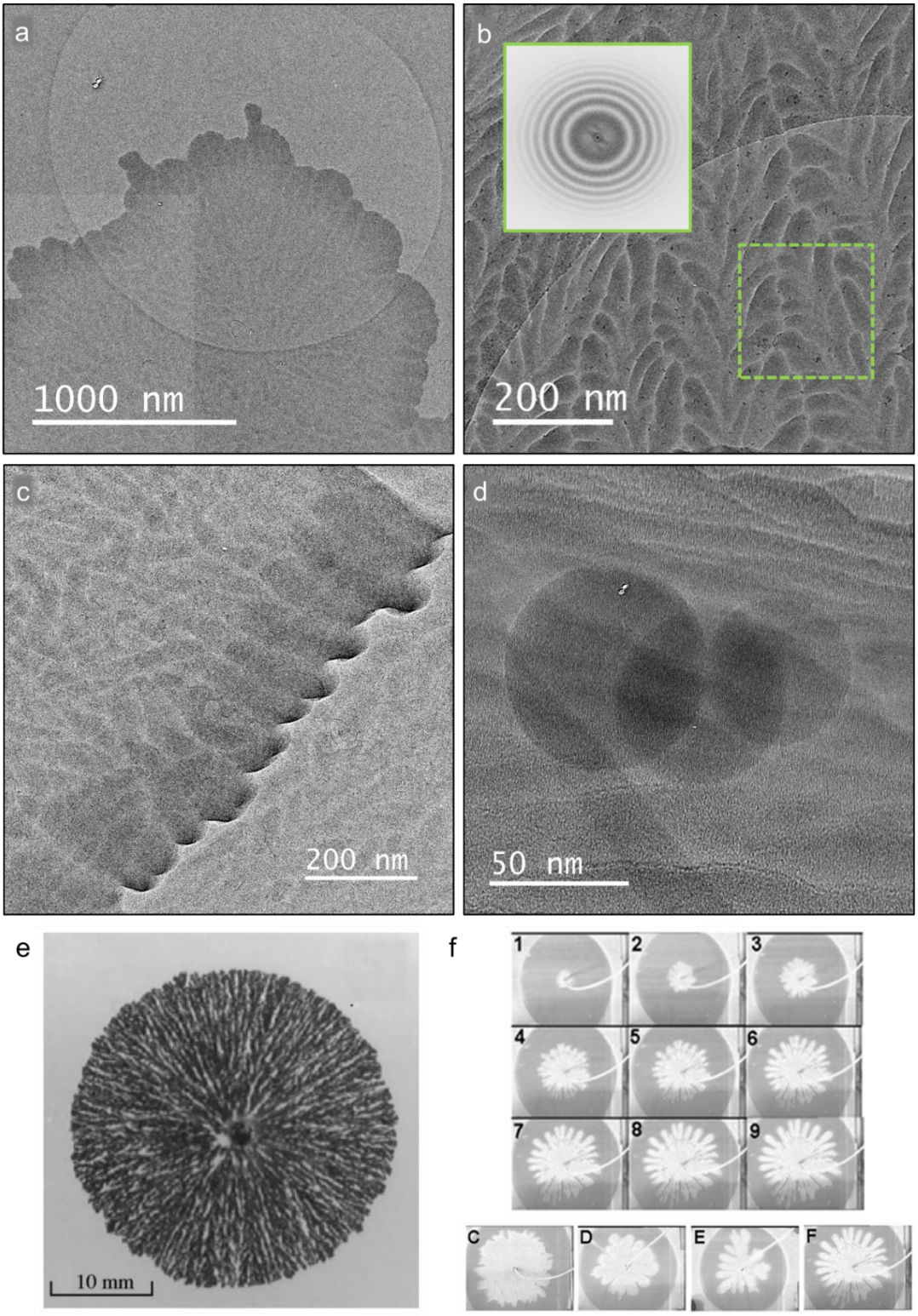


Figure 99; TEM analysis of growth structures seen in Figure 97. (a) Wide view TEM image of the doped silica structures that form on Cu. Contrast in the structure shows how it is composed of a network of individual branches which coalesce forming the overall domain. (b) Closer image of the branches in the domain. Inset is the FFT of the green dotted box which shows that the area is amorphous with no diffraction spots observed. (c) Image showing the edge of the domain. The darker contrast here suggests it is slightly thicker at the growth front. (d) Nanoparticles observed in the TEM sample, which also showed an amorphous structure. (e) Dense radial growth observed in zinc electrodeposits. Image taken from [314] (f) Structures formed in a Hele-Shaw cell over time (1-9) and at various viscosities (C-F). Image taken from [316]

electrolyte until deposited on the zinc metal. Similar structures have also been observed in fluid dynamics, particularly in Hele-Shaw flow, which is defined as Stokes flow (creeping flow) between two parallel, flat plates separated by a small gap (a similar geometry to our growth set-up) [316, 317]. In this type of fluid flow, viscous forces dominate, and it is the viscosity between two fluids which controls the shape and branching morphology in the resulting structures. Figure 99 (f) shows structures observed in a Hele-Shaw cell over time (1-9) and with varying viscosity of the second fluid (C-F) [316]. Similar branching morphologies are observed in our doped silica structures. Extrapolating this to our observations, we can infer that growth of these structures occurs in a similar fashion, via diffusion-controlled growth at an interface where two different viscosities exist; pure silica and doped silica. A comprehensive growth mechanism is further discussed in the next section, Section 5.3.5.

5.3.5. Proposed mechanism for B,N doped silica growth

The mechanism of formation for these doped silica domains is outlined in Figure 100. The growth of these B,N doped SiO_x 2D structures is likely facilitated through reaction of borates and other atypical decompsition products resulting from the low purity AB, with Si impurities in the Cu foil, which are deposited from the quartz wall. It has been well reported that quartz can become etched by H_2 gas at high temperatures [318]. In graphene CVD studies, quartz tubing has been known to exhibit aging due to the high temperatures of the CVD process which are close to the glass transition temperature of quartz (1200°C), and this etching ability of hydrogen on quartz. During CVD synthesis at high temperatures, hydrogen exposure induces the release of Si-O from the reactor wall which adsorbs on the surface of Cu via gas-phase transport where it is further reduced by hydrogen, with elemental Si dissolving into the Cu bulk [306, 307]. Typically, the amount of Si dissolved is low, and the near-surface Si concentration

remains below SEM detection, and hBN growth and crystalline quality is unaffected by its presence [306]. Still, small amount of Si is still detected via XPS of samples grown with high-purity AB. Appendix IV shows the survey scan for hBN grown on Cu with high purity AB from Chapter 3, where no Si impurities were observed via SEM, yet showing a clear Si peak in XPS.

In graphene CVD experiments, it has been shown that oxygen impurities in the CVD system react with the silicon dissolved in Cu, facilitating the growth of silicon dioxide particles on the Cu surface, disrupting graphene growth [307]. In graphene CVD synthesis, several sources have been proposed for the presence of oxygen impurities [319]; (a) the trapped air in quartz tube; (b) the native oxide layer on Cu surface; (c) the impure gas source and tiny leakages from environment. In the synthesis presented here, all three sources of oxygen can be considered to be negated through experimental controls; (a) three vacuum purge steps with Argon are used to remove any trapped air in the CVD tubing, (b) long annealing times of the Cu substrate with H_2 is employed to remove oxygen impurities in the Cu substrate and (c) the same gas purity and system set up is used here as in Chapter 3 for synthesis of hBN. Therefore, it is extremely likely that it is the oxygen related impurities in the low-purity AB that are creating the precipitation of doped silicate impurities on Cu. As mentioned previously, AB is hygroscopic and, as such, low-purity or degraded precursor likely contains significant borates or boric acid impurities [291]. When the Si-loaded Cu foil is exposed to oxygen via B-O impurities in the degraded or low-purity AB, Si segregates at the Cu surface where it forms doped silica structures. It is likely the borate that facilitates this growth, forming borosilicates, which are then further N doped from synthesis in the ammonia environment, producing the B, N doped silicate structures observed via XPS analysis.

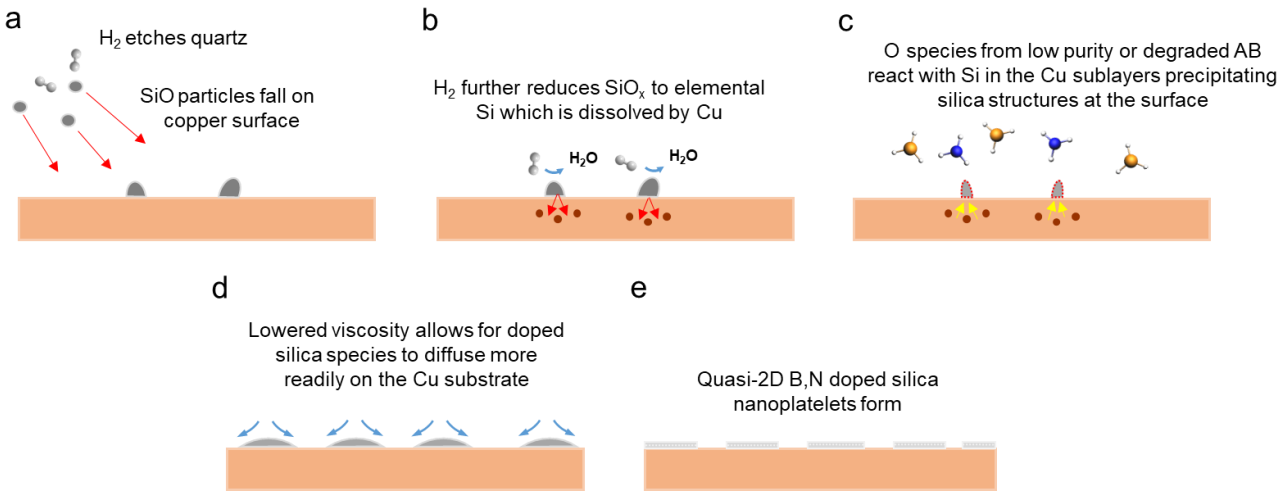


Figure 100; Growth mechanism for B,N doped silica layers on copper. (a) SiO attaches to the Cu surface via gas-phase transport from the quartz reactor, induced by H_2 and high synthesis temperatures. (b) Hydrogen further reduces Si-O on the surface of Cu, forming elemental Si which is readily absorbed into the Cu sublayers (c) Reactive oxide species which result from decomposition of the low purity precursor, ammonia borane, diffuse towards the surface of Cu where they interact with Si in the sublayer and precipitate doped silica structures, such as borosilicate and silicon oxynitride, on the surface of the nanoparticle. (d) These structures have a lower viscosity than pure SiO_2. Therefore, at elevated temperatures, they are more mobile on the growth substrate and grow outwards from the nucleation point. (e) When the Si in the sublayer has been spent, a 2D layer, or nanoplatelet, of B,N doped silica remains on the surface of Cu.

The 2-D quality of the structures likely results from the enhanced diffusivity of doped silica in comparison to SiO_x. It is well known that the viscosity of silica glass is reduced as it forms such doped structures, as shown in the Figure 101. At 1000 °C, $\log_{10}$(viscosity, η) of SiO_2 is > 12, whereas for borosilicate it is ~ 4. This means that at this temperature, there is a factor of 10^8 difference in viscosity between the two ($\eta_{sio2} = 10^8 \times \eta_{doped}$).

Viscosity is a parameter which influences diffusion, generally related via the Stokes Einstein equation;

$$D\eta = \frac{k_B T}{6\pi r_H} \qquad (29)$$

where D is the diffusion coefficient, η is the viscosity, k_B is Boltzmann's constant, r_H is the hydrodynamic radius and T is the absolute temperature. From this we observe that diffusivity is inversely proportional to viscosity. Therefore, as these silica species form on Cu and become increasingly doped via B and N reactive species, their diffusivity increases, such that they 'flow' and extend across the copper surface, forming 2D domains and becoming increasingly

visible under SEM as they form extended platelets and the beam interaction with them increases. This hypothesis is supported by TEM and SEM observations, where structures indicative of diffusion-controlled growth are observed (Figure 99), and growth often emanates from a central locus (Figure 96, c). Yet, SEM images also show a definite epitaxial relationship in the larger growth structures (Figure 97). Doped silica domains on the copper substrate show almost identical alignment on an individual growth facet with the homogenous domain only changing shape from one Cu facet to another. This suggests that diffusion-control is not the only aspect mediating growth here, and that the Cu substrate does have some epitaxial relationship with the growing domain.

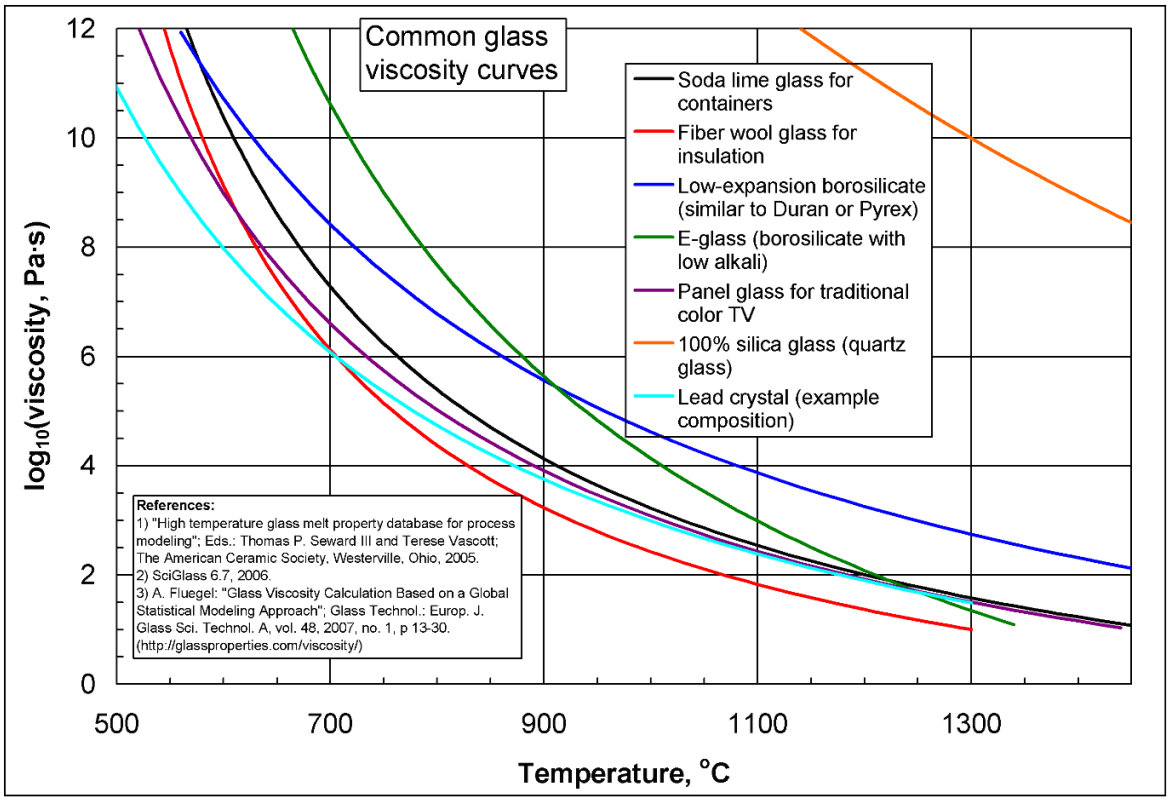


Figure 101; Viscosity of various silica based materials across a temperature scale. At 1000 °C, the viscosity of pure quartz is significantly higher than that of borosilicate (e-glass). Reproduced from *[320]*

5.4. Conclusion

In this section, a low purity ammonia-borane (AB) precursor was trialled which showed remarkably different growth structures in comparison to growth with high purity and fresh AB. These structures were characterised as SiO_x via EDX analysis, with XPS studies giving more information on the chemical environment in the silica structures. XPS analysis found the presence of boron and nitrogen in the structures which is interpreted as silica structures being doped with borosilicate and silicon oxynitride units from the interaction with the AB precursor.

Attempts were made to identify the source Si contamination by using alumina substrate holders and removing impurities from the Cu substrate. However, structures persisted. This suggests that the origin of the silica impurities arise from the CVD reactor itself. It follows then that quartz tubes are not an ideal experimental apparatus for CVD synthesis of hBN due to Si_xO_y contamination reacting with species produced from low-purity AB decomposition, something highlighted with the use of 85% purity AB precursor.

As this had not previously been an issue using fresh, high purity AB, attempts were made to improve the purity of the precursor, through recrystallization, and its decomposition profile, through ball milling with hBN powder. This *increased* the size of doped silica structures on the Cu substrate. This likely results from a lower concentration of reactive oxygen species in the AB, facilitating less nucleation, and promoting growth of larger individual domains. However oxide species still persist, and thus silica structures precipitate. A clear epitaxial relationship was observed with domains showing great alignment and homogeneity in shape on individual facets of copper. TEM characterisation found that the structures were amorphous and exhibited branching structures similar to those observed in diffusion-controlled interfacial growth [314-316].

A growth mechanism is proposed for the doped silica structures, using evidence gathered on their chemical composition and nanostructure, as well as other observations in the literature on graphene CVD and on diffusion-controlled growth; Si impurities in Cu, resulting from H_2 degradation of the quartz reactor, precipitate with reactive oxide species from the decomposition of low purity AB (likely borate species), forming silicates at the surface of Cu. As Si was detected in both control and experimental synthesis, Si is likely introduced to the Cu substrate through the pre-treatment H_2 annealing process, employed to remove any oxide layer on Cu and increase the Cu grain size. As borate species land on the Cu substrate, dissolved Si atoms in the Cu sub-layers are attracted towards the surface, precipitating as borosilicates structures. As the growth process proceeds, precipitated silicates on Cu are increasingly doped by the B and N vapours, forming borosilicate and silicon oxynitride species. The change in chemical composition and structure of silica changes the viscosity of the material significantly. At elevated temperatures, these doped structures are more mobile on the Cu growth substrate and grow outwards from the nucleation point forming extended doped, silica domains. Optical profilometry studies showed both domains and coalesced films as having a consistent height profile of ~20 nm. No layer plus island growth was observed, suggesting that growth of these structures is self-limiting on the Cu surface. As such, a copper-silica interaction likely exists within these structures and facilitates their growth, further evidenced by the epitaxial relationship of the silica domains on the Cu substrate.

In future work on CVD growth of hBN, researchers should avoid using a quartz CVD reactor, and instead employ a cold wall CVD technique, where only the substrate is inductively heated and not the surrounding reactor walls, preventing the occurrence of Si_xO_y impurities and thus promoting quality hBN deposition. Consideration should also be given to the purity and aging limitations of the ammonia borane precursor, as this was shown to have significant effects on the resulting growth. As AB is also used as a hydrogen storage material, there are a range of

AB products with different purities available on the market. However, many CVD studies on hBN growth fail to explicitly identify the purity of their ammonia-borane precursor [120, 198, 202, 206, 288, 292, 293], which evidently has implications when it comes to reproducibility of results. Future researchers should ensure that they are reporting the purity of their precursor accurately in their studies to enable effective comparisons and improve transparency of synthesis results.

Chapter 6

Porous Nanomaterial Foams and Composites

6.1. Introduction

Given the impressive properties of 2D materials such as graphene, hBN and hBCN, it is unsurprising that research has been focused on creating strategies for assembling 2D layers into 3D architectures for applications as battery electrodes [1, 321], supercapacitors [3, 4], sensors [20, 21] and catalysts [7, 11]. Several methods have been developed for producing 3D architectures of 2D materials from both "bottom-up" and "top-down" approaches. The purity and quality of the material formed is directly dependent on the synthesis method used to create it. Top-down approaches typically employ exfoliated 2D layers that are then either pyrolytically treated [322] or freeze-casted [323] to form 3D interconnected structures. Using these techniques, high throughput can be achieved but at the expense of having less control over the quality of 2D materials being synthesised.

Alternatively, bottom-up synthesis, such as CVD, allows for synthesis of high quality 2D materials with controllable layer number and defect concentrations. However, the higher cost associated with this technique limits its adoption. On the market, porous metal foam templates are commercially available but are often expensive. Foams are typically produced by melting metal with salts, packed alongside the metal powder, and annealed at high temperatures and pressures. After cooling, the salts can be leached from the structure, leaving the open pore morphology (see Figure 103 for an example of open pore morphology). Foams can also be produced by addition of foaming agents to the molten metal which decompose at a certain temperature, evolving gases to foam the material [324]. The high costs associated with these techniques mean that the overall cost for 2D material functionalised foams is high. For example, currently, the price of a 50 x 64 x 5 mm Cu foam piece from GoodFellow Cambridge Ltd. is £300 [325]. Such high prices can inhibit the economic feasibility of this CVD synthesis method for 3D architectures of 2D materials.

To circumvent this, the synthesis method presented here utilises inexpensive Cu metal powders to synthesise 3D porous metal scaffolds, costing in comparison ~ £10 for a similar sized porous substrate. The benefits of this method are not only lower cost, but also increased pore density in comparison to the commercially available foams. The method uses principles of diffusion bonding, where metal microparticles are heated close to their melting point such that they intersperse themselves over time, forming an interconnected porous scaffold onto which the 2D materials can be grown. Figure 102 shows a schematic of the processes involved. In this chapter, we use an up-scalable method developed in our group [326] to form porous metal templates from low-cost metal powders during an initial annealing stage, followed by CVD synthesis to produce a 3D Cu metal-2DM composite.

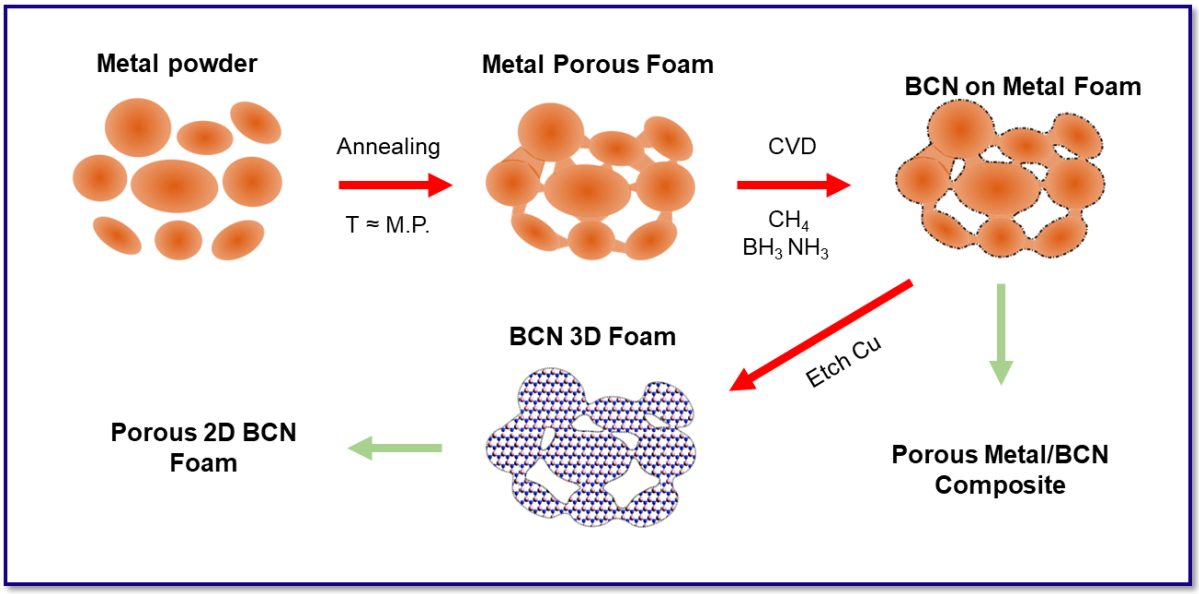


Figure 102; Synthesis schematic for the formation of 2DM-metal foam composites and 2DM foams via CVD.

Intrinsically, metal foams are a promising matrix due to their high surface area, porosity and both thermal and electrical conductivity. Existing commercial foam production is now being explored in combination with CVD in industry to produce novel composite structures [327]. By carrying out additional processing techniques to alter the surface of the metal foams, we can potentially enhance and tune its functionality.

Thus far within this thesis, we have used CVD methods to produce 2D layers of graphene, hBN and hBCN materials. On metal foils, production of these materials is achieved on a relatively small scale. By using a 3D architecture of the catalytic substrate, 2D material / metal composites can be synthesized on a far greater scale, with structures possessing a larger functional surface area. By adding a further processing step, whereby the metal foam scaffold is etched, 3D porous architectures of 2D materials can potentially be realised.

Metal foams functionalised with 2D graphene have previously been reported, with majority of reports focusing on Ni as the catalyst substrate [328-331]. Research into materials Cu is lacking in comparison, although graphene deposition has been achieved on 3D foams of Cu [332], and more recently, Cu-Ni [333], which could be of economic interest, as they are 47% the cost of Ni (Figure 103 g). Several of these studies detail how 2D material-metal composites can improve the performance of the intrinsic metal. Yang *et al.* studied Gr-Cu foams as effective anode materials in lithium batteries (Figure 103, a-d). Their study showed how depositing a graphene layer on the surface of the Cu foam enhanced its stability and performance, reducing the occurrence of Li dendrites even after long term cycling [332]. Madito *et al.* evaluated the performance of graphene coated Cu-Ni foams and found an improvement in capacitance performance with graphene deposition [333]. Similarly, Shah *et al.* compared the photo-electro-chemical performance of Ni and graphene coated Ni foams (Figure 103, e-f) for water splitting, and found that graphene significantly enhanced the material's performance [329]. Expanding this field into hBN and mixed BCN growth on Cu metal foams is thus of interest for the scientific community and developing methods for synthesising novel BN/BCN-metal composites could provide new functionalities in the aforementioned applications.

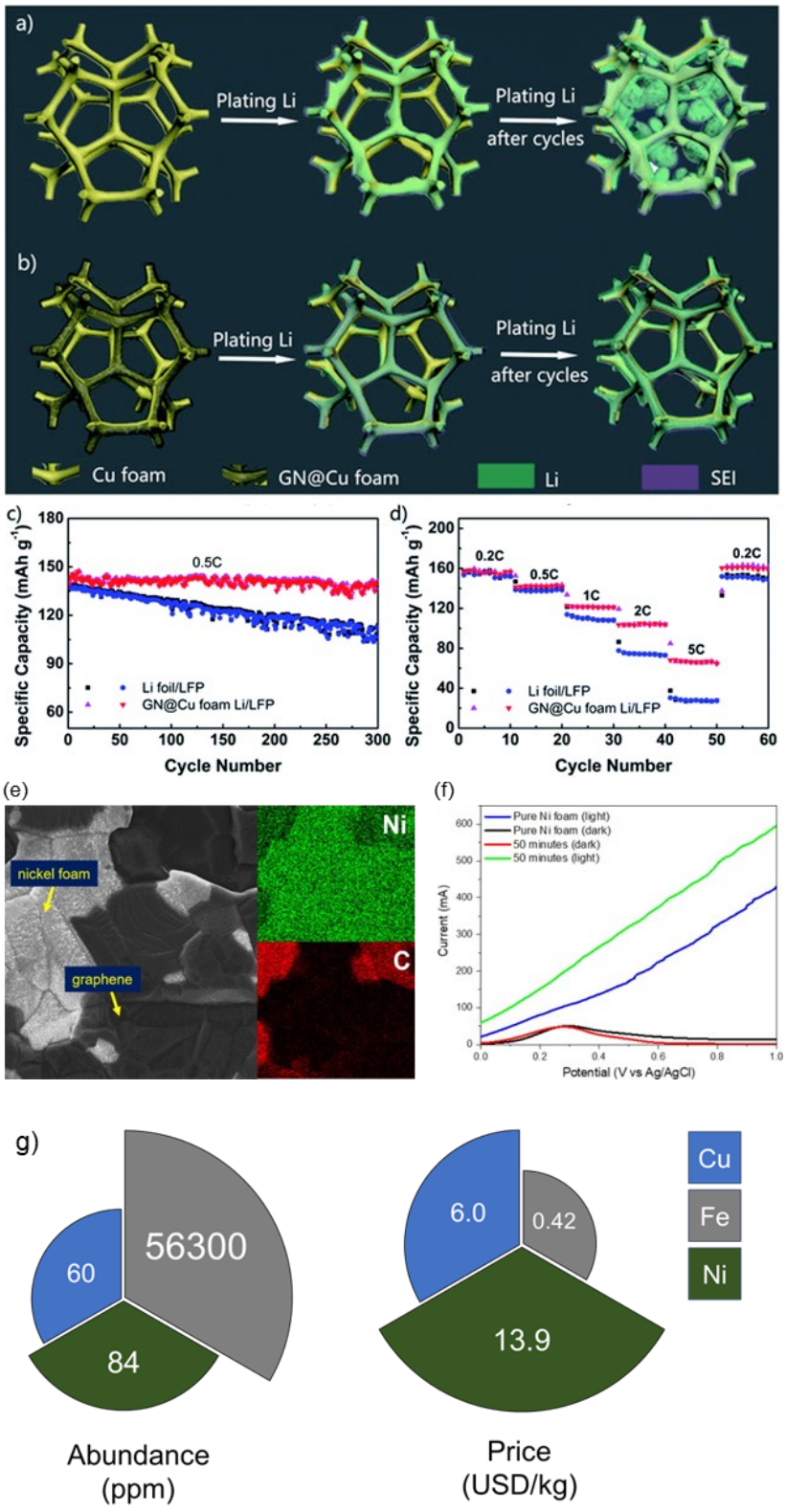


Figure 103; Applications of 2D graphene - 3D metal foam composites. Graphene-Cu foam composite showing enhanced uniformity and stability during Li deposition. (a) With bare Cu foams, Li deposition is unregulated, and dendritic Li deposits form. (b) On Gr-Cu foams, Li is deposited uniformly. (c,d) Enhanced cycling performance of the Gr-Cu composite in comparison to a Li foil anode. Reproduced with permissions from *[332]*. (e) EDX of Gr-Ni foam composites which shows (f) enhanced performance in photoelectrochemical water splitting in comparison to the bare Ni foam. Reproduced with permissions from *[329]*. (g) Economic advantages of using Cu and Fe foams. Fe is more abundant and significantly cheaper than Cu and Ni. Cu an Ni are similarly abundant, however, Cu is less than half the price of Ni.

Studies on freestanding 3D BCN foams have showcased enhanced performance of doped graphene structures. Xue *et al.* were able to synthesise B,N doped graphene foams on Ni, which showed good propensity for ORR (Figure 104) [16]. Interestingly, the B,N doped graphene foam showed enhanced current generation capability, and better stability in the presence of CO than traditional Pt/C based catalysts. However, the drawbacks of this study were the reactants used; tri-ethylborane and ammonia, which are highly flammable and corrosive, meaning upscaling of this technique could prove difficult. Similarly, Feng *et al.* used traditional Ni foams to synthesise freestanding N-doped graphene structures from ethylenediamine, which showed to be ultrasensitive electrochemical sensors for the detection of dopamine [334]. Again, the precursors used were toxic and highly flammable, which can be difficult to handle and pose obvious health risks. As such, there is room for designing a synthesis of B,N doped 3D graphene using safer and less toxic precursors, such as those used in this thesis; ammonia borane and methane. This research attempts to improve existing literature on 3D CA-CVD architectures of BCN by trialling non-toxic precursors of ammonia-borane and methane, and simple low-cost metal powders of Cu to form novel 3D Cu foam-2D BCN composites. These composite structures can be used as is or further processing steps can be carried out to obtain metal-free 3D structures comprised of 2D layers.

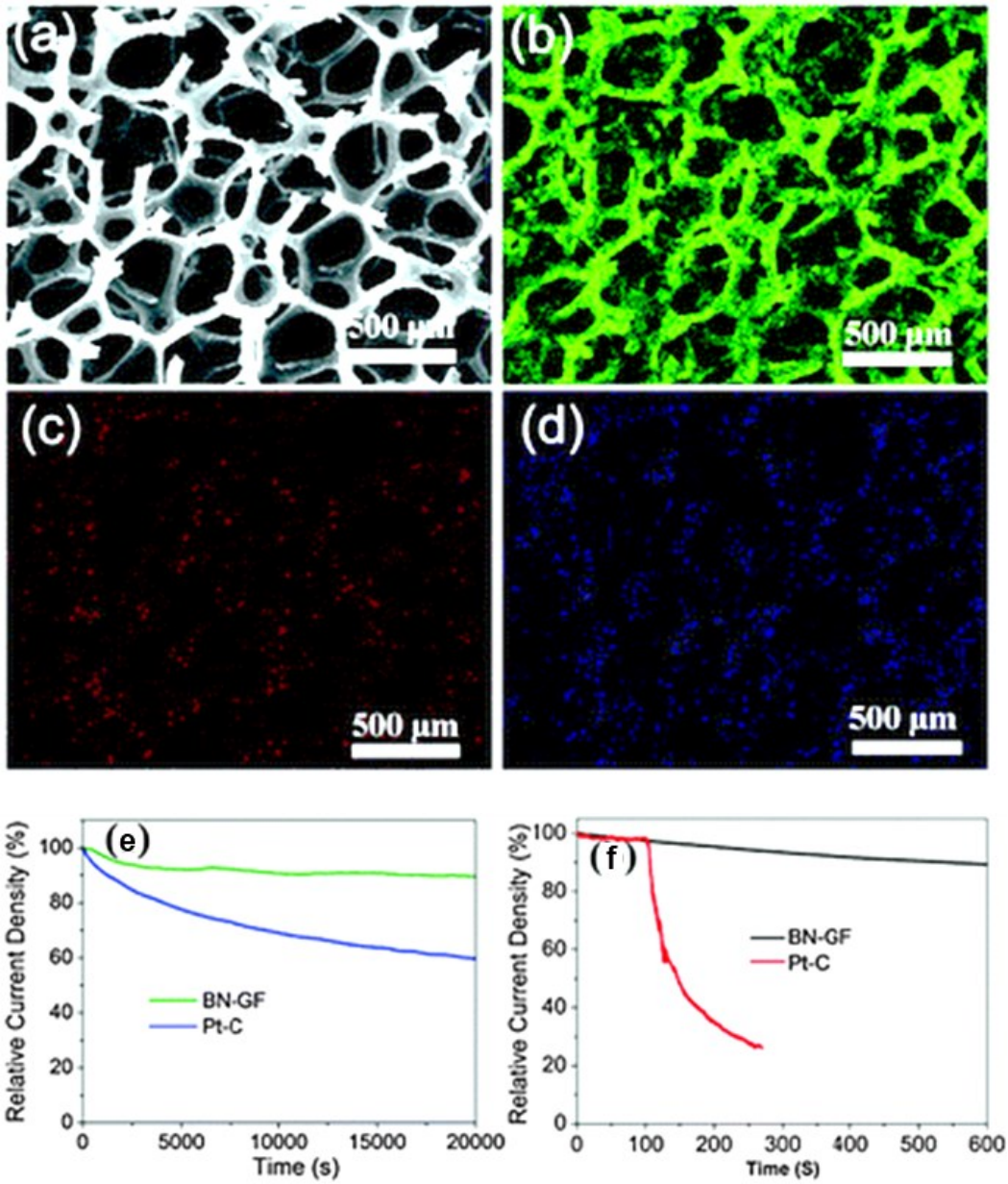


Figure 104; Applications of BCN freestanding foams. EDX maps of B,N doped graphene foams synthesised on Ni foams. (a) SEM micrograph of foam with (b) carbon, (c) boron and (d) nitrogen elemental maps. Current–time response of the B,N doped graphene foam/glassy carbon(GC) electrode, and the standard Pt–C/GC electrode under (e) standard conditions and (f) introduction of CO into the electrolyte. Reproduced from [16].

6.2. Materials and Methods

Materials

Copper powder (Alfa Aesar, spherical, APS 10 micron, 99.9% metals basis, CAS 7440-50-8), acetone (Sigma Aldrich - ACS reagent, ≥99.5% - 179124), IPA (Sigma Aldrich - ACS reagent, ≥99.5% - 190764), acetic acid (Sigma Aldrich - glacial, ACS reagent, ≥99.7% - 695092),

ammonium persulfate (Sigma Aldrich - 98%, reagent grade - 215589), ammonia borane complex (Sigma Aldrich - 682098 , ≥97%), methane gas (BOC Ltd., ≥99.995%) argon gas (BOC Ltd., ≥99.995%), hydrogen gas (BOC Ltd. ≥99.995%).

Methods

Metal micro-particle cleaning; Metal powders were sequentially washed and sonicated in DI water, acetone and acetic acid for 10 minutes each to remove impurities and organic residues. Afterwards, the particles were washed three times with DI water before filtering and drying under vacuum.

Copper foam-2DM composite synthesis; 5-10g of cleaned Cu powder was loaded into an alumina boat (97 x 17 x 12 mm) and loaded into the CVD system. The powder was annealed at atmospheric pressure at 900 °C in 200 sccm flow of H_2 (100%) for 60 minutes to clean and activate metallic microparticles to initiate 'necking', i.e. the initial formation of the foam template. Immediately after this step, the gas composition was changed to allow for 2DM growth.

Graphene growth on Cu foam; For graphene-Cu samples, gas flows were set to 1-20 sccm CH_4, 200-250 sccm H_2 for 30-60 minutes with the furnace temperature set to 1050 °C.

hBN growth on Cu foam; For hBN-Cu samples, 100-800 mg ammonia borane was heated at 80ºC under 10 sccm H_2 / 190 scccm Ar flow for 60-90 minutes with the furnace temperature set to 1050 °C.

Graphene-hBN growth on Cu foam; Graphene growth was first carried out for 20 minutes under 10 sccm CH_4, 200 sccm H_2 flow followed by 60 minutes of hBN growth where 800 mg ammonia borane was heated at 80 °C under 10 sccm H_2 / 190 scccm Ar flow. The temperature of the furnace was set at 1050 °C for both growth stages.

hBCN growth on Cu foam; 800 mg ammonia borane (T_{AB} = 80 ºC) was introduced simultaneously under the flow of 10 sccm CH_4 and 200 sccm H_2 for 40 minutes with the furnace temperature set at 1050 °C.

After all composite growths, the sample was slowly cooled by gradually shifting the furnace. This step was necessary to suppress any crack formation as the composite cools.

Removal of metal template to realise porous 2DM foam; the metal foam-2DM composite was placed in a solution of 0.3 M ammonium persulfate at 60 °C for 48 hours. After the metal template had been dissolved, the porous 2DM foam was transferred to a solution of DI water and soaked for 30 minutes before transferring to a fresh solution of DI water. This step was repeated a further to times to ensure removal of the etchant solution.

6.3. Results & Discussion

6.3.1. Synthesis of Porous 3D metal foam from Cu powder

Bare Cu foam structures synthesised from Cu powder are seen in Figure 105. First, Cu powder contained in an alumina crucible is placed in the CVD furnace (Figure 105, a). After the annealing process, the particles form a porous block, as seen in Figure 105 (b). SEM micrographs of the foam detail this porous structure, with pore diameters of size ~10 μm, far smaller than the typical pore size of the commercially available Cu foams [325], and exhibiting a convex ligament geometry as compared to the concave ligament geometries found in open-cell structures (Figure 105, c-e).

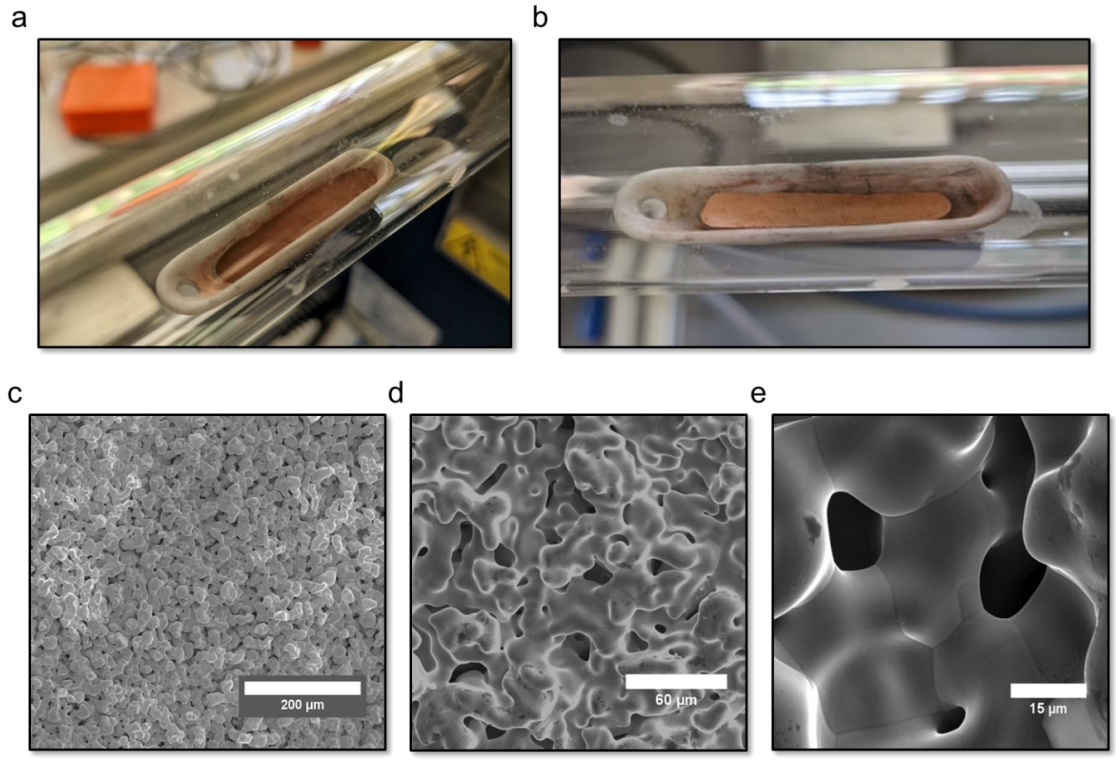


Figure 105; Synthesis of bare Cu foam template. (a) Cu powder loaded into the CVD furnace in an alumina boat. (b) Post annealing, a Cu foam block is realised. (c-e) Surface morphology of the Cu foam as shown by SEM analysis.

6.3.2. Graphene on copper foam

After the formation of the porous Cu substrate, CVD growth of the desired 2D material could be carried out. A gas composition ratio of 1:20 (10 sccm CH_4, 200 H_2) or lower was required to form fully converged domains on the Cu substrate. Higher ratios (1:25) produced patchy coverage of the Cu foam, as seen in the SEM micrographs Figure 106 (a,b). The morphology of these graphene domains is generally associated with diffusion-controlled growth [154, 224, 225], i.e. where the rate of hydrocarbon diffusion on Cu is significantly lower than the rate of 'edge attachment' [223, 224]. By increasing the partial pressure of CH_4, a fully converged graphene sheet is observed on the Cu template after 40 minutes of growth. As discussed in previous chapters, 2D growth on Cu is self-limiting, with the growth rate reducing significantly as the catalytic surface is coated. As such, small regions of bare Cu of size ~5 µm (Figure 106, c) are also observed.

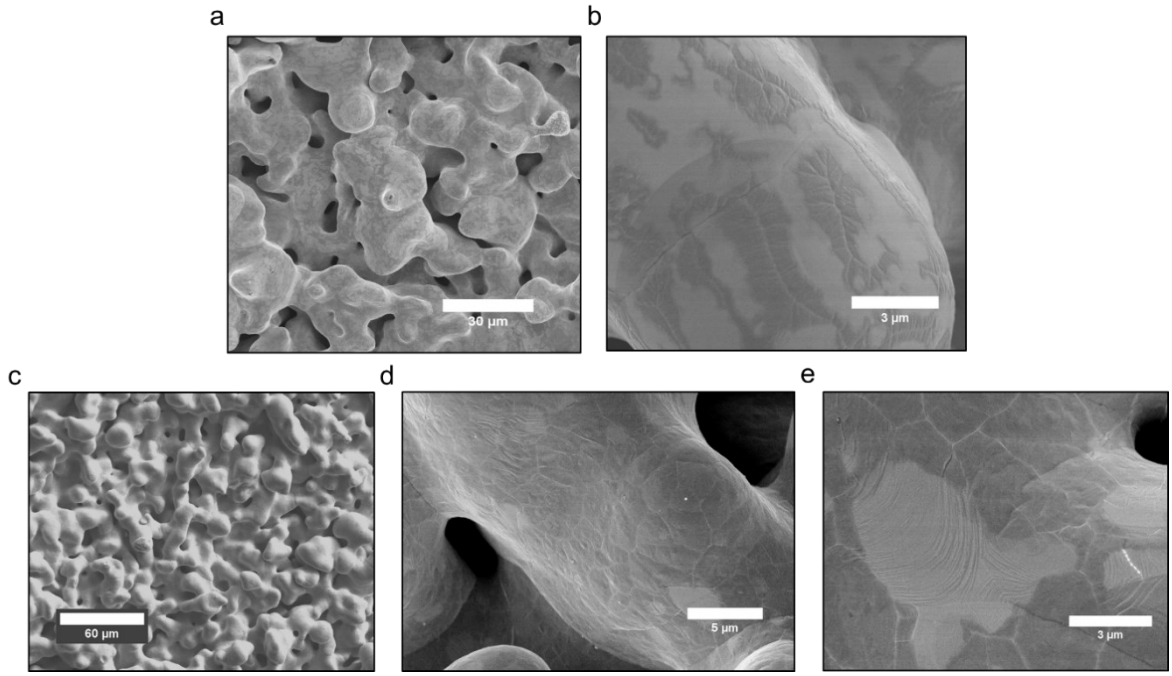


Figure 106; SEM analysis of graphene deposition on Cu foam. (a,b) Dendritic graphene domain growth is observed for low partial pressures of methane. (c-e) Increasing this, the Cu foam is almost fully coated with graphene after a deposition time of 40 mins.

After graphene deposition, the Cu template was removed via a gentle etching process, as seen in Figure 107. The Gr-Cu block was etched in 0.3 M ammonium persulfate solution over a period of 2 days. Figure 107 (b) exhibits this mid-process, where the black, porous graphene foam is observed alongside gas bubbles from the etching process. After complete removal of the Cu template, the resulting foam floats to the surface as a result of the low density and gas bubbles that get trapped in the structure during the etching process, which can then be collected, washed and dried.

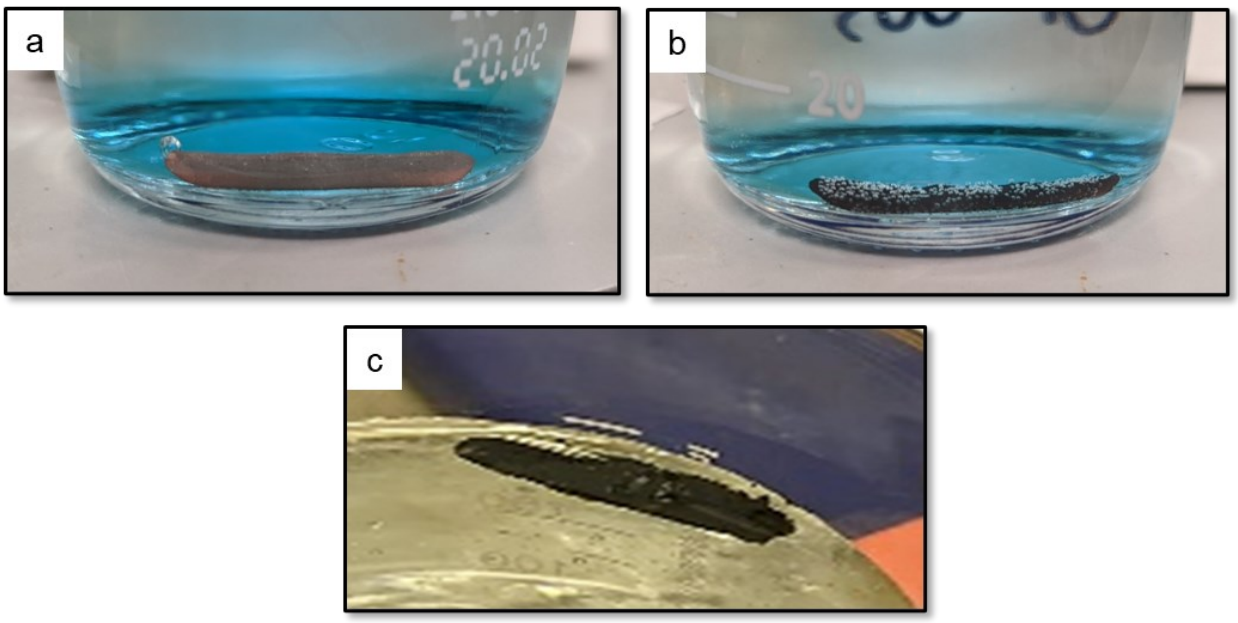


Figure 107; Etching and washing of Cu foam. OMs of the etching process of the Gr-Cu composite at (a) the beginning of the process, (b) mid-way through the process and (c) after the Cu metal had been fully etched.

SEM images detail the microstructure of the dried graphene foams in Figure 108 (a-c). In some areas of the foam, the structure is collapsed after the drying process. As the foam dries, surface tension from the evaporating liquid causes the 3D structure to give way and collapse in on itself, resulting in crumpled morphologies like those found in Figure 108 (a,b). In other regions of the foam, the 3D nature of the structure is retained (Figure 108, c). Raman spectroscopy on the graphene foam (Figure 108, d) showed similar defect concentrations as those synthesised on Cu foil, with a D/G ratio of 0.24, and thus the layers exhibit slight disorder. Few-layer graphene coverage was confirmed also with a 2D/G ratio of 0.4. TEM edge-analysis (Figure 108, e-f) shows a thickness of 3-4 nm in the walls of the foam structure, suggesting the sample is few-layered graphene of around 9-12 layers. Although not monolayer, this is still a very thin 3D structure, which may explain why the structure is partially collapsed after drying. Various methods of drying the foam were trialed, such as drying under vacuum, drying from ethanol, and freeze drying, which avoids capillary action of evaporative drying. However, none of these methods resulted in a fully self-supported 3D graphene foam.

The super-lightweight nature and nanometre thickness of the graphene foam also meant that handling the dried product was very difficult, and the foam would often tear after removing from the substrate upon which it was dried. As such, foams synthesised should be used in applications where drying-free processing methods are used. The etched foam structure can be swapped directly after washing to their desired liquid medium for application. For example, in catalysis, reactions are often carried out in liquid environments and so foams synthesised via this method could be used as active catalytic materials [16, 329, 335] or as catalytic supports [335].

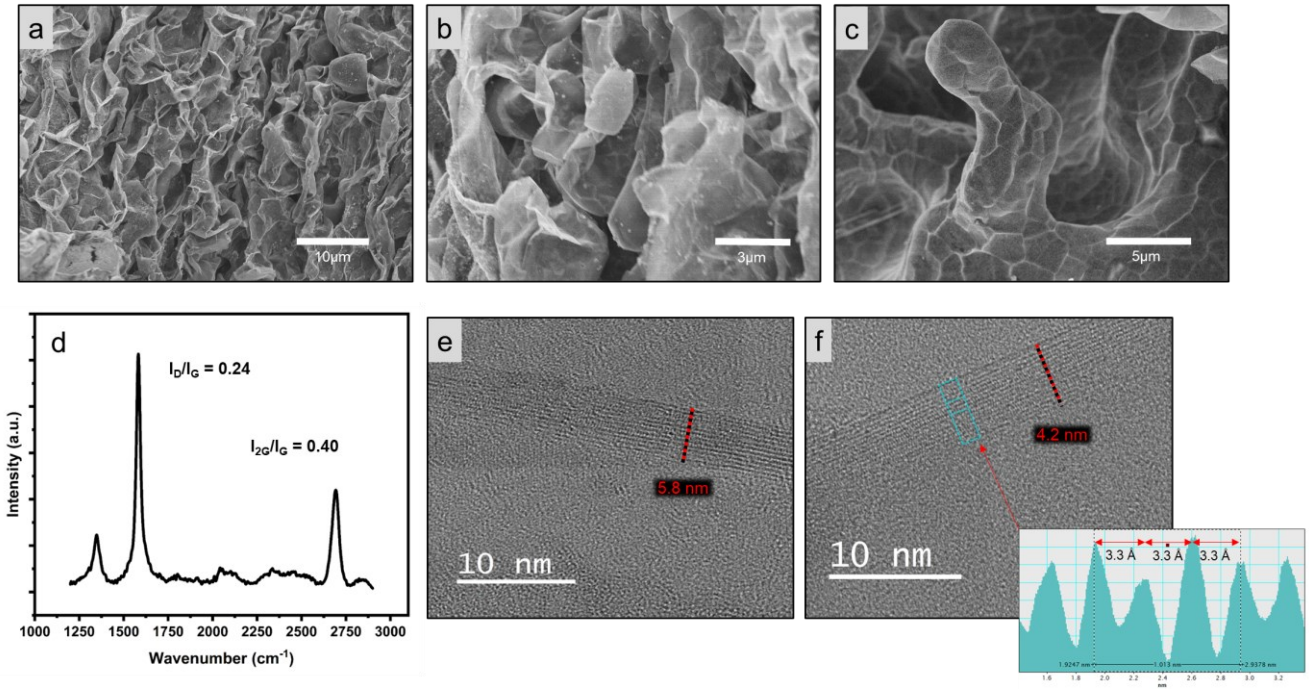


Figure 108; Removal of Cu template from Gr-Cu foam. (a-c) SEM images show the partially collapsed structure of the graphene foam upon etching of the Cu template (a,b) with some regions retaining their 3D structure (c). (d) Raman characterisation of the etched Gr foam (e) TEM image of a fold in the graphene foam. The fold here show a thickness of 5.8 nm, suggesting a wall thickness of 2.9 nm. (f) Edge analysis of the graphene foam shows lattice spacings identical to theoretical values (3.3 Å). The edge thickness is measured to be 4.2 nm, equivalent to 12 layers of graphene.

Similarly, applications as porous anode/cathode materials are feasible in battery systems where a liquid electrolyte is used [328, 331]. Here, graphene foams are particularly suited to improve the gravimetric energy density of lithium-based batteries due to their low density, interconnected, conductive structure as well as enhanced chemical resistance. As such,

although these foams fall short of achieving a stand-alone structure, their inherent benefits of high pore density, increased surface area can find application in other scientifically relevant areas.

6.3.3. hBN on copper foam

Similar to the case of graphene, the optimised synthesis parameters for hBN deposition on Cu had to be adjusted slightly in order to accommodate fully converged hBN domains. Figure 109 shows SEM micrographs detailing hBN synthesis on the Cu template at precursor, ammonia borane, loading capacities of 100 mg (Figure 109, a-c), 300 mg (Figure 109, d-f) and 800 mg (Figure 109, g-i). A 5% H_2 in Ar environment was used with the gas flow fixed at 250 sccm for all experiments. With precursor loading of 100 mg, only small hBN islands of ~1 μm are observed. Whilst growth is achieved, the rate is too slow. If we were to extend the growth time to accommodate full coverage, the porous nature of the Cu foam would likely be lost as the Cu particles would form a solid block. By increasing the loading amount to 300 mg, the nucleation density of the hBN domains increase on the Cu template and fully converged regions are observed (Figure 109, d-f). The domain sizes are still small, of the order of ~2 μm. Small, circular, nucleation points can be seen, also apparent in images (a-c), which suggest that the hBN domains are nucleating from defects on the surface of the Cu template. In Figure 109 (g-i), the loading of AB precursor is increased once more to 800 mg, almost full coverage is observed and thicker depositions are formed, exhibiting wrinkles that form during the cooling process.

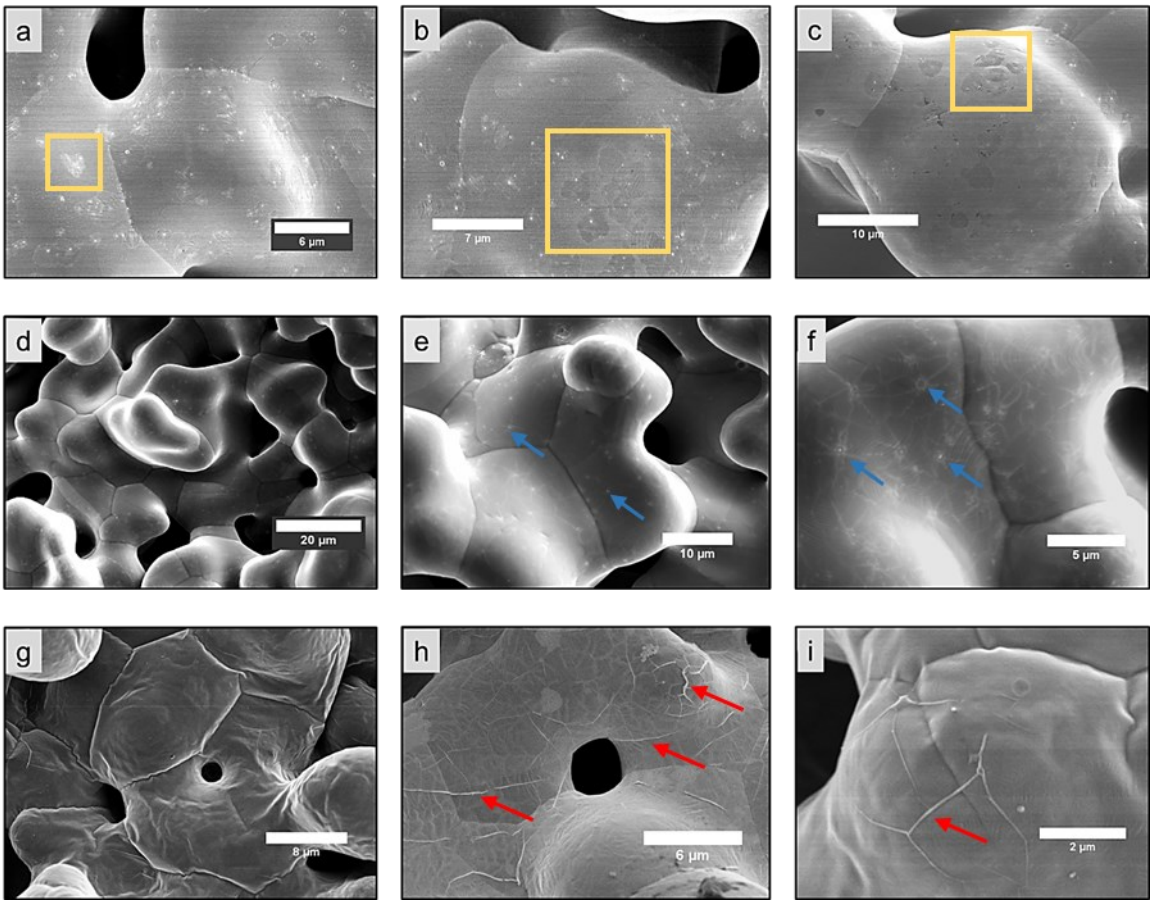


Figure 109; SEM analysis of hBN deposition on Cu foam. (a-c) hBN growth with AB loading of 100mg. Small islands are observed with lateral sizes ~2 µm, highlighted in the yellow boxes. (d-f) hBN growth with AB loading of 300 mg. Coalesced domains are observed, nucleating from defect points, highlighted by the blue arrows. Domain edges of hBN show a lighter contrast in the SEM image (g-i) hBN growth with AB loading 800 mg. Wrinkles are observed on the surface suggesting thicker growth, marked by the red arrows.

Composites like this can offer an increased durability to the Cu foam, in terms of chemical resistance. Recently, Yang *et al.* used graphene anchored on a Cu foam as a current collector in a lithium ion cell and found that the composite produces an increasingly uniform and stable Li deposition and exhibits excellent cycling performance [332]. In a similar vein, Xie *et al.* investigated hBN as a stable interface between Cu and Li for lithium metal anodes [40]. Their study found that Li plating/stripping at the h-BN/Cu foil interface was considerably more stable than that on pristine Cu, with lower overpotentials and higher coulombic efficiencies over long cycles. On account of these studies, it would be of interest to test hBN-Cu foam composites synthesised here as a 3D current collector in Li batteries.

Elemental analysis was carried out to confirm hBN on the Cu template for samples synthesised with 300 mg of AB. The B:N atomic ratio is determined to be 1.03 : 1. High resolution XPS spectra of the N1s and B1s regions are shown in Figure 110 (d-e). The N1s peak can be broken down into two components, a large peak at 398.0 eV and a small peak at 399.1 eV, corresponding to N-B and N-C bonding, respectively [10, 18, 336]. As metal powder is used to form the substrate, vacuum purges were not carried out at the beginning of the synthesis and thus some C contamination may exist, resulting in N-C bonding. The B1s spectrum is fitted with a singular peak at 190.4 eV, corresponding to B-N bonding in the sample [12, 18, 336].

The hBN-Cu composite was etched in a similar fashion as the Gr-Cu foam. It was observed that, once the scaffold was etched, the hBN foam showed no structural stability. The foam was extremely brittle and would break into pieces upon transferring from the etchant solution. Figure 110 (a-c) shows SEM images of a collected section of the foam with the structure collapsed in on itself and large regions lying flat on the silicon substrate. Small holes are also observed in the hBN, which may correlate with the defect sites observed in Figure 109 (e, f). The poor structural stability of the hBN foam is unsurprising, given that continuous multilayer growth on Cu is limited. Previous reports of hBN growth on Cu have shown that multilayer formation tends to occur between N precursors and B at the surface of the Cu substrate [134], i.e. only when precursors are in contact with the catalyst surface. It follows then that, as hBN is deposited, the growth rate decreases significantly, and multilayer growth is slow.

Figure 110 (f) shows TEM micrographs of folds within the foam structure. Edge-analysis of folds in the hBN foam showed the walls to be 4-5 layers thick, almost half as thin as walls of the Gr foam. It is understood then, why the hBN foam is even more prone to tearing and collapsing in on itself after washing and drying procedures due to a further reduced mechanical stability.

Raman spectroscopy of the hBN foam exhibited a peak at 1366.4 cm^{-1}, corresponding to the E_{2G} resonance of hBN (Figure 110, g). Analysis of the FWHM showed it to be 16.8 cm^{-1}, showing similar values to hBN synthesised on Cu foil in Chapter 3 and suggesting that this hBN adlayer is of good crystal quality.

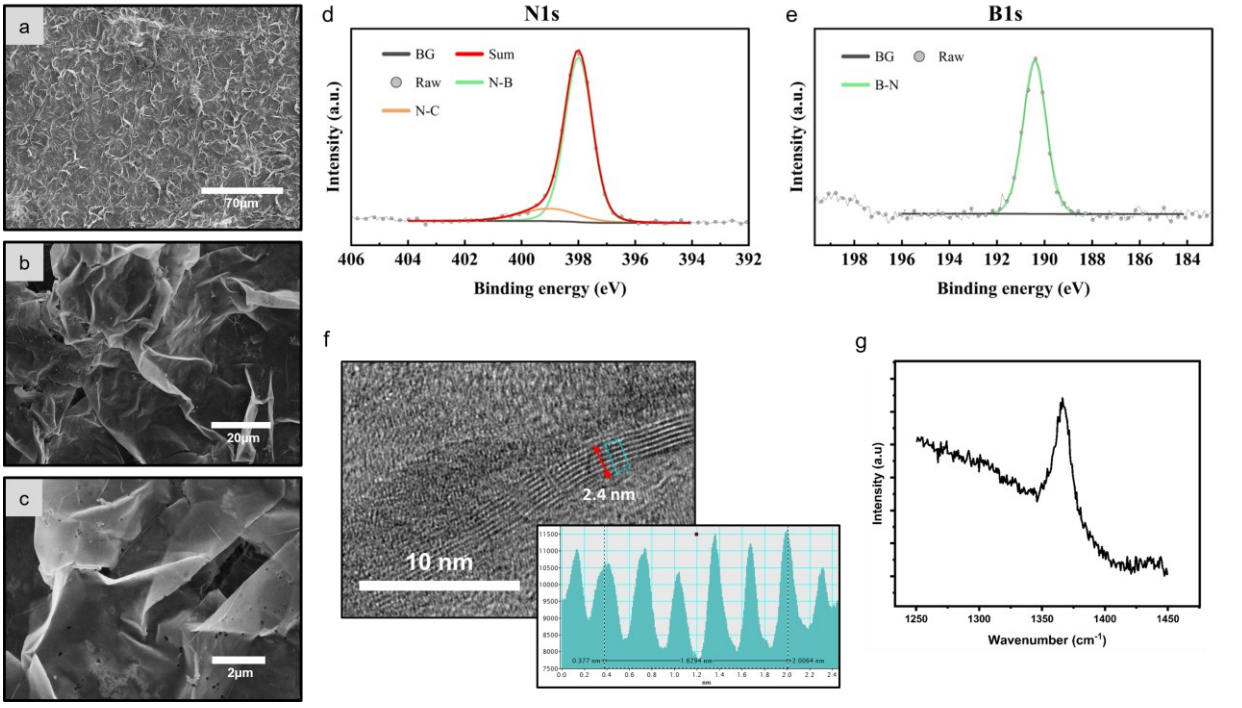


Figure 110; (a-c) Removal of Cu template from hBN-Cu foam. SEM analysis of the hBN foam shows the loss of its 3D structure upon etching of the Cu template. The hBN layers collapse in on themselves and lose the porous structure. Holes in the hBN layers are also observed in (c). (d,e) XPS analysis of hBN-Cu foam. High resolution XPS scan of the (d) N1s and (e) B1s spectra for the hBN-Cu foam sample. A small N-C peak is observed in th N1s spectrum, likely due to C organics present in the reaction chamber. (f) TEM analysis of folds in the hBN foam exhibit folds of 2-3nm, suggesting that the walls of the foam are 4-5 layers thick. Inset shows the interlayer spacing to be ~0.32 nm. (g) Raman spectrum of the hBN foam once the Cu template has been etched exhibiting the E_{2G} resonance of hBN.

6.3.4. Graphene-hBN on copper foam

Sequential deposition of graphene and hBN on the Cu foam was also trialled to produce lateral Gr-hBN heterostructures on the template, similar to Section 4.4.1. Graphene deposition was carried out for 20 minutes to leave some of the Cu foam uncoated, which was then followed by hBN deposition. Figure 111 shows SEM micrographs of the deposition product on the Cu

foam. Regions covered by hBN show a slightly different surface contrast than the bare Cu foam, observed in Figure 111 (a-b). In sections of the foam already fully coated with graphene, many particles and are observed along the grain boundaries of graphene domains, which could result from interaction of the BN precursor with graphene domain edges (Figure 111, c-d). Grain boundaries, being a zone of higher energy, are more likely to react with BN precursors than inside the respective domain.

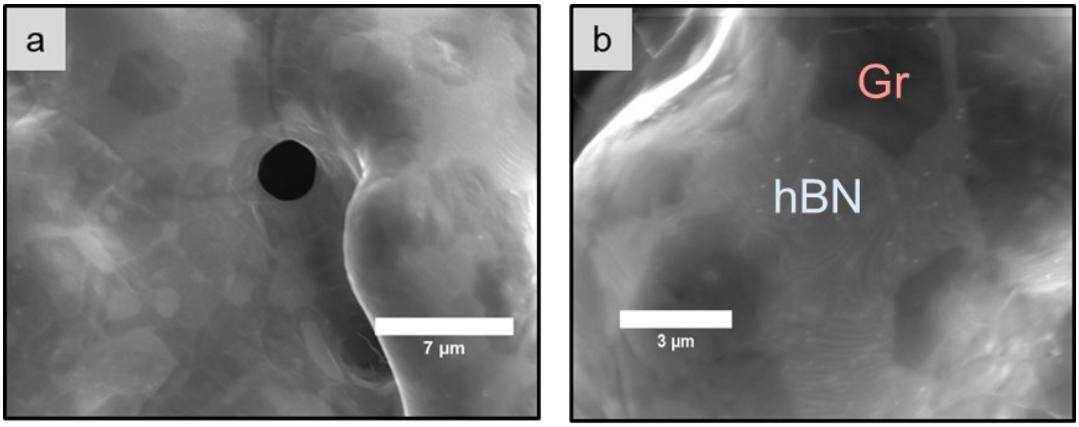


Figure 111; Sequential graphene-hBN deposition on Cu foam. SEM analysis of composite foams synthesised with sequential graphene and hBN deposition show regions of graphene and hBN growth (a, b) forming lateral heterostructures.

XPS analysis was carried out to confirm the presence of hBN and graphene regions on the Cu foam. Quantification of the XPS spectrum gives a B:C:N ratio of $B_{.01}C_{.96}N_{.03}$, suggesting the foam is mostly graphene with slight doping. High resolution XPS spectra of the N1s, C1s and B1s regions are shown in Figure 112. The N1s peak can be broken down into two components, a large peak at 399.5 eV and a smaller peak at 398.0 eV, corresponding to N-C and N-B bonding, respectively [10, 18, 336]. In the C1s spectrum, a large graphitic carbon peak is fitted at 284.3 eV using a standard Voigt function to which a decaying exponential tail function is added [337]. Two smaller peaks, fitted at 285.4 eV and 282.9 eV, reflect C-N and C-B bonding within the sample [18, 336]. Comparatively, the N-C peak is far more significant in contribution than C-B, which is also reflected in the N1s spectrum. The B1s spectrum is fitted

with peaks at 192.4 eV and 190.6 eV corresponding to B-O, B-N bonding in the sample [18, 336]. The small peak at 186.5 eV could be attributed atomic boron trapped in the Cu substrate, although this typically observed around 188 eV [134]. It could also be attributed to the formation of a boron carbide phase, which is typically observed in XPS around 186.7 eV [338].

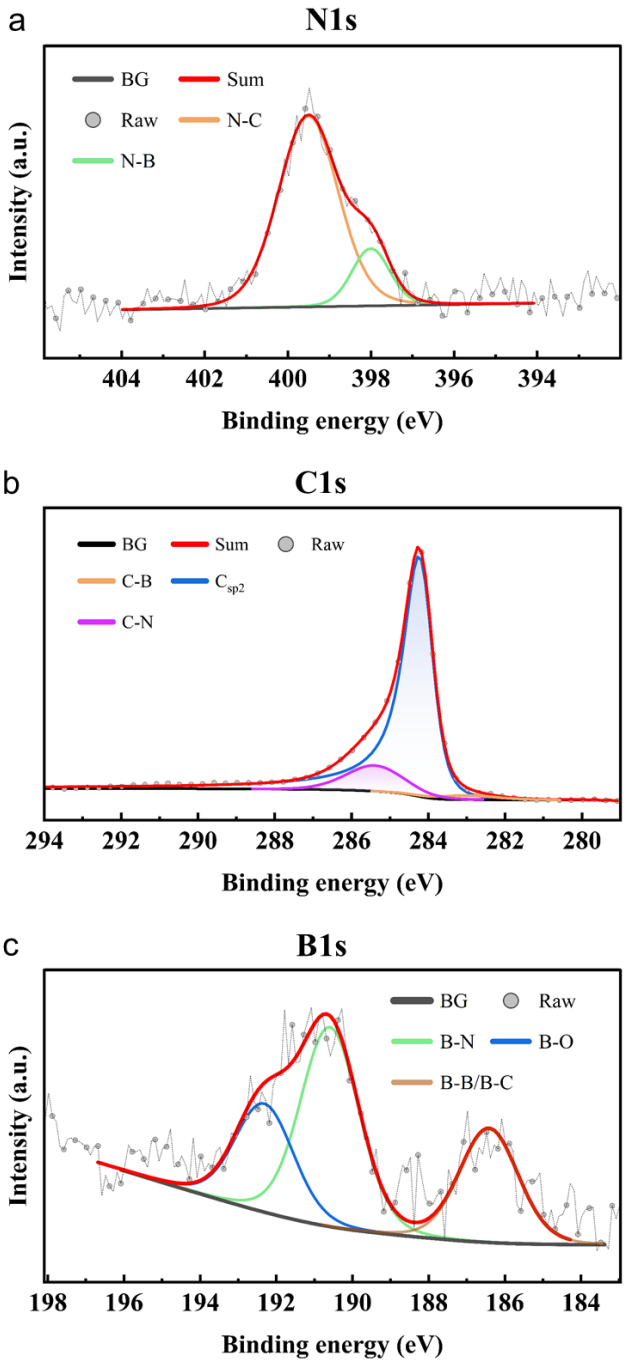


Figure 112; XPS of Gr-BN deposition on Cu foam. High resolution XPS scan of the (a) N1s (b) C1s and (c) B1s spectra for the Gr-hBN-Cu foam sample.

This could be facilitated through carbon reacting with B_2O_3, the presence of which is also detected in the B1s XPS spectrum [339]. From this data, it can be understood that only a small portion of the composite is comprised of hBN. We observe large contributions from N-C, suggesting the graphene is N-doped after exposing it to the BN precursor. It is likely then that competing reactions are occurring with these synthesis parameters; hBN deposition on exposed regions of the Cu, as well as B/N reactants attacking metastable sites of the already deposited graphene.

Removal of the Cu template resulted in foams that could be processed in liquids. However, the foam structure partially collapsed upon drying, similar to the case of graphene foams. Raman spectroscopy of the foam is presented in Figure 113. In comparison to the graphene foam, the defect level in the Gr-hBN foam is increased significantly, with the I_D/I_G ratio increasing from 0.24 to 0.50. A reduction in the intensity of the 2D peak, in comparison to graphene, is also observed ($I_{2D}/I_G = 0.18$). This could be as a result of increased layer number as well as doping density, as has been previously reported [340, 341].

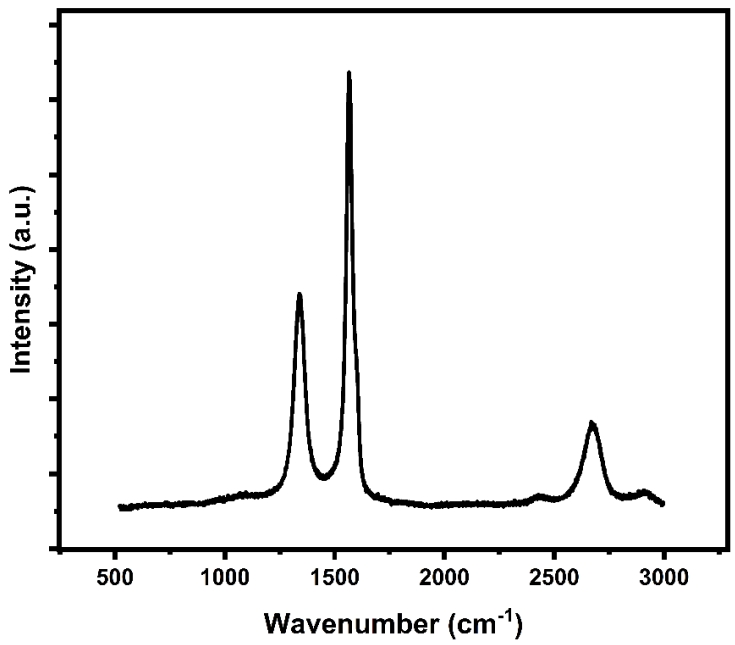


Figure 113; Raman analysis of the Gr-hBN foam once the Cu template has been etched.

6.3.5. hBCN on copper foam

To synthesise a BCN-Cu composite material, BN and C reactants were simultaneously introduced into the CVD furnace. Figure 114 shows SEM micrographs of the structure of the hBCN-Cu composite. Small, triangular defect patches of size ~ 0.6 μm can be seen, contrasted against the graphene coated surface. Interestingly, these defects occur mostly within the graphene domain and not at the edges, unlike our observations in Gr-hBN structures in the previous section. hBN islands likely nucleate on the Cu surface and are encompassed by the graphene domains, which grow at a faster rate. The triangular domains are often situated at the centre of the graphene ones, suggesting that graphene nucleates from the hBN islands. Srivastava *et al.* observed similar contrasted structures in SEM images of B-N co-doped graphene [19]. It is likely that these are defects incorporated into the graphene lattice. XPS analysis was carried out to determine their chemical composition.

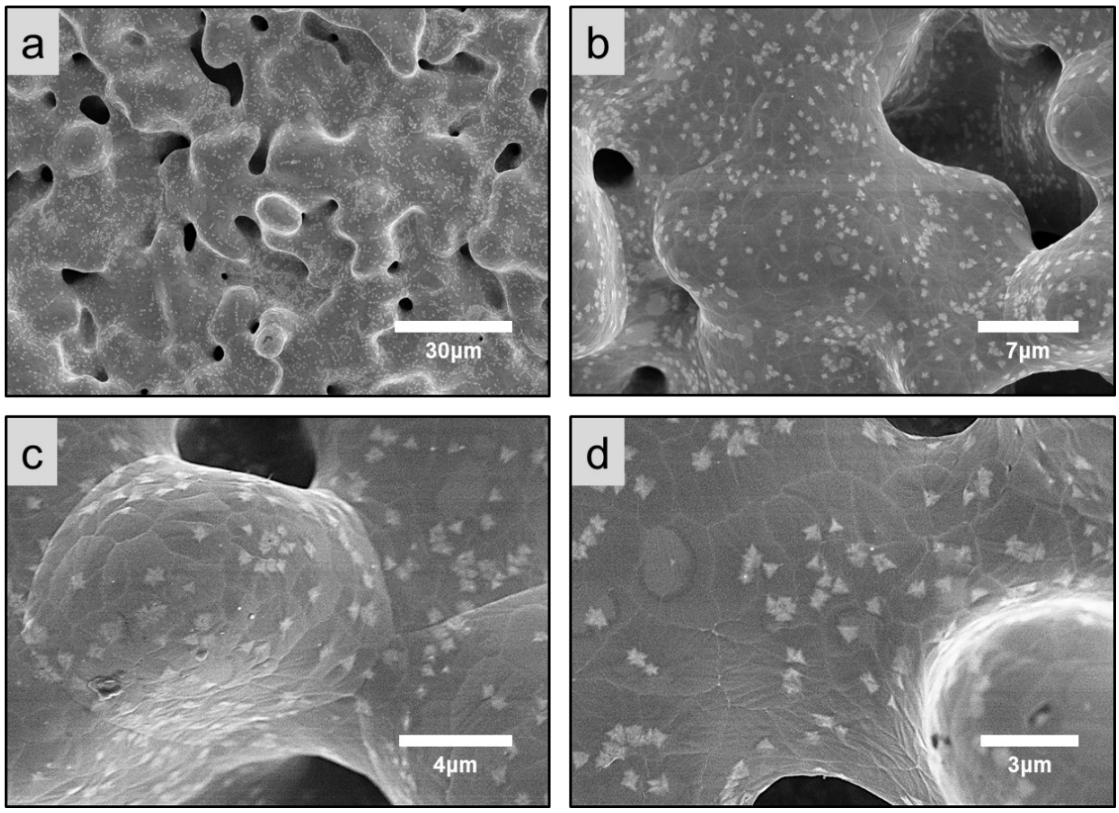


Figure 114; hBCN 'one-pot' synthesis on Cu foam template. Brightly contrasted triangular structures are observed ubiquitously across the surface of the substrate. The edges of the graphene domains, also slightly contrasted, do not overlap with the triangular structures suggesting the graphene domains grow outwards from them.

The presence of B and N in the composite was confirmed via XPS measurements. Quantification of the XPS survey spectrum gives a B:C:N atomic ratio of $B_{.06}C_{.88}N_{.06}$. Again, the structure is highly carbonaceous, although the BN incorporation has increased via this method (from $B_{.01}C_{.96}N_{.03}$ to $B_{.06}C_{.88}N_{.06}$). High resolution XPS spectra of the N1s, C1s and B1s regions are shown in Figure 115. The N1s peak is fitted with two peaks at 399.5 eV and 398.0 eV, corresponding to N-C and N-B bonding, respectively [18, 153]. The large contribution from the N-C peak suggests, again, that the graphene has been doped with nitrogen. The C1s spectrum is fitted with multiple peaks, at 283.8 eV, 284.5 eV, 285.5 eV, 286.7, and 289.5 eV which we attribute to C-B, C=C, C-N, C-O and C=O bonding, respectively [11]. The B1s peak can be broken down into three components, with peaks centred at 188.8 eV, 190.4 eV and 192.4 eV, which correspond to B-C, B-N and B-O bonding, respectively [12, 18, 153].

In this sample, with an increase in atomic % B and N incorporated, as well as larger peak contributions from B-C and N-C bonding in the HR-XPS spectra, we can infer that simultaneous introduction of B/N and C precursors is more effective at incorporating B and N dopants than the two-step method. Introduction of such heteroatoms in graphene influences the electron transfer from metals and the corresponding catalytic activity [342]. Previous DFT calculations have shown nitrogen doping in graphene/CNTs to increase the density of states close to the Fermi level [343], and the synergistic enhancement of the catalytic activity in the presence of transition metal atoms [344]. These doped graphene-Cu composites could be a new route in designing durable, non-precious heterogeneous electrocatalysts.

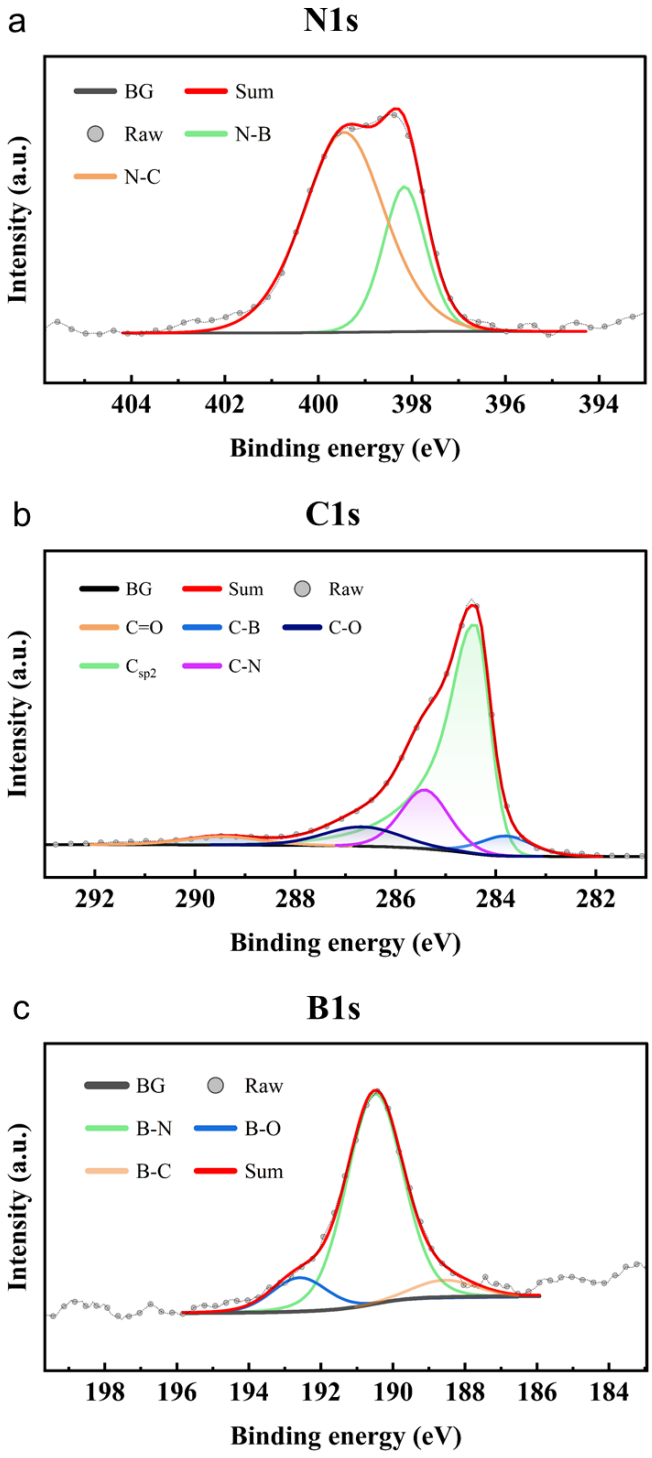


Figure 115; XPS analysis of hBCN-Cu foams. High resolution XPS scan of the (a) N1s (b) C1s and (c) B1s spectra for the hBCN-Cu foam sample.

Figure 116 shows SEM images of the microstructure of the hBCN foams after removal of the Cu template. The defect sites first observed in Figure 114, can still be faintly seen, marked by the red circles in SEM image in Figure 116 (d). The porous nature is retained in the freestanding

structure. However, similar to the previous foams synthesised, issues with structural stability upon drying remained.

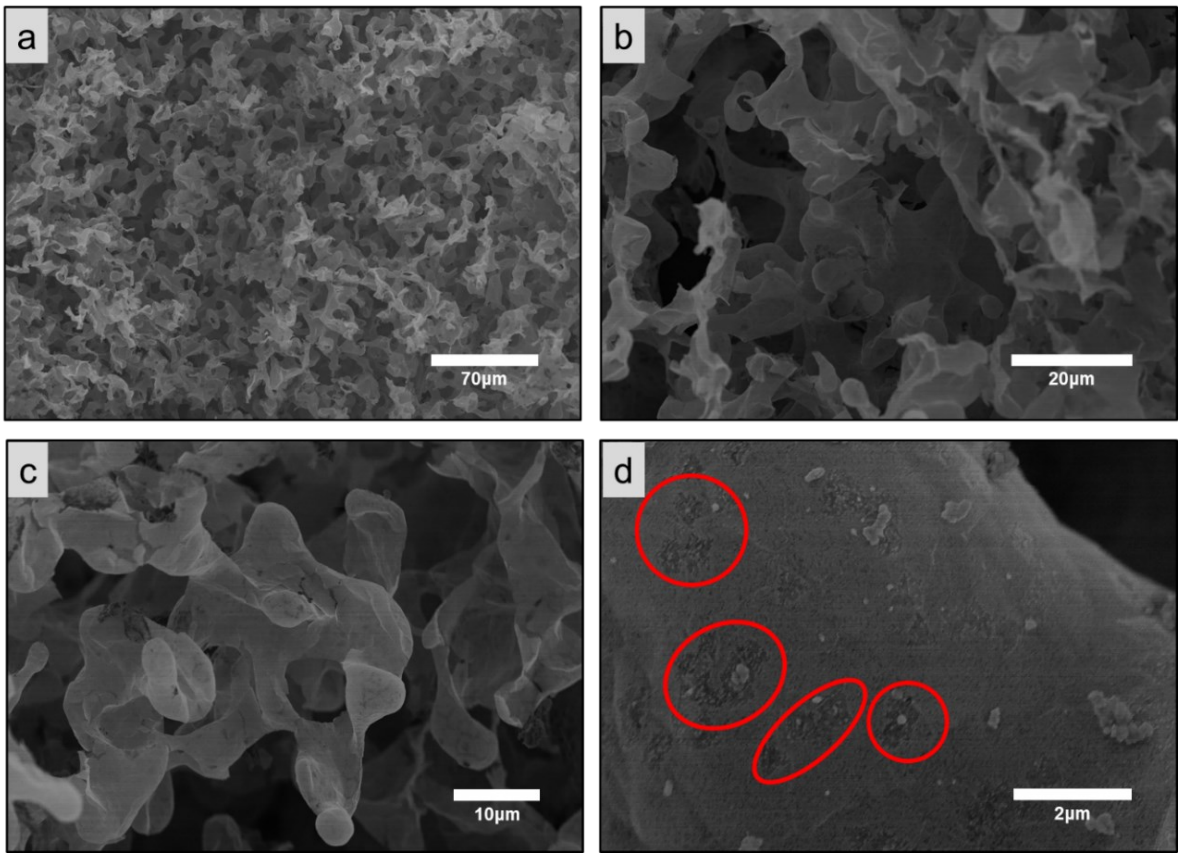


Figure 116; hBCN foam after removal of Cu template. (a-c) SEM analysis showing the 3D porous structure of the hBCN foam after removal of the Cu template. (d) Defect sites, observed previously in **Figure 114**, are still apparent in the foam, highlighted by the red circles.

Raman analysis of the hBCN foam shows an almost identical spectrum to that of the Gr-hBN foam. Analysis of the peak intensities gives similar I_{2G}/I_G and I_D/I_G ratios of 0.19 and 0.54 respectively. No E_{2G} peak of hBN was detected across multiple scans. This is likely due to the fact that the spot size of the Raman microscope is of the order of µm and thus, any interaction with a hBN region is likely overshadowed by resonances with the surrounding graphene lattice, which are far stronger in intensity [345]. The similarities between the spectra in Gr-hBN and hBCN foams suggest a similar level of defect doping of graphene. This is at odds with our XPS analysis, which clearly shows a significant increase in the level of B and N incorporation.

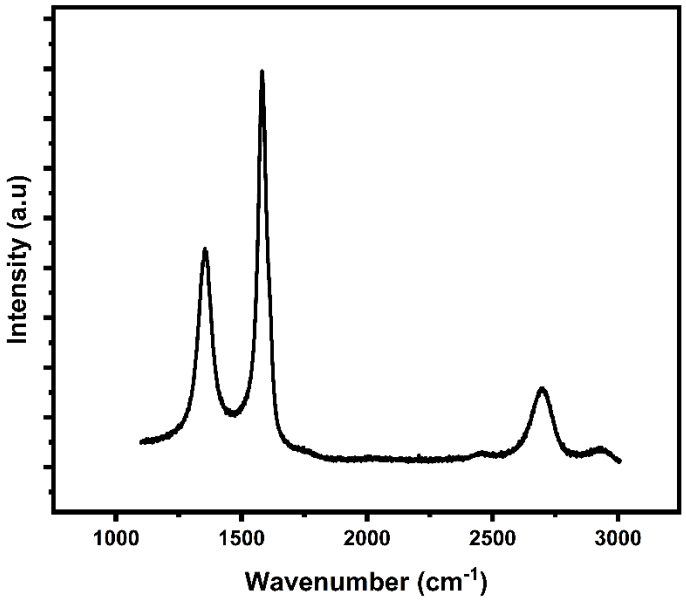


Figure 117; Raman analysis of the hBCN foam once the Cu template has been etched.

6.4. Conclusion

A novel method for the production of 3D architectures of graphene, hBN and hBCN on porous Cu foams, from Cu metal powders, is reported, improving upon previous literature which used toxic and pyrophoric precursors, triethyborane and ammonia [16]. Here, safe and easily handled precursors, ammonia-borane and methane, were used to form porous BCN@Cu foam composites with varying morphologies, which has not yet been reported in the literature. A one-step approach to hBCN growth was seen to produce BCN growth with enhanced B,N doping within the graphene lattice in comparison to sequential graphene and hBN growth. Upon removal of Cu and drying, foams exhibited poor structural integrity due to the thin nature of the structures, resulting in collapsed structures, and are unsuitable for production of freestanding BCN foams. This is likely due to the nature of the Cu growth substrate – it only allows for few-layered growth of hBN or graphene due to its low precursor solubility and thus growth is surface mediated, resulting in thin walls and low structural integrity in the metal-etched foams. As collapsed structures are not beneficial, the practical viability of these

structures is low unless these issue can be resolved. Other reports have managed to succesfully produce freestanding foams via CVD by employing a catalyst such as Ni, producing multilayed growth of 2D materials on the metal foam. This work's findings offer important contrast to the Ni substrate, whose thicker 2D material deposits results in improved structural stability and freestanding foams, and concludes that Cu is not the optimal substrate for producing freestanding BCN foams.

Further material processing optimisation, such as employing a polymer PMMA support on the surface of the 3D structure could potentially improve its mechanical properties, as has been shown in other similar studies [16, 346]. However, a polymer support reduces the overall quality of the foam structure and thus its economic viability, as pyrolytic techniques for producing BCN foams [347-349] woud likely achieve similar quality of material for a fraction of the cost. Improving the mechanical properties through increased film thickness is likely the most straightforward avenue for further progression of freestanding BCN foams. To achieve thicker 2DM growth, adopting a Fe or Ni catalyst, with enhanced solubility and multilayer formation, could be trialled in future.

As composite materials, the 3D $B_xC_yN_z$@Cu metal foam could have useful applications in several areas. As protective barriers, the 2D layers on the surface isolate the metal surface from aggressive environments and inhibiting its degradation, which can be used to extend the lifetime of Cu foams. Furthermore, the copper electrodes coated with 2D hBN or graphene has shown promise in tuning the electrodeposition uniformity in zinc [350, 351] and lithium [40, 332] metal anodes, reducing the occurrence of dendrite formation and thus improving cyclability. Coating with hBN will reduce the conductivity of the composite in comparison to graphene and instead offers enhanced chemical stability. Employing a BCN coating on Cu may offer a balance between the two.

The $B_xC_yN_z$@Cu metal foam composite could also find application as an electrocatalyst. Recent work on hBN@NiFe alloy showed that the hBN layer acts as a co-catalyst in the OER, with enhanced activity and performance observed in the composite material in with respect to the intrinsic metal [352]. Similarly, Cu/h-BN composites have shown high catalytic activity and good recycling performance as a non-precious catalyst for hydrogen generation from the hydrolysis of ammonia borane [353]. Theoretical studies on doped or defective hBN on Cu metal supports have similarly suggested excellent electrocatalytic ability in both the HER [72] and OER [73] reactions. A recent review by Dong *et al.* on hBN-metal structures for heterogeneous catalysis covers this topic in great detail [354]. Their review advises the scientific community to review the "inertness" of hBN, especially where "defective" hBN-metal composites are employed. As such, this novel synthesis method for composite 3D architectures of hBN and BCN derivatives coated on Cu could result in new catalyst materials.

Chapter 7

Conclusions and Future Work

The objective of this thesis is to contribute to this field of 2D BCN materials, investigating scalable CVD synthesis methods using low-cost and non-toxic precursors, and a simple synthesis protocol, atmospheric pressure CVD, to produce BCN materials with tuneable properties. Both experimental and theoretical approaches were undertaken in this work to obtain a holistic understanding of BCN growth and material properties. In this concluding chapter, an overview of the major findings in this study is presented alongside future research directions, proposing new avenues of further research in 2D CVD BCN materials, so that they may be soon implemented in real-world applications.

7.1. Summary of findings

7.1.1 "C doping" of hBN on Cu is heavily influenced by the relative chemical potentials of BN and C, forming structures of varying morphology, and doping is limited to μ_C below that of graphene formation.

Studying the growth of C doped hBN on Cu, starting from $\mu_C = 0$ (*ie* hBN growth) and increasing μ_C systematically, revealed significantly different growth morphologies. At low μ_C, hBN was effectively doped, exhibiting a reduction in the optical band gap from 5.95 eV down to as low as 5.42 eV. Growth proceeded in a similar fashion to intrinsic hBN, although small nuclei of dendritic carbon were observed along certain hBN edges. At higher μ_C, graphene was nucleated beneath the hBN domain, forming stacked hBN/graphene structures. The nucleated graphene acts as a carbon sink for any carbon adatoms on the surface of Cu and no doping of hBN was observed via UV-vis characterisation. As such, C doping of hBN is limited to μ_C below that at which graphene nucleation is possible.

Where graphene had nucleated, and stacked hBN/graphene heterostructures had formed, the nucleated graphene was characterised as being highly defective, although monolayer. The highly defective nature is likely due to boron doping, as characterised via XPS, as well as vacancy defects resulting from the slow diffusion of C precursors below the hBN domain. Employing more mobile and reactive carbon precursors, such as acetylene, or using an alloyed Cu-Ni substrate for enhanced C diffusion, could potentially improve upon this and form electronics grade stacked hBN/graphene structures. At the highest μ_C analysed, highly anisotropic, mixed-phase growth is observed. μ_C is substantial enough for graphene nucleation directly on the Cu surface (not along hBN domains) which competes with hBN nucleation for the growth on Cu, forming highly defective, lateral heterostructures. As such this work demonstrated the role of μ_C in 2D BCN growth on Cu and the tuneable morphology of the structures which depended upon it; from C doped hBN, to stacked hBN/defective-graphene

structures, to highly heterogenous lateral hBN/graphene based on this parameter, which has not been previously reported in the literature.

7.1.2 Precipitation mediated growth of C doped hBN on Fe allows for a more tractable synthesis of C doped hBN, producing multi-layered films with a tuneable band gap.

Carbon doping of hBN multilayer films is realised on Fe substrates. Precipitation mediated growth allows for the formation of thicker 2D layers, resulting in more robust films. Through carbon doping, the optical properties of the films exhibit a tuneable optical bandgap. The bandgap is reduced from 5.92 eV for intrinsic hBN to 5.31 eV at highest CH_4 flow. These results are the first to report modulation of the hBN bandgap by C doping of hBN films synthesised on Fe substrates. Interestingly, even at significantly higher partial pressures of methane, no sign of C and BN segregation is observed, suggesting that graphene nucleation is suppressed in segregation-mediated growth on Fe, making it an attractive growth substrate for hBN-C material system for future optoelectronic devices.

7.1.3 Theoretical calculations on the behaviour of B, C and N atoms on Cu(111) support experimental observations of hBN and "C doped" hBN domain growth and reveal insights into BCN growth on Cu.

First-principle calculations looking at the comparative energies of adsorption, diffusion and penetration of B, C and N atoms near the Cu(111) surface revealed how B and C atoms preferentially reside in the subsurface while N atoms favour residing at the surface. Furthermore, B and C experience low barriers of penetrating the Cu surface and higher barriers in the reverse direction, while N experiences high barriers of penetration. As such, for experimental set-ups that use a 1:1 B:N precursor such as ammonia borane, this results in a concentration gradient at the Cu surface whereby $c_N > c_B$. Equilibrium domain shapes of hBN typically exhibit triangular structures, which previous hBN growth studies have shown to form

while $\mu_N > \mu_B$ [134, 196]. Where a carbon source is introduced, BCN structures with increased N-C bonding to B-C bonding may result during surface-mediated growth. This was observed in our XPS analysis of hBNC structures synthesised under low pp_{CH4}, whereby "C doped" hBN resulted. Furthermore, on the surface, all atoms were found to have low energetic barriers to diffusion and, as such, can be considered to be highly mobile on Cu at typical CVD growth temperatures (~1000˚C). This suggests that atoms will tend to find the most energetically favourable configurations on the Cu substrate, most likely resulting in segregated regions of graphene and hBN. This is observed in hBNC sample where the critical concentration of C atoms is sufficient for graphene nucleation; C adatoms attach to growing graphene domains which act as C sinks instead of forming point defects in hBN, resulting in a higher quality hBN and a restoration of the bandgap from 5.42 eV to 5.89 eV. Below this concentration, C adatoms are still highly mobile but unable to reach the critical size for graphene nucleation, and as such are incorporated as point defects in hBN, reducing crystallinity.

7.1.4 Phase separated structures of graphene and hBN can be tuned towards activity in photocatalysis for the HER/OER.

With recent reports on the synthesis of super-ordered arrays of phase-separated graphene-hBN, computational modelling techniques were employed to investigate the relationship between domain sizes and their stability and opto-electronic properties as well as their efficacy as photo-catalysts in HER/OER. I identify three systems which show good viability for HER and OER at neutral pH. Out of these, two show absorbance spectra within the solar spectral irradiance range (1.5 – 3.5 eV) and, therefore, could potentially be suitable as photo-catalysts for future study.

7.1.3 Low purity ammonia borane reacts with amorphous silica from the quartz CVD reactor, forming B,N doped silica nanoplatelets on the Cu surface, preventing quality hBN growth.

This work highlighted the effects of impurities in the AB precursor, which was shown to have significant consequences in hBN synthesis. Although there are many CVD studies on hBN growth that fail to explicitly identify the purity of their ammonia-borane precursor [120, 198, 202, 206, 288, 292, 293], this work is the first to report on hBN growth using a *low purity* ammonia borane precursor (85% purity). Contaminant structures observed during hBN growth with low purity ammonia borane were characterised and found to be silica based. It was identified that impure ammonia borane species reacts preferentially with silicon deposited on Cu from H_2 etching of the CVD chamber, forming extended nanoplatelet structures on the surface of Cu via a diffusion limited growth mechanism. These structures were not observed in control experiments highlighting the role of low purity AB in their activation. It follows then that quartz tubes are not an ideal experimental apparatus for CVD synthesis of hBN due to Si_xO_y degradation and contamination, which is activated by the species produced from borate species resulting from atypical decomposition of AB, something highlighted with the use of a low-purity precursor. In future work on CVD growth of hBN, researchers should employ a cold wall CVD technique, where only the substrate is inductively heated and not the surrounding reactor walls, preventing the occurrence of Si contamination and thus promoting quality hBN deposition. Future researchers should also ensure that they are reporting the purity of their precursor accurately in their studies to enable effective comparisons and ensure reproducibility of results.

7.1.7 Novel method to produce BCN-Cu 3D foam composites is realised through a CVD approach using ammonia-borane and methane as precursors.

A simple and cost-effective method of forming porous 3D metal foams from low-cost metal powders is used to produce 3D porous templates on which 2D layers of graphene, hBN and hBCN are grown. This method improves upon existing literature on 3D CA-CVD architectures of BCN by employing non-toxic precursors of ammonia-borane and methane to produce 3D Cu foam-2D BCN composites. A one-step approach to hBCN growth on Cu was found to incorporate boron and nitrogen into the structure more effectively than sequential deposition. The Cu scaffold was seen to be unsuitable for production of freestanding BCN foam structures as removal of the Cu scaffold resulted in collapsed structures after drying (due to its few-layers thick nature). As such, future work should focus on applying these materials as a metal foam/2DM composite. For freestanding BCN foam synthesis, a metal catalyst producing thicker foams should be trialled.

7.2. Future Research Directions

7.2.1 Luminescence and photodetection studies of 2D C doped hBN

Luminescence and photodetection studies of "C doped" hBN synthesised via this CVD method could reveal enhanced functionality. Previous reports concerning modifying hBN with C inclusion has been seen to improve its DUV detection properties [25] and is responsible for the introduction of single photon emitters [22, 260]. However, these reports use costly and complicated synthesis techniques such as MBE, ion-implantation, IBSD and MOVPE. The CVD synthesis protocol here could provide a cheaper method of producing similar materials. "C doped" hBN was achieved here on Cu (at low partial pressures of methane) and on Fe which showed a modulation in the UV-vis characteristics of the films upon C doping. Future work

should test the opto-electronic properties of "C-doped" hBN films grown via CA-APCVD in terms of SPE properties and enhanced DUV photodetection.

7.2.2 Enhanced control of BCN synthesis using alloyed catalytic substrates.

While this work focused on BCN synthesis on pristine metals, alloyed metal catalytic substrates can offer new methods of tailoring the growth of 2D materials. Alloyed substrates allow for tuning of precursor solubility and mobility on the growth catalyst, extending of the synthesis temperature range, as well as modifying the overall catalytic activity of the growth substrate, which can enhance the quality of heterostructures grown. Highly-crystalline and defect-free hBN-Gr stacked heterostructures have already been reportedly synthesised on Cu-Ni alloys [116] [115]. Similarly, Fe-Ni foil was shown to improve the homogeneity on multilayer hBN films, which they attribute to Ni suppressing the local segregation of hBN on the Fe surface [167]. Applying this technique of alloyed metal substrates to the growth methods outline in this thesis could improve upon the quality of structures formed, such as the hBN/defective-graphene heterostructures formed on Cu in Chapter 3.

7.2.3 Multiscale modelling of BCN growth on Cu

Computational methods have advanced in recent years and could, in principle, describe sufficiently large systems to be relevant for understanding the growth of 2D domains from atomic precursors. Perhaps at the forefront of materials modelling 2D hBN growth, Liu et al. were able to construct a reactive force field in ReaxFF using results from DFT calculations on of the interactions of B and N structures on the surface of Ni(111) [355]. Where density functional theory (DFT) and molecular dynamics (MD) simulations are combined is known as *multiscale modelling* and, here, it allowed for a more accurate insight into the nucleation and growth of hBN domains on Ni(111), at timescales far greater than typical DFT studies.

Subsequently, Liu et al. were able to investigate the influence on atomic B:N ratio and synthesis temperature on the size and shape of the hBN domain. With new tools such as ParAMS [356] available, where DFT results can be input to build training data and optimize force field parameters, multiscale modelling is more accessible to the layperson, and force fields can be tailored for specific systems. There have been no such reports on modelling the growth of BCN materials, and as mentioned already, this is likely due to the complexity involved with modelling three atomic components. While not exhaustive, the systems modelled in Section 3.3.1 of Chapter 3 serve as a starting point for creating a B-C-N-Cu ReaxFF force field using tools such as ParAMS included in the SCM software package. Future work can the use optimised systems obtained here to train B-Cu, N-Cu and C-Cu potentials. In order to formulate a thorough dataset, computations on interatomic B-C-N interactions on the substrate should also be carried out.

7.2.4 Development of segregated hBN-graphene arrays for catalytic applications

Chapter 4 in this thesis used computational methods to look at hBN-graphene heterostructures and found that the opto-electronic properties and catalytic activity of the structures can be tuned towards being efficient photocatalysis for HER/OER by varying the relative sizes of the hBN and graphene domain. The CVD study on Gr-hBN structures grown by sequential deposition on solid metal Cu catalyst identified potential issues in producing high quality, and homogenous films of these structures. Recent work by M. Li *et al.* demonstrated super ordered hBN-graphene structures, with precise control over the domain sizes of hBN:C and density using a liquid metal catalyst of molten Cu as the growth substrate. Future work should verify the theoretical results derived here experimentally, employing similar synthesis techniques as M. Li *et al.* to test arrays of hBN-graphene as catalytic materials towards HER/OER as a function of relative hBN:C domain size.

7.2.5 Copper-silica interfacial studies.

Structures found in Chapter 5 of this thesis prevented an obstacle towards quality hBN film deposition. However, the realised silica structures could be used to investigate catalytic properties of the nanoscale Cu-SiO_x interface. Recently, structures with this copper-silica interface have garnered attention in fields such as heterogenous catalysis where the silica-metal interface has been seen to enhance catalytic activity [357-362]. In some cases, such silica structures may constitute a permeable membrane, where molecules can diffuse through to the underlying metal substrate and react. This has already been carried out for a number of metal surfaces [363], including Cu [364], yet not with the added functionality of N and B doping.

The Cu-SiO_x interface also adds functionality to the surface of copper, with new bonding interactions for the adsorbed species. Xu et al. were able to boost the catalytic efficiency in the hydrogenation of esters by a factor of 80 by wrapping copper particles with mesoporous SiO_2 [361]. Their results point towards the creation of new bonding species along the Cu-O-SiO_x interface which result in an impressive improvement in catalytic activity. In CO_2 reduction, copper has an adequate activation energy of CO_2 and can produce various hydrocarbons and alcohols at modest overpotentials. However, the process is very non-selective, forming many intermediates and producing a range of products simultaneously [365]. Silica on Cu can be employed as an 'oxide modulation strategy' in CO_2 electro-reduction towards ethylene synthesis [360]. Through modifying the surface chemistry of Cu with SiO_x interface stepped sites, Li et al. were able to promote the formation of certain intermediates, and in turn, improve the Faradaic efficiency toward ethylene production from <50% to 65%. Similarly, Wang et al. synthesised Cu/SiO_2 nanocatalysts for CO_2 methanation and found CO_2 conversion in in the heterostructures improved from 5% to 28%, close to the equilibrium conversion of CO_2 (30%) [366]. The homogeneity of these doped silica structures on the Cu substrate makes them a potentially interesting material to study the catalytic properties of the Cu-SiO_x interface. N and

B dopants within the silica-Cu interface, such as those observed in this work, are yet to be explored in the literature and could potentially offer up new and improved functionalities in the hetero-structure. Future work on these structures could focus on testing their efficacy as heterogenous catalysts in the CO_2RR.

7.2.5 Application testing of hBCN-3D metal foam composites.

Cu foams are potential materials for important catalytic processes such as water splitting [327]. They are inexpensive, recyclable, and environmentally friendly. Several reports on metal surfaces coated with 2D materials detail how the composite can improve performance of the intrinsic metal. Graphene coated on Ni was found to enhance the photo-electro-chemical performance for water splitting in comparison to bare Ni [329]. Similarly, as current collectors in an electrochemical cell, graphene coated Cu-Ni foams showed increased capacitance in comparison to intrinsic metal foams [333]. Enhanced electrocatalytic activity for the oxygen evolution reaction in alkaline solutions was also reported for CVD hBCN coated on titanium [18]. Cu/h-BN composites have shown high catalytic activity and good recycling performance as a non-precious catalyst for hydrogen generation from the hydrolysis of ammonia borane [353]. Theoretical studies on defective hBN on Cu metal supports showed excellent electocatalytic ability in both the HER [72] and OER [73]. Future work might look at hBCN coated Cu as a method to enhance the electrocatalytic activity and operational durability of these intrinsic metal foams.

8. Appendices

8.1. Appendix I: Cost analysis of Cu@BCN vs Pt-coated electrode

Considering two cases, Cu-BCN electrode and a Pt-based electrode, the costs of CVD materials for synthesis of a 5 x 5 cm^2 electrode would be;

Case A: Copper functionalised with BCN coating

Estimate of the cost of 5 x 5 cm^2 Cu foil for CVD experiment;

30 x 150 cm^2 0.025 mm 99.8% Cu foil = £58

5 x 5 cm^2 of same Cu foil = £0.32

Estimate of the cost of gas for a traditional CVD experiment;

400 sccm of gas consisting of 5% H_2, 0.025% CH_4, and 94.075% Ar for 2 hours (120 mins):

Total Volume = Flow Rate × Time = 400 sccm × 120 minutes = 48,000 scc = 48 litres

Given the mixture ratios (Ar:H_2:CH_4 - 94.075 : 5 : 0.025) :

- Volume of H_2: 0.05×48 l =2.4 litre
- Volume of CH_4: 0.00025×48 l =0.012 litre
- Volume of Ar: 0.94075×48 l =45.288 litre

Assuming prices (taken from BOC online):

H_2: £120.5 per m^3 (£0.121 /l), CH_4: £6.22 /l, Ar: £7.46 per m^3 (£0.00746 /l)

Costs are then:

- Cost of H_2: 2.4 l ×£0.121/litre = £0.2904
- Cost of CH_4: 0.012 l ×£6.22/litre= £0.07464
- Cost of Ar: 45.288 l ×£0.00746/litre = £0.3379

Cost of gas per CVD experiment = £0.2904 + £0.07464 + £0.3379 = £0.70294

Estimate of the cost of ammonia borane for CVD experiment;

10g of AB = £385 , 10 mg of AB used per CVD experiment = £0.385

Total cost of materials = £0.70 + £0.32 + £0.39 = £1.41

Case B: Pt coating on substrate

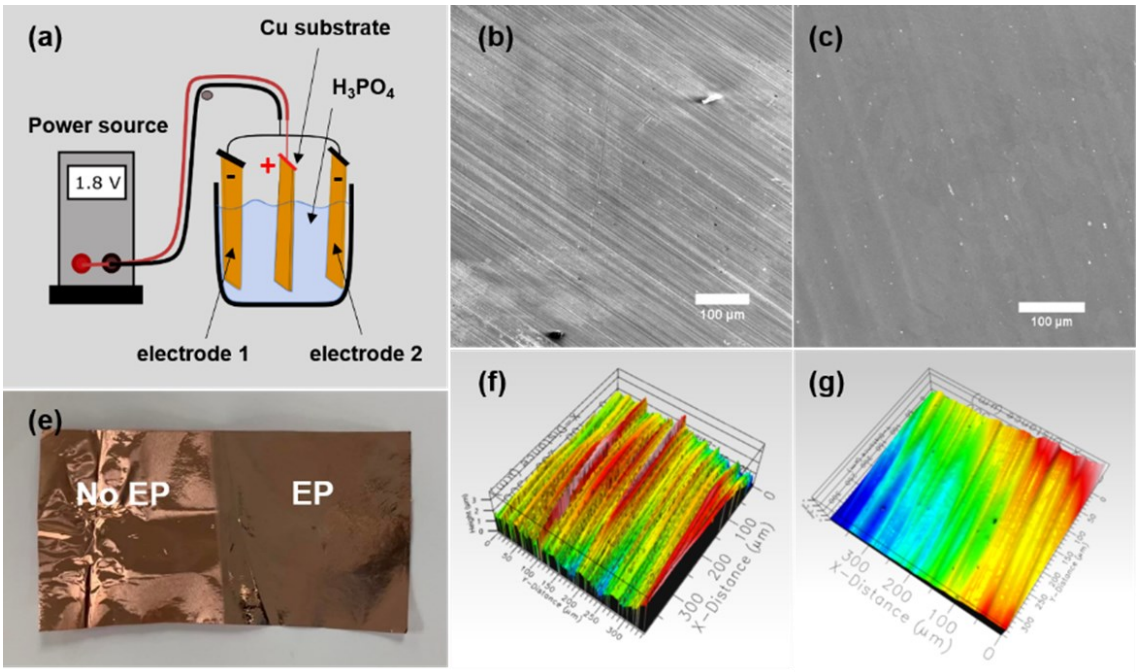
Estimate of cost of CVD Pt layer on 5 x 5 cm^2 conducting substrate (substrate not included in cost analysis – typically Cu/Ni/FTO/ITO):

- Thickness of Pt layer - 200 nanometers (taken from study by Contreras *et al.* [367])
- Surface area of the substrate: 5 x 5 cm^2 = 25 cm^2
- Volume of Pt coating: Volume = Thickness × Area = 0.0002 cm × 25 cm^2 =0.005 cm^3
- Density of Pt = 21.45 g/cm^3
- Mass of Pt coating = 0.005 cm^3 × 21.45 g/cm^3 = 0.10725 g
- Bulk cost of Pt = £25/g
- Cost of coating = £2.68

Total cost of materials = £2.68

8.2. Appendix II: Synthesis of 2D BCN Materials on Pristine Metal Foils

8.1.1. Cu foil EP set up and surface characterisation.



Supplementary Figure 1, Electropolishing of copper to reduce the surface roughness. (a) Schematic of electropolishing set up used. Counter electrodes were also Cu. (b,c) SEM images of (b) as received and (c) electropolished Cu foil. (d) OM image of non-EP and EP regions of Cu foil. An improved mirror like reflection is observed on the EP side of the foil. (f,g) Optical profilometry of the Cu substrate for (f) as received and (g) EP foil. As received foil had a RMS roughness of 350 nm and for the EP foil 120 nm for a 100 x 100 μm^2 region.

The schematic of the electropolishing set up for Cu foils is shown in Supplementary Figure 1 (a). The as received foil shows many rolling lines which can act as unwanted nucleation sites for the 2D material, as seen in SEM image in Supplementary Figure 1 (b). Optical profilometry analysis shows the RMS roughness of as-received foil to be 350 nm (Supplementary Figure 1, f) where electropolished foil has a roughness of 120 nm. After electropolishing, few rolling lines are observed under SEM (Supplementary Figure 1 c).

8.1.2. Irregular hBN isosceles growth

In several experiments, isosceles hBN domains were observed on Cu (Supplementary Figure 2, a). These asymmetric structures were previously reported by S. Sharma *et al.*, observed only

when the ammonia borane precursor was heated to elevated temperatures (>90 ˚C), although they offer no mechanism for their formation [293]. As mentioned previously, higher heating profiles result in the formation of structurally different species, some of which could be B_xO_y containing. In our experiments, however, the temperature was held at 70 ˚C, well below that used be Sharma *et al.* [293]. We suggest that the source may be from residual oxygen in the CVD chamber or adsorbed oxygen by the hydrophilic ammonia borane precursor which is old or exposed to air. These will typically react with the B species of the ammonia borane complex as the hydrogen atoms attached to boron are hydridic whereas those attached to nitrogen are somewhat acidic. XPS analysis of defective and pristine hBN islands are shown in Supplementary Figure 2 (c). In the case of the defective isosceles domains, a large B-O peak is apparent in the B1s spectrum. In pristine hBN samples, this peak is not observed and only the B-N peak at 190.4 eV is found.

Boron oxide species, once formed on the surface of copper, could significantly hinder the growth of the hBN domain due to its chemical inertness and high melting point (~1800 ˚C). At low hydrogen partial pressures, the below equation is pushed towards the reactants.

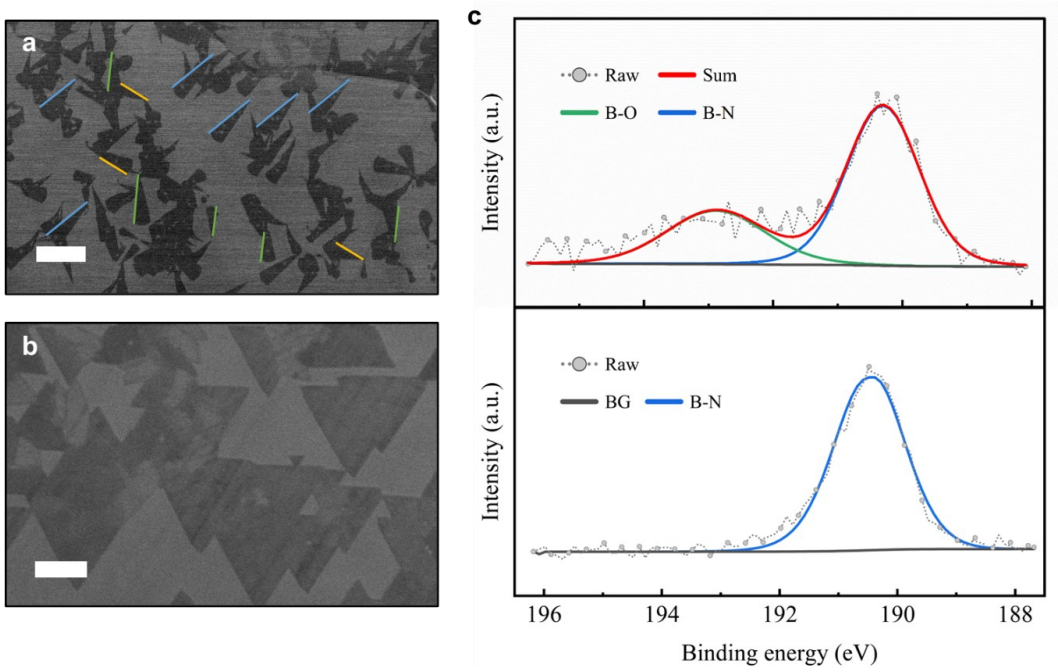
$$3H_2 + B_2O_3 \rightarrow 2B + 3H_2O$$

Furthermore, looking at the free energy of the reaction at 1300K, taken from the NIST database, we see that the free energy is positive;

$$\Delta G_{rxn} = (\Delta H_{prod} - \Delta H_{react}) - T(S_{prod} - S_{react})$$
$$= [3(-249.47) - (-1229.732)] - 1300[3(0.2440) + 2(0.0358) - 3(0.1743) - 0.2389]$$
$$= +426.982 \text{ kJ / mol}$$

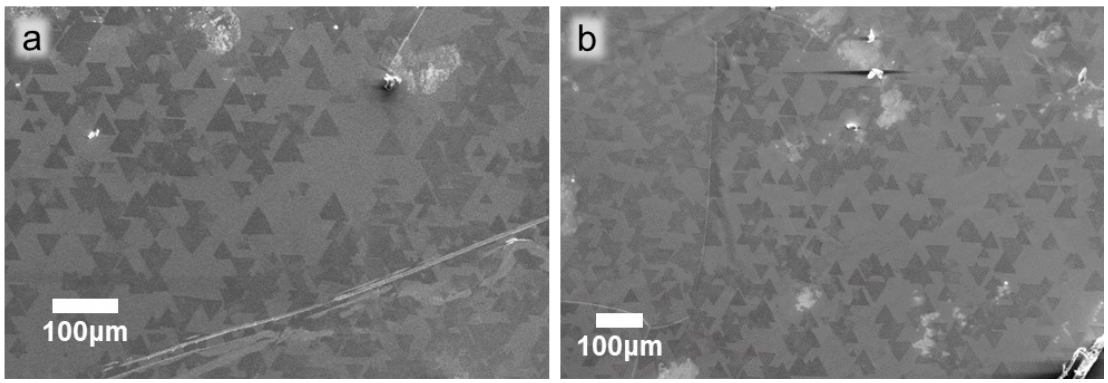
Therefore, etching of B_2O_3 is slow and unfavourable, and a build-up on the surface of the catalyst can result, impeding the growth of hBN. In order to minimise the chances of this occurring, extra vacuum and purging steps were added to the synthesis protocol at the

beginning of the synthesis and the precursor was always stored under vacuum. These two steps seemed to reduce the occurrence of isosceles hBN growth.



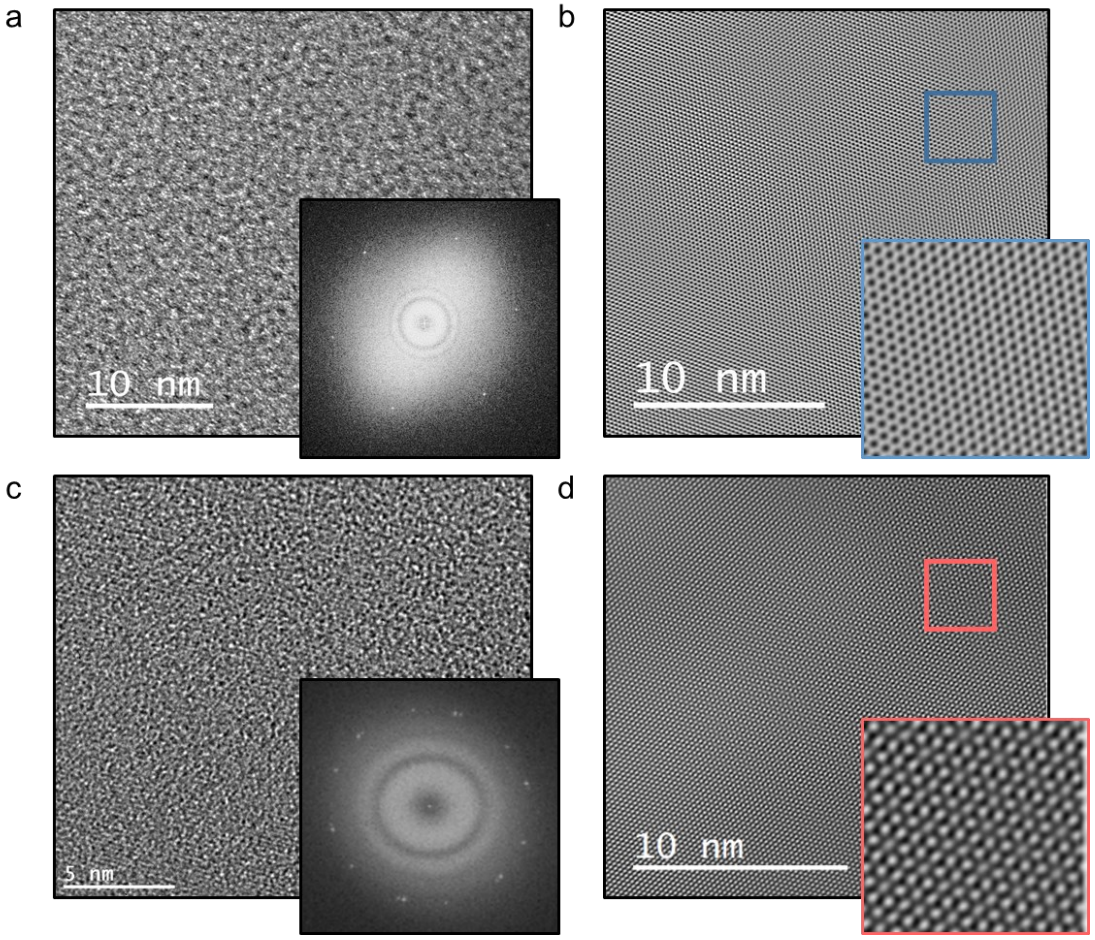
Supplementary Figure 2; Effects of impurities in the reaction chamber during growth. (a) SEM image of defective hBN growth, where isosceles domain growth is observed. Edge orientations are highlighted. (b) SEM image of pristine hBN growth, where equilateral domain growth is observed. Scalebars are 20 µm. (c) XPS B1s Spectrum showing the presence of a significant boron oxide peak in the defective hBN sample, post- growth. In the pristine sample, no boron oxide peak is observed.

8.1.3. Wide-view SEM images of optimised hBN growth on Cu



Supplementary Figure 3; (a,b) Wide view SEM images of optimised hBN growth on the Cu substrate (t ~ 60 mins). Domains with good symmetry and alignment are observed.

8.1.4. FFT TEM analysis of hBN sheet

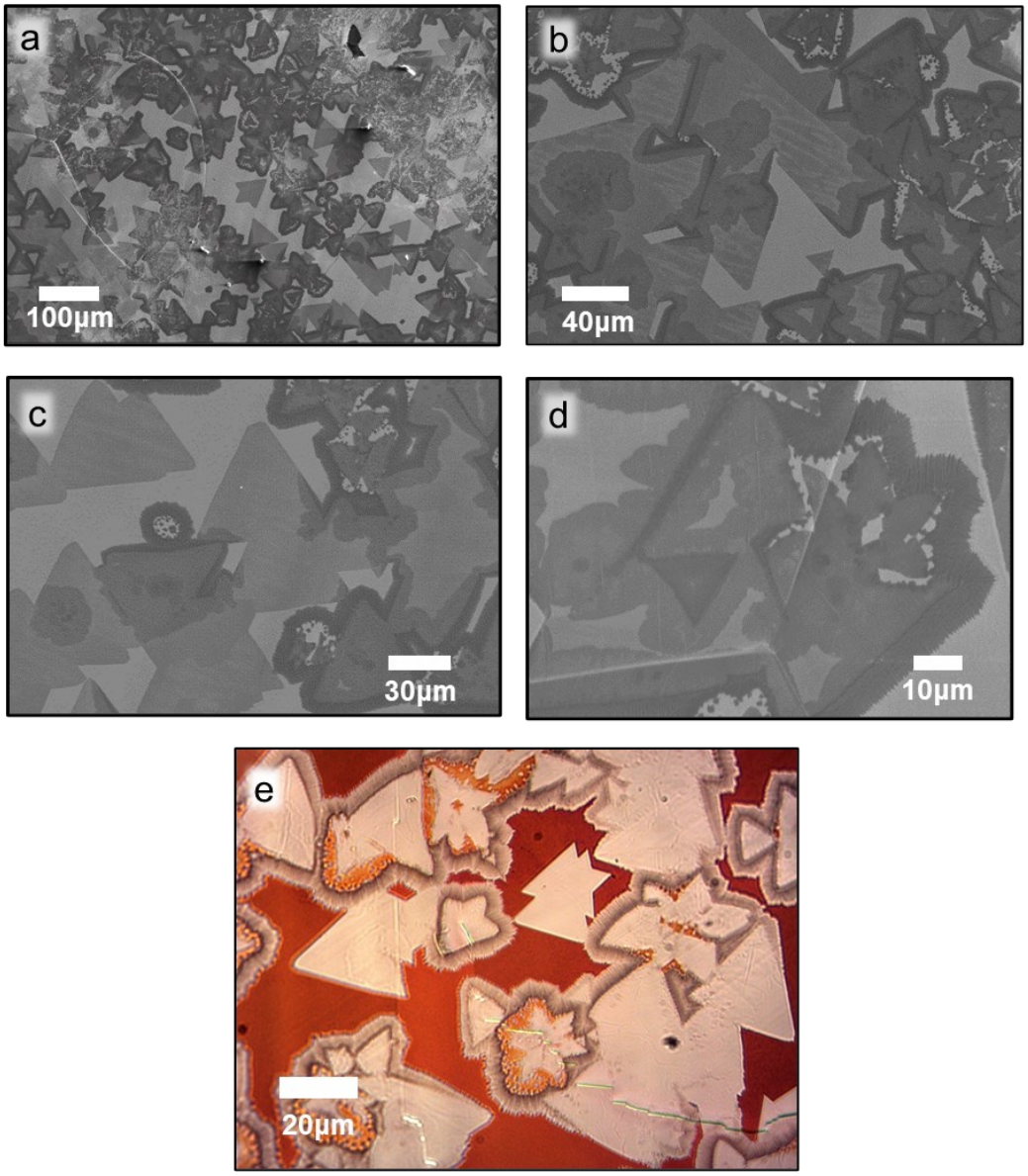


Supplementary Figure 4, Observing the lattice with FFT filtering; (a,c) Raw image and corresponding FFT for (a) AA' stacked hBN and (c) rotated lattice stacking. (b,d) Inverse FFT image for (b) AA' stacked and (d) rotated lattice stacking.

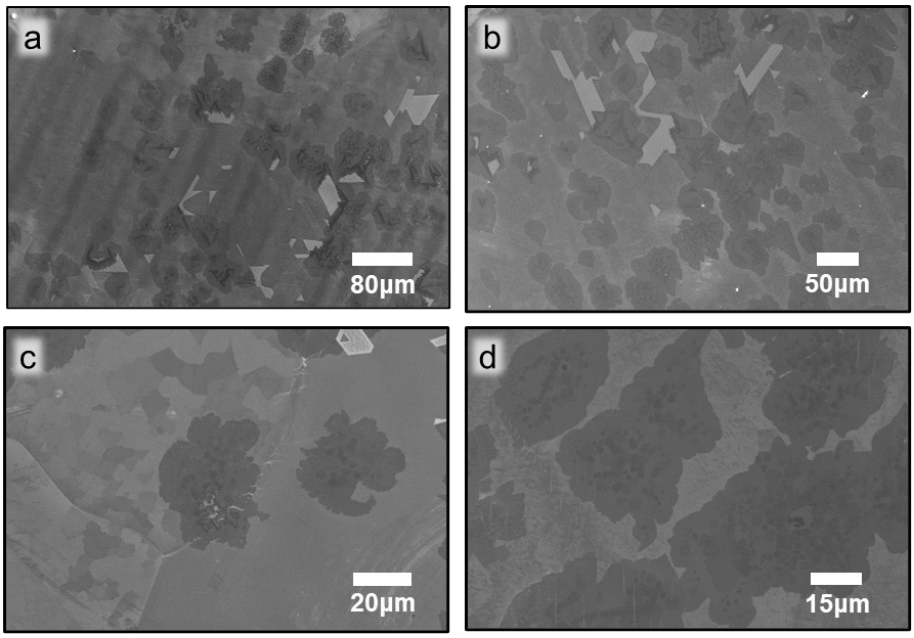
Supplementary Figure 4 shows region of hBN with multiple and single stacking rotations present within the same sample, showing how hBN regions may vary across the film. Such

mis-orientations have been previously reported in the literature [133, 198] and illustrate how, with hBN growth on copper, a deviation from AA' stacking is often observed. By filtering the FFT images, a clearer picture of the hBN lattice or superlattice can be seen (images b, d).

8.1.5. Additional characterisation of $hBNC_3$ sample (SEM, OM)

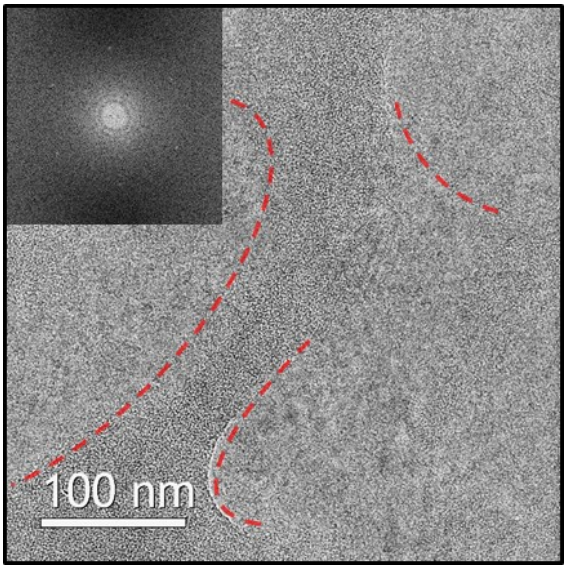


Supplementary Figure 5; SEM images of $hBNC_3$ sample on Cu for growth stopped prior to full film convergence (t ~ 60 mins). (a) wide view image showing how the various hBN, graphene/hBN and graphitic edge regions are observed across the substrate. (b-d) Close up SEM images exhibiting how growth of the congruent graphene typically nucleated along hBN edges and grows inwards. Congruent graphene growth is often accompanied by the graphitic edge regions (darkest contrast observed outside the edge of triangular hBN domains). (e) OM image of oxidised Cu substrate with structures observed in the $hBNC_3$ sample. The graphitic edge regions observed under SEM show slight oxidation (orange) in contrast to the hBN/graphene stacked heterostructures (white) and Cu substrate (red).



Supplementary Figure 6; SEM images of $hBNC_3$ sample on Cu for growth at full film convergence (t ~ 120 mins). (a,b) wide view images showing hBN, and stacked graphene/hBN formed on the Cu substrate. In regions where full convergence is not reached, the dendritic graphitic edge regions, shown in darker contrast. (c,d) close up SEM images of the highly irregular graphene domains which result from the guided growth along hBN domains. Darker contrasted regions are observed within individual domains, suggesting multilayered nucleation in some regions.

8.1.6. Amorphous regions observed in TEM of $hBNC_3$

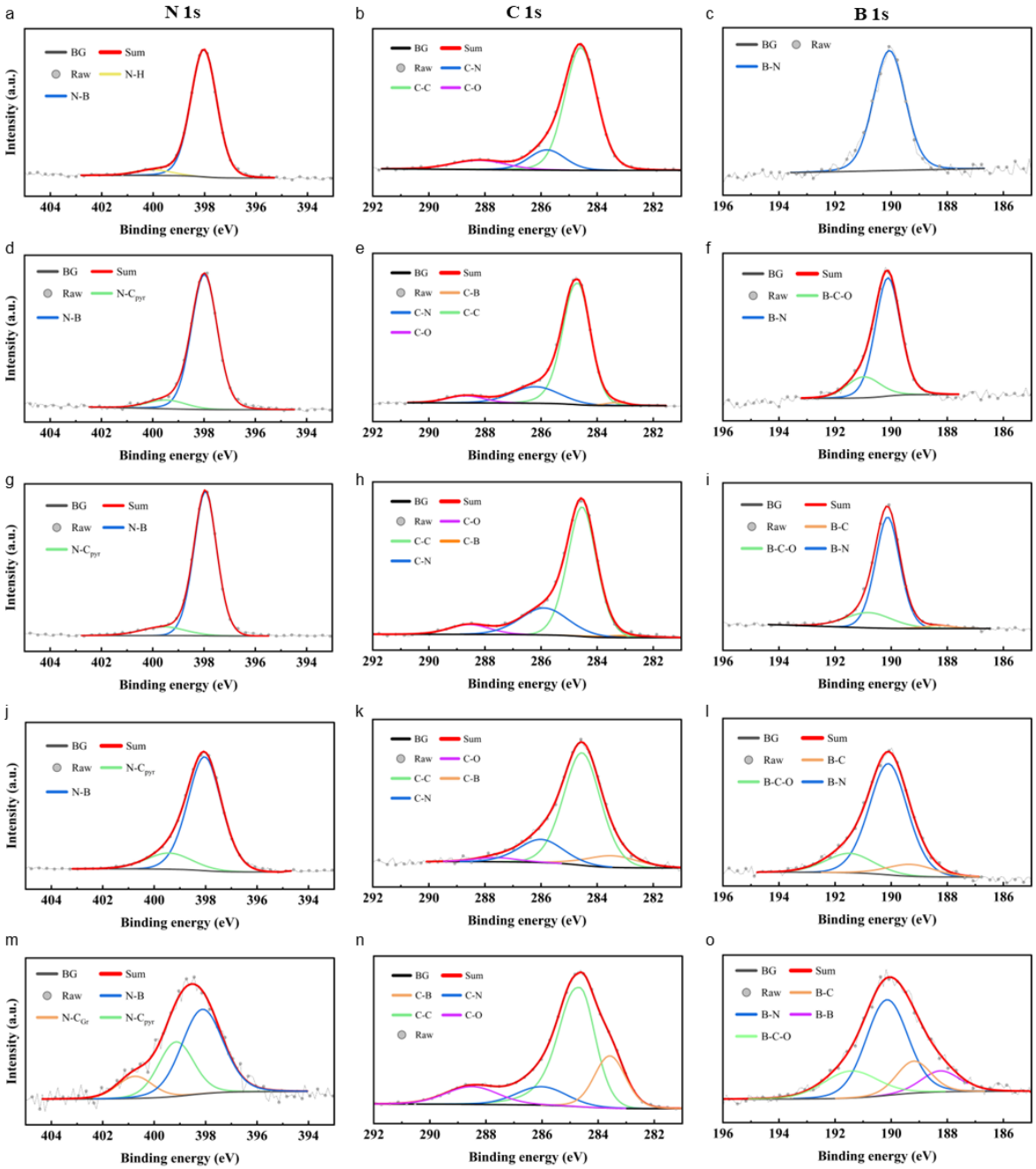


Supplementary Figure 7; TEM image of $hBNC_3$ exhibiting similar amorphous adlayers as $hBNC_2$. FFT inset showing a six-fold, hexagonal reflection, consistent with hexagonal material structures.

Amorphous regions, highlighted by the red dashed lines were observed in the $hBNC_3$. The FFT, inset, exhibits a single hexagonal pattern that is observed at regions both covered and

uncovered with the amorphous material. Similar amorphous regions ar observed in the $hBNC_2$ sample, which are thought to result from the dendritic graphitic regions degraded upon transfer of the 2D film.

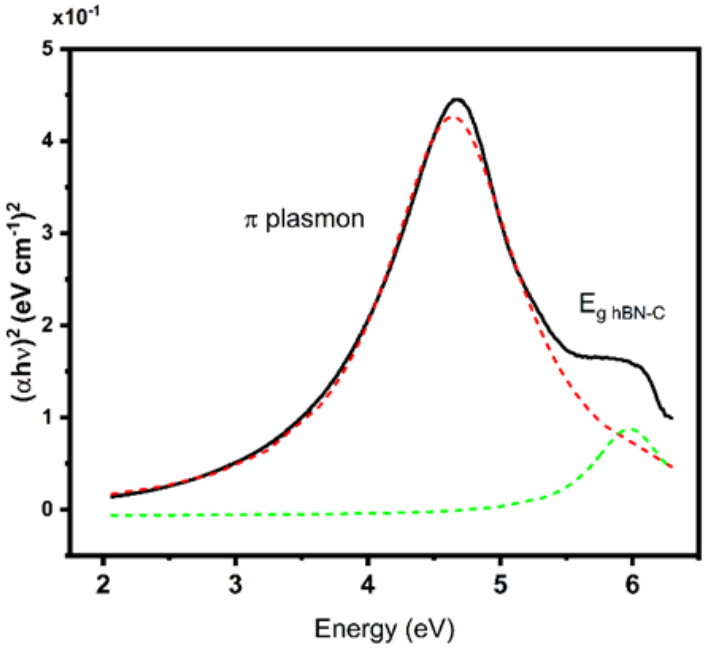
8.1.7. XPS HR-Spectra for $hBNC_x$ samples grown on Copper



Supplementary Figure 8, XPS high resolution spectra for samples (a-c) hBN, (d-f) $hBNC_1$, (g-i) $hBNC_2$, (j-l) $hBNC_3$, (m-o) $hBNC_4$.

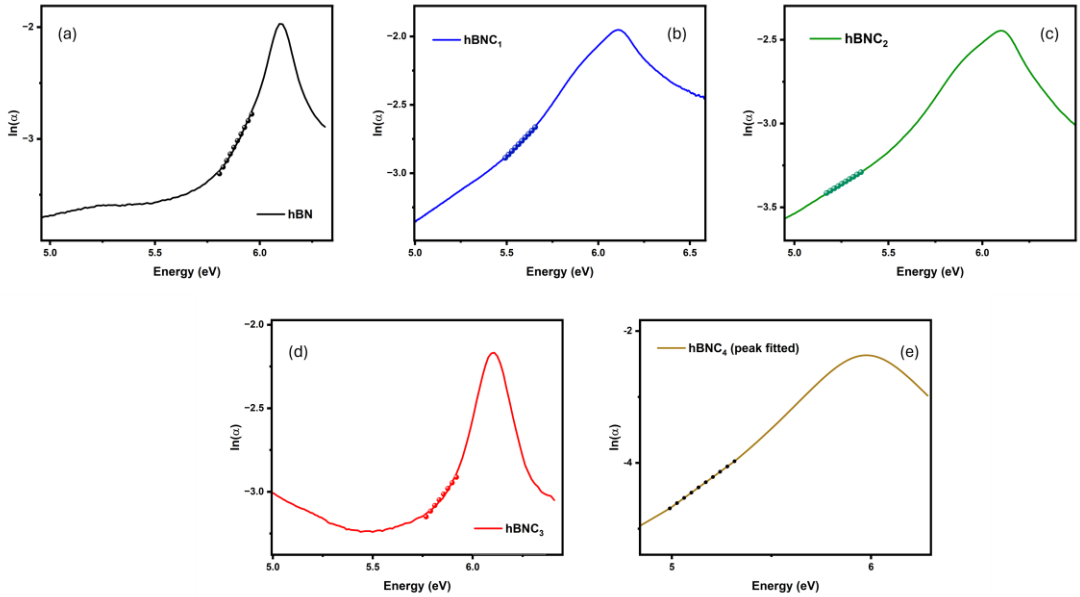
In the N1s spectra, peaks are fitted as follows; N-B peak at 398 eV, N-$C_{pyrolic}$ peak at 399.5 eV and an N-$C_{graphitic}$ defect peak fitted at 400.9 eV. In the hBN sample an N-H peak is fitted at 400 eV. In the C1s spectra, the C-C peak is centred at 284.8 eV, C-B at 283.4 eV, C-N at 286 eV and C-O at 288.6 eV. The B1s spectra are fitted with peaks at 190.1 eV for B-N, ~191.2 eV for O-B-C related bonding, and 189.2 eV for B-C bonding *[7, 9-11, 13, 17, 22, 23, 142, 150, 162]*. In the $hBNC_4$ sample, a small peak at 188.2 eV is observed, which could be attributed to either B-B bonding or a B_4C phase in the sample [368].

8.1.6. UV-Vis characterisation of $hBNC_x$ samples grown on Cu



Supplementary Figure 9, Peak fitting for $hBNC_4$ sample where Gr π-plasmon and E_g hBN absorption peaks are observed.

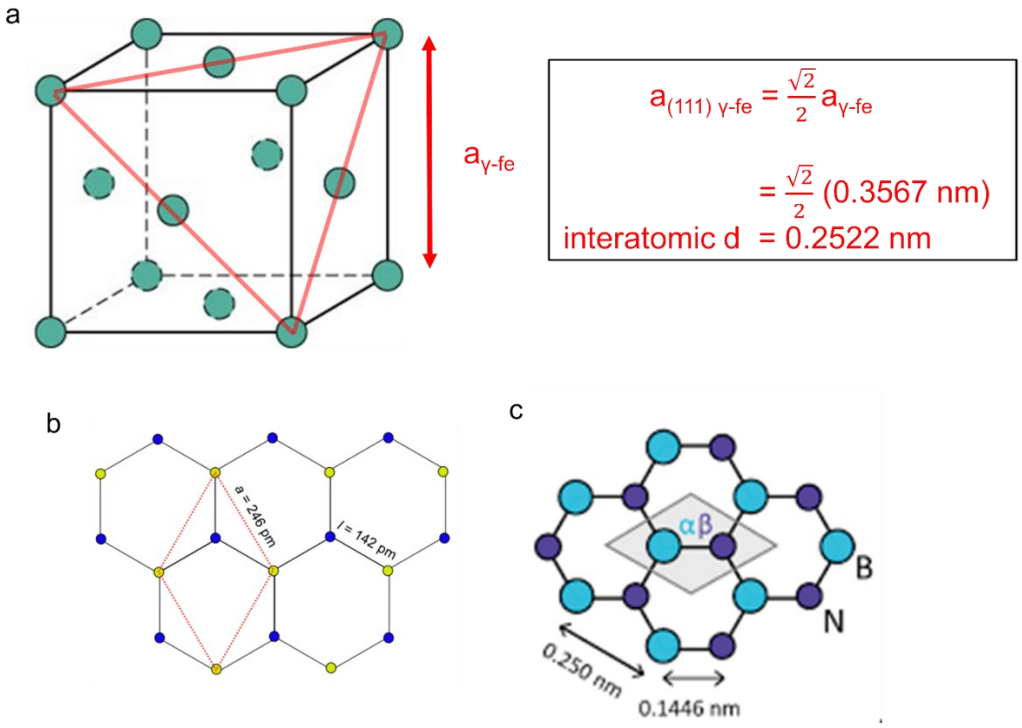
The $hBNC_4$ sample is comprised of both graphene and hBN regions. The large π-plasmon peak of graphene suggests that this is mostly composed of graphene material. The band gap of the hBN regions in the sample is calculated via the Tauc method and found to be 5.41 eV.



Supplementary Figure 10, Urbach Energy plots for hBN and hBNC samples grown on Cu. The inverse of the slope of the straight line plot below the material's band gap gives the Urbach Energy, E_U.

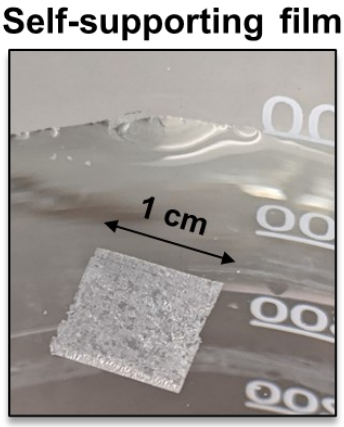
The Urbach plots for hBN and hBNC samples grown on Cu are shown in Supplementary Figure 12. To find the Urbach energy, E_U, we take the inverse of the slope of a straight line plot *below* the material's band gap value, as determined by the Tauc method.

8.1.7. Lattice Parameters of FCC-iron (111), graphene and hBN



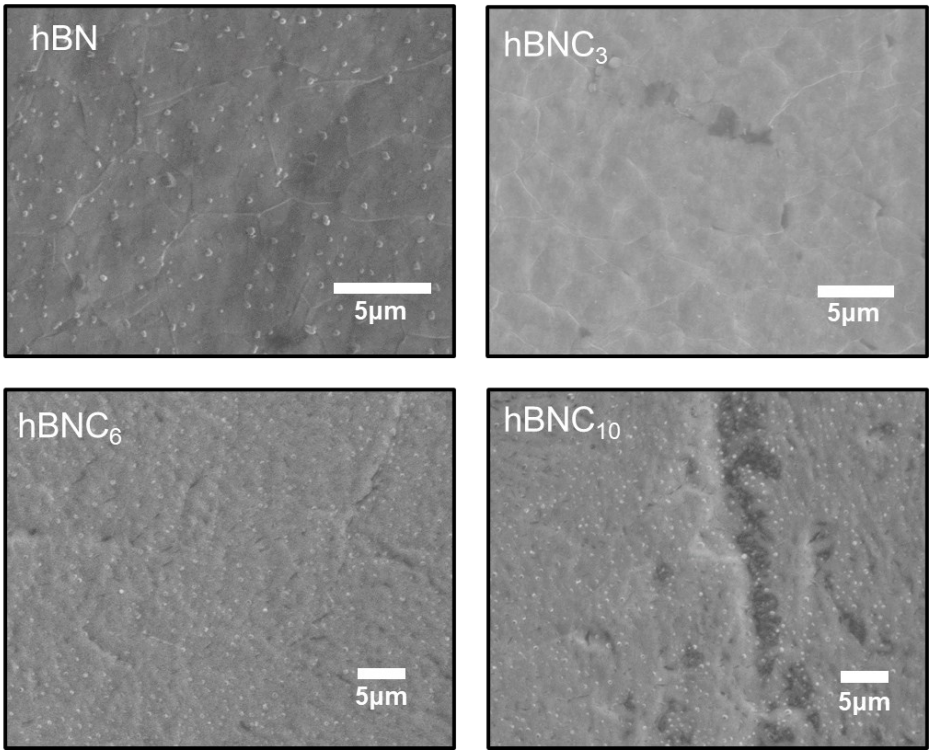
Supplementary Figure 11, (a) Face centred cubic (FCC) unit cell and calculation of the interatomic distance in γ-iron. (b,c) lattice parameters for (b) graphene and (c) hBN used to calculate the lattice mismatch %.

8.1.8. Polymer-Free transfer of thick hBN films grown on Fe



Supplementary Figure 12; Thicker hBN films grown on Fe could be readily transferred without the need for a polymer support

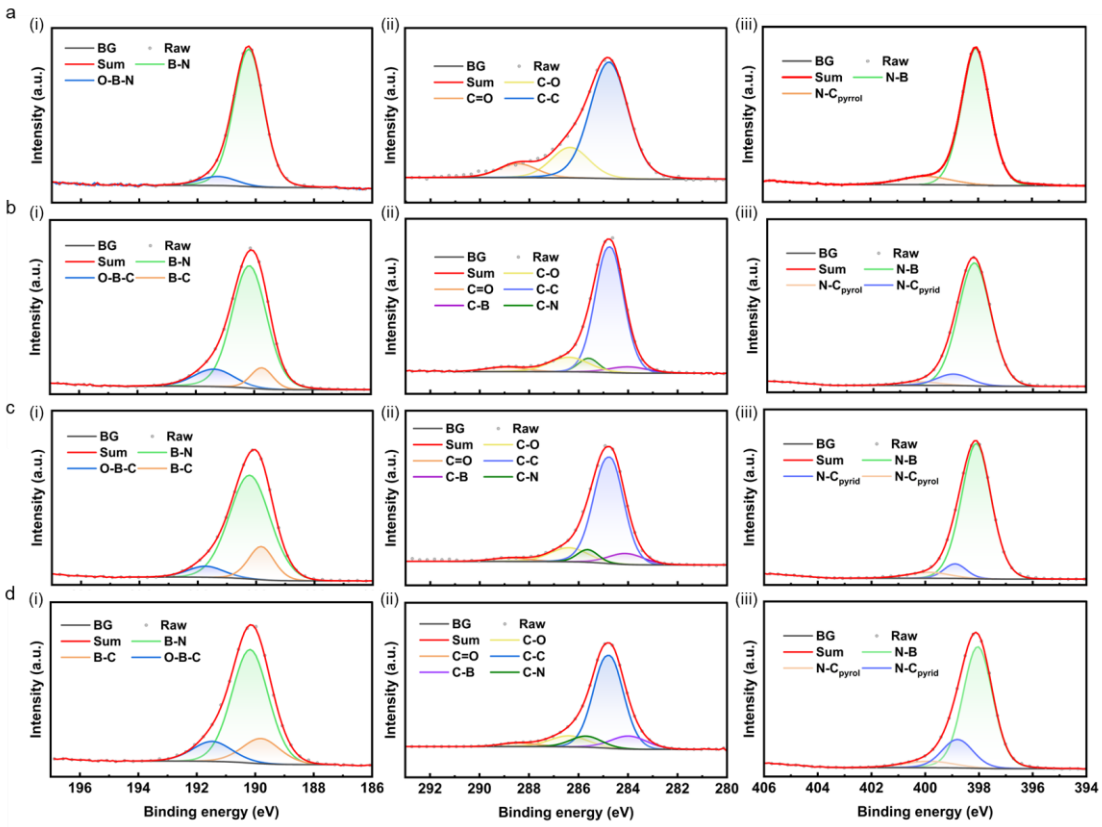
8.1.9. SEM images of $hBNC_x$ grown on Fe



Supplementary Figure 13, SEM images of the hBN and hBNC samples on Fe foil.

No apparent regions of graphitic material are observed in hBN-C growth on Fe, across all methane partial pressures. Small particles are observed on the surface of the material, hought to arise from impurities in the Fe foils.

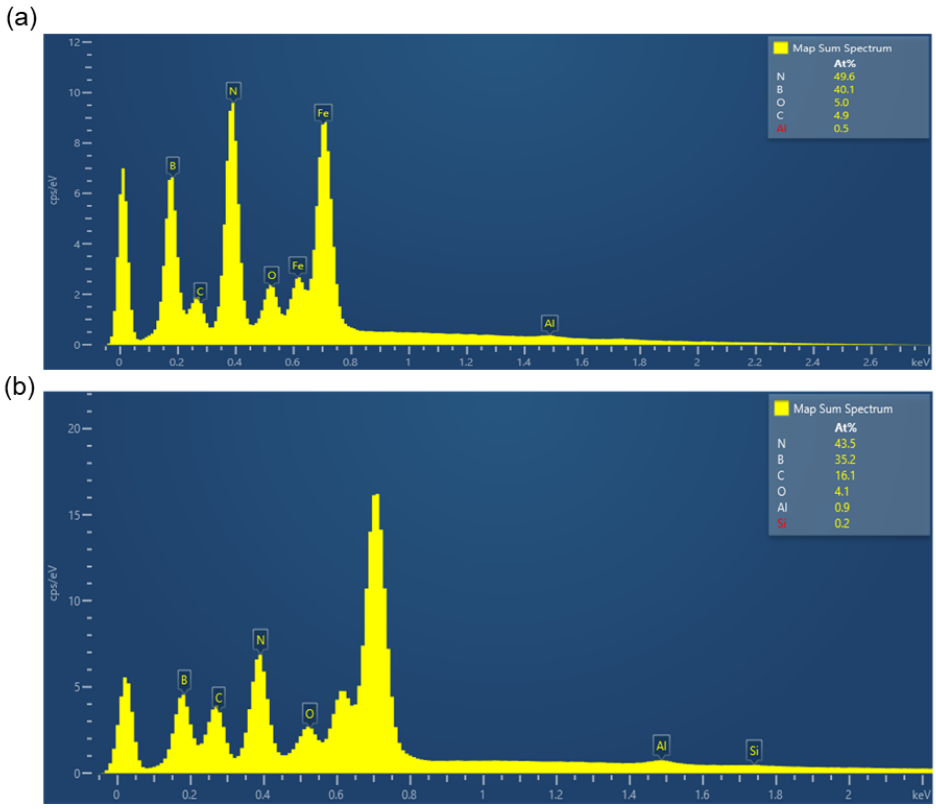
8.1.10. HR XPS Spectra of hBNC$_x$ samples grown on Fe



Supplementary Figure 14, XPS analysis of hBN and hBNC grown on Fe; (i) B1s (ii) C1s and (iii) N1s High-Res XPS spectra for (a) hBN (b) hBNC$_3$ (c) hBNC$_6$ and (d) hBNC$_{10}$ samples synthesised on Fe foil.

Three peaks can be identified in the B1s spectrum, located at 189.8 eV, 190.3 eV and 191.4 eV, which we attribute to B-C, B-N and O-B-C bonding in the sample [13, 147, 157, 168]. The O-B-C bonding peak falls below that of pure boron oxide (>192 eV) and so we attribute this peak to O-related defects of B-C which arise under increased methane flow. Five peaks are used to fit the C1s spectrum; peaks at 288.6 eV, 286.2 eV, 285.6 eV, 284.8 eV and 283.9 eV, which are attributed to C=O, C-O, C-N, C-C and C-B bonding resectively in the samples *[7, 9-11, 13, 17, 22, 23, 142, 150, 162]*. In the hBN sample (a, ii), a broad C-O peak is observed, presuable from the adventitious carbon on the sample. In C doped samples, the relative contribution of this peak is reduced and contributions from C-N and C-B increase, relatively. In the N1s spectra, three peaks are fitted; N-B peak at 398 eV, N-C$_{pyridinic}$ peak at 398.8 eV and an N-C$_{pyrrolic}$ defect peak fitted at 400.1 eV *[7, 9-11, 13, 17, 22, 23, 142, 150, 162]*.

8.1.11. EDX Spectra of hBN and $hBNC_6$ foil



Supplementary Figure 15; Full EDX spectrum and atomic % data with Fe content screened for (a) hBN and (b) $hBNC_6$ samples.

EDX spectra of hBN and $hBNC_6$ samples grown on Fe show the presence of B, C, N, O and Fe, as to be expected. Furthermore, Al and O impurities are observed in both samples, presumably coming from the Fe foil.

8.3. Appendix II: 2D lateral Graphene/hBN heterostructures toward catalysis - a DFT Study

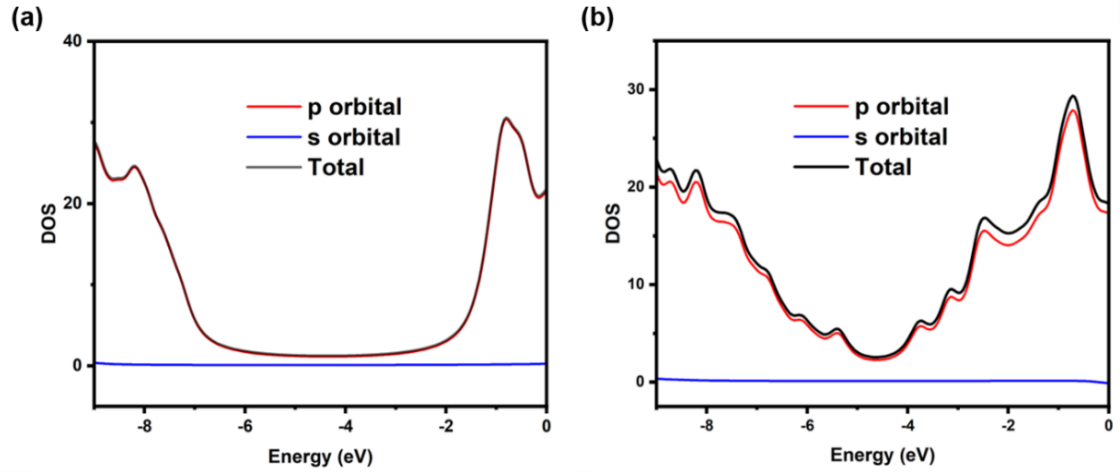
8.2.1. Band gaps and band edge potentials for various XC functionals trialled

Supplementary Table 1 - XC functional, calculated electronic band gap and % deviation from the fundamental bandgap of hBN, generally accepted as 5.95 eV.

XC functional	Bandgap of BN (eV)	% dev.	HOMO (eV)	LUMO (eV)
BP86D3	4.53	23.87	-6.208	-1.676
revtpss	4.77	19.83	-6.49	-1.715
TB-MBJ	6.19	4.03	-5.1639	1.02723
HSE06	5.94	0.17	-7.23514	-1.29652

The HSE06 functional closely aligns with the experimentally derived bandgap of hBN at 5.95 eV. Therefore it was chosen as the appropriate XC functional for deriving the opto-electronic properies of hBN-C systems in Chapter 4.

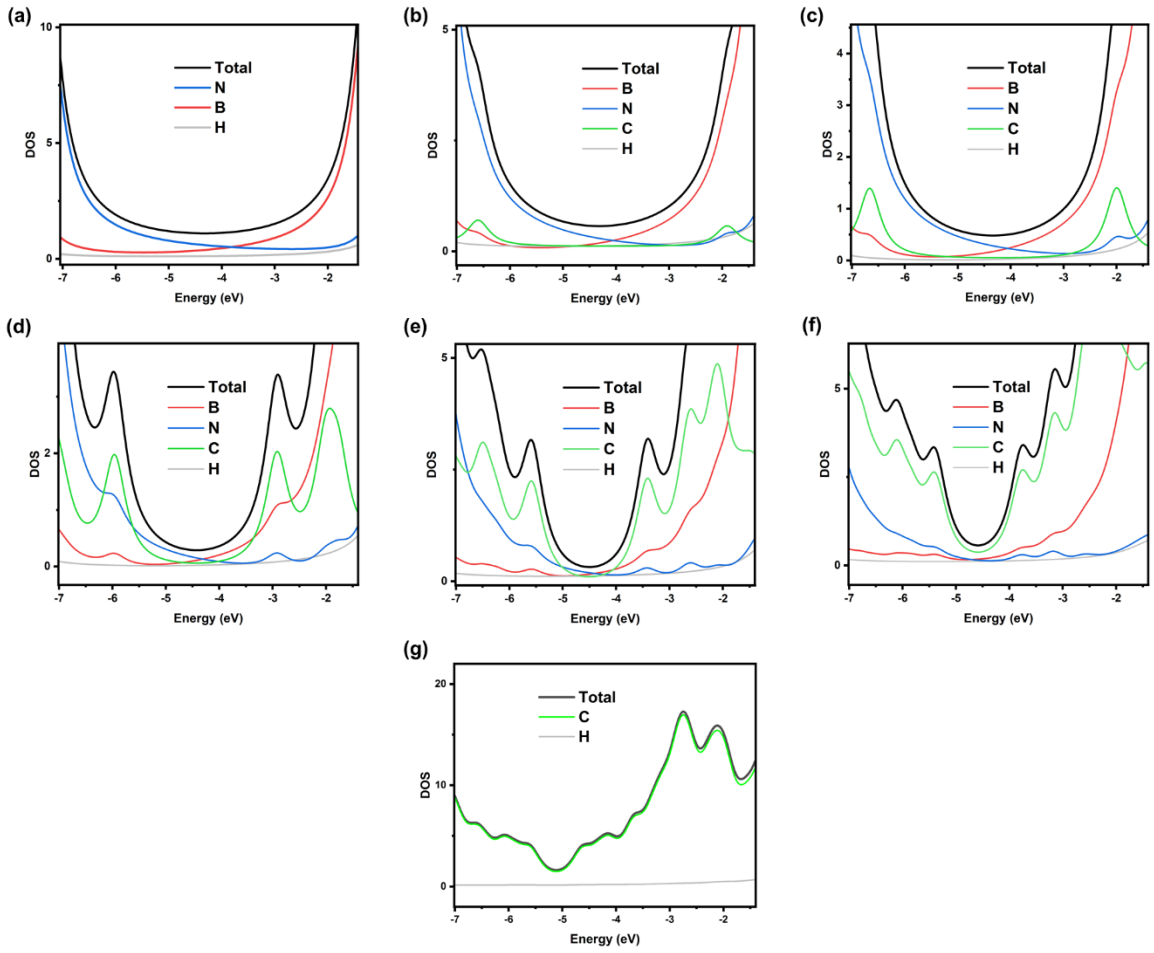
8.2.2. Contributions from s and p orbitals to the Total Density of States (TDOS)



Supplementary Figure 16, Partial density of states showing the s orbital and p orbital contributions in the (a) BN and (b) BN-C_{96} structure.

Supplementary Figure 16 shows the s and p contributions to the Partial Density of States in (a) BN and (b) BN-C_{96} structures. In both undoped and highly C doped structures, it is the p orbitals that contribute to the HOMO and LUMO states.

8.2.3. Atomic contributions from B, C and N to the Total Density of States (TDOS)



Supplementary Figure 17 - Partial density of states, as determined by the HSE06 XC functional, showing states closes to the structures electronic band gap for (a) BN, (b) BN-C_2 (c) BN-C_6 ,(d) BN-C_{24}, (e) BN-C_{54} and (f) BN-C_{96}.

Supplementary Figure 14 shows the PDOS close to the band gap of the various systems under study in Chapter 4. It can be seen that the relative contribution from B and N decreases as the C concentration increases, as C-C bonding states become the dominant feature near the fermi level. The pure carbon domain shows non-zero values for the DOS across the calculated band gap region (5.5 – 4.5 eV), presumably as the HSE06 functional does not predict discrete values for the DOS across the energy range.

8.4. Appendix III: Step-wise CVD growth of phase-separated Gr-hBN heterostructures on Cu metal foils

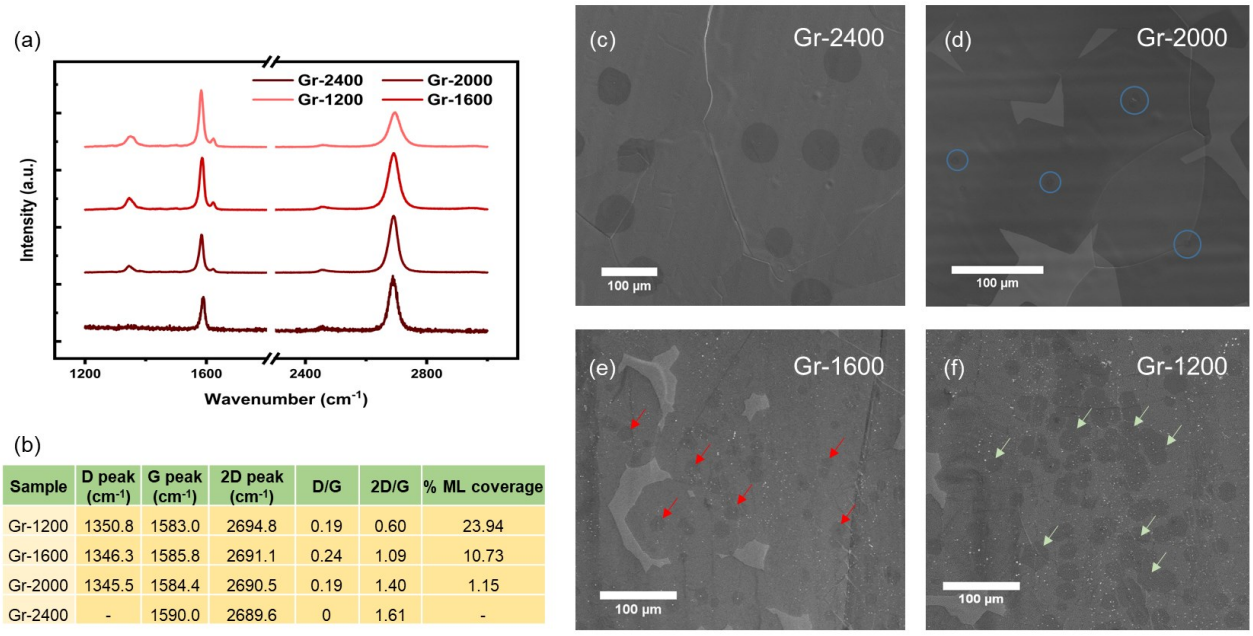
8.3.1. Graphene APCVD on Cu

For step-wise growth of lateral graphene / hBN heterostructures, growth of hBN and graphene was initially optimised. The optimisation of graphene synthesis is carried out, considering the parameters of *H_2:CH_4 ratio* and *synthesis time*.

H_2 : CH_4 ratio optimisation

The first parameter investigated was the H_2 : CH_4 ratio as this is reported to significantly affect the quality of the graphene synthesised, as well as the overall shape of the individual graphene domains [139, 369]. Partial pressure of the methane precursor in graphene growth is an essential parameter and directly affects the growth kinetics, nucleation density and domain sizes in the overall film. Previous work in APCVD graphene has shown that high quality monolayer graphene can be obtained using a low methane concentration [105]. Furthermore, at low H_2 : CH_4 ratios, inhomogeneous, few-layered graphene is often observed [370]. With higher methane concentrations, growth is not 'self-limiting' on the Cu surface. Here, multilayer growth is enhanced on top of the monolayer flakes, and these films show an increased number of defects [105], although an increased growth rate is also achieved [370]. Notable work by Lewis et al., gathered data from previously reported literature on graphene synthesis and used a data-driven approach to investigate the influence of gas phase chemistry on the CVD of graphene in a hot wall reactor [221]. In their study, they define a parameter space based on R_{CH} (the CH_4 : H_2 ratio), temperature and pressure, and correlated them with the final growth product (e.g. few-layer graphene, bilayer graphene, monolayer, defective monolayer, partial coverage, etc.). Their study concluded that, in all cases, high quality, monolayer graphene is favourable when R_{CH} is between .0004 – 0.20. For APCVD, more specifically, their study

suggested that film quality tends to improve for hydrocarbon flows more heavily diluted in hydrogen in the regime .0004 < R_{CH} < 0.011 (2500:1 < H_2:CH_4 < 909:1) [221, 370]. The parameter space for the H_2:CH_4 ratios investigated in this APCVD system has been chosen accordingly to fall within this defined regime.



(b)

Sample	D peak (cm^{-1})	G peak (cm^{-1})	2D peak (cm^{-1})	D/G	2D/G	% ML coverage
Gr-1200	1350.8	1583.0	2694.8	0.19	0.60	23.94
Gr-1600	1346.3	1585.8	2691.1	0.24	1.09	10.73
Gr-2000	1345.5	1584.4	2690.5	0.19	1.40	1.15
Gr-2400	-	1590.0	2689.6	0	1.61	-

Supplementary Figure 18; Investigating H_2 : CH_4 ratios for optimised graphene growth. (a) Raman spectra of the various graphene samples synthesised under varying R_{CH}^{-1}. Positions of the D, G and 2D peaks are shown in the bottom spectrum. (b) Table exhibiting Raman data such as peak centres, peak ratios for the samples as well as % ML coverage. Gr-2400 sample shows low defect density and monolayer coverage but small domains (low growth rate). Gr-2000 sample shows good monolayer coverage and improved growth rate. (c-f) SEM images showing graphene growth at various R_{CH}^{-1}. Blue circles in (d), highlight small regions of multilayer growth in Gr-2000 sample. Multilayer growth can clearly be seen in SEM images of Gr-1600 (e) and Gr-1200 (f) sample highlighted by the arrows.

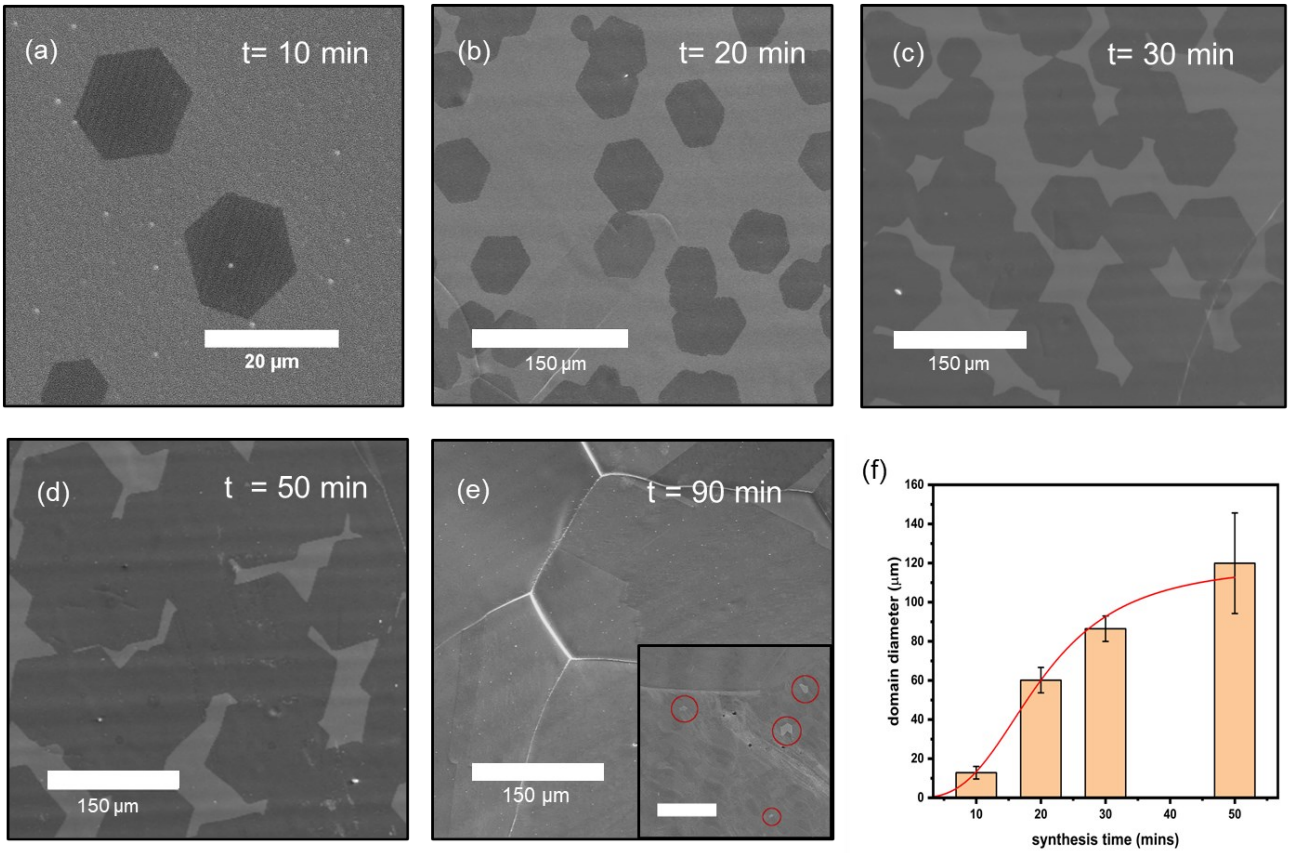
Graphene samples with four values of H_2:CH_4 were synthesised; 2400, 2000, 1600 and 1200 which are referred to as Gr-2400, Gr-2000, Gr-1600 and Gr-1200, respectively. Supplementary Figure 18 shows results from Raman spectroscopy and SEM experiments on the films. It was found that at the highest value for R_{CH}^{-1}, 2400, graphene domains with positive curvature were observed (Supplementary Figure 18, c). Domains of diameter 63.5 +/- 6.5 µm were obtained suggesting that long synthesis times would be required to achieve full coverage of the Cu substrate. However, domains showed little sign of multi-layered growth, as evidenced in the

SEM image as well as the associated Raman spectrum, which shows no D peak and the highest 2D/G ratio of 1.61. For the sample Gr-2000, hexagonal growth of graphene domains with negligible curvature were obtained, as seen in Supplementary Figure 18 (d). Domains with diameter 158.9 +/- 25.1 um are realised, which show signs of small multi-layer islands at the centre of the domain, highlighted in blue circles in Supplementary Figure 18 (d). Raman analysis of this sample shows presence of a D peak with a D/G ratio of 0.19. Ratio of 2D/G peaks suggests the film is mono/bilayer with a ratio of 1.5. Looking more closely at the G peak, we see the D' peak at ~1620cm^{-1}. Both D and D' modes require a defect for its activation and so the film grown here is not considered 'pristine'. For the purpose of this study, however, small amounts of defects are acceptable. Samples Gr-1600 and Gr-1200 show increased multilayered coverage as determined by intensity contrast measurements and lower 2D/G peaks via Raman analysis and so Gr-2000 was chosen as the optimal H_2:CH_4 ratio.

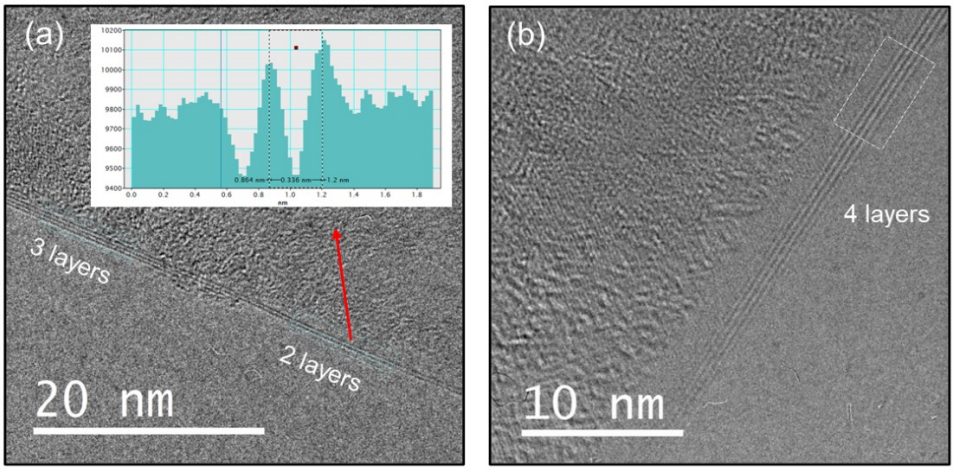
Time

From these experiments, we determined the growth rate of graphene (with R_{CH}^{-1} = 2000). The results of this set of experiments can be seen in Supplementary Figure 19 where SEM images of the graphene structures on Cu foil are used to estimate the mean domain diameter. The time evolution of the average domain size is plotted in Supplementary Figure 19 (f). Both the average and distribution of the domain sizes increase with the growth time. The domain size vs time plot follows a typical logistic curve, corresponding to an 'incubation' at the beginning of the growth process, where the solid-gas phase equilibrium at the surface of the substrate is set up so that graphene growth can proceed, followed by a linear growth region where domains increase in size significantly, and, finally, a slowing down period, as less catalyst surface area is available on the surface of Cu and domains merge. After 10 minutes growth, small domains of diameter 12.8 +/- 3.2 um are observed on the Cu substrate. After 20 minutes, the size of the

domains has increased significantly, to 60.2 +/- 6.5 um diameter. After 30 minutes domains of 86.4 +/- 7.2 um are realised and at 50 minutes, the size of the domains reaches 129.9 +/- 25.7 um. After this stage, the size of the domains is difficult to infer as many of them have merged with neighbouring ones. To obtain individual isolated domains under these parameters, a synthesis time of 20-30 minutes is advised. After a period of 90 minutes, we obtain almost total coverage of the Cu film. However, small regions of non-coated Cu or 'holes' in the graphene film were still observed, highlighted by red circles in the inset image of Supplementary Figure 19 (e).

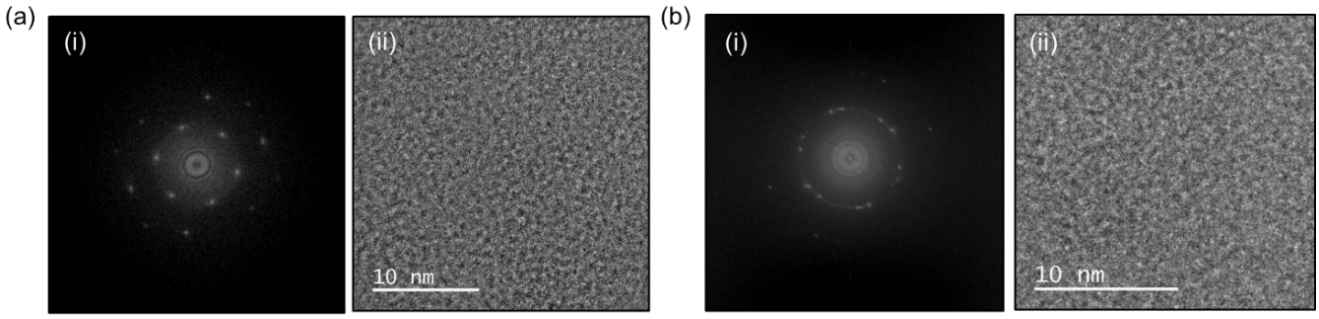


Supplementary Figure 19; Growth rate dynamics of graphene on Cu. (a-e) SEM images showing graphene domains nucleated on the surface of Cu at various synthesis times. Inset image of (e) shows gaps where the graphene film has not converged (scalebar is 40 µm). (f) Domain diameter vs. synthesis time shows a logistic curve shape, which is explained by an initial 'incubation time' to reach a critical concentration of CH_4 necessary for graphene nucleation, linear growth rate of graphene domains as CH_4 is continuously supplied, and finally, a slowed growth rate as availability of the catalytic Cu surface is reduced.



Supplementary Figure 20; TEM edge analysis of the graphene sample. (a) Graphene edge showing region with 2-3 layers. Interlayer spacing is measured at 0.336 nm. (b) Edge of graphene film showing 4 layers.

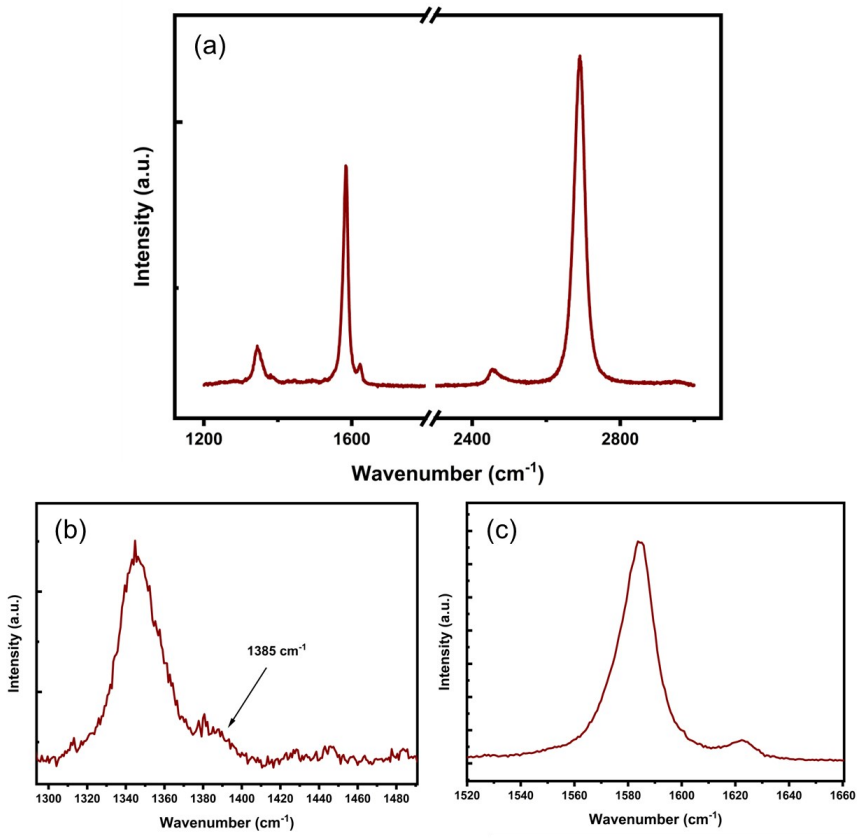
TEM analysis of the graphene films was also undertaken. Supplementary Figure 20 shows TEM edge analysis of the film and both (a) and (b) illustrate how the graphene layer number can vary. Overall, TEM analysis showed graphene films where regions of 2-4 layers were observed, with a lattice spacing of ~ 0.34 nm . No monolayer edge regions were found, suggesting that parameters used within this APCVD method require further tuning for monolayer growth.



Supplementary Figure 21; FFT analysis of graphene sample. (i) FFT and (ii) raw TEM image of a region of (a) AB stacking and (b) rotated stacking.

TEM analysis of the films also revealed regions of AB stacked graphene (Supplementary Figure 21 a, i) and turbostratic graphene (Supplementary Figure 21 b, i). It has been shown that superlattices formed by rotated layers can show additional peaks in the Raman spectrum of

graphene, observed at 1370-1470 cm^{-1} and ~1620 cm^{-1}, and peak positions are dependent on the angle of rotation between lattices [371]. Supplementary Figure 22 shows a close-up of these regions in the Raman spectrum. For samples synthesised with H_2:CH_4 = 2000, looking at the D peak of the Raman spectrum more closely, we see the presence of a small shoulder peak at 1385 cm^{-1}, similar to that reported in [371], whose intensity is ~ 30 times weaker than the G band and ~5 times weaker than the D band. Taking this into account, the peak at 1623 cm^{-1} can therefore be ascribed to a combination of the defect-induced (the presence of a D band evidences this) and rotational-induced intravalley double-resonance processes. The presence of these rotational-induced Raman signatures suggests that few-layered rotated graphene is likely being synthesised via this APCVD method which supports our TEM characterisation.



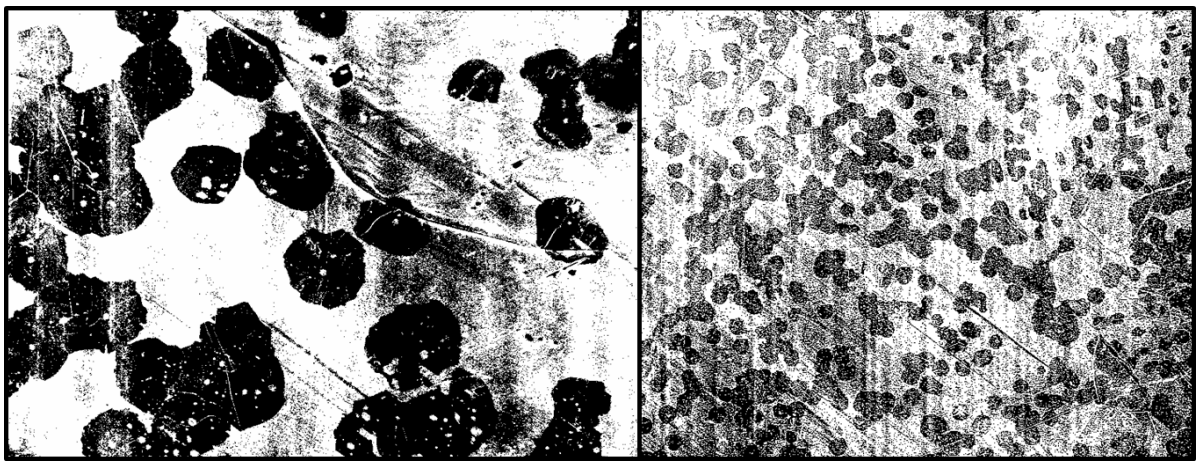
Supplementary Figure 22; Raman defect analysis of optimised graphene film. (a) Exemplar Raman spectrum of graphene with following the optimised synthesis protocol. (b) Analysis of the D peak, showing a shoulder peak in the region ~1385 cm^{-1}.(c) presence of small peak ~1620 cm^{-1} is also observed. These peaks have been previously observed in rotated graphene layers and are dependent on the degree of rotation *[371]*.

As such, imperfect graphene films are synthesised on Cu foil via APCVD. H_2 : CH_4 ratio is optimised based on film quality and reasonable growth times, settling on a ratio of $R_{CH} = 5 \times 10^{-4}$, validating results from a previous study by Lewis *et al*. [221]. Films synthesised with these parameters were characterised by TEM as few layer, showing regions of AB and turbostatic stacking. Raman spectroscopy also showed the presence of small peaks that can be attributed to interlayer rotation in the graphene film. Imperfect graphene was synthesised, although the level of defects was small ($I_D/I_G = 0.19$).

8.3.2. APCVD of Gr-hBN lateral heterostructures on Cu

C:BN coverage

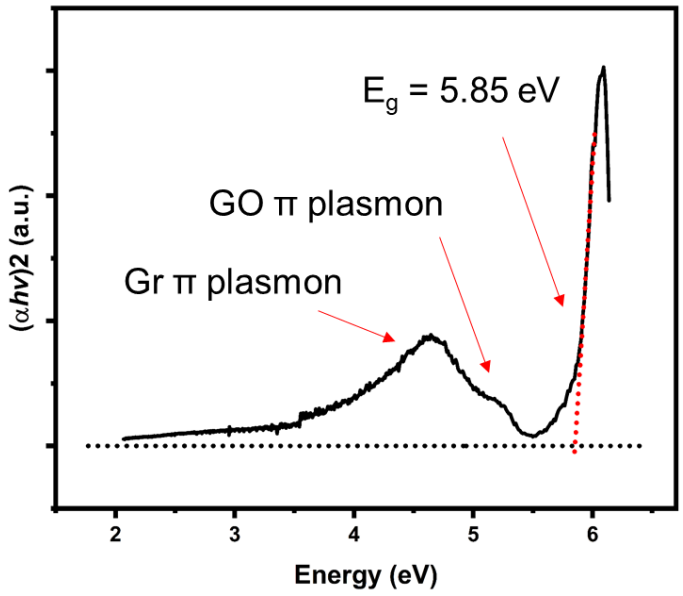
Graphene domains of size ~ 50 μm were synthesized after 25 minutes of deposition followed by hBN deposition for 2 hours to form a fully converged, continuous film. The Gr:hBN area ratio was determined via intensity threshold analysis of SEM images, shown in Supplementary Figure 23, and it was found that the film was composed of ~ 2:3 graphene to hBN.



Supplementary Figure 23, Intensity threshold analysis to measure the relative coverage of graphene : hBN. The film was found to be composed of ~ 40% graphene and 60% BN.

UV-Vis Characterisation

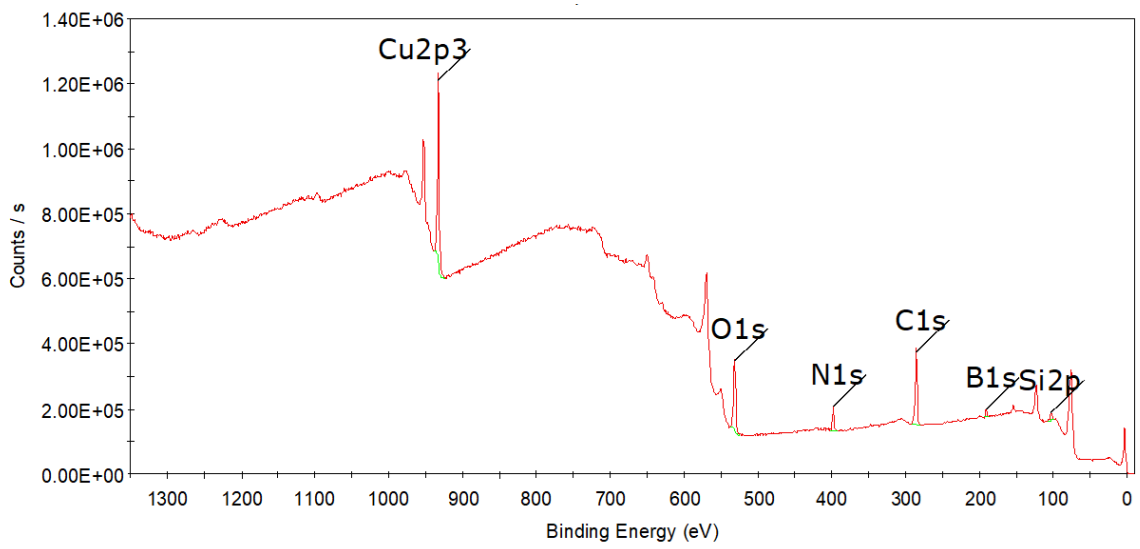
Opto-electronic characterisation of the Gr-hBN heterostructure was carried out via UV-vis spectroscopy, the Tauc plot of which is shown in Supplementary Figure 24. Two plasmon resonances are exhibited at 4.6 eV and 5.2 eV, which we attribute to graphene and defective graphene plasmon resonances, respectively. We also observe an absorption peak at ~ 6 eV from the hBN regions within the film, and the optical band gap is determined to be 5.85 eV, slightly reduced from intrinsic hBN (5.95 eV), likely due to reduction in crystallinity and states introduced via the BN-Gr interface. The blue-shifted π plasmon at 5.2 eV results from a reduction in sp^2 conjugation, typically observed in graphene oxide, and suggests that the defective, etched regions observed in Raman analysis are possibly oxygen-conjugated [246].



Supplementary Figure 24; Tauc plot for Gr-hBN sample. The main absorption peak of hBN has bandgap of 5.85 eV. Graphene and graphene oxide π-plasmon peaks are also observed suggesting the graphene regions are slightly oxidised

8.5. Appendix IV: B, N doped silica nanoplatelets on copper through low-purity ammonia borane activation

8.4.1 Survey Scan of hBN sample from Chapter 3



Supplementary Figure 25; XPS surver scan for hBN sample grown on Cu in Chapter 3 showing the presence of Si.

XPS survey scan of optimised hBN grown on Cu using high quality AB shows the presence of Si, although no Si deposits are observed in SEM analysis, suggesting Si is present in the near-surface region of Cu. This Si then reacts with ambient oxygen after the CVD experiment, forming intercalated silica, as has been observed in other CVD studies using a quartz reactor set up [306].

9. Bibliography

1. Jiang, H., et al., *Boron Carbonitride Lithium-Ion Capacitors with an Electrostatically Expanded Operating Voltage Window.* ACS Applied Materials & Interfaces, 2020. **12**(42): p. 47425-47434.
2. Chen, D., et al., *Facile fabrication of nanoporous BCN with excellent charge/discharge cycle stability for high-performance supercapacitors.* Materials Letters, 2019. **246**: p. 28-31.
3. Wang, S., et al., *Band gap-Tunable Porous Borocarbonitride Nanosheets for High Energy-Density Supercapacitors.* ACS Applied Materials & Interfaces, 2018. **10**(23): p. 19588-19597.
4. Guo, H. and Q. Gao, *Boron and nitrogen co-doped porous carbon and its enhanced properties as supercapacitor.* Journal of Power Sources, 2009. **186**(2): p. 551-556.
5. Sen, S., et al., *Excellent Performance of Few-Layer Borocarbonitrides as Anode Materials in Lithium-Ion Batteries.* Chemistry – An Asian Journal, 2014. **9**(1): p. 100-103.
6. Karbhal, I., et al., *Honeycomb Boron Carbon Nitride as High-Performance Anode Material for Li-Ion Batteries.* ChemNanoMat, 2022. **8**(7): p. e202200056.
7. Zheng, M., et al., *Metal-Free Dehydrogenation of N-Heterocycles by Ternary h-BCN Nanosheets with Visible Light.* Angewandte Chemie International Edition, 2018. **57**(19): p. 5487-5491.
8. Yuan, T., et al., *Ceramic boron carbonitrides for unlocking organic halides with visible light.* Chemical Science, 2021. **12**(18): p. 6323-6332.
9. Joshi, P., et al., *Contribution of B,N-co-doped reduced graphene oxide as a catalyst support to the activity of iridium oxide for oxygen evolution reaction.* Journal of Materials Chemistry A, 2021. **9**(14): p. 9066-9080.
10. Chang, B., et al., *Metal-free boron carbonitride with tunable boron Lewis acid sites for enhanced nitrogen electroreduction to ammonia.* Applied Catalysis B: Environmental, 2021. **283**: p. 119622.
11. Ahsan, M.A., et al., *Tuning the Intermolecular Electron Transfer of Low-Dimensional and Metal-Free BCN/C60 Electrocatalysts via Interfacial Defects for Efficient Hydrogen and Oxygen Electrochemistry.* Journal of the American Chemical Society, 2021. **143**(2): p. 1203-1215.
12. Zhang, M., et al., *Molten salt assisted assembly growth of atomically thin boron carbon nitride nanosheets for photocatalytic H2 evolution.* Chemical Communications, 2020. **56**(17): p. 2558-2561.
13. Zhou, M., et al., *Boron Carbon Nitride Semiconductors Decorated with CdS Nanoparticles for Photocatalytic Reduction of CO2.* ACS Catalysis, 2018. **8**(6): p. 4928-4936.
14. Guo, F., et al., *Carbon-Doped BN Nanosheets for the Oxidative Dehydrogenation of Ethylbenzene.* Angewandte Chemie International Edition, 2017. **56**(28): p. 8231-8235.
15. Tabassum, H., et al., *A catalyst-free synthesis of B, N co-doped graphene nanostructures with tunable dimensions as highly efficient metal free dual electrocatalysts.* Journal of Materials Chemistry A, 2016. **4**(42): p. 16469-16475.
16. Xue, Y., et al., *Three-dimensional B,N-doped graphene foam as a metal-free catalyst for oxygen reduction reaction.* Physical Chemistry Chemical Physics, 2013. **15**(29): p. 12220-12226.
17. Wang, S., et al., *BCN Graphene as Efficient Metal-Free Electrocatalyst for the Oxygen Reduction Reaction.* Angewandte Chemie International Edition, 2012. **51**(17): p. 4209-4212.
18. Jiménez-Arévalo, N., et al., *Ultrathin Transparent B–C–N Layers Grown on Titanium Substrates with Excellent Electrocatalytic Activity for the Oxygen Evolution Reaction.* ACS Applied Energy Materials, 2020. **3**(2): p. 1922-1932.
19. Srivastava, S., et al., *Ultrasensitive Boron–Nitrogen-Codoped CVD Graphene-Derived NO2 Gas Sensor.* ACS Materials Au, 2022. **2**(3): p. 356-366.
20. Bi, Y.-S., et al., *A h-BCN for Electrochemical Sensor of Dopamine and Uric Acid.* Journal of Nanomaterials, 2020. **2020**: p. 4604820.

21. Jerome, R. and A.K. Sundramoorthy, *Preparation of hexagonal boron nitride doped graphene film modified sensor for selective electrochemical detection of nicotine in tobacco sample.* Analytica Chimica Acta, 2020. **1132**: p. 110-120.
22. Mendelson, N., et al., *Identifying carbon as the source of visible single-photon emission from hexagonal boron nitride.* Nature Materials, 2021. **20**(3): p. 321-328.
23. Liu, H., et al., *Rational Control on Quantum Emitter Formation in Carbon-Doped Monolayer Hexagonal Boron Nitride.* ACS Applied Materials & Interfaces, 2022. **14**(2): p. 3189-3198.
24. Song, S.-B., et al., *Deep-ultraviolet electroluminescence and photocurrent generation in graphene/hBN/graphene heterostructures.* Nature Communications, 2021. **12**(1): p. 7134.
25. Wang, Y., et al., *Deep Ultraviolet Photodetectors Based on Carbon-Doped Two-Dimensional Hexagonal Boron Nitride.* ACS Applied Materials & Interfaces, 2020. **12**(24): p. 27361-27367.
26. Novoselov, K.S., et al., *Electric Field Effect in Atomically Thin Carbon Films.* Science, 2004. **306**(5696): p. 666-669.
27. Öztürk, B., S. Öztürk, and A.A. Adigüzel, *Effect of Type and Relative Amount of Solid Lubricants and Abrasives on the Tribological Properties of Brake Friction Materials.* Tribology Transactions, 2013. **56**(3): p. 428-441.
28. Castro Neto, A.H., et al., *The electronic properties of graphene.* Reviews of Modern Physics, 2009. **81**(1): p. 109-162.
29. Attaccalite, C., et al., *Two-photon absorption in two-dimensional materials: The case of hexagonal boron nitride.* Physical Review B, 2018. **98**(16): p. 165126.
30. Atkins, P.W. and R. Friedmanm, *Molecular Quantum Mechanics*. 5th edition ed. 2011, Oxford: Oxford University Press.
31. Greber, T., *Graphene and Boron Nitride Single Layers.* arXiv [cond-mat.mtrl-sci], 2009.
32. Naclerio, A.E. and P.R. Kidambi, *A Review of Scalable Hexagonal Boron Nitride (h-BN) Synthesis for Present and Future Applications.* Advanced Materials, 2023. **35**(6): p. 2207374.
33. *Lattice constants for hBN*. May 2023]; Available from: https://www.ioffe.ru/SVA/NSM/Semicond/BN/basic.html.
34. Chan, M.Y., et al., *Suppression of thermally activated carrier transport in atomically thin MoS2 on crystalline hexagonal boron nitride substrates.* Nanoscale, 2013. **5**(20): p. 9572-9576.
35. Withers, F., et al., *Electron transport of WS2 transistors in a hexagonal boron nitride dielectric environment.* Scientific Reports, 2014. **4**(1): p. 4967.
36. Britnell, L., et al., *Electron Tunneling through Ultrathin Boron Nitride Crystalline Barriers.* Nano Letters, 2012. **12**(3): p. 1707-1710.
37. Liu, L., et al., *Ultrafast non-volatile flash memory based on van der Waals heterostructures.* Nature Nanotechnology, 2021. **16**(8): p. 874-881.
38. Wu, L., et al., *Atomically sharp interface enabled ultrahigh-speed non-volatile memory devices.* Nature Nanotechnology, 2021. **16**(8): p. 882-887.
39. Sasaki, T., et al., *Ultrafast Operation of 2D Heterostructured Nonvolatile Memory Devices Provided by the Strong Short-Time Dielectric Breakdown Strength of h-BN.* ACS Applied Materials & Interfaces, 2022. **14**(22): p. 25659-25669.
40. Xie, J., et al., *Stitching h-BN by atomic layer deposition of LiF as a stable interface for lithium metal anode.* Science Advances. **3**(11): p. eaao3170.
41. Li, G., et al., *Suppressing Li Dendrite Puncture with a Hierarchical h-BN Protective Layer.* ACS Applied Materials & Interfaces, 2021. **13**(47): p. 56109-56115.
42. Cassabois, G., P. Valvin, and B. Gil, *Hexagonal boron nitride is an indirect bandgap semiconductor.* Nature Photonics, 2016. **10**(4): p. 262-266.
43. Elias, C., et al., *Direct band-gap crossover in epitaxial monolayer boron nitride.* Nature Communications, 2019. **10**(1): p. 2639.
44. Caldwell, J.D., et al., *Photonics with hexagonal boron nitride.* Nature Reviews Materials, 2019. **4**(8): p. 552-567.
45. Schue, L., et al., *Direct and indirect excitons with high binding energies in hBN.* 2018.

46. Watanabe, K. and T. Taniguchi, *Hexagonal Boron Nitride as a New Ultraviolet Luminescent Material and Its Application.* International Journal of Applied Ceramic Technology, 2010. **8**.
47. Watanabe, K., T. Taniguchi, and H. Kanda, *Direct-bandgap properties and evidence for ultraviolet lasing of hexagonal boron nitride single crystal.* Nature Materials, 2004. **3**(6): p. 404-409.
48. Vuong, T.Q.P., et al., *Deep ultraviolet emission in hexagonal boron nitride grown by high-temperature molecular beam epitaxy.* 2D Materials, 2017. **4**(2): p. 021023.
49. Kaushik, S., et al., *Deep-Ultraviolet Photodetectors Based on Hexagonal Boron Nitride Nanosheets Enhanced by Localized Surface Plasmon Resonance in Al Nanoparticles.* ACS Applied Nano Materials, 2022. **5**(5): p. 7481-7491.
50. Liu, H., et al., *High-performance deep ultraviolet photodetectors based on few-layer hexagonal boron nitride.* Nanoscale, 2018. **10**(12): p. 5559-5565.
51. Veeralingam, S., et al., *Record-High Responsivity and Detectivity of a Flexible Deep-Ultraviolet Photodetector Based on Solid State-Assisted Synthesized hBN Nanosheets.* ACS Applied Electronic Materials, 2021. **3**(3): p. 1162-1169.
52. Wang, G., et al., *Direct growth of hexagonal boron nitride films on dielectric sapphire substrates by pulsed laser deposition for optoelectronic applications.* Fundamental Research, 2021. **1**(6): p. 677-683.
53. Tran, T.T., et al., *Quantum emission from hexagonal boron nitride monolayers.* Nature Nanotechnology, 2016. **11**(1): p. 37-41.
54. Bourrellier, R., et al., *Bright UV Single Photon Emission at Point Defects in h-BN.* Nano Letters, 2016. **16**(7): p. 4317-4321.
55. Fernandes, J., et al., *Room-temperature emitters in wafer-scale few-layer hBN by atmospheric pressure CVD.* FlatChem, 2022. **33**: p. 100366.
56. Kim, G., et al., *Blue emission at atomically sharp 1D heterojunctions between graphene and h-BN.* Nature Communications, 2020. **11**(1): p. 5359.
57. Fischer, M., et al., *Controlled generation of luminescent centers in hexagonal boron nitride by irradiation engineering.* Science Advances. **7**(8): p. eabe7138.
58. Korona, T. and M. Chojecki, *Exploring point defects in hexagonal boron-nitrogen monolayers.* International Journal of Quantum Chemistry, 2019. **119**(14): p. e25925.
59. Tran, T.T., et al., *Quantum Emission from Defects in Single-Crystalline Hexagonal Boron Nitride.* Physical Review Applied, 2016. **5**(3): p. 034005.
60. Li, S., et al., *Ultraviolet Quantum Emitters in Hexagonal Boron Nitride from Carbon Clusters.* The Journal of Physical Chemistry Letters, 2022. **13**(14): p. 3150-3157.
61. Cai, Q., et al., *High thermal conductivity of high-quality monolayer boron nitride and its thermal expansion.* 2019. **5**.
62. Balandin, A.A., et al., *Superior Thermal Conductivity of Single-Layer Graphene.* Nano Letters, 2008. **8**(3): p. 902-907.
63. Kostoglou, N., K. Polychronopoulou, and C.J.V. Rebholz, *Thermal and chemical stability of hexagonal boron nitride (h-BN) nanoplatelets.* 2015. **112**: p. 42-45.
64. Li, L.H., et al., *Strong Oxidation Resistance of Atomically Thin Boron Nitride Nanosheets.* ACS Nano, 2014. **8**(2): p. 1457-1462.
65. Liu, L., et al., *Graphene Oxidation: Thickness-Dependent Etching and Strong Chemical Doping.* Nano Letters, 2008. **8**(7): p. 1965-1970.
66. Yang, G., et al., *Highly Thermal Conductive Poly(vinyl alcohol) Composites with Oriented Hybrid Networks: Silver Nanowire Bridged Boron Nitride Nanoplatelets.* ACS Applied Materials & Interfaces, 2021. **13**(27): p. 32286-32294.
67. Shi, H., et al., *Magnetic Field-Induced Orientation of Modified Boron Nitride Nanosheets in Epoxy Resin with Improved Flame and Wear Resistance.* Langmuir, 2021. **37**(27): p. 8222-8231.
68. Grant, J.T., et al., *Selective oxidative dehydrogenation of propane to propene using boron nitride catalysts.* Science, 2016. **354**(6319): p. 1570-1573.

69. Du, M., et al., *One-step synthesis of magnetically recyclable Co@BN core–shell nanocatalysts for catalytic reduction of nitroarenes.* RSC Advances, 2017. **7**(56): p. 35451-35459.
70. Sheng, J., et al., *Preparation of oxygen reactivity-tuned FeOx/BN catalyst for selectively oxidative dehydrogenation of ethylbenzene to styrene.* Applied Catalysis B: Environmental, 2022. **305**: p. 121070.
71. Wang, Y., et al., *Boosting selectivity and stability on Pt/BN catalysts for propane dehydrogenation via calcination & reduction-mediated strong metal–support interaction.* Journal of Energy Chemistry, 2021. **67**.
72. Perilli, D., C. Di Valentin, and F. Studt, *Can Single Metal Atoms Trapped in Defective h-BN/Cu(111) Improve Electrocatalysis of the H2 Evolution Reaction?* The Journal of Physical Chemistry C, 2020. **124**(43): p. 23690-23698.
73. Perilli, D., et al., *Computational Electrochemistry of Water Oxidation on Metal-Doped and Metal-Supported Defective h-BN.* ChemSusChem, 2019. **12**(9): p. 1995-2007.
74. Nozaki, H. and S. Itoh, *Structural stability of BC2N.* Journal of Physics and Chemistry of Solids, 1996. **57**(1): p. 41-49.
75. Yuge, K., *Phase stability of boron carbon nitride in a heterographene structure: A first-principles study.* Physical Review B, 2009. **79**(14): p. 144109.
76. Liu, Y., S. Bhowmick, and B.I. Yakobson, *BN White Graphene with "Colorful" Edges: The Energies and Morphology.* Nano Letters, 2011. **11**(8): p. 3113-3116.
77. Thomas, S. and S.U. Lee, *Atomistic insights into the anisotropic mechanical properties and role of ripples on the thermal expansion of h-BCN monolayers.* RSC Advances, 2019. **9**(3): p. 1238-1246.
78. Wang, Z., et al., *2D van der Waals heterostructures of graphitic BCN as direct Z-scheme photocatalysts for overall water splitting: the role of polar π-conjugated moieties.* Physical Chemistry Chemical Physics, 2020. **22**(41): p. 23735-23742.
79. Angizi, S., et al., *Review—Two-Dimensional Boron Carbon Nitride: A Comprehensive Review.* ECS Journal of Solid State Science and Technology, 2020. **9**(8): p. 083004.
80. Thomas, S. and M. Asle Zaeem, *A new planar BCN lateral heterostructure with outstanding strength and defect-mediated superior semiconducting to metallic properties.* Physical Chemistry Chemical Physics, 2020. **22**(38): p. 22066-22077.
81. Zhang, H., et al., *Electronic structure of covalent networks of triangular graphene flakes embedded in hBN.* Japanese Journal of Applied Physics, 2023. **62**(2): p. 025001.
82. Karmakar, S. and S. Dutta, *Strain-tuneable photocatalytic ability of BC6N monolayer: A first principle study.* Computational Materials Science, 2022. **202**: p. 111002.
83. Ali Khan, A., et al., *CO2 capture and separation from H2/CH4/N2 gas mixtures by a novel ternary pentagonal monolayer "Penta-BCN": First principles investigation.* Journal of Molecular Liquids, 2022. **348**: p. 118474.
84. Mir, S.H., V.K. Yadav, and J.K. Singh, *Boron–Carbon–Nitride Sheet as a Novel Surface for Biological Applications: Insights from Density Functional Theory.* ACS Omega, 2019. **4**(2): p. 3732-3738.
85. Ren, X.-Y., et al., *Non-phase-separated 2D B–C–N alloys via molecule-like carbon doping in 2D BN: atomic structures and optoelectronic properties.* Physical Chemistry Chemical Physics, 2018. **20**(35): p. 23106-23111.
86. Ngamprapawat, S., et al., *Current Injection into Single-Crystalline Carbon-Doped h-BN toward Electronic and Optoelectronic Applications.* ACS Applied Materials & Interfaces, 2022. **14**(22): p. 25731-25740.
87. Chen, H., et al., *Introduction of defects in hexagonal boron nitride for vacancy-based 2D memristors.* Nanoscale, 2023. **15**(9): p. 4309-4316.
88. Thomas, S., et al., *Strain-induced work function in h-BN and BCN monolayers.* Physica E: Low-dimensional Systems and Nanostructures, 2020. **123**: p. 114180.

89. Wang, C., X. Zhou, and Y. Li, *Penta-BCN monolayer: a metal-free photocatalyst with a high carrier mobility for water splitting.* Physical Chemistry Chemical Physics, 2022. **24**(43): p. 26863-26869.
90. Shirodkar, S.N., et al., *Engineering the electronic bandgaps and band edge positions in carbon-substituted 2D boron nitride: a first-principles investigation.* Physical Chemistry Chemical Physics, 2015. **17**(20): p. 13547-13552.
91. Fan, X., et al., *Band gap opening of graphene by doping small boron nitride domains.* Nanoscale, 2012. **4**(6): p. 2157-2165.
92. Zhang, Y.-Y., et al., *Thermal conductivity of a h-BCN monolayer.* Physical Chemistry Chemical Physics, 2017. **19**(40): p. 27326-27331.
93. Attri, R., et al., *Low thermal conductivity of 2D borocarbonitride nanosheets.* Journal of Solid State Chemistry, 2020. **282**: p. 121105.
94. McDougall, N.L., et al., *Influence of point defects on the near edge structure of hexagonal boron nitride.* Physical Review B, 2017. **96**(14): p. 144106.
95. Min, Y., et al., *Integrating single-cobalt-site and electric field of boron nitride in dechlorination electrocatalysts by bioinspired design.* Nature Communications, 2021. **12**(1): p. 303.
96. Sun, Q., et al., *In-plane graphene/boron-nitride heterostructures as an efficient metal-free electrocatalyst for the oxygen reduction reaction.* Nanoscale, 2016. **8**(29): p. 14084-14091.
97. Wyss, K.M., et al., *Converting plastic waste pyrolysis ash into flash graphene.* Carbon, 2021. **174**: p. 430-438.
98. Wang, X.-B., et al., *Biomass-Directed Synthesis of 20 g High-Quality Boron Nitride Nanosheets for Thermoconductive Polymeric Composites.* ACS Nano, 2014. **8**(9): p. 9081-9088.
99. Wu, P., et al., *A template-free solvent-mediated synthesis of high surface area boron nitride nanosheets for aerobic oxidative desulfurization.* Chemical Communications, 2016. **52**(1): p. 144-147.
100. Moses, K., et al., *Few-Layer Borocarbonitride Nanosheets: Platinum-Free Catalyst for the Oxygen Reduction Reaction.* Chemistry – An Asian Journal, 2014. **9**(3): p. 838-843.
101. Liu, W., et al., *Synthesis of carbon-doped boron nitride nanosheets and enhancement of their room-temperature ferromagnetic properties.* Journal of Alloys and Compounds, 2019. **792**: p. 1206-1212.
102. Kang, Y., et al., *Incorporate boron and nitrogen into graphene to make BCN hybrid nanosheets with enhanced microwave absorbing properties.* Carbon, 2013. **61**: p. 200-208.
103. Lab, Z. *Molecular Beam Epitaxy (MBE)*. 2023; Available from: https://capricorn.bc.edu/wp/zeljkoviclab/research/molecular-beam-epitaxy-mbe/.
104. Hernández-Mínguez, A., et al., *Luminescent Defects in a Few-Layer h-BN Film Grown by Molecular Beam Epitaxy.* Physical Review Applied, 2018. **10**: p. 044031.
105. Bhaviripudi, S., et al., *Role of Kinetic Factors in Chemical Vapor Deposition Synthesis of Uniform Large Area Graphene Using Copper Catalyst.* Nano Letters, 2010. **10**(10): p. 4128-4133.
106. Hedayat, S.M., J. Karimi-Sabet, and M. Shariaty-Niassar, *Evolution effects of the copper surface morphology on the nucleation density and growth of graphene domains at different growth pressures.* Applied Surface Science, 2017. **399**: p. 542-550.
107. Oh, H. and G.-C. Yi *Synthesis of Atomically Thin h-BN Layers Using BCl3 and NH3 by Sequential-Pulsed Chemical Vapor Deposition on Cu Foil*. Nanomaterials, 2022. **12**, DOI: 10.3390/nano12010080.
108. Jia, K., et al., *Superclean Growth of Graphene Using a Cold-Wall Chemical Vapor Deposition Approach.* Angewandte Chemie International Edition, 2020. **59**(39): p. 17214-17218.
109. Singhal, R., et al., *Synthesis of hexagonal boron nitride films on silicon and sapphire substrates by low-pressure chemical vapor deposition.* Thin Solid Films, 2021. **733**: p. 138812.
110. Qin, B., et al., *Substrates in the Synthesis of Two-Dimensional Materials via Chemical Vapor Deposition.* Chemistry of Materials, 2020. **32**(24): p. 10321-10347.

111. Wu, M., et al., *Seeded growth of large single-crystal copper foils with high-index facets.* Nature, 2020. **581**(7809): p. 406-410.
112. Chen, T.-A., et al., *Wafer-scale single-crystal hexagonal boron nitride monolayers on Cu (111).* Nature, 2020. **579**(7798): p. 219-223.
113. Kim, S.M., et al., *Synthesis of large-area multilayer hexagonal boron nitride for high material performance.* Nature Communications, 2015. **6**(1): p. 8662.
114. Hui, F., et al., *Synthesis of large-area multilayer hexagonal boron nitride sheets on iron substrates and its use in resistive switching devices.* 2D Materials, 2018. **5**(3): p. 031011.
115. Lu, G., et al., *Synthesis of High-Quality Graphene and Hexagonal Boron Nitride Monolayer In-Plane Heterostructure on Cu–Ni Alloy.* Advanced Science, 2017. **4**(9): p. 1700076.
116. Lu, G., et al., *Synthesis and stacking sequence characterization of h-BN/graphene heterostructures on Cu–Ni alloy.* Carbon, 2019. **152**: p. 521-526.
117. Lee, J.S., et al., *Wafer-scale single-crystal hexagonal boron nitride film via self-collimated grain formation.* Science, 2018. **362**(6416): p. 817-821.
118. Jankowski, M., et al., *Real-Time Multiscale Monitoring and Tailoring of Graphene Growth on Liquid Copper.* ACS Nano, 2021. **15**(6): p. 9638-9648.
119. Li, M., et al., *Growth and Etching of Centimeter-Scale Self-Assembly Graphene–h-BN Super-Ordered Arrays: Implications for Integrated Electronic Devices.* ACS Applied Nano Materials, 2022. **5**(1): p. 774-781.
120. Geng, D., et al., *In situ epitaxial engineering of graphene and h-BN lateral heterostructure with a tunable morphology comprising h-BN domains.* NPG Asia Materials, 2019. **11**(1): p. 56.
121. Saeed, M., et al. *Chemical Vapour Deposition of Graphene—Synthesis, Characterisation, and Applications: A Review*. Molecules, 2020. **25**, DOI: 10.3390/molecules25173856.
122. Wang, M., et al., *Synthesis of Large-Area Single-Crystal Graphene.* Trends in Chemistry, 2021. **3**(1): p. 15-33.
123. Wang, L., et al., *Epitaxial growth of a 100-square-centimetre single-crystal hexagonal boron nitride monolayer on copper.* Nature, 2019. **570**(7759): p. 91-95.
124. Zhang, Q., et al., *Self-aligned stitching growth of centimeter-scale quasi-single-crystalline hexagonal boron nitride monolayers on liquid copper.* Nanoscale, 2022. **14**(8): p. 3112-3122.
125. Geng, D., et al., *From Self-Assembly Hierarchical h-BN Patterns to Centimeter-Scale Uniform Monolayer h-BN Film.* Advanced Materials Interfaces, 2019. **6**(1): p. 1801493.
126. Babenko, V., et al., *Time dependent decomposition of ammonia borane for the controlled production of 2D hexagonal boron nitride.* Scientific Reports, 2017. **7**(1): p. 14297.
127. Tay, R.Y., et al., *A systematic study of the atmospheric pressure growth of large-area hexagonal crystalline boron nitride film.* Journal of Materials Chemistry C, 2014. **2**(9): p. 1650-1657.
128. Rao, A. and S. Raghavan, *Mechanistic insights into supersaturation mediated large area growth of hexagonal boron nitride for graphene electronics.* Journal of Materials Chemistry C, 2022. **10**(28): p. 10412-10423.
129. Liu, H., et al., *Structure evolution of hBN grown on molten Cu by regulating precursor flux during chemical vapor deposition.* 2D Materials, 2022. **9**(1): p. 015004.
130. Sompalle, B., et al., *Role of sublimation kinetics of ammonia borane in chemical vapor deposition of uniform, large-area hexagonal boron nitride.* Journal of Vacuum Science & Technology A, 2021. **39**(4): p. 042202.
131. Guo, N., et al., *Controllable growth of triangular hexagonal boron nitride domains on copper foils by an improved low-pressure chemical vapor deposition method.* Nanotechnology, 2012. **23**(41): p. 415605.
132. Felter, J., et al., *In situ study of two-dimensional dendritic growth of hexagonal boron nitride.* 2D Materials, 2019. **6**(4): p. 045005.
133. Jang, S.K., et al., *Synthesis and Characterization of Hexagonal Boron Nitride as a Gate Dielectric.* Scientific Reports, 2016. **6**(1): p. 30449.

134. Kidambi, P.R., et al., *In Situ Observations during Chemical Vapor Deposition of Hexagonal Boron Nitride on Polycrystalline Copper.* Chemistry of Materials, 2014. **26**(22): p. 6380-6392.
135. Caneva, S., et al., *Controlling Catalyst Bulk Reservoir Effects for Monolayer Hexagonal Boron Nitride CVD.* Nano Letters, 2016. **16**(2): p. 1250-1261.
136. Ismach, A., et al., *Toward the Controlled Synthesis of Hexagonal Boron Nitride Films.* ACS Nano, 2012. **6**(7): p. 6378-6385.
137. Shinde, D.B., et al., *Unique role of dimeric carbon precursors in graphene growth by chemical vapor deposition.* Carbon Trends, 2021. **5**: p. 100093.
138. Jungrok, K., et al., *The effect of various parameters for few-layered graphene synthesis using meth- ane and acetylene.* Journal of Ceramic Processing Research, 2012. **13**.
139. Vlassiouk, I., et al., *Role of Hydrogen in Chemical Vapor Deposition Growth of Large Single-Crystal Graphene.* ACS Nano, 2011. **5**(7): p. 6069-6076.
140. Li, P., Z. Li, and J. Yang, *Dominant Kinetic Pathways of Graphene Growth in Chemical Vapor Deposition: The Role of Hydrogen.* The Journal of Physical Chemistry C, 2017. **121**(46): p. 25949-25955.
141. Ci, L., et al., *Atomic layers of hybridized boron nitride and graphene domains.* Nature Materials, 2010. **9**(5): p. 430-435.
142. Wang, S., et al., *Epitaxial Intercalation Growth of Scalable Hexagonal Boron Nitride/Graphene Bilayer Moiré Materials with Highly Convergent Interlayer Angles.* ACS Nano, 2021. **15**(9): p. 14384-14393.
143. Wang, M., et al., *A Platform for Large-Scale Graphene Electronics – CVD Growth of Single-Layer Graphene on CVD-Grown Hexagonal Boron Nitride.* Advanced Materials, 2013. **25**(19): p. 2746-2752.
144. Wei, W., et al. *In Situ Monitoring of Growth of Vertically Stacked h-BN/Graphene Heterostructures on Ni Substrates and Their Interface Interaction*. Surfaces, 2020. **3**, 328-336 DOI: 10.3390/surfaces3030024.
145. Guo, H., et al., *Lateral Heterostructures of Graphene and h-BN with Atomic Lattice Coherence and Tunable Rotational Order.* Small, 2023. **n/a**(n/a): p. 2207217.
146. Zhuang, P., et al., *Growth of lateral graphene/h-BN heterostructure on copper foils by chemical vapor deposition.* Nanotechnology, 2019. **30**(3): p. 03LT01.
147. Leardini, F., et al., *Chemical vapor deposition growth of boron–carbon–nitrogen layers from methylamine borane thermolysis products.* Nanotechnology, 2018. **29**(2): p. 025603.
148. Tay, R.Y., et al., *Trimethylamine Borane: A New Single-Source Precursor for Monolayer h-BN Single Crystals and h-BCN Thin Films.* Chemistry of Materials, 2016. **28**(7): p. 2180-2190.
149. Seo, T.H., et al., *Dominant formation of h-BC2N in h-BxCyNz films: CVD synthesis and characterization.* Carbon, 2021. **182**: p. 791-798.
150. Huang, C., et al., *Carbon-doped BN nanosheets for metal-free photoredox catalysis.* Nature Communications, 2015. **6**(1): p. 7698.
151. Zheng, R., et al., *Precipitation growth of graphene under exfoliated hexagonal boron nitride to form heterostructures on cobalt substrate by molecular beam epitaxy.* Applied Physics Letters, 2017. **111**(1): p. 011903.
152. Biswas, A., et al., *Unravelling the room temperature growth of two-dimensional h-BN nanosheets for multifunctional applications.* Nanoscale Horizons, 2023.
153. Cheng, L., et al., *Two-dimensional hexagonal boron–carbon–nitrogen atomic layers.* Nanoscale, 2019. **11**(21): p. 10454-10462.
154. Hao, Y., et al., *The Role of Surface Oxygen in the Growth of Large Single-Crystal Graphene on Copper.* Science, 2013. **342**(6159): p. 720-723.
155. Kudryavtsev, A., et al., *Autocalibration method for scanning electron microscope using affine camera model.* Machine Vision and Applications, 2020. **31**.
156. *MyScope SEM training*. Available from: https://myscope.training/#/SEMlevel_2_9.

157. Scientific, T. *EDX Analysis with SEM: How Does it Work?* November 2019; Available from: https://www.thermofisher.com/blog/materials/edx-analysis-with-sem-how-does-it-work/#:~:text=X%2Drays%20are%20generated%20using,characteristic%20X%2Dray%20is%20released.
158. Bradbury, S., Joy, . David C. and Ford, . Brian J. *transmission electron microscope. Encyclopedia Britannica*. 2023, March 20; Available from: https://www.britannica.com/technology/transmission-electron-microscope.
159. *Profilm 3D, Filmetrics, specifications*. 2023; Available from: https://www.filmetrics.com/profilometers/profilm3d?src=google&cid=P3D-English&gid=60033671447&key=3d%20optical%20profiler&d=c&m=p&gclid=CjwKCAjw67ajBhAVEiwA2g_jEIrU4Seb0DMQ7Xi_PtrzdSagEj3wHRRmaOZ1LwdN5H13WgZSVsKw7hoCE5QQAvD_BwE.
160. *NIST XPS database.* 2023.
161. Chusuei, C. and D.W. Goodman, *X-Ray Photoelectron Spectroscopy*. 2013.
162. Zhang, H., et al., *Isoelectronic analogues of graphene: the BCN monolayers with visible-light absorption and high carrier mobility.* Journal of Physics: Condensed Matter, 2019. **31**(12): p. 125301.
163. Materials, A. *An Introduction into Raman Spectroscopy*. Available from: https://www.azom.com/article.aspx?ArticleID=13372.
164. Malard, L.M., et al., *Raman spectroscopy in graphene.* Physics Reports, 2009. **473**(5): p. 51-87.
165. Ferrari, A.C., et al., *Raman Spectrum of Graphene and Graphene Layers.* Physical Review Letters, 2006. **97**(18): p. 187401.
166. Stenger, I., et al., *Low frequency Raman spectroscopy of few-atomic-layer thick hBN crystals.* 2D Materials, 2017. **4**(3): p. 031003.
167. Fukamachi, S., et al., *Large-area synthesis and transfer of multilayer hexagonal boron nitride for enhanced graphene device arrays.* Nature Electronics, 2023. **6**(2): p. 126-136.
168. Shi, Z., et al., *Vapor–liquid–solid growth of large-area multilayer hexagonal boron nitride on dielectric substrates.* Nature Communications, 2020. **11**(1): p. 849.
169. Uddin, M.R., et al., *Layer-structured hexagonal (BN)C semiconductor alloys with tunable optical and electrical properties.* Journal of Applied Physics, 2014. **115**: p. 093509-093509.
170. Urbach, F., *The Long-Wavelength Edge of Photographic Sensitivity and of the Electronic Absorption of Solids.* Physical Review, 1953. **92**(5): p. 1324-1324.
171. Cramer, C.J., *Essentials of computational chemistry : theories and models*. 2002: West Sussex, England ; New York : J. Wiley, [2002] ©2002.
172. Pauli, W., *Über den Zusammenhang des Abschlusses der Elektronengruppen im Atom mit der Komplexstruktur der Spektren.* Zeitschrift für Physik, 1925. **31**(1): p. 765-783.
173. Roothaan, C.C.J., *New Developments in Molecular Orbital Theory.* Reviews of Modern Physics, 1951. **23**(2): p. 69-89.
174. Hohenberg, P. and W. Kohn, *Inhomogeneous Electron Gas.* Physical Review, 1964. **136**(3B): p. B864-B871.
175. Kohn, W. and L.J. Sham, *Self-Consistent Equations Including Exchange and Correlation Effects.* Physical Review, 1965. **140**(4A): p. A1133-A1138.
176. Perdew, J.P. and K. Schmidt, *Jacob's ladder of density functional approximations for the exchange-correlation energy.* AIP Conference Proceedings, 2001. **577**(1): p. 1-20.
177. Perdew, J.P., K. Burke, and M. Ernzerhof, *Generalized Gradient Approximation Made Simple.* Physical Review Letters, 1996. **77**(18): p. 3865-3868.
178. Garza, A.J. and G.E. Scuseria, *Predicting Band Gaps with Hybrid Density Functionals.* The Journal of Physical Chemistry Letters, 2016. **7**(20): p. 4165-4170.
179. Heyd, J., G.E. Scuseria, and M. Ernzerhof, *Hybrid functionals based on a screened Coulomb potential.* The Journal of Chemical Physics, 2003. **118**(18): p. 8207-8215.

180. Heyd, J., G.E. Scuseria, and M. Ernzerhof, *Erratum: "Hybrid functionals based on a screened Coulomb potential" [J. Chem. Phys. 118, 8207 (2003)].* The Journal of Chemical Physics, 2006. **124**(21): p. 219906.
181. Yao, Y., et al., *Controlled Growth of Multilayer, Few-Layer, and Single-Layer Graphene on Metal Substrates.* The Journal of Physical Chemistry C, 2011. **115**(13): p. 5232-5238.
182. Xue, Y., et al., *Synthesis of large-area, few-layer graphene on iron foil by chemical vapor deposition.* Nano Research, 2011. **4**(12): p. 1208-1214.
183. Datta, M., et al., *Mass transport effects during electropolishing of iron in phosphoric-sulfuric acid.* Electrochimica Acta, 1992. **37**(13): p. 2469-2475.
184. Chen, S., et al., *Millimeter-Size Single-Crystal Graphene by Suppressing Evaporative Loss of Cu During Low Pressure Chemical Vapor Deposition.* Advanced Materials, 2013. **25**(14): p. 2062-2065.
185. Chen, C.-C., et al., *Growth of Large-Area Graphene Single Crystals in Confined Reaction Space with Diffusion-Driven Chemical Vapor Deposition.* Chemistry of Materials, 2015. **27**(18): p. 6249-6258.
186. Dai, C.-Y., et al., *Spatial Confinement Approach Using Ni to Modulate Local Carbon Supply for the Growth of Uniform Transfer-Free Graphene Monolayers.* The Journal of Physical Chemistry C, 2020. **124**(42): p. 23094-23105.
187. Rümmeli, M.H., et al., *On the Role of Vapor Trapping for Chemical Vapor Deposition (CVD) Grown Graphene over Copper.* Chemistry of Materials, 2013. **25**(24): p. 4861-4866.
188. Jeong, H.J., et al., *Improved transfer of chemical-vapor-deposited graphene through modification of intermolecular interactions and solubility of poly(methylmethacrylate) layers.* Carbon, 2014. **66**: p. 612-618.
189. Li, X., et al., *Transfer of Large-Area Graphene Films for High-Performance Transparent Conductive Electrodes.* Nano Letters, 2009. **9**(12): p. 4359-4363.
190. te Velde, G. and E.J. Baerends, *Precise density-functional method for periodic structures.* Physical Review B, 1991. **44**(15): p. 7888-7903.
191. SCM. *BAND*. [2022.1] 2022.1.
192. Tran, R., et al., *Surface energies of elemental crystals.* Scientific Data, 2016. **3**(1): p. 160080.
193. Meng, J.H., et al., *Synthesis of atomic layers of hybridized h-BNC by depositing h-BN on graphene via ion beam sputtering.* Applied Physics Letters, 2016. **109**(17): p. 173106.
194. J?Nsson, H., G. Mills, and K.W. Jacobsen, *Nudged elastic band method for finding minimum energy paths of transitions*, in *Classical and Quantum Dynamics in Condensed Phase Simulations*. 1998, WORLD SCIENTIFIC. p. 385-404.
195. Yue, C., et al., *Formation of copper boride on Cu(111).* Fundamental Research, 2021. **1**(4): p. 482-487.
196. Zhang, Z., et al., *Growth Mechanism and Morphology of Hexagonal Boron Nitride.* Nano Letters, 2016. **16**(2): p. 1398-1403.
197. Stehle, Y., et al., *Synthesis of Hexagonal Boron Nitride Monolayer: Control of Nucleation and Crystal Morphology.* 2015. **27**: p. 8041-8047.
198. Song, L., et al., *Large Scale Growth and Characterization of Atomic Hexagonal Boron Nitride Layers.* Nano Letters, 2010. **10**(8): p. 3209-3215.
199. Koepke, J.C., et al., *Role of Pressure in the Growth of Hexagonal Boron Nitride Thin Films from Ammonia-Borane.* Chemistry of Materials, 2016. **28**(12): p. 4169-4179.
200. Sompalle, B., et al. *Chemical Vapour Deposition of Hexagonal Boron Nitride for Two Dimensional Electronics*. 2018.
201. Ji, Y., et al., *Chemical Vapor Deposition Growth of Large Single-Crystal Mono-, Bi-, Tri-Layer Hexagonal Boron Nitride and Their Interlayer Stacking.* ACS Nano, 2017. **11**(12): p. 12057-12066.
202. Kim, K.K., et al., *Synthesis of Monolayer Hexagonal Boron Nitride on Cu Foil Using Chemical Vapor Deposition.* Nano Letters, 2012. **12**(1): p. 161-166.

203. Lee, K.H., et al., *Large-Scale Synthesis of High-Quality Hexagonal Boron Nitride Nanosheets for Large-Area Graphene Electronics.* Nano Letters, 2012. **12**(2): p. 714-718.
204. Khan, M.H., et al., *Synthesis of Large and Few Atomic Layers of Hexagonal Boron Nitride on Melted Copper.* Scientific Reports, 2015. **5**(1): p. 7743.
205. Gilbert, S.M., et al., *Alternative stacking sequences in hexagonal boron nitride.* 2D Materials, 2019. **6**(2): p. 021006.
206. Ren, X., et al., *Grain boundaries in chemical-vapor-deposited atomically thin hexagonal boron nitride.* Physical Review Materials, 2019. **3**(1): p. 014004.
207. Wang, W., et al., *Free-Molecular-Flow Modulated Synthesis of Hexagonal Boron Nitride Monolayers.* Crystal Growth & Design, 2019. **19**(12): p. 7007-7014.
208. Sharma, K.P., et al., *Edge controlled growth of hexagonal boron nitride crystals on copper foil by atmospheric pressure chemical vapor deposition.* CrystEngComm, 2018. **20**(5): p. 550-555.
209. Wood, G.E., et al., *In situ gas analysis during the growth of hexagonal boron nitride from ammonia borane.* Materials Research Express, 2017. **4**(11): p. 115905.
210. Malik, M.W., et al., *Oxygen activated CVD growth of large-area multilayer h-BN on polycrystalline copper foils.* Journal of Crystal Growth, 2023. **606**: p. 127088.
211. Wang, L., et al., *Water-assisted growth of large-sized single crystal hexagonal boron nitride grains.* Materials Chemistry Frontiers, 2017. **1**(9): p. 1836-1840.
212.

Stehle, Y., et al., *Synthesis of Hexagonal Boron Nitride Monolayer: Control of Nucleation and Crystal Morphology.* 2015. **27**: p. 8041-8047.
213. Schiller, J.A., et al., *Crowd-Sourced Data and Analysis Tools for Advancing the Chemical Vapor Deposition of Graphene: Implications for Manufacturing.* ACS Applied Nano Materials, 2020. **3**(10): p. 10144-10155.
214. Song, X., et al., *Chemical vapor deposition growth of large-scale hexagonal boron nitride with controllable orientation.* Nano Research, 2015. **8**(10): p. 3164-3176.
215. Tay, R.Y., et al., *Synthesis of aligned symmetrical multifaceted monolayer hexagonal boron nitride single crystals on resolidified copper.* Nanoscale, 2016. **8**(4): p. 2434-2444.
216. Chang, R.-J., et al., *Growth of Large Single-Crystalline Monolayer Hexagonal Boron Nitride by Oxide-Assisted Chemical Vapor Deposition.* Chemistry of Materials, 2017. **29**(15): p. 6252-6260.
217. Hayashi, T., et al., *Determination of the stacking order of curved few-layered graphene systems.* Nanoscale, 2012. **4**(20): p. 6419-6424.
218. Robertson, A.W., et al., *Structural Distortions in Few-Layer Graphene Creases.* ACS Nano, 2011. **5**(12): p. 9984-9991.
219. Kim, K.K., et al., *Synthesis and Characterization of Hexagonal Boron Nitride Film as a Dielectric Layer for Graphene Devices.* ACS Nano, 2012. **6**(10): p. 8583-8590.
220. Tay, R.Y., et al., *Growth of Large Single-Crystalline Two-Dimensional Boron Nitride Hexagons on Electropolished Copper.* Nano Letters, 2014. **14**(2): p. 839-846.
221. Lewis, A.M., B. Derby, and I.A. Kinloch, *Influence of Gas Phase Equilibria on the Chemical Vapor Deposition of Graphene.* ACS Nano, 2013. **7**(4): p. 3104-3117.
222. Eckmann, A., et al., *Probing the Nature of Defects in Graphene by Raman Spectroscopy.* Nano Letters, 2012. **12**(8): p. 3925-3930.
223. Jacobberger, R.M. and M.S. Arnold, *Graphene Growth Dynamics on Epitaxial Copper Thin Films.* Chemistry of Materials, 2013. **25**(6): p. 871-877.
224. Meca, E., et al., *Epitaxial Graphene Growth and Shape Dynamics on Copper: Phase-Field Modeling and Experiments.* Nano Letters, 2013. **13**(11): p. 5692-5697.
225. Zhang, Y., et al., *Vapor Trapping Growth of Single-Crystalline Graphene Flowers: Synthesis, Morphology, and Electronic Properties.* Nano Letters, 2012. **12**(6): p. 2810-2816.
226. Fei, W., et al., *Dendritic graphene domains: Growth, morphology and oxidation promotion.* Materials Letters, 2013. **110**: p. 225-228.

227. Castillo, J.J., et al., *Orientation of Pterin-6-Carboxylic Acid on Gold Capped Silicon Nanopillars Platforms: Surface Enhanced Raman Spectroscopy and Density Functional Theory Studies %J Journal of the Brazilian Chemical Society.* 2016. **27**: p. 971-977.
228. Scardamaglia, M., et al., *Comparative study of copper oxidation protection with graphene and hexagonal boron nitride.* Carbon, 2021. **171**: p. 610-617.
229. Zhang, C., et al., *Direct growth of large-area graphene and boron nitride heterostructures by a co-segregation method.* Nature Communications, 2015. **6**(1): p. 6519.
230. Meng, L., et al., *Graphene adlayer growth between nonepitaxial graphene and the Ni(111) substrate: a theoretical study.* Physical Chemistry Chemical Physics, 2021. **23**(3): p. 2222-2228.
231. Yang, Y., et al., *Creating a Nanospace under an h-BN Cover for Adlayer Growth on Nickel(111).* ACS Nano, 2015. **9**(12): p. 11589-11598.
232. Mu, R., et al., *Visualizing Chemical Reactions Confined under Graphene.* Angewandte Chemie International Edition, 2012. **51**(20): p. 4856-4859.
233. Preobrajenski, A.B., A.S. Vinogradov, and N. Mårtensson, *Monolayer of h-BN chemisorbed on Cu(111) and Ni(111): The role of the transition metal 3d states.* Surface Science, 2005. **582**(1): p. 21-30.
234. Joshi, S., et al., *Boron Nitride on Cu(111): An Electronically Corrugated Monolayer.* Nano Letters, 2012. **12**(11): p. 5821-5828.
235. Jung, D.H., et al., *Surface Diffusion Directed Growth of Anisotropic Graphene Domains on Different Copper Lattices.* Scientific Reports, 2016. **6**(1): p. 21136.
236. Novoselov, K.S., et al., *A roadmap for graphene.* Nature, 2012. **490**(7419): p. 192-200.
237. Bord, J., et al., *An Atomistic View of Platinum Cluster Growth on Pristine and Defective Graphene Supports.* Small, 2023. **n/a**(n/a): p. 2207484.
238. Cheng, Z., et al., *Large vacancy-defective graphene for enhanced lithium storage.* Carbon Trends, 2023. **10**: p. 100237.
239. Chang, H., et al., *Defect mediated lithium adsorption on graphene-based silicon composite electrode for high capacity and high stability lithium-ion battery.* Journal of Electroanalytical Chemistry, 2023. **931**: p. 117179.
240. Liu, Y., et al., *Mechanism of Metal Intercalation under Graphene through Small Vacancy Defects.* The Journal of Physical Chemistry C, 2021. **125**(12): p. 6954-6962.
241. Zheng, Y., et al., *Two-Step Boron and Nitrogen Doping in Graphene for Enhanced Synergistic Catalysis.* Angewandte Chemie International Edition, 2013. **52**(11): p. 3110-3116.
242. Martini, L., et al., *Scalable High-Mobility Graphene/hBN Heterostructures.* ACS Applied Materials & Interfaces, 2023. **15**(31): p. 37794-37801.
243. Garcia, J.M., et al., *Graphene growth on h-BN by molecular beam epitaxy.* Solid State Communications, 2012. **152**(12): p. 975-978.
244. Wang, L., et al., *Monolayer Hexagonal Boron Nitride Films with Large Domain Size and Clean Interface for Enhancing the Mobility of Graphene-Based Field-Effect Transistors.* Advanced Materials, 2014. **26**(10): p. 1559-1564.
245. Du, M., Y. Wu, and X. Hao, *A facile chemical exfoliation method to obtain large size boron nitride nanosheets.* CrystEngComm, 2013. **15**(9): p. 1782-1786.
246. Johra, F.T., J.-W. Lee, and W.-G. Jung, *Facile and safe graphene preparation on solution based platform.* Journal of Industrial and Engineering Chemistry, 2014. **20**(5): p. 2883-2887.
247. Asadipour, H., F. Ashrafizadeh, and M. Alizadeh, *The Role of Graphene Defects in Graphene-Coated Copper Oxidation Behavior.* Transactions of the Indian Institute of Metals, 2024. **77**(2): p. 469-475.
248. Greczynski, G. and L. Hultman, *Towards reliable X-ray photoelectron spectroscopy: Sputter-damage effects in transition metal borides, carbides, nitrides, and oxides.* Applied Surface Science, 2021. **542**: p. 148599.
249. Coulter, J.B. and D.P. Birnie Iii, *Assessing Tauc Plot Slope Quantification: ZnO Thin Films as a Model System.* physica status solidi (b), 2018. **255**(3): p. 1700393.

250. Kim, S., et al., *Anomalous Behaviors of Visible Luminescence from Graphene Quantum Dots: Interplay between Size and Shape.* ACS Nano, 2012. **6**(9): p. 8203-8208.
251.

Nesládek, M., et al., *Study of UV and Subgap Photocurrent Response in Diamond and BCN Thin Films for Detector Applications.* 2001. **185**: p. 107-113.
252. Knobloch, T., et al., *The performance limits of hexagonal boron nitride as an insulator for scaled CMOS devices based on two-dimensional materials.* Nature Electronics, 2021. **4**(2): p. 98-108.
253. Caneva, S., et al., *From Growth Surface to Device Interface: Preserving Metallic Fe under Monolayer Hexagonal Boron Nitride.* ACS Applied Materials & Interfaces, 2017. **9**(35): p. 29973-29981.
254. Lee, H.Y., et al., *Strong and Localized Luminescence from Interface Bubbles Between Stacked hBN Multilayers.* Nature Communications, 2022. **13**(1): p. 5000.
255. Bhadeshia, H.K.D.H. and S. Honeycombe, *Iron and its Interstitial Solid Solutions*. 2006. p. 1-16.
256. Babenko, V., et al., *Oxidising and carburising catalyst conditioning for the controlled growth and transfer of large crystal monolayer hexagonal boron nitride.* 2D Materials, 2020. **7**(2): p. 024005.
257. Xie, M., J. Wang, and Y.K. Yap, *Mechanism for Low Temperature Growth of Boron Nitride Nanotubes.* The Journal of Physical Chemistry C, 2010. **114**(39): p. 16236-16241.
258. Li, Y., et al., *High thermal conductivity in pressureless densified SiC ceramics with ultra-low contents of additives derived from novel boron–carbon sources.* Journal of the European Ceramic Society, 2014. **34**(10): p. 2591-2595.
259. Wu, J., et al., *Support Effect of the Fe/BN Catalyst on Fischer–Tropsch Performances: Role of the Surface B–O Defect.* Industrial & Engineering Chemistry Research, 2018. **57**(8): p. 2805-2810.
260.

Mackoit-Sinkevičienė, M., et al., *Carbon dimer defect as a source of the 4.1 eV luminescence in hexagonal boron nitride.* 2019. **115**: p. 212101.
261. Blase, X., et al., *Theory of composite BxCyNz nanotube heterojunctions.* Applied Physics Letters, 1997. **70**(2): p. 197-199.
262.

Wang, Y., et al., *Deep Ultraviolet Photodetectors Based on Carbon-Doped Two-Dimensional Hexagonal Boron Nitride.* 2020. **12**: p. 27361-27367.
263. Lu, J., et al., *Order–disorder transition in a two-dimensional boron–carbon–nitride alloy.* Nature Communications, 2013. **4**(1): p. 2681.
264. Geng, D., et al., *One-Pot Confined Epitaxial Growth of 2D Heterostructure Arrays.* ACS Materials Letters, 2021. **3**(2): p. 217-223.
265. Becke, A.D., *Density-functional exchange-energy approximation with correct asymptotic behavior.* Physical Review A, 1988. **38**(6): p. 3098-3100.
266. Perdew, J.P., et al., *Workhorse Semilocal Density Functional for Condensed Matter Physics and Quantum Chemistry.* Physical Review Letters, 2009. **103**(2): p. 026403.
267. Tran, F. and P. Blaha, *Accurate Band Gaps of Semiconductors and Insulators with a Semilocal Exchange-Correlation Potential.* Physical Review Letters, 2009. **102**(22): p. 226401.
268. Koller, D., F. Tran, and P. Blaha, *Improving the modified Becke-Johnson exchange potential.* Physical Review B, 2012. **85**(15): p. 155109.
269. Xia, F., et al., *Two-dimensional material nanophotonics.* Nature Photonics, 2014. **8**(12): p. 899-907.
270. Tarrio, C. and S.E. Schnatterly, *Interband transitions, plasmons, and dispersion in hexagonal boron nitride.* Physical Review B, 1989. **40**(11): p. 7852-7859.
271. Geim, A.K. and K.S. Novoselov, *The rise of graphene.* Nature Materials, 2007. **6**(3): p. 183-191.

272. Guan, Z., S. Ni, and S. Hu, *Band gap opening of graphene by forming a graphene/PtSe2 van der Waals heterojunction.* RSC Advances, 2017. **7**(72): p. 45393-45399.
273. Sofo, J.O., A.S. Chaudhari, and G.D. Barber, *Graphane: A two-dimensional hydrocarbon.* Physical Review B, 2007. **75**(15): p. 153401.
274. Hu, W., et al., *Electronic structure and aromaticity of large-scale hexagonal graphene nanoflakes.* The Journal of Chemical Physics, 2014. **141**(21): p. 214704.
275. Seo, D.-H., A. Urban, and G. Ceder, *Calibrating transition-metal energy levels and oxygen bands in first-principles calculations: Accurate prediction of redox potentials and charge transfer in lithium transition-metal oxides.* Physical Review B, 2015. **92**(11): p. 115118.
276. Lanzillo, N.A., N. Kharche, and S.K. Nayak, *Substrate-induced Band Gap Renormalization in Semiconducting Carbon Nanotubes.* Scientific Reports, 2014. **4**(1): p. 3609.
277. Trasatti, S., *The absolute electrode potential: an explanatory note (Recommendations 1986).* Pure and Applied Chemistry, 1986. **58**(7): p. 955-966.
278. Sun, Z., et al., *Fundamentals and Challenges of Electrochemical CO2 Reduction Using Two-Dimensional Materials.* Chem, 2017. **3**(4): p. 560-587.
279. Hoffmann, M.R., et al., *Environmental Applications of Semiconductor Photocatalysis.* Chemical Reviews, 1995. **95**(1): p. 69-96.
280. Nørskov, J.K., et al., *Origin of the Overpotential for Oxygen Reduction at a Fuel-Cell Cathode.* The Journal of Physical Chemistry B, 2004. **108**(46): p. 17886-17892.
281. Yu, E.T., J.O. McCaldin, and T.C. McGill, *Band Offsets in Semiconductor Heterojunctions*, in *Solid State Physics*, H. Ehrenreich and D. Turnbull, Editors. 1992, Academic Press. p. 1-146.
282. Zhou, Z., et al., *Electrocatalytic hydrogen evolution under neutral pH conditions: current understandings, recent advances, and future prospects.* Energy & Environmental Science, 2020. **13**(10): p. 3185-3206.
283. Gu, Y., et al., *Enriching H2O through boron nitride as a support to promote hydrogen evolution from non-filtered seawater.* EcoEnergy, 2023. **1**(2): p. 405-413.
284. Bernard Valeur, M.N.B.-S., *Molecular Fluorescence: Principles and Applications, 2nd Edition.* 2012.
285. van Gisbergen, S.J.A., J.G. Snijders, and E.J. Baerends, *Implementation of time-dependent density functional response equations.* Computer Physics Communications, 1999. **118**(2): p. 119-138.
286. University, S.P.L.A.S. *Standard Solar Spectrum - ASTM G-173*. 12/03/23]; Available from: https://www.pveducation.org/pvcdrom/appendices/standard-solar-spectra.
287. Han, G.H., et al., *Continuous Growth of Hexagonal Graphene and Boron Nitride In-Plane Heterostructures by Atmospheric Pressure Chemical Vapor Deposition.* 2013. **7**: p. 10129-10138.
288. Liu, L., et al., *Heteroepitaxial Growth of Two-Dimensional Hexagonal Boron Nitride Templated by Graphene Edges.* Science, 2014. **343**(6167): p. 163-167.
289. Horri, A. and R. Faez, *Lateral BN-BCN Heterostructure Tunneling Transistor with Large Current Modulation.* ACS Applied Electronic Materials, 2022. **4**(7): p. 3520-3524.
290. Zhang, D., et al., *Interface engineering of electronic properties of graphene/boron nitride lateral heterostructures.* 2D Materials, 2015. **2**(4): p. 041001.
291. Komova, O.V., et al., *The Effect of Storage-Induced Changes in Ammonia Borane on Hydrogen Release during Its Low-Temperature Thermolysis.* 2019. **7**(8): p. 96.
292. Han, J., et al., *Synthesis of wafer-scale hexagonal boron nitride monolayers free of aminoborane nanoparticles by chemical vapor deposition.* Nanotechnology, 2014. **25**(14): p. 145604.
293. Sharma, S., et al., *Morphology-Controlled Synthesis of Hexagonal Boron Nitride Crystals by Chemical Vapor Deposition.* Crystal Growth & Design, 2016. **16**(11): p. 6440-6445.
294. Komova, O.V., et al., *Dehydrogenation of ammonia borane recrystallized by different techniques.* Renewable Energy, 2022. **184**: p. 460-472.

295. Ding, W., et al., *An XPS study on the chemical bond structure at the interface between SiOxNy and N doped polyethylene terephthalate.* The Journal of Chemical Physics, 2013. **138**(10): p. 104706.
296. Singh, P., et al., *Angle-dependent XPS analysis of silicon nitride film deposited on screen-printed crystalline silicon solar cell.* Solar Energy Materials and Solar Cells, 2009. **93**(1): p. 19-24.
297. Zhang Rui, S.Q., Zhang Huayu, Jin Zelong, Zhang Xiaoliang, *Preparation and Pervaporation Desalination Performance of Boron-Doped Silica Hybrid Membranes* 2021. **72**(4): p. 2317-2327.
298. Oprea, B., T. Radu, and S. Simon, *XPS investigation of atomic environment changes on surface of B2O3–Bi2O3 glasses.* Journal of Non-Crystalline Solids, 2013. **379**: p. 35-39.
299. Viard, J., et al., *XPS and FTIR study of silicon oxynitride thin films.* Journal of the European Ceramic Society, 1997. **17**(15): p. 2025-2028.
300. Diéguez, L., et al. *Optical Gratings Coated with Thin Si3N4 Layer for Efficient Immunosensing by Optical Waveguide Lightmode Spectroscopy*. Biosensors, 2012. **2**, 114-126 DOI: 10.3390/bios2020114.
301. Kaur, A., P. Chahal, and T. Hogan, *Selective Fabrication of SiC/Si Diodes by Excimer Laser Under Ambient Conditions.* IEEE Electron Device Letters, 2016. **37**(2): p. 142-145.
302. Biesinger, M.C., *Advanced analysis of copper X-ray photoelectron spectra.* Surface and Interface Analysis, 2017. **49**(13): p. 1325-1334.
303. Lenshin, A.S., et al., *Investigations of the composition of macro-, micro- and nanoporous silicon surface by ultrasoft X-ray spectroscopy and X-ray photoelectron spectroscopy.* Applied Surface Science, 2015. **359**: p. 550-559.
304. Kaky, K.M., et al., *X-ray photoelectron spectroscopy (XPS) and gamma-ray shielding investigation of boro-silicate glasses contained alkali/alkaline modifier.* Results in Physics, 2019. **14**: p. 102438.
305. Stebbins, J.F. and Z. Xu, *NMR evidence for excess non-bridging oxygen in an aluminosilicate glass.* Nature, 1997. **390**(6655): p. 60-62.
306. Kratky, T., et al., *The fate of graphene on copper: Intercalation / de-intercalation processes and the role of silicon.* Carbon, 2024. **226**: p. 119172.
307. Ge, X., et al., *Mechanism of SiOx particles formation during CVD graphene growth on Cu substrates.* Carbon, 2018. **139**: p. 989-998.
308. Al-Kamiyani, S. and T. Mohiuddin, *Improved control in elimination of white impurities on graphene by chemical vapor deposition (CVD).* AIP Advances, 2018. **8**(12): p. 125325.
309. Murdock, A.T., et al., *Targeted removal of copper foil surface impurities for improved synthesis of CVD graphene.* Carbon, 2017. **122**: p. 207-216.
310. Seidel, H., et al., *Anisotropic Etching of Crystalline Silicon in Alkaline Solutions: I . Orientation Dependence and Behavior of Passivation Layers.* Journal of The Electrochemical Society, 1990. **137**(11): p. 3612.
311. Cui, N., F. Wang, and H. Ding *Acetic Acid and Ammonium Persulfate Pre-Treated Copper Foil for the Improvement of Graphene Quality, Sensitivity and Specificity of Hall Effect Label-Free DNA Hybridization Detection*. Materials, 2020. **13**, DOI: 10.3390/ma13071784.
312. Neiner, D., et al., *Promotion of Hydrogen Release from Ammonia Borane with Mechanically Activated Hexagonal Boron Nitride.* The Journal of Physical Chemistry C, 2009. **113**(3): p. 1098-1103.
313. Neiner, D., et al., *Decomposition Pathway of Ammonia Borane on the Surface of Nano-BN.* The Journal of Physical Chemistry C, 2010. **114**(32): p. 13935-13941.
314. Mhíocháin, T.R.N. and J.M.D. Coey, *Chirality of electrodeposits grown in a magnetic field.* Physical Review E, 2004. **69**(6): p. 061404.
315. Grier, D.G., D.A. Kessler, and L.M. Sander, *Stability of the dense radial morphology in diffusive pattern formation.* Physical Review Letters, 1987. **59**(20): p. 2315-2318.

316. Rautaray, D., R. Kavathekar, and M. Sastry, *Using the dynamic, expanding liquid–liquid interface in a Hele–Shaw cell in crystal growth and nanoparticle assembly.* Faraday Discussions, 2005. **129**(0): p. 205-217.
317. Islam, T.u. and P.S. Gandhi, *Viscous Fingering in Multiport Hele Shaw Cell for Controlled Shaping of Fluids.* Scientific Reports, 2017. **7**(1): p. 16602.
318. Iso, S.T. and J.A. Pask, *Reaction of Silicate Glasses and Mullite with Hydrogen Gas.* Journal of the American Ceramic Society, 1982. **65**(8): p. 383-387.
319. Hu, J., et al., *Roles of Oxygen and Hydrogen in Crystal Orientation Transition of Copper Foils for High-Quality Graphene Growth.* Scientific Reports, 2017. **7**(1): p. 45358.
320. Fluegel, A., *Glass viscosity calculation based on a global statistical modelling approach.* Glass Technology - European Journal of Glass Science and Technology Part A, 2007. **48**(1): p. 13-30.
321. Yi, Y., et al., *Few-Layer Boron Nitride with Engineered Nitrogen Vacancies for Promoting Conversion of Polysulfide as a Cathode Matrix for Lithium–Sulfur Batteries.* Chemistry – A European Journal, 2019. **25**(34): p. 8112-8117.
322. Cui, H., et al., *Understanding the Formation Mechanism of Graphene Frameworks Synthesized by Solvothermal and Rapid Pyrolytic Processes Based on an Alcohol–Sodium Hydroxide System.* ACS Applied Materials & Interfaces, 2015. **7**(21): p. 11230-11238.
323. Thomas, T. and A. Agarwal *A Facile and Scalable Approach in the Fabrication of Tailored 3D Graphene Foam via Freeze Drying*. Materials, 2021. **14**, DOI: 10.3390/ma14040864.
324. Kulshreshtha, A. and S.K. Dhakad, *Preparation of metal foam by different methods: A review.* Materials Today: Proceedings, 2020. **26**: p. 1784-1790.
325. *Cu foam - Goodfellow*. 2023; Available from: https://www.goodfellow.com/uk/en-gb/displayitemdetails/p/cu00-fa-000105/copper-foam.
326. Babenko, V. and N. Grobert, *Porous Materials Comprising Two-Dimensional Nanomaterials*. 2017.
327. Sun, H., et al., *Copper foam-derived electrodes as efficient electrocatalysts for conventional and hybrid water electrolysis.* Materials Reports: Energy, 2022. **2**(2): p. 100092.
328. Lu, L., J.T.M. De Hosson, and Y. Pei, *Three-dimensional micron-porous graphene foams for lightweight current collectors of lithium-sulfur batteries.* Carbon, 2019. **144**: p. 713-723.
329. Mohd Shah, N.R.A., et al., *Effect of annealing time on chemical vapor deposition growth of 3D graphene for photoelectrochemical water splitting.* Materials Today: Proceedings, 2022. **57**: p. 1215-1219.
330. Cao, X., et al., *Preparation of Novel 3D Graphene Networks for Supercapacitor Applications.* Small, 2011. **7**(22): p. 3163-3168.
331. Yang, J., et al., *Graphene foam as a stable anode material in lithium-ion batteries.* International Journal of Energy Research, 2022. **46**(4): p. 5226-5234.
332. Yang, G., et al., *Graphene anchored on Cu foam as a lithiophilic 3D current collector for a stable and dendrite-free lithium metal anode.* Journal of Materials Chemistry A, 2018. **6**(21): p. 9899-9905.
333. Madito, M.J., et al., *Nickel-copper graphene foam prepared by atmospheric pressure chemical vapour deposition for supercapacitor applications.* Surface and Coatings Technology, 2020. **383**: p. 125230.
334. Feng, X., et al., *Three-dimensional nitrogen-doped graphene as an ultrasensitive electrochemical sensor for the detection of dopamine.* Nanoscale, 2015. **7**(6): p. 2427-2432.
335. Ion-Ebrașu, D., et al. *Nitrogen Functionalization of CVD Grown Three-Dimensional Graphene Foam for Hydrogen Evolution Reactions in Alkaline Media*. Materials, 2021. **14**, DOI: 10.3390/ma14174952.
336. Cheng, L., et al., *Two-dimensional hexagonal boron–carbon–nitrogen atomic layers.* 2019. **11**: p. 10454-10462.

337. Gengenbach, T.R., et al., *Practical guides for x-ray photoelectron spectroscopy (XPS): Interpreting the carbon 1s spectrum.* Journal of Vacuum Science & Technology A, 2021. **39**(1): p. 013204.
338. Hendrickson, D.N., J.M. Hollander, and W.L. Jolly, *Core-electron binding energies for compounds of boron, carbon, and chromium.* Inorganic Chemistry, 1970. **9**(3): p. 612-615.
339. Bose, D.K., K.U. Nair, and C.K. Gupta, *Production of High Purity Boron Carbide.* 1986. **7**(2-3): p. 133-140.
340. Das, A., et al., *Monitoring dopants by Raman scattering in an electrochemically top-gated graphene transistor.* Nature Nanotechnology, 2008. **3**(4): p. 210-215.
341. Casiraghi, C., *Doping dependence of the Raman peaks intensity of graphene close to the Dirac point.* Physical Review B, 2009. **80**(23): p. 233407.
342. Deng, J., et al., *Highly active and durable non-precious-metal catalysts encapsulated in carbon nanotubes for hydrogen evolution reaction.* Energy & Environmental Science, 2014. **7**(6): p. 1919-1923.
343. Deng, D., et al., *Iron Encapsulated within Pod-like Carbon Nanotubes for Oxygen Reduction Reaction.* Angewandte Chemie International Edition, 2013. **52**(1): p. 371-375.
344. Vinogradov, K.Y., et al., *Density Functional Theory Study of the Oxygen Reduction Reaction Mechanism on Graphene Doped with Nitrogen and a Transition Metal.* ACS Omega, 2022. **7**(8): p. 7066-7073.
345. Gorbachev, R.V., et al., *Hunting for Monolayer Boron Nitride: Optical and Raman Signatures.* Small, 2011. **7**(4): p. 465-468.
346. Ashton, T.S. and A.L. Moore, *Three-dimensional foam-like hexagonal boron nitride nanomaterials via atmospheric pressure chemical vapor deposition.* Journal of Materials Science, 2015. **50**(18): p. 6220-6226.
347. Paul, R., et al., *Boron–carbon–nitrogen foam surfaces for thermal physisorption applications.* Thin Solid Films, 2013. **528**: p. 187-193.
348. Paul, R., et al., *Microwave-Assisted Surface Synthesis of a Boron–Carbon–Nitrogen Foam and its Desorption Enthalpy.* Advanced Functional Materials, 2012. **22**(17): p. 3682-3690.
349. Jiang, H., et al., *Three-dimensional porous boron nitride foam for effective CO2 adsorption.* Solid State Communications, 2019. **294**: p. 1-5.
350. Wong, H., et al., *Dual role of hBN as an artificial solid–electrolyte interface layer for safe zinc metal anodes.* Journal of Materials Chemistry A, 2024. **12**(7): p. 4195-4203.
351. Xiong, T., et al., *Interfacial design towards stable zinc metal-free zinc-ion batteries with high energy density.* Journal of Materials Chemistry A, 2024. **12**(9): p. 5499-5507.
352. Lu, Y., et al., *One-atom-thick hexagonal boron nitride co-catalyst for enhanced oxygen evolution reactions.* Nature Communications, 2023. **14**(1): p. 6965.
353. Qiu, X., et al., *The release of hydrogen from ammonia borane over copper/hexagonal boron nitride composites.* RSC Advances, 2016. **6**(108): p. 106211-106217.
354. Dong, J., L. Gao, and Q. Fu, *Hexagonal Boron Nitride Meeting Metal: A New Opportunity and Territory in Heterogeneous Catalysis.* The Journal of Physical Chemistry Letters, 2021. **12**(39): p. 9608-9619.
355. Liu, S., et al., *Predicting the preferred morphology of hexagonal boron nitride domain structure on nickel from ReaxFF-based molecular dynamics simulations.* Nanoscale, 2019. **11**(12): p. 5607-5616.
356. Komissarov, L., et al., *ParAMS: Parameter Optimization for Atomistic and Molecular Simulations.* Journal of Chemical Information and Modeling, 2021. **61**(8): p. 3737-3743.
357. Zhong, J.-Q. and H.-J. Freund, *Two-Dimensional Ultrathin Silica Films.* Chemical Reviews, 2022. **122**(13): p. 11172-11246.
358. Bawaked, S. and K. Narasimharao, *Structural and catalytic properties of copper silicate nanomaterials.* Scientific Reports, 2020. **10**(1): p. 518.

359. Wang, S., et al., *Stable Cu Catalysts Supported by Two-dimensional SiO2 with Strong Metal–Support Interaction.* Advanced Science, 2022. **9**(9): p. 2104972.
360. Li, J., et al., *Silica-copper catalyst interfaces enable carbon-carbon coupling towards ethylene electrosynthesis.* Nature Communications, 2021. **12**(1): p. 2808.
361. Xu, C., et al., *Interfacing with silica boosts the catalysis of copper.* Nature Communications, 2018. **9**(1): p. 3367.
362. Yuan, X., et al., *Controllable Cu0-Cu+ Sites for Electrocatalytic Reduction of Carbon Dioxide.* Angewandte Chemie International Edition, 2021. **60**(28): p. 15344-15347.
363. Li, L., et al., *Transition Metal Induced Crystallization of Ultrathin Silica Films.* Chemistry of Materials, 2017. **29**(3): p. 931-934.
364. Xu, J., C. Mu, and M. Chen, *Structure and Properties of Ultrathin SiOx Films on Cu(111).* Langmuir, 2022. **38**(37): p. 11414-11420.
365. Hori, Y., et al., *PRODUCTION OF METHANE AND ETHYLENE IN ELECTROCHEMICAL REDUCTION OF CARBON DIOXIDE AT COPPER ELECTRODE IN AQUEOUS HYDROGENCARBONATE SOLUTION.* Chemistry Letters, 1986. **15**(6): p. 897-898.
366. Wang, Z.-Q., et al., *High-Performance and Long-Lived Cu/SiO2 Nanocatalyst for CO2 Hydrogenation.* ACS Catalysis, 2015. **5**(7): p. 4255-4259.
367. García-Contreras, M.A., S.M. Fernández-Valverde, and J.R. Vargas-García, *Pt, PtNi and PtCoNi film electrocatalysts prepared by chemical vapor deposition for the oxygen reduction reaction in 0.5M KOH.* Journal of Alloys and Compounds, 2010. **504**: p. S425-S428.
368. Jacobsohn, L.G., et al., *X-ray photoelectron spectroscopy investigation of boron carbide films deposited by sputtering.* Surface Science, 2004. **572**(2): p. 418-424.
369. Wu, B., et al., *Self-organized graphene crystal patterns.* NPG Asia Materials, 2013. **5**(2): p. e36-e36.
370. Wu, W., et al., *Control of thickness uniformity and grain size in graphene films for transparent conductive electrodes.* Nanotechnology, 2012. **23**(3): p. 035603.
371. Carozo, V., et al., *Raman Signature of Graphene Superlattices.* Nano Letters, 2011. **11**(11): p. 4527-4534.